ALGERIAN DEMOCRATIC AND POPULAR REPUBLIC
MINISTRY OF HIGH EDUCATION AND SCIENTIFIC RESEARCH

UNIVERSITY FRERES MENTOURI CONSTANTINE 1
FACULTY OF EXACT SCIENCES
PHYSICS DEPARTMENT

Order N°:
Series:

THESIS OF DOCTORAT IN SCIENCE

SPECIALITY

MATERIALS SCIENCE

Option: Semi-conductor

THEME

Deposition of ZnO Thin Films for Treatment of Water

By

FOUZIA BOURFA

Defended on: 27/12/2020

Jury committee:

President:	**Z. OUILI**	**Prof.**	**Univ. Frères Mentouri Constantine 1**
Supervisor:	**N. ATTAF**	**Prof.**	**Univ. Frères Mentouri Constantine 1**
Examiners:	**A. ZERTAL**	**Prof.**	**Univ. Frères Mentouri Constantine 1**
	A. AZIZI	**Prof.**	**Univ. Ferhat Abbes Sétif 1**
	A. Djeloul	**Prof.**	**Univ. Abbès Laghrour Khenchla**
	A. ATTAF	**Prof.**	**Univ. Mohamed Khider Biskra**

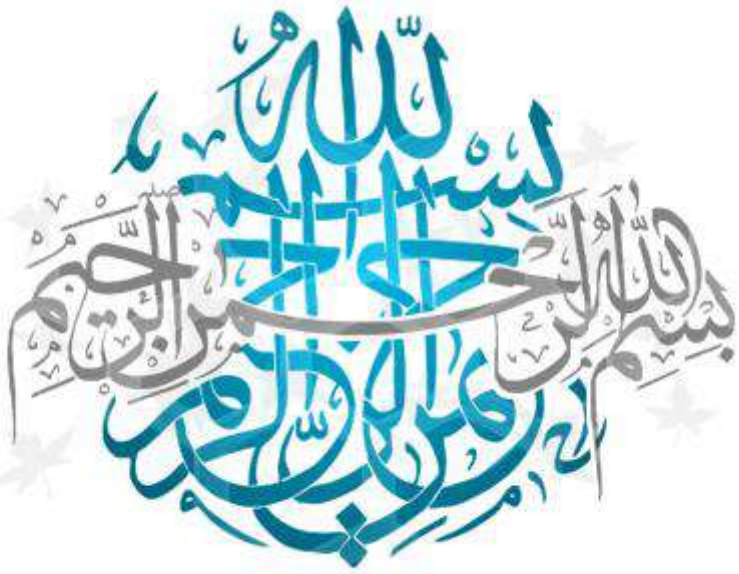
بسم الله الرحمن الرحيم

Acknowledgments

All praise goes to ALLAH, who created the whole universe and selected human as the best among all creation. This is a memorable occasion in my life to finish the writing of my PhD thesis. I begin my acknowledgement while expressing my thanks to Almighty ALLAH who always blessed and granted me the capabilities to comprehend, learn and work very hard to reach the execution of this research work.

In the course of completion of this PhD thesis, many people have directly or indirectly supported. That includes my family members, teachers, colleagues and all friends especially; ***Mouna*** *and* ***Fatima****. At this moment, I am deeply indebted to all of them and my gratitude is beyond the words.*

Firstly, I would like to express my heartiest gratitude to my supervisors Prof. ***Mohamed Salah Aida*** *and* ***Nadir Attaf*** *for their useful and inspiring guidance, and consistent encouragement. I greatly appreciate their supervision during entire PhD studies.*

I *would like to pay my sincere thanks to Prof.* ***Yusuf Selim Ocak*** *for his magnanimous guidance and support to work successfully on ZnO nanostructures and ZnO based solar cells for collaboration at SMART LAB in Dicle University Diyar Bakir, Turkey.*

I *would like to thank Prof.* ***Rayhen Gul Guven*** *and* ***Fatah Merouane*** *for her contribution, patience and guidance during my research work on antibacterial activity at Dicle University Diyar Bakir, Turkey and Laboratory of Microbiology University of Constantine 1.*

I *am also thankful to Prof.* ***Z. Ouili****, Prof.* ***A. Azizi****, Prof.* ***A. Zertal, A. Djeloul*** *and Prof.* ***A. Attaf*** *for their cooperation and acceptance to judge this modest work.*

***W**ords are lacking to express my heartiest gratitude to Dr. **Abderhamane Boutelala** for the continuous support of my PhD study and research, for his patience, motivation, enthusiasm, and immense knowledge. His guidance helped me in all the time of research and working this and without him which this thesis have not been completed.*

***F**or my family, my Mother, my father, all sisters and brothers; my words cannot describe my immense feeling of appreciation for them. Thanks for your prayers, encouragement and unforgettable sacrifices with patience throughout my life and PhD studies abroad.*

***L**ast but not least, my small family my sweet child **Anis**, my little princess **Mayssane** and their father. Words are hardly enough to express my gratitude to all of them and their endurance for my PhD studies. May **Allah** bless on all of us; Ameen.*

Fouzia Bourfaa

……"Learn from yesterday, live for today, hope for tomorrow. The important thing is not to stop questioning."

Albert Einstein

"The best way to have a good idea is to have lots of ideas."

... Linus Pauling

This thesis is dedicated to my family (Mom, Dad, my Sisters and my Brothers); and especially For my Son, my daughter and my Husband.

Contents

Contents

Chapter I

Photocatalysis : Review and Process

Chapter II

Zinc Oxide : Properties, Applications and Characterization

Chapter III

Results and Discussion : ZnO Thins Films and One Dimensional (1D) Nanostructure

III.1 ZnO THIN FILMS

Chapter IV

Applications of ZnO : Antibacterial activity, Solar Cells; Photodiode and Photosensing

Antibacterial Activity

Escherichia coli Bacterium

Dye Synthesis Solar Cells

Figure Captions

Figure Captions

INTRODUCTION

Chapter I

Chapter II

Chapter III

Chapter IV

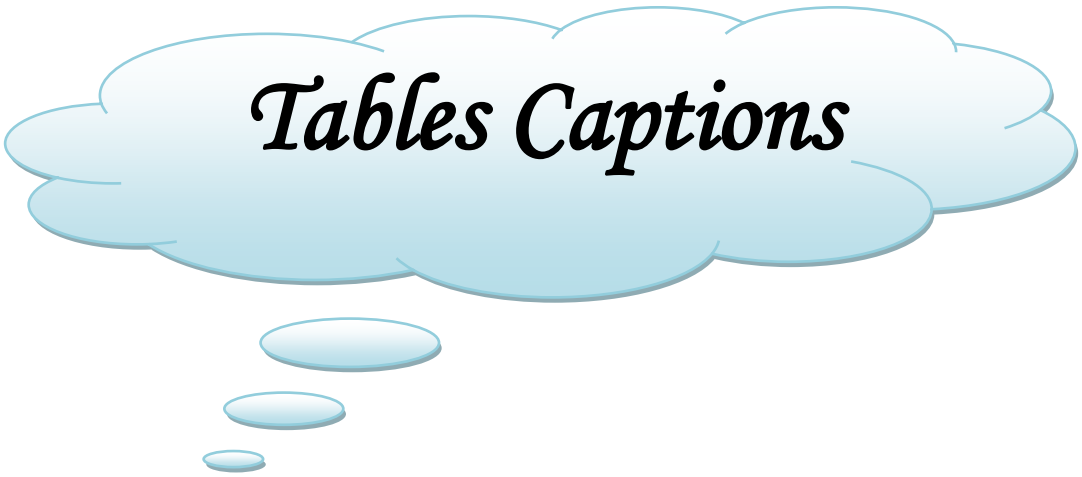
Tables Captions

Table Captions

Chapter I

Chapter II

Chapter III

Chapter IV


Introduction

Introduction

Environmental pollution and industrialization on a global scale have drawn great attention to the vital need for developing new hygienically friendly purification technologies. There is no possible living world without water. In general, water accounts almost 70 to 90 % of the weight of living organisms. One cannot imagine life without clean water. No doubt, there is no raw material in the world that more than water. Thus, the quality of this valuable resource will directly influence the normal life of human being. In general, water pollution refers to the degradation of water quality. Although natural phenomena may change the water quality and also the ecological status of water, however it cannot be considered as pollution unless it is not suitable to be used in particular application.

The growth of the world's population and industry has increased the demand for water supply. The domestic use and industrial activity especially in developed countries produce large amount of wastewater which then disposed into natural channels that may lead to high pollution risk. From a long time, many research commented that color in water can be resulted either from natural phenomenon like the presence of humic substances or from artificial phenomenon such as the disposal of dyes effluents. Light played a major role for proper development of aquatic life. Thus, the presence of large quantities of colored wastewater blocked the penetration of light into the water and subsequently causes an imbalance in their ecosystem.

According to the previous research, textile industries are one of the industries that consumed large volumes of water in the processing operations including pre-treatment, dyeing, printing and finishing. In dyeing process, water vapor is used as heating agent for the dye baths, while liquid water ensures the transmission of the dyes onto the fiber. The release of the treatment baths which are highly toxic and heavily colored after the dyeing process contributes to water pollution. One cannot estimate the total amount of pollutants being generated each time the dyestuff is discharged into the water stream. Therefore, colored water required costly treatment operations before being consumed as drinking water. The critical state of the water bodies has raised public concern and awareness as well as stringent legislations being imposed by the government. This has encouraged researchers in developing techniques such

as electro-flocculation, reverse osmosis, chlorination, adsorption and ozonation to minimize water pollution and restoring the natural state of the water bodies.

During the past several decades, fast and relatively uncontrolled population growth and also industrial, agricultural and technological developments have adversely affected the environment and human health [1, 2]. Especially wastewater effluents of industrial manufacturing companies contain toxic organic compounds [3].

Textile dyes and other industrial dyestuffs constitute one of the largest groups of organic compounds that represent an increasing environmental danger. About 1–20% of the total world production of dyes is lost during the dyeing process and is released in the textile effluents [4]. The release of those colored waste waters in the environment is a considerable source of pollution and can originate dangerous byproducts through oxidation, hydrolysis, or other chemical reactions taking place in the wastewater phase [5].

Decolorization of dye effluents has therefore received an increasing attention. For the removal of dye pollutants, traditional physical techniques (adsorption on activated carbon, ultrafiltration, reverse osmosis, coagulation by chemical agents, ion exchange on synthetic adsorbent resins, etc.) can generally be used efficiently. Nevertheless, they are non-destructive, since they just transfer organic compound from water to another phase, thus causing secondary pollution. Consequently, regeneration of the adsorbent materials and post-treatment of solid-wastes, which are expensive operations, are needed [6-9].

Due to the large amount of aromatics present in dye molecules and the stability of modern dyes, conventional biological treatment methods are ineffective for decolorization and degradation [10]. Furthermore, the majority of dyes is only adsorbed on the sludge and is not degraded [11, 12].

Utilization of solar light is important for decontamination of large outdoor areas. Heterogeneous photocatalytic systems via metal oxide semiconductors like TiO_2 and ZnO are capable of operating effectively and efficiently for waste water treatment which has been discussed along with other nanotechnology routes that can be useful for water treatments. In recent years, Zinc Oxide (ZnO) as a transparent conducting oxide (TCO) films has aroused much interest with their outstanding properties such as high optical and electrical properties, doping suitability, being non-toxic, its high resistivity control, its high chemical, mechanical, and thermal stability, as well as being abundant in nature, and cost effective. Due to these superior properties, ZnO is a good candidate for various fields and applications. Among all applications, we are interesting to use ZnO thin films in photocatalysis activity, solar cells and

antibacterial activity. Figure 1 shows an advertisement label for zinc oxide in1868 by USA Library of Congress. This figure indicates that from a long times ago until now, further investigations and studies in several areas is still demanded to benefit from the unique features of ZnO with different shapes and morphologies and from to date successful studies.

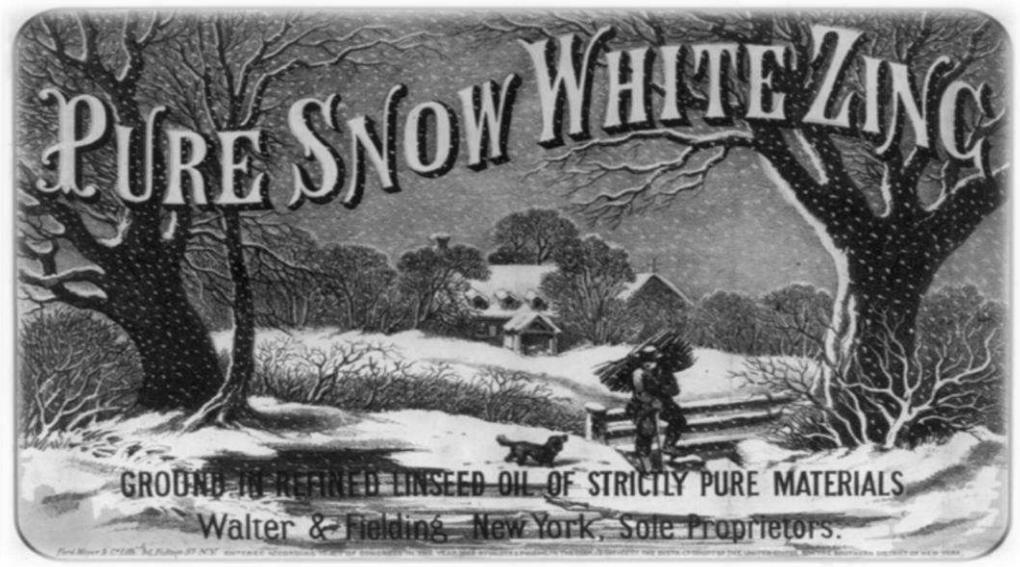

Figure 1: *Advertisement label for zinc oxide, 1868 (USA Library of Congress) [13]*

Bacterial infectious diseases are serious health problem that has drawn the public attention in worldwide as a human health threat, which extends to economic and social complications. Increased outbreaks and infections of pathogenic strains, bacterial antibiotic resistance, emergence of new bacterial mutations, lack of suitable vaccine in underdeveloped countries, and hospital-associated infections, are global health hazard to human, particularly in children. For example, infections by Shigella flexneri cause 1.5 million deaths annually, due to contaminated food and drinks by these bacteria [14]. Thus, developing novel antibacterial agents against bacteria strains, mostly major food pathogens, such as *Escherichia coli O157: H, Campylobacter jejuni, Staphylococcus aureus, Pseudomonas aeruginosa, Enterococcus faecalis, Salmonella types, and Clostridium perfringens*, has become utmost demand. In this section of this survey, the bacterial test used two kind of bacteria; gram negative of k. Pneumoniae and E. coli on ZnO films on tissue and glass.

In this thesis work, we are also interested in NPs of metallic silver. Silver-based compounds, being biocompatible at effective concentrations, are particularly studied as agents for combating microorganisms when they are in the form of non-agglomerated and well dispersed particles [15-19]. On the one hand, the antibacterial effect of silver cations is well

known and has already been studied in detail in the literature [20]. On the other hand, metallic silver NPs have recently shown promising potential as anti-bacterial or anti-microbial agents [21]. The use of metallic silver NPs with unique physico-chemical properties thus opens up the possibility of a new generation of active antibacterial materials whose mechanisms of action are still insufficiently understood [22]. The second section of this survey is regard about the synthesized silver nanoparticles with zinc oxide for testing against Gram – of K. Pneumoniae and Gram – of E. coli.

Another interesting was focused on solar cells based on ZnO thin films. Heterojunction solar cells consisting of a wide band gap transparent conductive oxide (TCO) on a single crystal silicon wafer have a number of potential advantages such as an excellent blue light response, simple processing steps, and low processing temperatures [23]. One promising type of TCO/Si solar cells uses undoped ZnO on Si wafer. ZnO/Si heterojunctions are of particular interest in the integration of optoelectronic devices utilizing the hybrid advantages of the large exaction binding energy of the ZnO thin film and the cheapness of Si substrates. A huge number of research and studies were used zinc oxide for photovoltaic applications. However, the purpose of this thesis is to synthesize and characterize ZnO thin films using zinc nitrate as a precursor through the ultrasonic spray deposition method for a possible application for the photovoltaic conversion of solar energy.

The thesis is organized as the following chapters:

Chapter I presents the global environment problem and the need for an eco-green and high efficient photocatalysis. The heterogeneous photocatalysis, photocatalysts, Applications of photocatalysts and the mechanism of photocatalytic degradation will be briefly described. The focus will be on the photodegradation of organic dyes and the role of each parameter will play in improving the degradation efficiency of these dyes.
The Objective of this chapter is to review the photocatalysis, the degradation mechanism and investigation of the operational conditions of the photocatalytic degradation processes in order to achieve the best removal efficiency to guarantee complete decolorization of Reactive red (RR) 184 and Methylene Blue (MB).

Chapter II reviews the general properties of Zinc oxide semiconductor, and the different applications of ZnO in diverse fields. Different synthesis methods (chemical and physical) are illustrated and described to grow ZnO thin films and ZnO nanostructures. A review of past

literature efforts is presented for the described synthesis methods and the characterization techniques. This chapter is aimed at providing a broad introductive background for the growth of ZnO thin films and one Dimensional ZnO Nanostructure.

Chapter III presents the details of the synthesized methods and characterization properties of the ZnO thin films and Nanostructures. Morphology, Structural, optical and electrical characterizations for ZnO thin films and ZnO nanostructures are analyzed. This chapter provides experimental details applied during my PhD research for different ZnO thin films and nanostructures for their use in photodegradation of Reactive Red 184 and Methylene Blue.

Chapter IV describes the procedure of deposition zinc oxide thin films, the synthesized silver (Ag) Nanoparticles and preparation of bacteria. Structural, morphological and optical Characterization of the films prepared with and without Ag NPs were presented and analyzed. This chapter based on the application of ZnO thin films as antibacterial agent, against strains of Gram - of Klebsiella Pneumoniae and Escherichia coli, and as dye synthesis solar cell. This chapter summarizes the major findings made during this doctoral research, and concludes with recommendations for future work in this very promising class of processed photovoltaic devices.

Chapter I

Photocatalysis: Review and Process

This Chapter is about the photocatalysis activity; a brief review on the Heterogeneous photocatalysis, photocatalysts, Applications of photocatalysts and the mechanism of photocatalytic degradation. Above this survey, various parameters affecting the photocatalysis such as Adsorption, Intensity of light, pH, Size, Surface properties, and Activation wavelength.

I. Introduction

The world faces a growing challenge for adequate clean water due to threats coming from increasing demand and decreasing supply. Although there are existing technologies for water disinfection, their limitations, particularly the formation of disinfection-by-products, have led to researches on alternative methods.

*Dy*es are stable chemical compounds, easy to synthesize and present a wide variety of colors. They are widely used in the textile and printing industries. However, their discharge into the environment causes water pollution both on aesthetic and toxicological profiles [1, 2]. The degradation of these organic pollutants by photocatalysis, in a sustainable development option, has become one of the alternative modern techniques for wastewater treatment, particularly when using a renewable energy source [3]. Research is continuously developing to find future catalysts with adequate photo-catalytic properties [4, 5]. Generally speaking, the activity of these photocatalysts is tested in the degradation of the model molecules [6]. Indeed, these dyes must be transparent in the range of the working wavelength.

I.1.Background on Photocatalysis

I.1.1 Heterogeneous photocatalysis

The term photocatalysis can be defined as a combination of the words ‘photoreaction’ and ‘catalysis’. It refers to a chemical transformation of a species induced by the absorption of electromagnetic radiation, or photoreaction, which is accelerated by the presence of a catalyst. This definition includes photosensitization, where a chemical compound may undergo a transformation due to the absorption of light by another compound - the photosensitiser, but it does not apply to the acceleration of a thermal reaction by electromagnetic irradiation. The photocatalyst can accelerate the photoreaction in one of two ways: it can interact with a substrate in its original or excited state, or it can interact with the products of the photoreaction.

Heterogeneous photocatalysis can be described as the acceleration of a photoreaction in which the reactant and the photocatalyst exist in different phases, and where reactions occur on the surface of the photocatalyst. There are two main categories that reactions in heterogeneous photocatalysis can be grouped into and this depends on whether it is the reactant or the photocatalyst that is the subject of the initial photoexcitation. When the photocatalyst is

induced into a photo-excited state, and transfer of an electron to an adsorbed molecule in its ground state occurs, this is termed a sensitised photoreaction. If the adsorbed molecule, such as a dye molecule for example, is initially photo-excited and reacts with a ground state photocatalyst, this is known as a catalyzed photoreaction. These two definitions represent different pathways under which photocatalytic reactions can occur. In both cases the end result is the reduction or oxidation of a target compound resulting in its subsequent conversion into a desired product or products.

The initial interest in heterogeneous photocatalysis with semiconductors for the purposes of solar fuel production and other photocatalytic reactions such as the breakdown of organic pollutants, was driven by the work of Fujishima and Honda in 1972 [7]. They reported the photolysis of water by the UV light irradiation of a titanium dioxide (TiO_2) single crystal subject to a small electrical bias with a platinum counter electrode. Their discovery represents a landmark into the research of photo-induced redox reactions on TiO_2 photocatalysts via solar energy conversion.

I.1.2 Photocatalysts

Semiconductor solids that promote chemical reactions in the presence of light without being consumed are known as photocatalysts. To be a good photocatalyst the semiconductor material should be photoactive, non-toxic, and photostable and should offer the ability to be photocatalytically activated under sunlight. TiO_2, ZnO, WO_3, CdS, ZnS, $SrTiO_3$, SnO_2, WSe_2, Fe_2O_3, etc. are among semiconductor solids used as photocatalysts [8].

Heterogeneous photocatalysis utilizing different semiconductor photocatalysts such as TiO_2, ZnO, SnO_2, ZrO_2 and CdS has established their effectiveness in pollutant degradation and eventually complete mineralization [9-15].

Photocatalyst when compared to other photocatalysts is due to its high activity, chemical stability, very low aqueous solubility, non-toxicity, low cost and environmentally friendly characteristics [16].

The range of the optical spectrum where these semiconductor metal oxides are activated is important to determine whether or not the optical activation is possible under sunlight. Semiconductors with superior photocatalytic properties are those with wide band gaps such as TiO_2 and ZnO. Their photocatalytic performance is determined through the process of optical absorption of the incident photons in the UV, and subsequent photogeneration of electron-

hole pairs that exhibit dissimilar parity in the respective conduction and valence bands, leading to low recombination rates [7]. On the other hand, a high photocatalytic activity in daylight can be achieved with photocatalysts that have bandgap energies smaller than 3 eV to cover a significant part of the solar spectrum but small bandgap semiconductors have low photoactivities [17].

The nanoscaled catalyst has much higher photocatalytic activity than the bulk catalyst due to the following reasons;

- Quantum size effect: as the particle diameter within the nanoscale (1-100 nm) got smaller, the valence band and conduction band change into discrete levels, the energy gap change broader means that the valence band electric potential changes more positive, otherwise the conduction electric potential changes more negative. Then the oxidation reduction capability of the holes and electrons is enhanced, and the oxidation activity of nano catalyst is improved;

- Bigger specific surface area: There are more atoms on the surface; it improves the adsorption capability of the catalyst to organic pollutants due to improved larger number of active sites.

The efficiency of photocatalysis is related with the time spent by electrons and holes to get to the surface of the particles. To the nanoparticles, the particle diameter is very small, so it's very easy for the carriers moving from the inside to the surface, and causing oxidation or reduction reaction. The smaller the particle diameter, the shorter time may be spent by carriers diffusing from inside to the surface. It can get higher separated efficiency, and lower probability of electrons and holes' combination. As a result, the higher photocatalytic activity can be got. Therefore, the nano-zinc oxide has more photocatalytic efficiency than the common zinc oxide [18-23].

I.1.3 Process underlying behind photocatalysis

Degradation of many pollutants, especially organic ones, on the surface of a photocatalyst is promoted in the presence of oxygen and water, with incident light having photon energies larger than the bandgap energy of semiconductor photocatalyst. The photons absorbed in the photocatalyst excite the electrons from the valence band to the conduction band of the semiconductor photocatalyst, producing electron-hole pairs. Following optical absorption of

light, two reactants are adsorbed on the surface of the photocatalyst. They are reduced and oxidized. These reactions are allowed by the band energy position of semiconductor and the redox potentials of the adsorbates. In the reduction mechanism, the redox potential of the adsorbate (acceptor) is below the conduction band of the semiconductor. Excited electron is transferred from the conduction band to the adsorbed particle. In the oxidation mechanism, the redox potential of the adsorbate (donor) is above the valence band of the semiconductor to donate an electron to the vacant hole in the valence band. Oxygen and water are the adsorbates in the photocatalytic reactions [24].

I.1.4 Applications of Photocatalysts

Photocatalysts are of particular interest because one of the reactants, light, is in essentially limitless supply. Photocatalysts have widely varying applications. One such application is waste water treatment [25], which was developed and used in Japan in as early as 2001. This reactor decomposes dioxins and environmental hormones using UV light instead of incineration or harsh chemicals. Photocatalysts have also been identified as able to degrade toxic chlorinated carbons such as carbon tetrachloride [26], generating relatively harmless carbon dioxide and hydrochloric acid as byproducts. Using photocatalysis to safely degrade chlorinated hydrocarbons would cut down on a tremendous amount of waste, as these compounds are common chemical solvents. Additionally, photocatalysts can be used for sterilization of microbial cells [27]. This was achieved using a titanium dioxide photocatalyst to oxidize a coenzyme, preventing respiration in the cells. Finally, photocatalyst find tremendous potential in their use to split water into its elements, hydrogen and oxygen [24]. Much effort has been put into this ‘artificial photosynthesis’ where light is turned into an energy source though artificial means. The products generated, hydrogen and oxygen, have wide uses, including in fuel cells to power cars or generate electricity. Photocatalysts have the potential to remove us from dependence on the dwindling supply of fossil fuels and move toward abundant, cheap energy.

I.1.5 Semiconductors

Semiconductors are ideal materials for heterogeneous photocatalysis since their unique electronic structure allows for the spatial separation of excited charge carriers upon the absorption of photons with energies larger than or equal to the semiconductor energy band

gap. The spatially separated charge carriers can then react with target species adsorbed to the surface of the semiconductor in reduction or oxidation (redox) reactions. If the semiconductor remains unchanged after continuous and exothermic interfacial charge transfer, the process can be described as heterogeneous photocatalysis [28].

I.1.5.1 Origin of the electronic band structure of semiconductors

The electrons associated with a single atom are known to occupy atomic orbitals at discrete energy levels. When a number of atoms come together to form a solid the electron wavefunctions occupying neighboring atoms begin to overlap. The Pauli Exclusion Principle states that the electrons within a system cannot occupy the same 36 quantum state and this leads to the splitting of the energy levels within the atomic orbital. Since the number of electrons associated with the large quantity of atoms that make up a solid is so vast, and the difference between the energy states of the electrons is infinitesimally small, the electronic structure can be approximated to a continuous band. Figure I.1 shows the splitting of the energy levels within the electron orbitals 2s and 2 p as a function of the interatomic separation, where the 2 s orbital contains 2 N states and the 2 p orbital contains 6 N states (N being the number of atoms in the solid). As the distance between the orbitals decreases, the orbitals merge and split into two bands each containing 4 N states.

At a temperature of zero Kelvin the lower band, known as the valence band (VB) is completely filled with electrons while the higher band, or conduction band (CB) is completely empty.

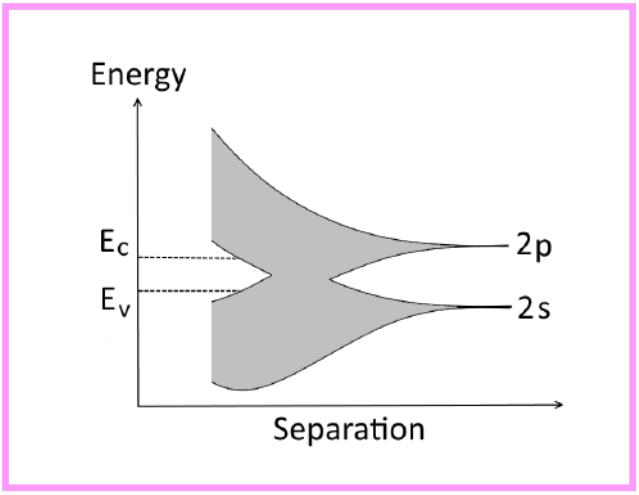

Figure I.1: *The splitting of electronic energy levels results in the formation of a continuous electronic band*

The band structure of semiconductors is an extension of the concept of molecular orbitals where the regions of interest are the highest occupied molecular orbital (HOMO), which in the semiconductor forms the VB and the lowest unoccupied molecular orbital (LUMO), which is the CB.

The region that makes up the difference in energy between the highest energy level in the VB and the lowest energy level in the CB is a forbidden zone where electrons cannot exist and is known as the energy band gap (Eg). The origin of the band structure as a function of the number of electronic orbitals is shown in Figure I.2.

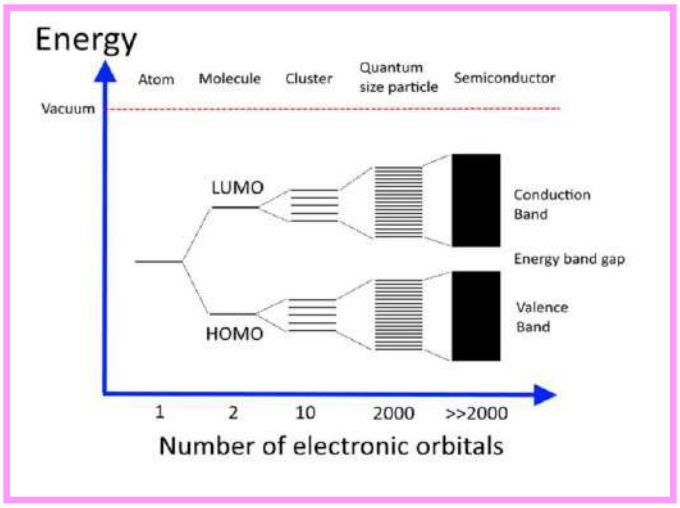

Figure I.2: *Origin of the band structure of semiconducting materials [29]*

The electrical conductivity of a material requires the movement of electrons to occupy partially filled states in the CB of that material. In the case of metals, there is an overlap of the CB and the VB, and so the vacant states in the CB can be readily occupied. Insulators have a relatively large Eg such that electrons cannot be promoted to the CB and so the material is not electrically conductive. However, the Eg for semiconductors is sufficiently small that electrons may be promoted from the VB to the CB via some transfer of energy to the material. The promotion of an electron to the CB creates an electron vacancy in the VB that can be thought of as a positively charged hole.

The hole is a mobile entity since it can be filled by another electron, which in turn creates a vacancy in the space where it transferred from. The conductivity of metals, semiconductors and insulators as a function of the Eg is shown in Figure I.3.

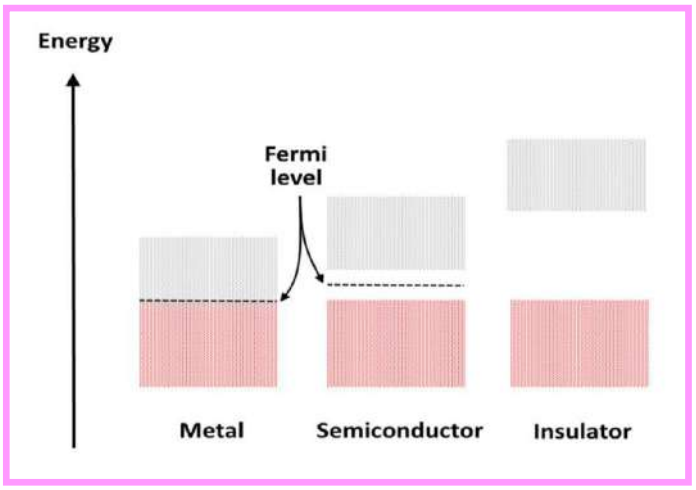

Figure I.3: *The conductivity of solid state materials in terms of the band gap value*

Electron transfer from the VB to the CB in a semiconductor can be achieved via an excitation that is sufficiently energetic to overcome Eg. Furthermore, there are two different types of band gap that exist for semiconductors and the type of transition that an electron has to make is determined by the lattice structure of the semiconductor. The crystal structure of semiconductors can be described by its Bravais lattice. The Fourier transform of this lattice gives the reciprocal lattice of the crystal in what is known as momentum or k space. The minimum energy state of the CB and the maximum energy state of the VB, and consequently the type of transition that electrons must make, are determined by the value of the k vector. If the values of the k vector for the VB and CB are equal to each other the band gap is known as direct, Figure I.4 a. However, if the k vectors are not equal the band gap is known as indirect, Figure I.4 b.

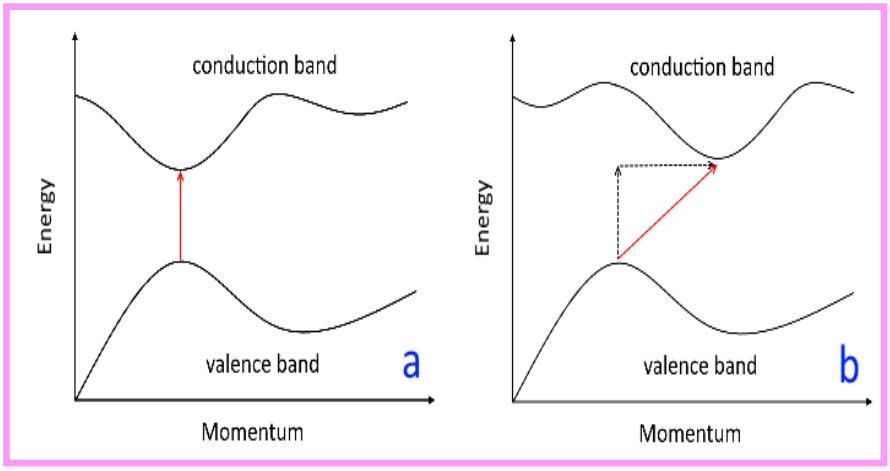

Figure I.4: *The type of transition electrons make in semiconductors that have (a) a direct band gap and (b) an indirect band gap*

In semiconductors with a direct band gap, the absorption of photons can provide the energy required to produce an electron-hole pair as there is no change in momentum. However, if the band gap is indirect a change in momentum is required and the absorbed photon must interact with a lattice vibration, known as a phonon, in order to gain or lose the momentum necessary to complete the transition to the conduction band. The absorption process can also proceed in reverse where photons are emitted as the electrons and holes recombine in the valence band. The transitions are significantly slower for semiconductors with an indirect band gap since three entities; an electron, a photon and a phonon must intersect as opposed to just two, as is the case of semiconductors with a direct band gap.
The photocatalytic properties of a semiconductor are thus directly related to the magnitude of its Eg (and type of transition), which is typically between 1 and 4 electron volts (eV). The band gap is 0 eV for conductors and greater than 4 eV for insulators [30].

There is a large range of materials that have been discovered over the last few decades with suitable Eg values for photocatalytic reactions and some of these common elemental and compound semiconductors are shown in Table I.1.

Table I.1: *Eg values of some well known semiconductors [31].*

Semiconductor	*Band gap Energy (eV)*	*Wavelenght (nm)*
ZnO	3.35	370
TiO_2 (anatase)	3.20	387
TiO_2 (rutile)	3.00	413
CdS	2.42	512
GaP	2.30	539
CdSe	1.70	729
CdTe	1.50	827
GaAs	1.40	886
InP	1.35	918
Si	1.17	1060

I.1.5.2 Band engineering

The Eg of a semiconductor can be manipulated by a process called doping. Doping consists of the introduction of impurities to the bulk of the material. These impurities occupy energy states close to either its VB or CB edges, Figure I.5. This results in electrons or holes occupying energy states, and requiring less energy to be promoted to the CB. A semiconductor is considered p-type if the impurities introduced create vacant states, or holes, close to the upper edge of the VB thus promoting easier transition of electrons. The majority carriers in p-type semiconductors are holes. N-type semiconductors are doped with impurities that introduce electron states close to its CB where the majority carriers are electrons.

Doped semiconductors are classed as extrinsic, while undoped semiconductors are known as intrinsic and may also be p-type or n-type. In extrinsic semiconductors the redistribution of charge carriers within the material will alter the position of the Fermi level.

The Fermi level is an important parameter in solid state materials that determines its electronic properties. At thermodynamic equilibrium, the Fermi level represents a region of energy states at which there is a 50% probability of it being occupied by electrons. In an intrinsic semiconductor, the Fermi level lies at a value equidistant from the CB and the VB. For p-type semiconductors, the Fermi level lies close to the VB, while for n-type semiconductors the Fermi level lies close to the CB.

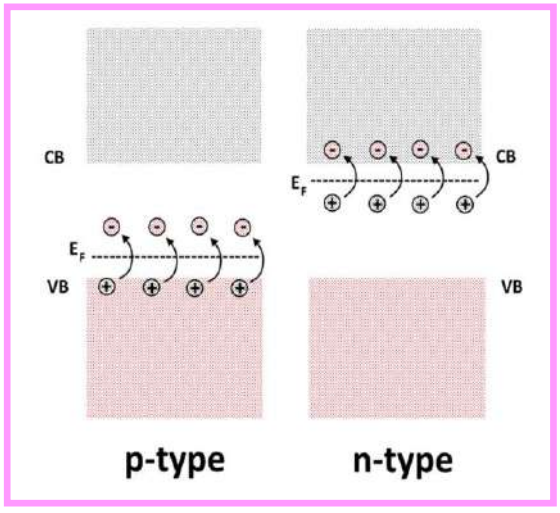

Figure I.5: *Impurities introduced to a material increasing the number of vacant energy states close to the VB results in a p-type semiconductor (left). Impurities that add electronic states close to the CB edge results in an n-type semiconductor*

As described above, the doping of semiconductors results in the modification of its band structure and this can have beneficial effects in terms of improving its physical properties for photocatalytic applications.

I.2. Semiconductor photochemistry

The generation of an electron-hole pair in a semiconductor allows for the conversion of light into electrical or chemical energy and is the basic principle that underpins the study of photoelectrochemistry and photocatalysis [29, 31–34]. The absorption of a super-band gap photon, leading to photocatalytic redox reactions on the surface of the semiconductor is illustrated in Figure I.6. Photocatalysis can be summarized as the photoexcitation and separation of charge carriers, the transportation of charge within the material, and surface charge transfer. Photoexcitation of a semiconductor with electromagnetic radiation equal to or exceeding Eg induces a charge separation in the material. Incident super-band gap photons are absorbed by electrons which are promoted from the semiconductor VB to its CB. As the excited electrons are delocalized from the VB, electron-hole pairs are created and diffuse towards the surface of the material.

$$e^- + A \rightarrow A^- \quad \textbf{(I.1)}$$

$$h^+ + D \rightarrow D^+ \quad \textbf{(I.2)}$$

Photogenerated electrons and holes that reach the surface of the semiconductor react with electron acceptors in reduction reactions or with electron donors in oxidation reactions (represented by A and D in Figure I.6), which are chemical species adsorbed on the surface of the material

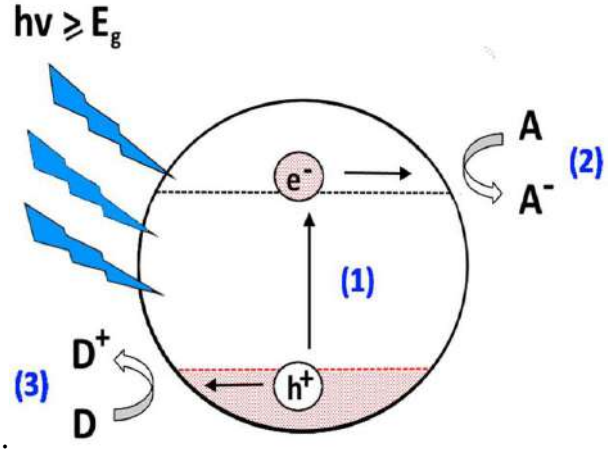

Figure I.6: *The origin of the generation of an electron-hole pair as a result of the absorption a super-band gap photon due to incident irradiation on a semiconductor particle*

One of the main limitations in semiconductor photocatalysis is the recombination of photogenerated carriers. This process occurs between the photo-generation of an electron-hole pair and the surface charge transfer in the process described in Figure I.6. After the photo-induced charge separation in the semiconductor, electrons and holes must reach the surface of the material to react with adsorbed chemical species via surface charge transfer. However, a large proportion of the excited charge carriers recombine before reaching the surface, dissipating the absorbed energy as heat and as a result no redox reactions can take place with adsorbed species.

I.2.1 Parameters affecting photocatalysis: adsorption, intensity of light, pH, size, surface properties, and activation wavelength

Degradation mechanism takes place on the surface of the photocatalyst. The concentration of the adsorbate directly affects the photocatalytic degradation rate of the pollutants to be degraded [35, 36]. Photocatalytic degradation rate is linearly dependent with light intensity at low intensities. It depends on the square root of light intensity for medium intensities. At high intensities photocatalytic degradation rate is independent of the intensity of light [37, 38].

* The effect of pH on photocatalytic degradation varies due to the kind of semiconductor used and the kind of adsorbed pollutant [39]. Increasing or decreasing pH affects the adsorption of the pollutant and thus, the degradation rate. PH affects the surface charge of the photocatalyst and the ionizability of the pollutant. Adsorption is enhanced at lower pH values. Strongly adsorbed pollutants degrade faster. At higher pH values above pH 9, degradation rate is also enhanced due to the increased OH^- anions on the photocatalyst surface. Therefore all these rates depend on the type of catalyst and the adsorbed pollutant [35, 40, and 41].

* The particle size of photocatalysts is an important parameter that affects photocatalytic activity. Decreasing the size of the catalyst, surface to volume ratio is increased, thus photocatalytic activity is increased. Nanosized semiconductors are widely used for their superior photocatalytic properties [42, 43].

* The surface properties of semiconductor photocatalysts also affect the photocatalytic activity. It was shown that surface morphology and crystal structure have a direct

effect on the photocatalytic activity of TiO_2 sol-gel films. Heat treatment can modify crystal structure leading to an increased photocatalytic activity [44].

* The degradation mechanism is promoted with the absorption of light by the semiconductor photocatalyst. In optical activation, electrons are excited from the valence band to the conduction band leading to e-h pair formation. The photon energy of the incident light should be above the band gap energy of the semiconductor. So activation wavelength is an important parameter for the photocatalytic reactions. Most commonly used photocatalysts are wide band gap semiconductors that can be activated in UV light. However electromagnetic radiation of sun has only 7% UV content that strikes the atmosphere, which decreases more during penetrating the atmosphere [45]. According to Sasaki [46], the UV part of solar radiation detected on the Earth in 1990-1992 was not more than 0.145% at 290-320 nm and 4.1% at 320-400 nm.

* Many properties of photochemical processes change as the semiconductors change scale from bulk to nanorange. Nanosized semiconductors exhibit special thermodynamic, magnetic, photochemical, photo-physical, and electro-physical properties. When semiconductors are in the nanoscale regime, their size has significant effects on their properties. Changing the size of such semiconductor nanoparticles opens up the opportunity to control their characteristics [47].

* Varying semiconductor nanoparticle size strongly affects the semiconductor light wave interaction and the resulting processes. These processes depend on the optical absorption of light, dynamics of photo-generated exciton, the consequences of electron-hole recombination, and the photo-chemical reactions in the presence of reagents adsorbed on the semiconductor surface [48]. The size effects in semiconductor nanoparticles can be divided into two. The first one is the result of increased surface to volume ratio and change in surface roughness is observed in semiconductor nanoparticles of 10-100 nm in size. The other is the change in the electronic state of the semiconductor due to the quantum size effects dominating especially below a critical size (~10 nm) at room temperature. The critical size, which is the threshold for the quantum size effects, differs for different semiconductors,

depending on the chemical structure of the nanoparticle. It is comparable to the De Broglie wavelength of the free electron [49].

I.2.2 Factors influencing photoactivity of semiconductors

The value of Eg, the recombination rate of charge carriers and the surface charge transportation properties in semiconductors are the main parameters that can significantly affect their photoactivity. These mechanisms are influenced by the electronic, bulk and surface structure, which are intrinsic properties of the semiconductor. Other factors that influence the photocatalytic efficiency of a reaction are associated with the semiconductor size and morphology, and are considered extrinsic factors.

The conductive properties of semiconductors arise from their unique electronic band structure which allows for the movement of electrons induced via thermal or photochemical excitation. Nonetheless, this band structure can be a limiting factor to the photoactive properties of a photocatalytic material concerning reactions under solar or visible light irradiation. This is because the energy required to initiate the movement of electrons can be greater than the energy associated with the incident light, in which case, electrons cannot be promoted to the CB. Another limiting factor is the lifetime of the excited charge carriers and the charge transportation properties within the material, which is highly dependent on its crystal structure [50]. The other parameter affecting the photocatalytic activity of a semiconductor is related to the transportation of charge carriers at its surface to adsorbed species. This may be influenced by the introduction of heterostructures on the catalyst surface.

Approaches to improving the limitations of semiconductors in photocatalytic reactions fall into three general categories: crystal growth, doping and heterostructuring. These aspects of semiconductor modification can have a significant impact on the optical response range, the redox potentials of excited charge carriers and on the bulk and surface charge transportation properties of the material.

One of the most widely studied semiconductors for photocatalytic applications in the last few decades has been TiO_2 and ZnO. As such, the modification processes and subsequent effects are among the most documented in the field.

Its use in a vast range of photo-driven applications has been largely due to the beneficial modification of its physical properties via a greater understanding of the mechanisms

governing the crystal structure, the concentration and nature of dopants, and the heterostructure engineering. This correlation between the main aspects of the crystal growth, doping and heterostructuring are shown in Figure I.7.

Figure I.7: *The relation between crystal growth, doping and heterostructure in semiconductor photocatalysis [51]*

I.4 Photocatalytic degradation mechanism

Generally, there are four essential key steps in the mechanism of heterogeneous photocatalysis on the surface of semiconductor, as follows: (1) charge carriers generation, (2) charge carriers trapping, (3) charge carriers recombination and (4) photocatalytic degradation of organic pollutants.

I.4.1 Charge carriers generation

Upon irradiation of semiconductor with UV light energy of equivalent or greater than its band gap energy, an electron is excited from the valence band to the conduction band. Figure I.8 illustrates the mechanism of electron–hole pair's generation when the semiconductor particle is irradiated with sufficient light energy *(hv)*. The excitation leaves behind a positive hole in the valence band and therefore creating the electron–hole pair.

$$MO + h\upsilon\ (UV) \rightarrow MO\ (h^{+}+e^{-});\ MO:\ metal\ oxide \qquad (I.3)$$

I.4.2 Charge-carriers trapping

The $e–h+$ pair is trapped by electron and hole scavengers and inhibited from recombination.

The positive hole is a strong oxidant which can either directly oxidize adsorbate pollutants or react with water or electron donors such as hydroxyl ions OH^- to form hydroxyl radical $HO^{\bullet}$, which is also a potent oxidizing agent.

$$h^{+} + H_2O \rightarrow OH^{\bullet} + H^{+} \qquad (I.4)$$

$$h^{+} + OH^{-} \rightarrow OH^{\bullet} \qquad (I.5)$$

On the other hand, it is important for the electron in the conduction band (CB) to be scavenged by an electron acceptor to suppress its recombination with the trapped hole. One of the efficient electron acceptors is molecular oxygen (O_2). Through the reduction of O_2 with electron, reactive superoxide radical anions $O_2^{\bullet-}$ are produced. Together with other oxidizing species such as hydroperoxyl radicals $HO_2^{\bullet}$ and hydrogen peroxide (H_2O_2) are also subsequently formed. The additional $OH^{\bullet}$ radicals are generated through the following reactions:

$$O_2 + e^{-} \rightarrow O_2^{\bullet-} \qquad (I.6)$$

$$O_2^{\bullet-} + H^{+} \rightarrow HO_2^{\bullet} \qquad (I.7)$$

$$H_2O_2 + e^{-} \rightarrow OH^{\bullet} + OH^{-} \qquad (I.8)$$

$$H_2O_2 + O_2^{\bullet-} \rightarrow OH^{-} + OH^{\bullet} + O_2 \qquad (I.9)$$

$$H_2O_2 + h\nu \rightarrow 2OH^{\bullet} \qquad (I.10)$$

I.4.3 Charge-carriers recombination

In competition with charge transfer process, there is the opportunity that both $e–h+$ pair recombination and trapped carrier recombination happen. This recombination can occur either in the volume of the photocatalyst or on the surface of photocatalyst with a byproduct of heat liberation.

$$MO\ (e^{-}+h)^{+} \rightarrow MO + heat \qquad (I.11)$$

I.4.4 Photocatalytic degradation of organic compounds

The primary photoreactions **(**I.3**)–(**I.15**)** indicate the important role of e^- – h^+ pairs in photocatalytic degradation. Essentially $OH^\bullet$, $HO^\bullet_2$ and $O^\bullet_2$ radicals as well as photogenerated hole (h^+) are highly reactive intermediates that will attack repeatedly in the reacting system and ultimately lead to complete mineralization of the organic pollutant. The following reactions illustrate the role of OH• *h*+ and *e*- as oxidative reductive species [52].

$$R\text{-}H + OH^\bullet \rightarrow R^\bullet + H_2O \quad (I.12)$$

$$R + h^+_{vb} \rightarrow R^+ \quad (I.13)$$

$$R + e^- \rightarrow R^\bullet \quad (I.14)$$

$$R^\bullet + O_2 + HO_2^\bullet \rightarrow CO_2 + H_2O \quad (I.15)$$

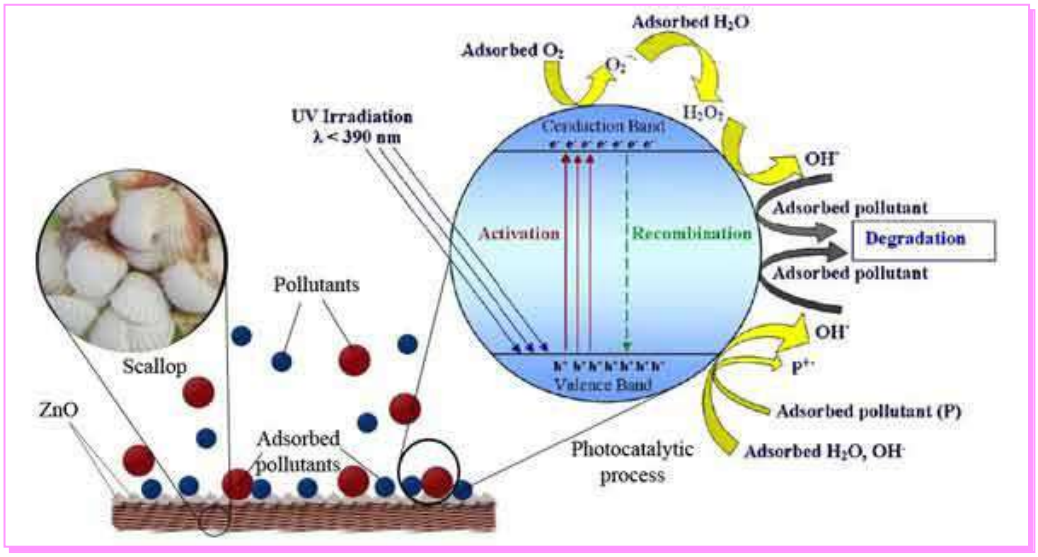

Figure I.8: *Schema summarizing mechanism of photocatalytic degradation of organic compounds utilizing metal oxide semiconductor as photocatalyst (ZnO) [53]*

I.5 Dyes

I.5.1. Definition of Dye

A dye is a colored substance that has specific affinity to a given substrate. Dyes are applied to various substrates (textiles, leather, paper, hair *etc*.) from liquid in which they are completely, or at least partially soluble. The dye is generally applied in an aqueous solution, and may require a mordant to improve the fastness of the dye on the fiber.

Both dyes and pigments are colored, because they absorb only some wavelengths of visible light. Dyes are usually soluble in water whereas pigments are insoluble. Some dyes can be rendered insoluble with the addition of salt to produce a lake pigment.

Coloration is a key factor in the commercial success of textile products, particularly those with high fashion content, especially garments, furnishings and upholstery. Excluding fluorescent brighteners, the dye consumption per capita is approximately 150 g per year, serving an average consumption of textile fiber of about 1.45 million per year per inhabitant. Despite, the high economic importance of the textile industry in the world, this is responsible for over 7×10^5 metric tons of about 10,000 different types of dyes on pigment produced each year. During dye use among the several industries responsible for pollution of the aquatic ecosystems, the textile dyeing and printing industries are major players, around a half of a ton of these dyestuffs are lost per day to the environment. Approximately 200 liters of water are required, for every kilogram of finished cotton fabric. The reactions necessary to fix these dyes to the fibers are not very efficient. Therefore, residual dyes, several types of chemicals and salts are dumped into the water and are discharged in the water system. At least 15 % of those not used dyes might enter the environment through effluents from wastewater treatment plants [54].

I.5.2. Classification of Dye

Dyes are classified according to their chemical structure or according to the method of application [54]. According to Christie et al. [54], dyes contain two groups which are responsible for their color. They consist of a group of atoms responsible for the dye color, called chromophores and the other group is auxochromes, which can be defined as an electron withdrawing or donating substituents that essential for the color enhancement of the chromophores. The most important chromophores are the azo (–N=N–), carbonyl (–C=O), methine (–CH=) and nitro ($–NO_2$) groups. The most important auxochromes are amine ($–NH_3$), carboxyl (–COOH), sulfonate ($–SO_3H$) and hydroxyl (–OH) groups.

In term of method of application, dye molecules are carefully designed to ensure that they have suitable properties for a particular application. For textile applications, dye molecules are designed so that they are strongly attached to the fiber molecules to which they are applied. Acid dyes and mordant dyes are mostly applied to protein fibers whereas direct dyes,

reactive dyes and vat dyes are used for cellulose fibers. Disperse dyes and basic dyes are suitable for acrylic fibers.

(a) Acid dyes

Acid dyes are water-soluble anionic dyes that are applied to fibers such as silk, wool, nylon and modified acrylic fibers using neutral to acid dye baths. Attachment to the fiber is attributed, at least partly, to salt formation between anionic groups in the dyes and cationic groups in the fiber. Acid dyes are not substantive to cellulosic fibers. Most synthetic food colors fall in this category.

(b) Basic dyes

Basic dyes are water-soluble cationic dyes that are mainly applied to acrylic fibers, but find some use for wool and silk. Usually acetic acid is added to the dye bath to help the uptake of the dye onto the fiber. Basic dyes are also used in the coloration of paper.

(c) Direct dyes

Direct or substantive dyeing is normally carried out in a neutral or slightly alkaline dye bath, at or near boiling point, with the addition of either sodium chloride (NaCl) or sodium sulfate (Na_2SO_4). Direct dyes are used on cotton, paper, leather, wool, silk and nylon. They are also used as pH indicators and as biological stains.

(d) Mordant dyes

Mordant dyes require a mordant, which improves the fastness of the dye against water, light and perspiration. The choice of mordant is very important as different mordants can change the final color significantly. Most natural dyes are mordant dyes and there is, therefore, a large literature base describing dyeing techniques. The most important mordant dyes are the synthetic mordant dyes, or chrome dyes, used for wool; these comprise some 30% of dyes used for wool, and are especially useful for black and navy shades. The mordant, potassium dichromate, is applied as an after treatment.

It is important to note that many mordants, particularly those in the heavy metal category, can be hazardous to health and extreame care must be taken in using them.

(e) Vat dyes

Vat dyes are essentially insoluble in water and incapable of dyeing fibers directly. However, reduction in alkaline liquor produces the water soluble alkali metal salt of the dye, which, in this leuco form, has an affinity for the textile fiber. Subsequent oxidation reforms the original insoluble dye. The color of denim is due to indigo, the original vat dye. Covalent bonds that attach reactive dye to natural fiber.

(f) Reactive dyes

Reactive dyes utilize a chromophore attached to a substituent that is capable of directly reacting with the fiber substrate. The covalent bonds that attach reactive dye to natural fiber make them among the most permanent of dyes. “Cold” reactive dyes, such as Procion MX, Cibacron F, and Drimarene K, are very easy to use because the dye can be applied at room temperature. Reactive dyes are by far the best choice for dyeing cotton.

(g) Dispers dyes

Disperse dyes were originally developed for the dyeing of cellulose acetate, and are substantially water insoluble. The dyes are finely ground in the presence of a dispersing agent and then sold as a paste, or spray-dried and sold as a powder. Their main use is to dye polyester but they can also be used to dye nylon, cellulose triacetate, and acrylic fibers. In some cases, a dyeing temperature of 130 °C cellulose triacetate and a pressurized dye bath is used. The very fine particle size gives a large surface area that acids dissolution to allow uptake by the fibers. The dyeing rate can be significantly influenced by the choice of dispersing agent used during the grinding.

(h) Azo dyeing

Azo dyeing is a technique in which an insoluble azoic dye is produced directly onto or within the fiber. This is achieved by treating a fiber with both diazoic and coupling compents. With suitable adjustment of dyebath conditions the two components react to produce the required insoluble azo dye. This technique of dyeing is unique, in that the final color is controlled by the choice of the diazoic and coupling components.

(i) Sulfur dyes

Sulfur dyes are the most commonly used dyes manufactured for cotton in terms of volume. They are cheap, generally have good wash-fastness and are easy to apply. The dyes are absorbed by cotton from bath containing sodium sulfide or sodium hydrosulfite and are made insoluble within the fiber by oxidation.

I.5.3 Methods for Treating Dye Effluents

Generally, the release of colored wastewater from textile industry into water bodies such as lakes, oceans and rivers has created severe environmental problems. Most of the colored effluents are toxic and potentially carcinogenic hence considered as a threat for human survival. These issues have caused public concern and awareness on water pollution. Although various chemical and physical processes have been employed in the removal of colored effluents, however, those methods do not lead to complete destruction of the dyes. Moreover, further treatment is needed since the methods employed just transfer the contaminants from one phase to another. This will indirectly enhance the operational cost.

In last decade, advanced oxidation processes (AOPs) have been growing since they are able to deal with the problem of dye destruction in aqueous systems [55]. The generation of hydroxyl radicals (•OH) that oxidize various pollutants quickly and non-selectively have improved the degradation of organic compounds compared to conventional methods.

Among AOPs, semiconductor photocatalysis appears as the most emerging destructive technology. The main advantages of this process are highlighted below:

- Inherent destructive nature;
- No mass transfer involved;
- Can be carried out under ambient conditions and using atmospheric oxygen as the oxidant;
- May lead to complete mineralization of organic carbon into CO_2.

I.5.4 Aims and Objectives

Photocatalytic degradation of two dyes: Reactive red (RR) 184 and Methylene Blue (MB) by suitable metal oxide (ZnO) photocatalyst as thin layer will be investigated in this study, and the operational conditions of the photocatalytic degradation processes such as: time of irradiation, initial dye concentration, pH of solution, energy of radiation, effect of seed layers

and photocatalysts (ZnO thin layer and Nanorods) will be investigated to be optimized in order to achieve the best removal efficiency to guarantee complete decolorization of the two dyes ; Reactive Red-184 and Methylene Blue (MB) .

In this study, Reactive Red-184 (RR-184) azo dye was selected as pollutant due to its recalcitrant stability. This dye is used for wool fiber, tops, scattered wool dyeing, also can be used for wool, silk fabric printing. The characteristic absorption band centered at λ_{max} 542nm of RR-184 was determined on a double-beam Shimadzu UV/Vis/NIR spectrophotometer.

Methylene Blue (MB) is a basic cationic dye widely used as a redox colored indicator, histological dye or antiseptic for example. It is also widely used as a model molecule of pollutant because, even if it is a molecule not dangerous from the environmental point of view, it has reactivity quite similar to aromatic pollutants because of its structure. In addition, its kinetics of degradation is easy to follow by UV-visible spectroscopy because of its intense blue color, which allows us to follow the degradation according to the fading of the solution.

MB has both photo-oxidation and photoreduction on the surface of ZnO. There are two characteristic absorption bands centered at the λ_{max} = 664 nm (ε_{max} = $1.0x10^{5}$ $mol^{-1}L^{-1}$ cm^{-1}) and λ_{max} = 612 nm (ε_{max} =$1.0 x10^{4}$ $mol^{-1}L^{-1}$ cm^{-1}) [56], which make it possible to perform photocatalytic study even with diluted solution and it is easy to monitor the whole process of the reaction. Furthermore, it is transparent in the range between 350 and 500 nm that correspond to the irradiation wavelengths of the ultraviolet source used in this study. Therefore, Methylene blue was chosen for the study of photocatalytic degradation.

Therefore, Methylene blue was chosen for the study of photocatalytic degradation. Standard curve for the both dyes was illustrated in figure I.9 (a), (b) and some chemical properties of the dyes used were presented in Table I.2.

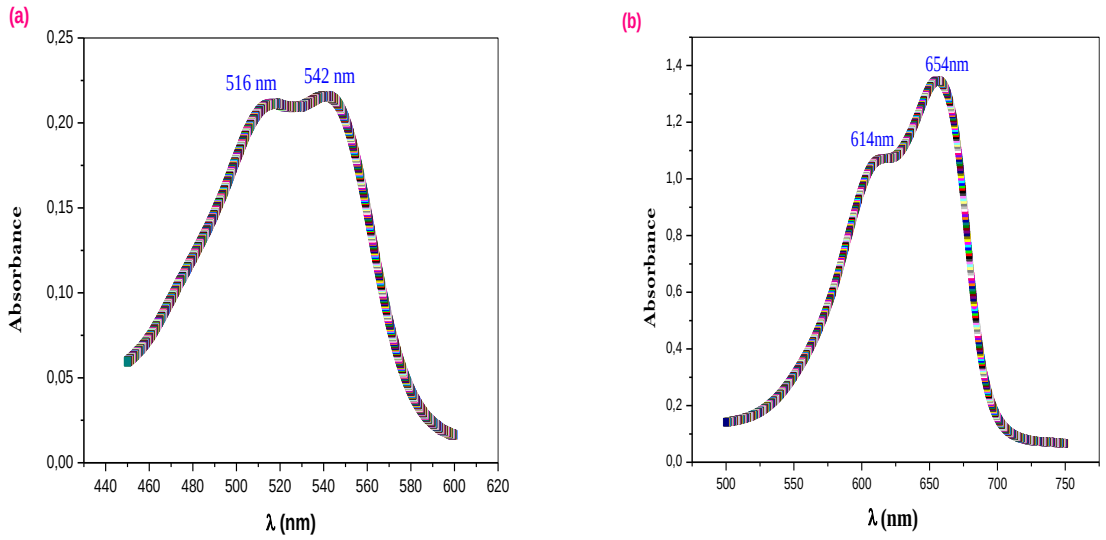

Figure I.9: *Visible spectrum of (a) Red Reactive -184 and (b) Methylene Blue*

Table I.2: *Some chemical properties of the both dyes*

Dye	Reactive Red 84	Methylene Bleu
Names	Reactive Red 84; disodium 6-amino 5-[[4-[(2-bromo-1-oxoallyl)amino]-2-[(4-methyl-3-sulphonatophenyl)sulphonyl]phenyl] azo]naphthalene-2-sulphonate;	Methylene blue; 61-73-4; Methylthioninium chloride; Basic blue 9; Swiss Blue; Chromosmon
Molar mass	753.53 g/mol	319.85 g/mol
Chemical formula	$C_{26}H_{19}BrN_4Na_2O_9S_3$	$C_{16}H_{18}ClN_3S$
Color	Dark Red Powder	Dark green crystals or powder from chloroform-ethyl ether
Solution	Pink color	A deep blue color
Category	Azoic	Basic cationic
Melting point	N.A	100-110 °C (with decomposes)

Water Solubility	100 g/l (at 30°C)	43.600 mg/l (at 25°C)

II.3.7.1.3. Experimental protocol

In this work, we used sun light and a UV light of LAMAG brand with two lamps of wavelength 254 and 366 nm. The sample is introduced into dye solution with a specific concentration. The whole is put under gentle stirring and under UV irradiation, in order to homogenize the solution and maintain the constant conditions of adsorption / desorption during UV irradiation. Before irradiation, the system is kept in the dark for a few minutes in order to obtain a balance of adsorption of the dye on the surface of the photocatalyst. After this step the whole is irradiated. Kinetic measurements were carried out at room temperature. The stopwatch is started at the start of irradiation. The conversion of organic dye is measured over time by UV-visible spectroscopy. The experimental setup used in this study is shown in Figure I.10.

Figure I.10: *Photograph representing the experimental setup; (a) Sun light (b) UV light.*

Chapter II

Zinc Oxide: Properties and Applications

The interesting in this second chapter is focused on Zinc oxide; definitions, properties and its applications in diverse fields.

In this chapter we will cite the chemical, physical, electronic properties of Zinc oxide and its applications in different fields with the techniques of characterization.

II. Zinc Oxide

Zinc oxide is an organic compound with the formula ZnO. It's usually appears as a white powder, nearly insoluble in water. The powder is widely used as an additive into numerous materials and products including plastics, ceramics, glass, cement, rubber (e.g. car types), lubricants, paints, ointments, adhesives, sealants, pigments, foods (source of Zn nutrient), batteries, ferrites, fire retardants, first aid tapes, ect. ZnO is present in the Earth crust as a mineral zincite, however, most ZnO used commercially is produced synthetically [1].

In materials science, ZnO is often called an II-VI compound semiconductor because zinc and oxygen belong to the 2 nd and 6 th groups of periodic table, respectively. This semiconductor has several favorable properties; good transparency, high electron mobility, wide bandgap, strong room temperature luminescence, ect.

II.1 Properties of Zinc oxide

II.1.1 Chemical Properties

ZnO occurs as a white powder known as zinc white or as the mineral zincite. The mineral usually contains a certain amount of manganese and other elements and is of yellow to red color. Crystalline zinc oxide is thermochromic, changing from white to yellow when heated and in air reverting to white cooling. This color change is caused by a very small loss of oxygen and high temperatures to form the non-stoichiometry $Zn_{1+x}O$, where at 800°C, x= 0.00007. Zinc oxide is an amphoteric oxide. It is nearly insoluble in water and alcohol but it is soluble in (degraded by) most acids such as hydrochloric acid;

$$ZnO + 2\ HCl \rightarrow ZnCl_2 + H_2O \qquad (II.1)$$

Bases also degrade the solid to give soluble zincates;

$$ZnO + 2\ NaOH + H_2O \rightarrow Na_2\ (Zn\ (OH)_4) \qquad (II.2)$$

It reacts with hydrogen sulfide to give the sulfide: this reaction is used commercially in removing H_2S using ZnO powder (e.g. deodorant)

$$ZnO + H_2S \rightarrow ZnS + H_2O \qquad (II.3)$$

When ointments containing ZnO and water are melted and exposed to ultraviolet light, hydrogen peroxide is produced.

In Table II.1 we regrouped some properties of the ZnO semiconductor.

Table II.1: *Physical properties of Zinc oxide [2-13].*

Properties	*Zinc oxide*
Chemical names	ZINC OXIDE Zinc White, Zincite Oxozinc, Amalox Permanent White
Molecular formula	ZnO
Appearance	Amorphous white or yellowish white powder
Solubility in water	0.16 mg/100 mL
Odour	Odourless
Molar mass (g/mol)	81.408
Density (g/cm^3)	5.606
Melting point (°C)	1975
Boiling point (°C)	2360
Refractive index	2.0041
Lattice Constants	a_o = 0.32469 Å c_o = 0.52069Å
Relative Dielectric Constant	8.66
Energy Gap	3.4 eV Direct
Intrinsic Carrier Concentration	< 10^6 /cc
Exciton Binding Energy	60 meV
Electron effective mass	0.24
Electron mobility (at 300 K)	200 cm^2/V.sec.
Hole Effective mass	0.59
Hole mobility (at 300 K)	5-50 cm^2/V.sec

II.1.2 Physical Properties

Crystal structure: ZnO can crystallize in a variety of crystal structures including wurtzite, zinc blende and the rarely rocksalt. The stable structure at ambient temperatures, pressures and thus most common is the hexagonal, wurtzite structure shown in Figure I.1 below. The zinc blende can be stabilized by growing ZnO on substrates with cubic lattice structure. In both cases, the zinc and oxide centers are tetrahedral. The rock salt (NaCl- type) is only observed at relatively high pressures about 10 GPa.

ZnO has a stable wurtzite structure (space group $P6_3mc$) with a = 0.325 nm and c = 0.521 nm [14]. The wurtzite structure has an ABAB hexagonal close packing (HCP) structure. The structure of ZnO consists of alternating planes composed of O^{2-} and Zn^{2+} ions which are tetrahedrally co-ordinated and stacked along the c-axis on an alternate basis (Figure II.1). The Zn^{2+} and O^{2-} ions create a normal dipole moment and instant polarization which results in a diversification of surface energy. The tetrahedral coordination in ZnO results in noncentral symmetric structure and consequently results in piezoelectricity and pyroelectricity in ZnO. Another important characteristic of ZnO is its polar surfaces. The most common polar surface is the basal plane. Extensive surface reconstructions are a means of obtaining a stable structure but ZnO - ± (0001) are exceptions. They are atomically flat, stable and without reconstruction. Efforts to understand the superior stability of the ZnO ± (0001) polar surfaces are at the forefront of research in today's surface physics. The other two most commonly observed facets for ZnO are {2 $\bar{1}$ $\bar{1}$ 0} and {01 $\bar{1}$ 0}, which are non-polar surfaces and have lower energy than the {0001} facets [15- 20].

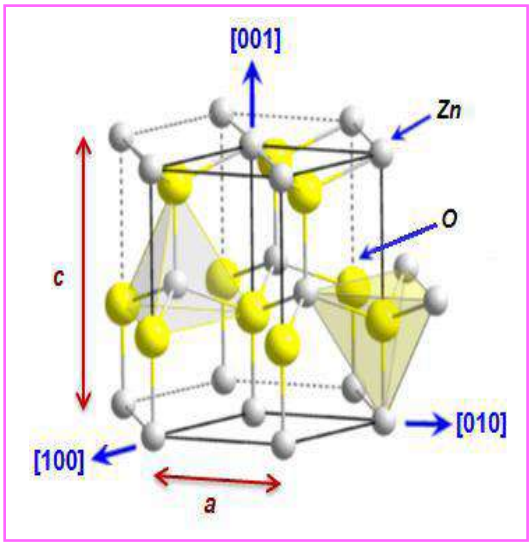

Figure II.1: *ZnO crystalline structure - Wurtzite structure* [21]

Together with the polar surfaces due to atomic terminations, ZnO exhibits a large scale of novel structures that can be grown by varying the growth rates along these directions. One of the most important factors determining the morphology involves the relative surface activities of various growth facets under given conditions. Macroscopically, a crystal has different kinetic parameters for different crystal planes, which are emphasized under controlled growth conditions. Thus, after an initial period of nucleation and incubation, a crystallite will commonly develop into a 3 D object with well-defined, low index crystallographic faces.

A few typical growth morphologies of 1-dimensional nanostructures for ZnO is shown in Figure II.2. Semiconducting nanowires represent interesting solid state systems with unique geometry offering great possibility for further development of optoelectronic devices and sensors applications with numerous possibilities for studying exciting physical phenomena arising from carrier confinement and the large surface-to-volume ratio [22- 27].

Recently, one dimensional (1D) nanostructures such as wires, rods/rods belts and tubes have become the focus of intensive research due to their unique geometry. Nanowires exhibit different cross section shapes (Figure II.2) circular, squared, triangular and hexagonal [28]. The Nanobelts exhibit the rectangular cross section shape. The nanotubes have a tubular shape that has a low mass density, a high porosity, and an extremely large surface to weight ratio.

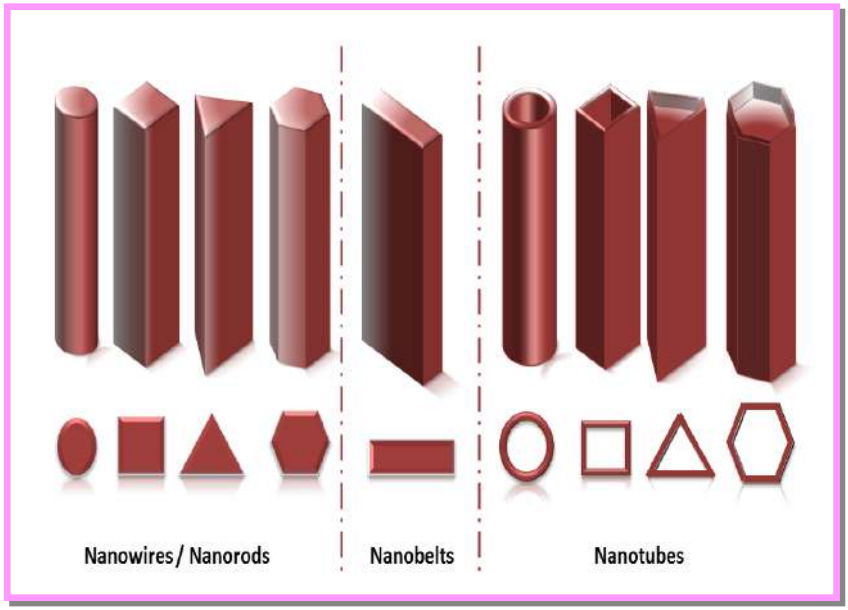

Figure II.2: *Growth morphology of one dimensional ZnO nanostructures [29]*

It is observed that when the dimensions of a semiconducting material keep decreasing i.e. from macro to micro to nano scale, some of the physical properties of that material undergo changes. This phenomenon is known as "quantum size effect" [4].

II.1.3 Electronic Properties

Zinc oxide has a direct wide band gap (Eg ~ 3.3 eV at 300 K) [30]. The top of the valence band is formed from the oxygen 2p levels, while the bottom of the conduction band is formed mainly from the Zn 4s levels [31]. Zinc oxide is commonly n-type while p-type behavior has proved to be extremely hard to achieve. In every semiconductor there will be defects and unintentionally incorporated impurities, and in ZnO the most common defects are zinc and oxygen vacancies (V_{Zn} and V_O respectively), since the formation energy for V_{Zn} and V_O are lowest for O-rich and Zn-rich conditions, respectively [30, 32]. Zinc vacancies, which are dominant for oxygen rich conditions, have charge -2 in n-type ZnO. The transition level between the -1 and -2 charge states of the zinc vacancy occurs at ~ 0.8 eV above the valence band, making the vacancy a deep acceptor [30]. In his paper Van de Walle [33] determined that oxygen vacancies are deep donors in ZnO and the transition from the +2 state to the neutral state occurs ~2.7 eV above the valence band. However the +2 state of V_O is unstable and is hence not expected to be observable. Oxygen vacancies are dominant under Zn-rich conditions. Zinc interstitials (Zni) are also likely to form, but Zni has a higher formation energy than V_O and hence the oxygen vacancies are dominant. Hydrogen is a common impurity in semiconductors because incorporation during growth is nearly impossible to avoid [34]. In common semiconductors hydrogen acts as a donor (H^+) in p-type materials and an acceptor (H^-) in n-type materials, whereas in ZnO hydrogen always acts as a donor [35].

From the point of view of potential technological applications zinc oxide has a number of notable properties:

- ✓ It has a wide direct bandgap (~ 3.37 eV at 300 K) and thus is receiving renewed attention for device applications due to a number of advantages it presents in comparison with GaN (bandgap ~ 3.4 eV at 300 K), for example larger exciton binding energy, availability of large area substrates for homo-epitaxy, etc [36]. The high exciton binding energy of 60 meV (which is larger than the thermal energy at room temperature) leads to excitonic emission at room temperature and above [37]. In this regard ZnO is a promising photonic

material for UV/blue devices such as short wavelength light emitting diodes and laser diodes in optoelectronics.

- ✓ ZnO is a semiconducting, piezoelectric material. It shows a high degree of surface "activity" in terms of interacting via ad- and chemi-sorption with the surrounding ambient. This leads to potential applications in e.g. field emission displays, gas sensors, nanoresonators, and Nanocantilevers etc. These devices may have important applications in nanosystems and biotechnology [38- 41].
- ✓ ZnO naturally forms a wide variety of nanostructures using a range of growth techniques, including nanorods, nanowires, nanobelts, nanorod/nanowall, nanotubes etc. These structures in many cases display a degree of crystal perfection which far exceeds that of thin films, even on lattice mismatched surfaces. In combination with properties 1 and 2 above, this wide range of high crystal quality nano-morphologies open even more potential applications [42- 46].
- ✓ P-type ZnO is predicted to display spin polarized carrier behavior when doped with magnetic impurities and as such is a promising material for spintronics applications [44].
- ✓ ZnO is bio-safe and biocompatible, and it can be directly used for biomedical applications without coating [47, 48].

With these unique characteristics, ZnO is one of the most important materials for future research and applications. Perhaps the three most important challenges in ZnO research generally are:

(a) The p-type doping problem: ZnO is a naturally unipolar semiconductor, like many other wide bandgap materials, e.g. GaN. However, the solution to this problem in ZnO has proved far more difficult to date than for GaN [49].

(b) The high degree of surface activity: This can strongly affect electronic conduction mechanisms via creation of surface depletion and accumulation layers, altering the electronic characteristics. These effects vary over time and in different gas atmospheres and illumination levels. This means that reliable doping and measurements of doping are very difficult [50]

(c) Control of the nanostructure morphology: the wide variety of nanostructure morphologies in which ZnO can grow almost by definition means that the growth process is highly sensitive to growth conditions.

II.2 ZnO and its applications

ZnO has got a wide array of applications. The reactivity of ZnO makes it ideal to be used as a precursor for obtaining other compounds of Zn. ZnO has proved to be a boon for materials science as it has got a combination of unique properties like UV absorption, anti microbial properties, steady thermal and optical properties. Be it ceramics, lubricants, ointments, adhesives or the rubber industry, ZnO has got a very significant contribution [51].

II.2.1 ZnO as LED

A light emitting diode (LED) is a pn-junction[1] where the current is injected in forward bias. Whereas in a solar cell photons excite carriers, which can contribute to the current, the LED operates oppositely. Current is passed through the device in forward bias, and e−-h+ recombinations occur within the neutral (depletion) region of the pn-junction. When excited electrons and holes recombine in a direct band gap semiconductor, the energy is released by emitting photons. The emitted light will have the color corresponding to the band gap energy [52]. Since electrons and holes form tightly bound excitons in ZnO, near-band-gap recombinations are efficient at room temperature, and ZnO is highly suited for LED devices [53]. P-type ZnO were fabricated and violet electroluminescence from homostructural p-i-n junctions were demonstrated by Tsukazaki et al. [54]. The report involved nitrogen doped p-type ZnO thin films and junction devices grown by laser MBE. The p-ZnO had a hole concentration of 2×10^{16} cm^{-3}, and i-ZnO and n-ZnO had electron concentrations of 2×10^{16} cm^{-3} and 2×10^{19} cm^{-3}, respectively. The electroluminescence spectrum showed luminescence from violet to green regions with multi-reflection interference fringes. Chu et al. [55] reported a UV LED with a ZnO p-n homojunction. The homojunction was grown on a Si (100) substrate with MgO/ZnO as a buffer layer between the substrate and the homojunction. The n-type ZnO was doped with Ga, while the p-type ZnO was Sb-doped. The hole concentration in the p-layer was lower than the electron concentration in the n-layer, and hence the depletion region was mainly in the p-region. The diode showed good UV emissions at different temperatures.

II.2.2 ZnO as TCO

A transparent conductive oxide (TCO) can act as the top electrode of a solar cell. For a TCO to be efficient as an electrode (front and back), the material must possess some crucial

properties; the resistivity should be as low as possible, meanwhile the carrier concentration is reduced to reduce unwanted free carrier absorption in the infra-red range. The mobility of the carriers on the other hand should be as large as possible, to increase the TCOs conductivity, while at the same time keeping the absorption coefficient low [56]. Park et al. [57] deposited Ga-doped ZnO on quartz substrates using pulsed laser deposition. A resistivity of 8.12×10^{-5} Ωcm and a visible transmittance of above 90% was obtained for sample deposited at 300°C. Chen et al. [58] used pulsed direct current (DC) magnetron sputtering to grow ZnO thin films co-doped with Mg and Ga, with variation of the H_2 gas flow, for TCO applications. They found that Mg-doped ZnO (MGZO) deposited on glass, with a H_2 flow rate ratio of 4/59 sccm and the remaining 55 sccm Ar, yield the thin films with lowest resistivity (1.96×10^{-3} Ωcm) and with an average transmittance of 80.5% in the wavelength range from 340 nm to 1100 nm. The hydrogen flow rate was also varied in the work of Tian et al. [59]. In this work, TCO ZnO thin films were grown and co-doped with Mg and Ga by using magnetron sputtering. The hydrogenated Mg and Ga co-doped ZnO (HMGZO) thin film grown with a H_2 flow rate ratio 9/64 sccm and the remaining 55 sccm Ar, gave a resistivity of 4.4×10^{-3} Ωcm. The average transmittance was 88.6% in the wavelength range from 330 nm to 1100 nm.

[1] *A pn-junction is a p-type material brought together with an n-type material. The electrons on the n-side and holes on the p-side will then diffuse to the opposite side, leaving behind uncompensated donors and acceptors, respectively. As more carriers diffuse, an electric field will be built up in the transition (depletion) region, preventing further diffusion. Band bending occurs in order to keep the Fermi level constant throughout the device, and the potential difference between the n- and p-side is called the contact potential. When the junction is in equilibrium, the carrier diffusion due to the concentration gradient and the carrier drift due to the electrical field in the transition region cancel each other out, resulting in no net current [52].*

II.2.3 ZnO as a Powder

ZnO as a powder has been commonly used for over a hundred years in a wide range of applications as cited in the following;

II.2.3.1 Medical uses

A mixture of ZnO with 0.5% Fe_2O_3 is known as Calamine and is used in manufacturing Calamine lotions. Fine particles of ZnO have anti microbial and deodorizing qualities and hence they are used for packaging purposes. These properties along with its ability of neutralizing acids makes it ideal for use in antiseptic creams, healing creams etc. they are also an important component of toothpastes and dental prosthetics. Due to its ability to absorb ultraviolet light, ZnO is also used in sunscreens and sunblocks to prevent sunburns. ZnO is also used in the making of cigarette filters as it helps in removing harmful substances like H_2S and HCN without affecting the flavour.

II.2.3.2 Food additive

ZnO is added to many breakfast cereals acting as a source of zinc that is a necessary nutrient for ZnO based medicament for preventing and treating diarrhea in farm animals [60]. Furthermore, ZnO is usually added to food products as a source of Zn, which is considered to be a necessary nutrient, as it helps in the performance of various physiological activities like growth and proper functioning of the sexual organs. ZnO is also added to fodder as a Zn supplement for livestock. Zinc oxide is used to manufacture zinc gluconate which is nowadays found in cold prevention lozenges.

II.2.3.3 Pigment

Over the past century, the paint industry (in its constant development of improved products) has utilized various aspects of those properties to high degree. Manufacturers discovered that they could produce the coatings of brushing consistency and good suspension properties by incorporation of ZnO into their pastes.

Zinc white is used as a pigment in paints. In general, zinc white is more opaque than lithopone, but it is less opaque than titanium dioxide. It is also used in coating for paper. Chinese white is a special grade of zinc white used in artists' pigments, because it can absorb both UVA and UVB rays of ultraviolet light. Interestingly, the current state-of-the-art thermal control coatings (TCCs) system utilizes ZnO pigment to maintain solar reflectance over a long exposure time [60].

II.2.3.4 Cosmetic applications

ZnO is applied in cosmetics to protect the UV radiation for human. ZnO can be used in ointments, creams, and lotions to protect against sunburn and other damages to the skin caused by ultraviolet light. It is the broadest spectrum UVA and UVB absorber that is approved for use as a sunscreen by the Food and Drug Administration (FDA), and is completely photostable and it is also a main ingredient of mineral make up [60].

II.2.3.5 Rubber manufacture

The rubber industry is responsible for consuming about 50% of the ZnO that's produced globally. ZnO along with stearic acid are a must for activating the process of vulcanization in rubber manufacture. Rubber curing becomes faster and more controlled when a combination of these two substances is used. It's also a very important additive in car tyres. It helps in improving their thermal conductivity which helps the tyres to dissipate heat quickly when they are in motion thereby increasing their life span.

II.2.3.6 Plastic applications

Zinc compounds can provide a variety of properties in the plastic field. Heat resistance and mechanical strength are imparted to acrylic composites by ZnO.
Addition of ZnO to epoxy resins cured with aliphatic polyamines imparts higher tensile strength and water resistance. ZnO is also useful in the preparation of nylon polymers and in increasing their resistance and reacts with unsaturated polyesters to form higher viscosity and a thixotropic body. ZnO increases the transparency of poly (chlorofluoro ethylene) molding resin. Polyolefin's are improved in color, tensile strength, and vulcanization properties by addition of ZnO. Applications in development for zinc oxide-stabilized polypropylene and high-density polyethylene include safety helmets, stadium seating, insulation, pallets, bags, fiber and filament, agricultural and recreational equipment [61].

II.2.3.7 Anti corrosive coatings

Zinc oxide is an excellent inhibitor of fungi, mildew and mould. Paints which have ZnO are usually used as anti corrosive coatings for various metals like galvanized Zn which is especially hard to protect as it makes organic coatings brittle and unsuitable for adhesion. ZnO paints on the other hand maintain their flexibility and adhesive properties for years on

end. The UV blocking abilities of ZnO also play an important role in improving the resilience of the paint. Unlike some lead pigments that are available commercially, ZnO is impervious to the effect of sulphur compounds that are present in the atmosphere.

II.2.3.8 Electronic applications

The wide band gap of ZnO enables it to be used for the purpose of making LEDs and laser diodes. Transparent thin-film transistors (TTFT) can also be produced with ZnO. Nanorod sensors made of ZnO are devices that detect fluctuations in electric current passing through the wires as a result of the adsorption of gas molecules. The nanorods can be made partial towards H_2 gas by sputtering Pd clusters on the surface which help in dissociating the H_2 molecules thereby increasing the sensitivity of the nanorods. H_2 concentrations up to 10 ppm can be detected at room temperature without any response to O_2 [62]. Properties like biocompatibility have enabled ZnO to be used as a biomimic material to modify and immobilize biomolecules. As Field-effect transistors (FETs), they can function without even a p-n junction thus bypassing doping problems. This is why some FETs use nanorods made of ZnO as conducting channels. ZnO is also used in making Zn-C dry cells, Ni-Cd oxide batteries, Zn-Ag oxide batteries and also some secondary batteries. Another major area of ZnO application is fuel cell where it's used to make various parts like the electrodes and sometimes also as the fuel. It can also act as a photo catalyst in places like the solar cell.

II.2.3.9 Sensor applications

ZnO can use for pyroelectric sensors. It possesses the advantages of being integrable with on-chip circuitry, un-cooled detecting, room-temperature operation, fast and wide spectral response with high sensitivity and low cost.

ZnO material can be used in sensing and/or monitoring different types of gases both toxic and harmful gases as chlorine (Cl_2) due to it low cost, high sensitivity, excellent selectivity quick response behavior, sulfur hexafluoride, butane ethanol and gasoline.

II.3 ZnO Thin films and applications

Due to its versatility, ZnO has drawn considerable attention and has been prepared and investigated in various physical forms such as single crystals, sintered/ceramic pellets, thick films, thin films and nanostructures etc. [63, 64-65, 66, 67-70]. Among different physical forms, the thin films of ZnO find a multitude of immensely important applications in

electronic and optoelectronic devices such as photothermal conversion systems, transparent conductors, gas sensors for toxic and combustible gases and heat mirrors among many others [71- 74]. It is also being considered as a potential candidate in the new frontiers of research like spintronics [69].

Thin films form the basic for many electronic components and are of particular interest for fabrication of large area arrays. Thus most of the device applications require ZnO in polycrystalline thin film form. Simultaneous occurrence of high optical transparency (≥ 80%) in the visible region and high conductivity may be conveniently obtained by controlling the non-stoichiometry and/or dopants. Thus the thin films have been widely studied during the last few decades because of their technological applications, particularly in the field of semiconductor electronics.

A thin film can be visualised as a near surface region of a material whose properties are different from those of the bulk. In general any solid or liquid system possessing at most two-dimensional order of periodicity may be called a thin film. Thus a thin film is a microscopically thin layer of material that is deposited onto a substrate [75].

The substrate may be glass, mica, metal or ceramic etc. Though a thin film, in general, has a thickness of 1.0 μm or less, in practice, the thickness of a thin film may range from a few hundred angstroms to several microns (0.01 - 10 μm). Films typically used in thin film applications range from a few angstroms to 100 μm thick (the width of a human hair). Films of the order of few nanometer thicknesses are possible to fabricate in which case they are called 'Ultra thin films'. Thin materials may also be formed from a liquid or a paste, in which case it is called a 'thick film'.

The physical properties of polycrystalline thin films are different from those of bulk single crystals in the sense that they are modified by their thickness as well as the crystallite size. The physical properties include structural properties, electrical properties, optical properties, mechanical properties etc. The change in structural properties includes change in lattice parameters, particle size or grain size, stress, strain, etc. The change in optical properties occurs in terms of band gap and other optical constants. The change in electrical properties refers to change in carrier density, mobility etc. Also the way the film is prepared affects its microstructure and properties. These perturbations affect the electrical properties much more than optical properties since the band structure is unaltered inside the bulk. In addition to thickness and crystallite size, the lattice impurity and other structural defects also affect the electrical properties (e.g. conductivity) of the films [76].

For polycrystalline thin films, the electrical properties are modified by the grain boundaries as well. For polycrystalline oxide materials, such as zinc oxide, the electrical properties are further modified by the adsorption of oxygen at the grain boundaries and also on the surface. These grain boundaries generally contain fairly high density of interface states which trap carriers from the bulk of the grain and scatter free carriers by virtue of their inherent disorders and the presence of trapped charges. The interface states result in a space charge limited region at the grain boundaries [77] which results in potential barriers to charge transport.

Pure zinc oxide thin films have certain limitations in their application. They are not stable against corrosive environments and in humid ambient and lack stability in terms of thermal edging in air [78-79]. Adsorption of oxygen in the films modifies its electrical conductivity and also modifies the surface morphology. To stabilize the ZnO system against such changes and also to widen the potential areas where ZnO thin films can be applied, dopant ions have to be incorporated into them to obtain certain desired properties like wider or narrower band gap, higher optical absorbance, lower or higher melting point, ferromagnetism, etc. Therefore polycrystalline ZnO films have been doped with metals of group I. group II, group III and group V. Accordingly doped ZnO thin films with improved stability and suitable structural, electrical and optical properties are in constant demand for their potential application prospects.

II.4 Thin films and their deposition techniques

Thin films can be synthesized by many different processes. A thin film deposition technique involves three steps: (i) Creation of atomic/molecular/ionic species, (ii) transport of these species through a medium, and (iii) condensation of the species on a substrate. The growth of a thin film can take place by different modes. One such is layer by- layer mode. In this case thin film is formed layer by layer on the substrate. This is followed by formation of three-dimensional nuclei. Another possible mode is direct three-dimensional growths of discrete nuclei. Depending on whether the species has been created by a physical or a chemical process, thin film deposition techniques can be broadly divided into two categories: physical and chemical [75]. In physical methods the film material is moved from a target source with some form of energy to the substrate. Chemical film fabrication methods involve chemical reactions and the precursors are mostly components undergoing reaction at the substrate surface or in the vicinity of the substrate.

In physical deposition technique, film is formed by atoms directly transported from source to the substrate through gas phase [75]. The physical routes include different forms of sputtering and evaporation. Commercial physical deposition systems require a low-pressure environment and are classified as Physical vapor deposition or PVD. The different physical vapor deposition systems includes evaporation, thermal evaporation, electron beam evaporation, sputtering, reactive PVD etc. The material to be deposited is placed in such a way that particles of material escape from the surface. They are then allowed to arrive on a substrate to form a solid layer. The whole system is kept in a vacuum deposition chamber. Since particles tend to follow a straight path, films deposited by physical means are commonly directional, rather than conformal.

- The Evaporation, sputtering, ion plating and laser ablation techniques are classified in this category of PVD method.
- The variety of this methods as well as PECVD, PACVD, MOCVD, LPCVD), spray, electrodeposition, chemical Bath and dip coating; sol gel are listed to the CVD (Chemical Vapor Deposition) methods where the films are formed by chemical reaction between incoming species on the substrate.

Till now, ZnO thin films can be deposited by a number of different methods such as: sol-gel spin coating method [80], low pressure chemical vapor deposition (LPCVD) [81, 82], Chemical Both Deposition (CBD) [83], thermal evaporation [84], pulsed laser deposition (PLD) [85], metal organic chemical vapor deposition (MOCVD) [86], sputtering [87], molecular beam epitaxy [88], spray-pyrolysis [89, 90], sol-gel; dip coating [91] and Hydrothermal technique [92].

In my thesis, several methods like spray pyrolysis and sol-gel; dip coating were used to prepare undoped and doped ZnO films on glass, silicon, tissue for photocatalysis of organic dye, antibacterial activity and solar cells. Furthermore, ZnO thin films with different thickness were deposited by the Radio Frequency Sputtering in order to synthesize ZnO nanostructures (Nanorods, Nanobelts and Nanoflowers) by means of the hydrothermal process at 120°C for diverse time deposition. The detail of elaboration conditions of each method is well presented in chapter III and chapter IV.

II.4.1 The technique of Spray Pyrolysis

Spray pyrolysis is widely used because of its simplicity, commercial viability, and potential for cost-effective mass production. The spray-pyrolysis technique has been successfully applied to synthesize ZnO thin films and analyzed their growing characteristics, atomic composition, surface morphology, microstructure and optical properties. Spray pyrolysis method is especially efficient in producing thin films, transparent, multi-component oxide layers of many compositions on various substrates, including glass.

Spray pyrolysis is a method of depositing films having thicknesses in the region between thin film and thick film. Film deposition is carried out by spraying a solution containing soluble salts of the constituent atoms of the desired compounds onto a substrate. The substrate is maintained at elevated temperatures (typically 300-700°C).

The sprayed droplet reaches the hot substrate and undergoes pyrolytic (endothermic) decomposition and forms a single crystallite or a cluster of crystallites of the product. The thermal energy required for decomposition is provided by the hot substrate. The other volatile by-products and the excess solvent escape in the vapor phase. Post deposition sintering helps to the recombination of the constituent species and clustering. Finally a coherent film is obtained. Several parameters affecting the deposition mechanism and film properties are ZnO solution concentration, solvent, solution flow rate (spray rate), substrate temperature, nature of the substrate, sprayer tip to substrate distance, post deposition annealing, annealing atmosphere and film thickness etc. The novel results derived from this situation have encouraged the researchers to increase their interest in the field of chemically sprayed ZnO thin films. This is the reason why we focus our attention mainly on the contributions on chemically sprayed ZnO thin films. Spray deposited films generally have a rough microstructure. Oxides, sulphides and selenides are prepared by this technique.

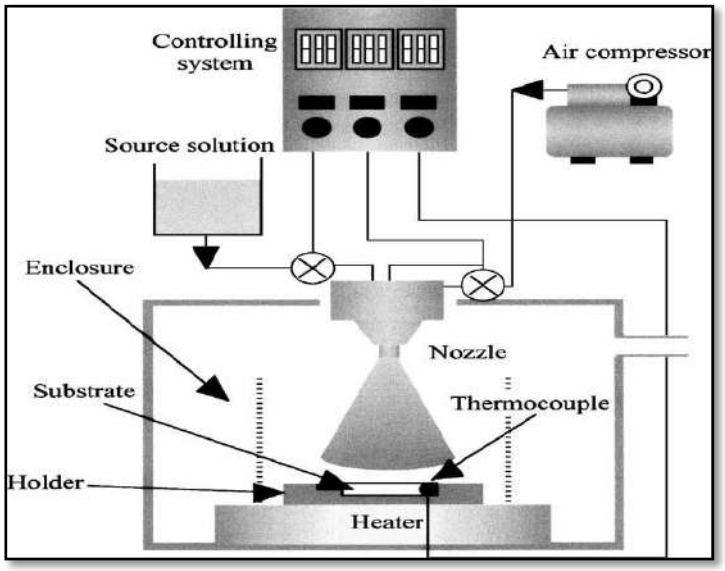

Figure II.3: *Schematic representation of a spray pyrolysis deposition (SPD) apparatus.*

The spray used in this thesis is HOLMARC ultrasonic spray pyrolysis system as shown in Figure II.4.

Figure II.4: *The deposition system of ultrasonic spray pyrolysis (Holmarc)*

II.4.2 Sol-gel; Dip coating

The Sol-gel process, also called soft chemistry, allows elaborating a solid material from a solution, using a sol or a gel as an intermediate step and at considerably lower temperature

than traditional methods. It enables the powderless processing of thin films. In the Figure II.5 the main steps of materials elaboration through sol-gel technique are shown.

For thin film, we can summarize the process in three steps: 1) preparation of the precursor solution, 2) deposition of the sol onto a determined substrate and 3) heat treatment of the xerogel film. This xerogel is the dried gel at ambient pressure (the dried gel in supercritical conditions, is called, aerogel).

ZnO thin films elaboration involves a set of parameters affecting its final properties:

- nature of the precursor and its concentration,
- type of solvent,
- type of additive species and their concentrations,
- aging time of the early mixture,
- method of coating substrates and its speed,
- nature of the substrate,
- pre- and post- heat treatment of the material.

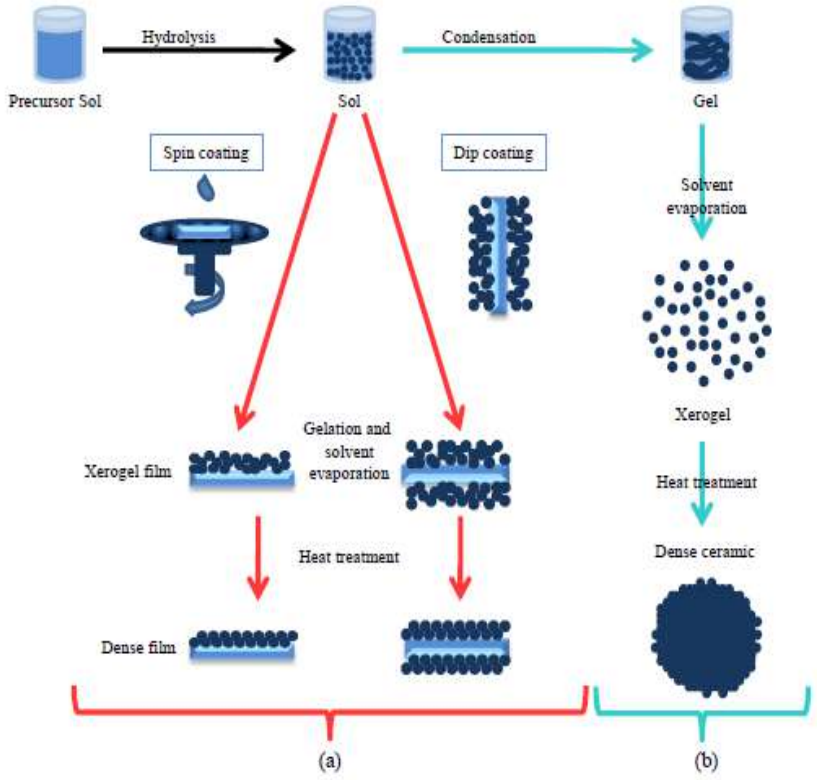

Figure II.5: *Overview showing two synthesis examples by sol-gel method; (a) films and (b) powder*

In our work, the dip-coating system, of the HOLMARC brand with a hot chamber for drying samples, used for deposition of ZnO thin films was shown in Figure II.6.

Figure II.6: *Deposition system of sol-gel dip coating*

II.4.3 Radio frequency Sputtering method (RFS)

One of the most commonly-used and effective methods, that has produced excellent films (dense and crystallographically-oriented) at temperatures close to room temperature, is the RF magnetron sputtering technique. This is partly due to the simplicity of the RF magnetron sputtering technique, easy parameter control and film reproducibility together with the fact that films can be sputtered over large areas on a variety of substrate materials. Sputtered ZnO films have been used as transparent conducting electrodes in photo-voltaic applications, organic light emitting diodes (OLEDs), active channels in TFTs, resistive elements in heated mirrors and glasses, smart windows and as chemical/biological or gas sensors [93-100].

If a solid or liquid at any temperature is subjected to bombardment by suitably high energy particles (usually ions), it is possible for individual surface atoms to acquire enough energy via collision processes to escape. This means of causing ejection of atoms from a surface is known as "*sputtering*". The incident ions lose their energy mainly by momentum transfer as they come to rest within the solid target. Thus, sputtering also leads to ion

implantation into the lattice. In this process, the ions displace atoms within the sample, introducing some disorder and impurities. The incident projectiles need not be ions; as neutral beam bombardment causes sputtering also, but ions are frequently used due to their high yield (i.e. average number of atoms sputtered per incident primary ion; this, however, depends on the sample or target material, its crystallographic orientation, and the nature, energy and incidence angle of the primary ions).

The sputtering technique often produces dense and crystallographically oriented films with good uniformity over large areas [101-102]. It is the easy parameter control coupled with the high deposition rate (although strongly dependent on parameter), that renders sputtering an attractive technique in semiconductor manufacturing where large-area deposition and/or mass production is desired.

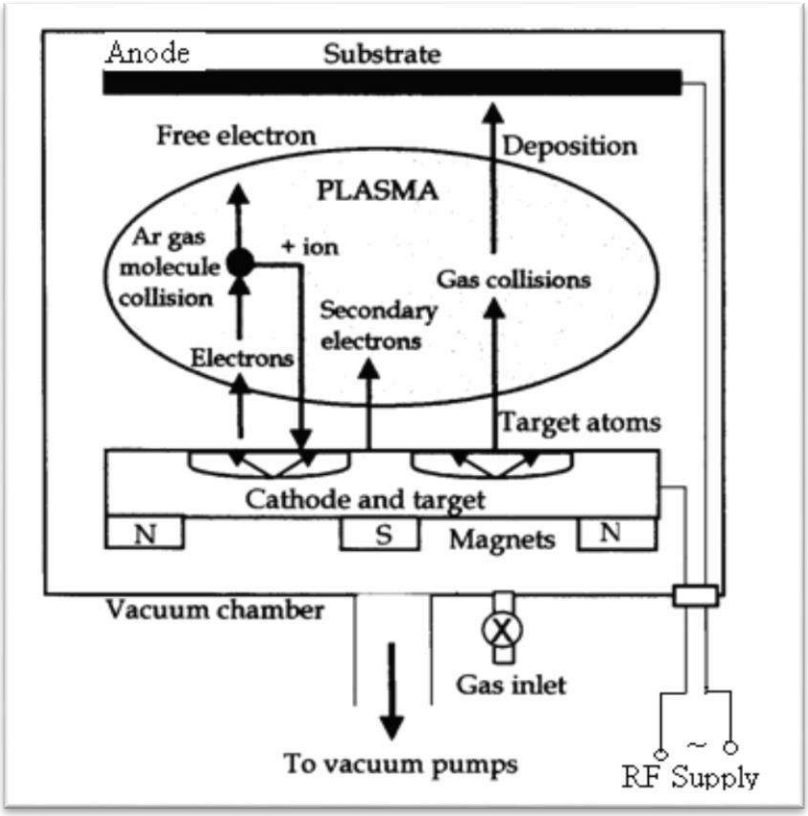

Figure II.7: *RF Magnetron sputtering process, modified from [103]*

The RF sputtering deposition system of ZnO thin film with different thickness is shown on Figure II.8.

Figure II.8: *RF sputtering deposition system of ZnO thin film with different thickness*

II.4.4 Hydrothermal process

There are several high and low temperatures ZnO and CuO nanostructures growth methods and both have some advantages and disadvantages. Comparatively hydrothermal methods are attractive due to many reasons. This method attained much interest in the scientific community when Vayssieres et al. [104] successfully demonstrated the growth of ZnO microstructures on a glass substrate. It does not require sophisticated equipment; it is low cost, environment friendly, and thus suitable for scale-up. Different morphologies of the nanostructures can be readily obtained by tuning the hydrothermal conditions [105-107]. In addition, the hydrothermal growth occurs at very low temperature and therefore holds great promise for nanostructures synthesis on a variety of flexible/soft plastic and paper substrates [108, 109]. The hydrothermal method has been demonstrated as a powerful and versatile method for synthesizing metal oxide nanostructures and so has been reported in the fabrication of electronic and sensing devices. The functioning of these devices is critically linked to the morphology of the nanostructures and hence requires tuning of the growth parameters for the optimal performance.

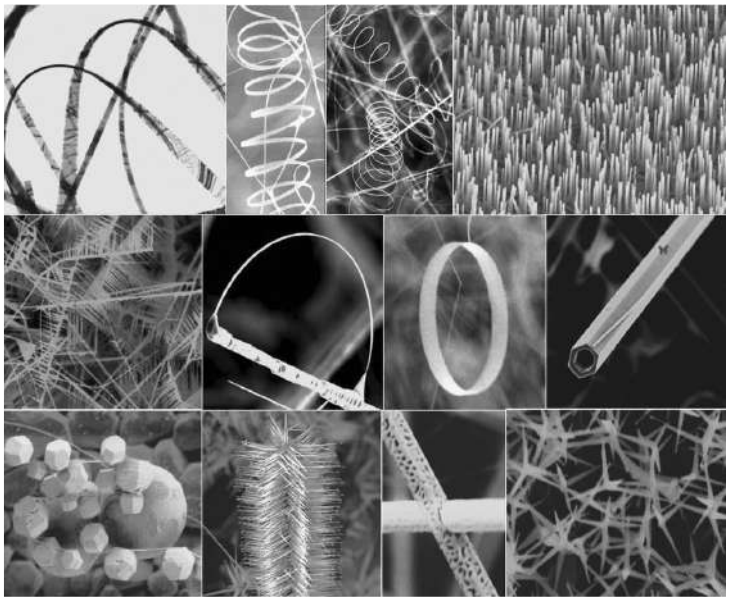

Figure II.9: *A collection of nanostructures of ZnO synthesized under controlled conditions by thermal evaporation of solid powders [110]*

There are several other reactors commonly used for the treatment of materials under hydrothermal conditions, Figure II.10; (a) and (b) represent the autoclave images used in our work, which is a polymer which is chemically stable and temperature resistant and Teflon Lined Sealed Stainless Steel Autoclave, respectively.

Figure II.10: *Autoclave used for preparation of ZnO Nanostructured; (a) polymer and (b) Teflon Lined Sealed Stainless Steel*

II.5 ZnO Nanorods, Nanostructures and Applications

It's well known that ZnO naturally forms a wide variety of nanostructures with excellent crystal quality (superior to thin films and even bulk crystals in some cases) by a self

organization process and thus recently significant research has been dedicated to exploring these aspects of ZnO material as part of the general trend towards the study of nanotechnology and self-organized processes generally among the scientific and materials communities. A great deal of attention has been focused on synthesis and analysis of ZnO nanostructures due to their particular material properties. The combination of the material properties and self-organized nanostructure synthesis promise applications in optoelectronics, nanoelectronics, nanomechanics, nanoelectrochemical systems, sensors and treatment of water (Table II.1).

Table II.2: *Important application areas of ZnO nanostructures*

OPTOELECTRONICS	* Optical devices, date storage [111] * Photodetectors [112] * Light emitting diodes (LEDs) [113] *Laser diodes (LDs) [114]
NANOELECTRONICS	*Field-effect transistors [115] *Field emission sources [116]
NANOMECHANICS	*Nanocantilevers [117]
NANOELECTROCHEMICAL SYSTEM	*Biochemical and chemical sensors [118-120]
TREATMENT OF WATER	*Photocatalysis activity [121]

1D and quasi 1D ZnO nanoscale structures, such as nanorods [122], nanowires [123], nanobelts [124], nanorod / nanowall [125], nanotubes [126] are ideal systems for investigating the dependence of optical properties, electrical transport and mechanical properties on size and dimensionality. They are expected to play an important role as both interconnects and functional components in the fabrication of nanoscale electronic and optoelectronic devices. Optical and electronic properties of nanomaterials are controlled by their size and shape [127,128]. Therefore different nanostructures can have various applications. The key challenge for future nanotechnological applications is to control the size, structure and morphology of nanomaterials in order to control and tailor their properties.

From the narrower perspective of ZnO nanostructure research, perhaps the most important aims and challenges were cited as the following:

(1) Controlled growth is required to define nanostructure size, size distribution and shape. A thorough understanding of the growth mechanism(s) is the key to this control. In

many cases, a suitable way to control the size and morphology of the ZnO nanostructures is to properly control the temperature, catalyst conditions and growth time, etc.

(2) Techniques are required to grow the nanorods into aligned arrays, onto patterned substrates. Achieving this goal will enable superior performance of a variety of device architectures, including LEDs, LDs and field emission electronic sources where such alignment e.g. automatically generates multiple parallel lasing cavities in LDs and high field enhancement factors for field emission. Aligned arrays of nanostructures are easier to contact and also tend to present a more monodisperse surface area to volume ratio, which is important in sensor applications.

(3) For sensor applications, the nanorods may have the required sensitivity due to their morphology, but the selectivity needs to be improved. This may require the synthesis of composite nanobelts, such as heterostructures. Surface functionalization of the nanobelts is also an important direction [129].

(4) Ultimately the growth techniques should be scaleable for industrial level applications.

II.6 Characterization Techniques

II.6.1 The thickness measurement

The thickness of ZnO films were measured via ellipsometry and from transmission experimental spectra data. In Figure II.11 we have reported the theoretical calculation and the experimental data for ZnO thin films using Zinc acetate as precursor which deposited at 350°C as substrate temperature.

The optical transmission data for normal incidence, for an absorbing thin film on a nonabsorbing substrate, is given by the following relation:

$$T = Ax / B - Cx + Dx^2 \ (A1) \qquad \text{(II.4)}$$

$$A = 16n_s (n^2 + k^2) \qquad \text{(II.5)}$$

$$B = [(n + 1)^2 + k^2][(n + 1)(n + ns^2) + k^2] \qquad \text{(II.6)}$$

$$C = [(n^2 - 1 + k^2)(n^2 - ns^2 + k^2) - 2k^2 (ns^2 + 1)]^2 \cos(\phi) - k[2(n^2 - ns^2 + k^2) + (ns^2 + 1)(n^2 - 1 + k^2)]^2 \sin\phi \qquad \text{(II.7)}$$

$$D = [(n - 1)^2 + k^2][(n - 1)(n - ns^2) + k^2 \qquad \text{(II.8)}$$

$$\phi = 4\pi nd / \lambda \qquad \text{(II.9)}$$

$$x = \exp(-\alpha d) \qquad \text{(II.10)}$$

$\alpha = 4\pi k / \lambda$ (II.11)

n and k are the real and imaginary parts of thin film refractive index, d is the film thickness and ns is the (real) substrate refractive index. The latter is assumed to be constant (i.e., = 1.51). The recorder experimental transmittances are fitted to the theoretical transmission (equ.A.1) by varying the values of n and d until both sides are reasonably equal. The values of n and d ensuring a well fitting are taken as the film thickness and refractive index.

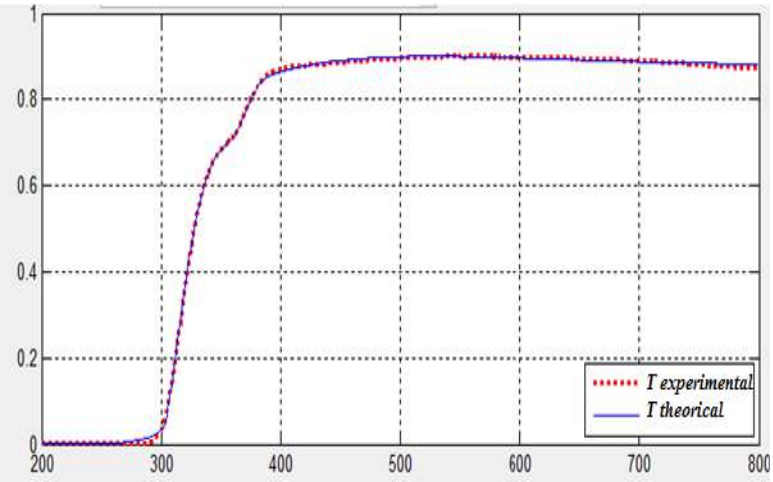

Figure II.11: *The theoretical calculation and experimental transmittance spectra of ZnO thin films deposited at 350°C using Zinc acetate*

II.6.2 Structural properties

II.6.2.1 X- ray diffraction (XRD)

X-ray diffraction is a powerful tool to study the crystal structure of semiconductors. XRD gives information about crystalline phase, quality, orientation, composition, lattice parameters, defects, stress, and strain of samples. Every crystalline solid has its unique characteristic X-ray diffraction pattern, which is identified by this unique ‘‘fingerprint’’. Crystals are regular arrays of atoms and they are arranged in a way that a series of parallel planes separated from one another by a distance d. Figure II.12 shows the detail of the process of x-ray diffraction. If an x-ray beam with a λ wavelength strikes the sample with an incident angle θ then the scattered ray is determined by Bragg’s law:

$$n\lambda = 2d \sin\theta \quad \text{(II.12)}$$

Where n is an integer, λ is the wavelength of the beam, d is the spacing between diffracting planes, and is the incident angle of the beam. The set of d-spacing in a typical x-ray scan provides a unique characteristic of the samples in question.

The X-Rays Diffraction (XRD) type of X'Pert PANalytical system with Cu-kα radiation of wavelength λ = 1.5406 Å was used to characterize the structural properties of all ZnO samples. The XRD analyses were taken at room temperature and the values of diffracted angle 2θ were ranged from 20 to 80°.

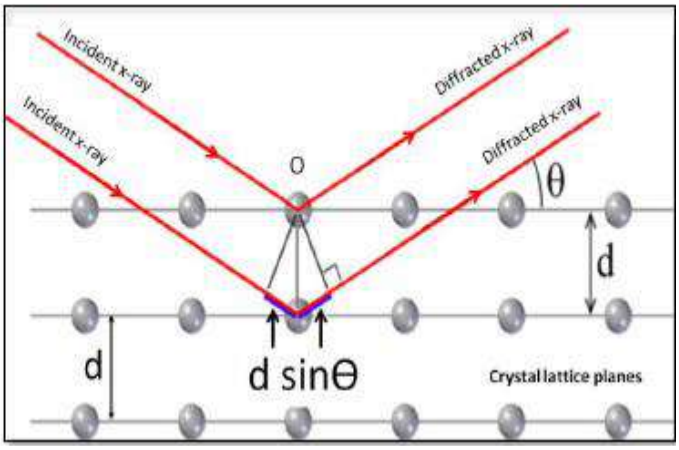

Figure II. 12: *Schematic diagram of Bragg's reflection from lattice planes in a crystalline structure.*

The estimated values of structural parameters for all ZnO films such as crystallites size, lattice strain, dislocation density and number of crystallites are calculated from the XRD pattern.

The crystallites size was computed using both formulas of the Scherer's and Hall–Williamson equation as expressed [130]:

$$D = (0.94\,\lambda) / \beta\,(\cos\theta) \qquad \text{(II.12)}$$

$$\beta\cos\theta / \lambda = 1/D + \varepsilon \sin\theta / \lambda \qquad \text{(II.13)}$$

Herein β is the FWHM (full width at half maximum) of diffraction peaks, θ is the Bragg angle, λ is the wavelength of the used X-rays, D is the crystallite size and ε is the internal strain. D is determined from the last square fit of β cos (θ) / λ vs. sin (θ) / λ of different peaks. The intercept of the equation plot with the y axis yields to the crystallite size.

The lattice strain is calculated from two following equation [130]:

$$\varepsilon = \beta/4\tan\theta \qquad \text{(II.14)}$$

$$\beta \cos\theta / \lambda = 1/D + \varepsilon \sin\theta / \lambda \quad \text{(II.15)}$$

The strain is equal to the slope of the plot of β cos (θ) / λ vs. sin (θ) / λ of different peaks. In Figure II.13 we have presented the plot of the Hall–Williamson equation for Zinc chloride deposited at 350°C for 5 min.

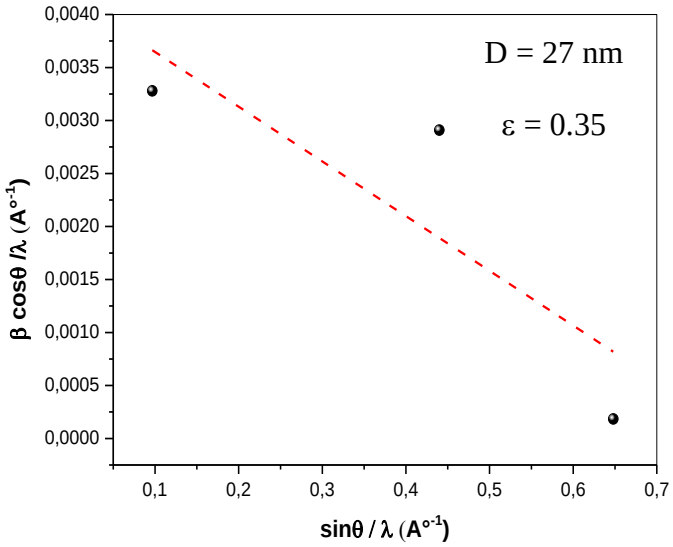

Figure III.13: *Plot of Hall equation for ZnO film using Zinc chloride as precursor*

The dislocation density (δ) is calculated through the relation [130]:

$$\delta = 1/D^2 \quad \text{(II.16)}$$

Where δ is the dislocation density and D is the crystallite size.

The number of crystallites (N) per unit area is computed by this equation [130]:

$$N = d / D^3 \quad \text{(II.17)}$$

Where N is the number of crystallites per unit area, d is the film thickness and D is crystallite size.

II.6.2.2 Raman spectroscopy

Raman spectroscopy is used in condensed matter physics and chemistry to study vibrational, rotational, and other low-frequency modes in a system. It relies on inelastic scattering (Raman scattering) of monochromatic light, usually from a laser in the visible, near infrared, or near ultraviolet range. The laser light interacts with phonons or other excitations in the system,

resulting in the energy of the laser photons being shifted up by absorption of a phonon (anti-Stokes process) or down by generation of a phonon (Stokes process). The shift in energy gives information about the phonon modes in the system and thus about the structural properties of the material. Consequently each material has its own corresponding Raman spectra.

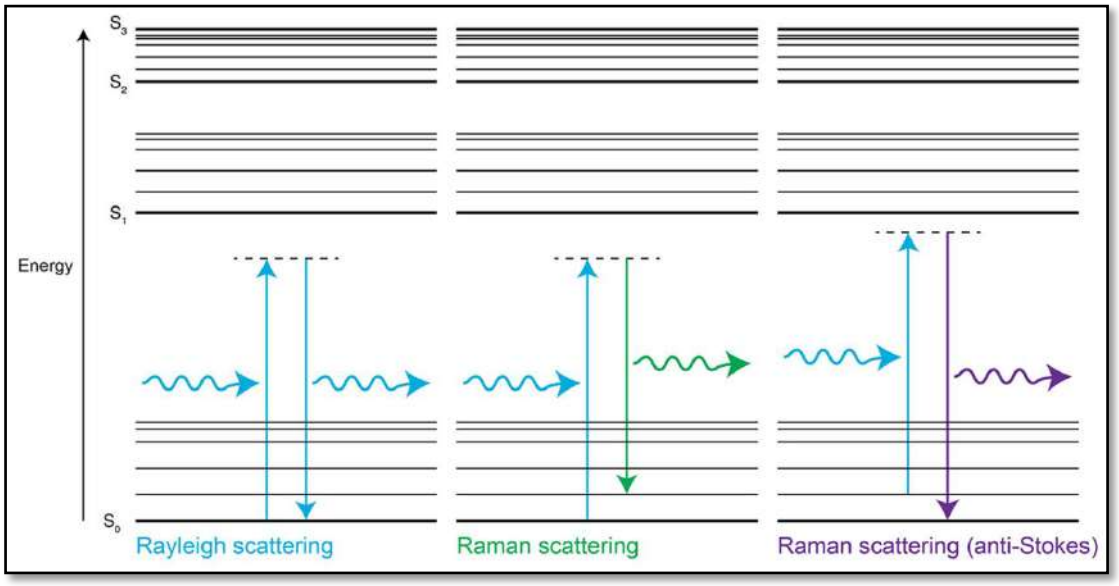

Figure II.14: *Raman spectroscopy; Stokes process and anti-Stokes process*

In my PhD thesis, the micro-Raman analysis was carried out at room temperature using is BRUKER RAMAN SENTEERA R 200 L (Germany) spectroscopy with an Argon laser power of 25 mW with an excitation line at 532 nm at room temperature.

II.6.3 Films morphology

II.6.3.1 Scanning Electron Microscopy (SEM)

Scanning electron microscopy (SEM) is widely used within different scientific fields for the characterization of thin films, nanomaterials, nanostructures, and is an excellent technique for investigating the surface morphology at the nanoscale dimensions. By using SEM it is often possible to distinguish features on the scale of 10 nm or less [131]. Imaging of nanostructures materials using SEM mostly does not require complex sample preparation (the sample needs only to be conductive and vacuum compatible). The basic working principle of SEM [132] is shown in the schematic diagram of Figure II.15. The SEM uses electrons instead of light to generate an image; an electron beam is focused and scanned over a selected area of the

surface of the sample under investigation, hence the name scanning electron microscope. In an SEM, when an electron beam strikes a sample, a large number of signals are generated. Depending on the type of detector, the detected signal is converted to an image of sample's surface topography or to investigate its composition.

The surface morphology of the prepared films was analyzed by means of Scanning Electron Microscope Jeol 5400 SEM microscope and the diameter of ZnO nanostructures is estimated from the SEM images.

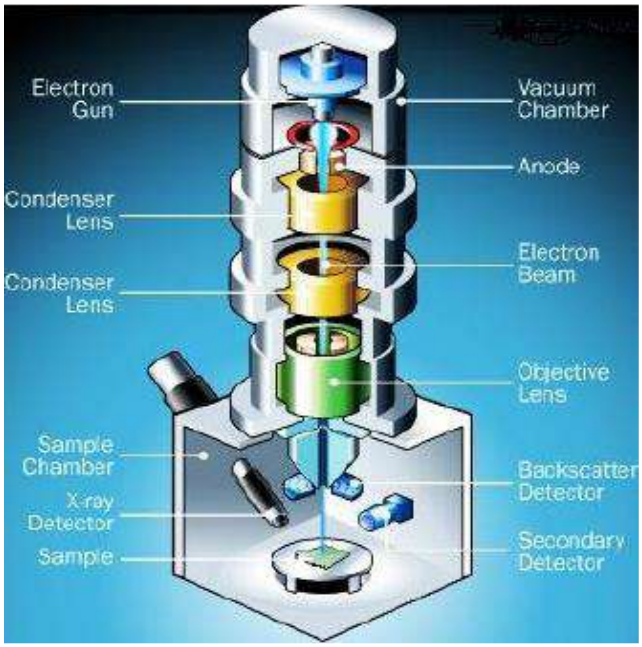

Figure II.15: *Schematic diagram of a scanning electron microscope [133]*

II.6.2.1 Atomic force microscopy (AFM)

Atomic force microscopy (AFM) is a non destructive and very high resolution imaging technique, with demonstrated resolution in the order of fractions of a nanometer. The AFM is one of the most widely used tools for imaging, measuring, and manipulating samples at the nanoscale. There is no special sample preparation required in this technique and the measurements can be carried out at ambient environment. Figure II.16 illustrate the block diagram of AFM. In AFM the information is gathered by "feeling" the surface with a mechanical probe. Piezoelectric scanners that facilitate tiny but accurate and precise movements on command enable very precise scanning. The AFM consists of a cantilever with a sharp tip (probe) at its end is used to scan the specimen surface. When the tip is brought into

proximity of a sample surface, forces between the tip and the sample lead to a deflection of the cantilever according to Hooke's law.

Typically, the deflection is measured using a laser spot reflected from the top surface of the cantilever into an array of photodiodes. If the tip was scanned at a constant height, a risk would exist that the tip collides with the surface, causing damage. Hence, in most cases a feedback mechanism is employed to adjust the tip-to-sample distance to maintain a constant force between the tip and the sample. Traditionally, the sample is mounted on a piezoelectric tube, which can move the sample in the z direction for maintaining a constant force, and the x and y directions for scanning the sample. The resulting map of the area z = f (x, y) represents the topography of the sample [134,135].

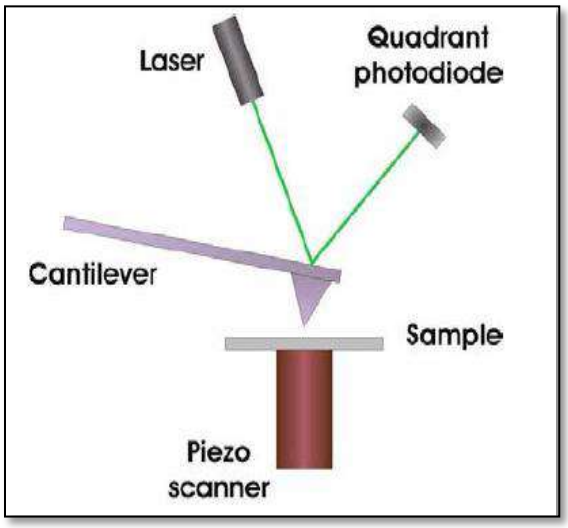

Figure II. 16: *Shows the block diagram of Atomic Force Microscope [136].*

The surface of our ZnO films is characterized by Atomic Force Microscopy (AFM) Nanosurf easy scan 2 and the roughness values are specified from this analysis.

II.6.4 Optical properties

All optical properties of ZnO thin films, ZnO nanostructures and also the photocatalysis measurement were characterized through UV-Visible spectroscopy by means of Shimadzu 3101PC double beam spectrophotometer. The optical band gap, absorption coefficient and the refractive index was also measured using the giving expression:

- ✓ The absorption coefficient (α): in the spectral region of the light's absorption, was deduced from the Beer-Lambert law using the following expression [137]:

$$\alpha = - (1 / d) \ln (100/T) \quad \text{(II.18)}$$

Where α is absorption coefficient, d is the film thickness and T is the transmittance.

- ✓ The optical band gap (Eg): The study of the spectrum of the absorption coefficient α of a semiconductor in the fundamental region and near the fundamental edge provides us with valuable information about the energy band structure of the material [137].
  The absorption coefficient α can be divided into two regions the higher values and the low of the absorption coefficient region.

In this region absorption coefficient takes the form [138]:

$$(\alpha h\nu) = A (h\nu - Eg)^{r} \quad \text{(II.19)}$$

$$A = (4\pi\sigma / nc\, Ec) \quad \text{(II.20)}$$

Where Eg is the optical energy gap of the material, r is the power which characterizes the transition process, c is the speed of light, σ is the minimum metallic conductivity (extrapolated dc conductivity at T= ∞), Ec is a measure of the width of the tail states distribution and n is the refractive index.

In semiconductors there exist two types of band to band transitions (i) allowed and (ii) forbidden (forbidden transition take into account the small but finite momentum of photon these transitions are less probable). Direct band gap semiconductor transitions mostly occur between two bands of the same k values as. The allowed transition can occur in all values of k however forbidden can only occur at $k \neq 0$. r = 2 and 2/3 for direct allowed and forbidden transitions, respectively. In indirect semiconductor, a phonon is involved in the transition in order to conserve momentum. In the indirect transitions, r = 1/2 and 1/3 for indirect allowed and forbidden transitions, respectively.

We usually used the graph $(\alpha h\upsilon)^{r}$ against hυ for the determination of the width of Eg. Figure II.17 shows that plot of $(\alpha h\upsilon)^{2} = f(h\upsilon)$ is linear function for ZnO films. The linearity indicates the existence of the direct allowed transitions. The extrapolation of linear portion of the spectrum to αhυ = 0 give us the value of Eg.

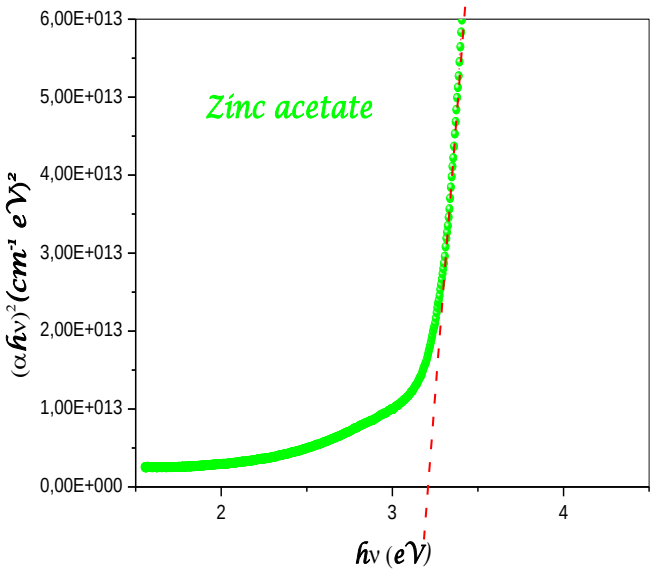

Figure III.17: *Typical variation of $(\alpha h\upsilon)^2$ as a function of hυ for Zinc acetate film for the determination of the optical gap*

Figure II.18 illustrated the curve of the estimated refractive index as function of wavelength in the range 200-800 nm. As showed in this Figure II.18, in the wavelength range between 750 and 800 nm the refractive index was found to be ~1.51.

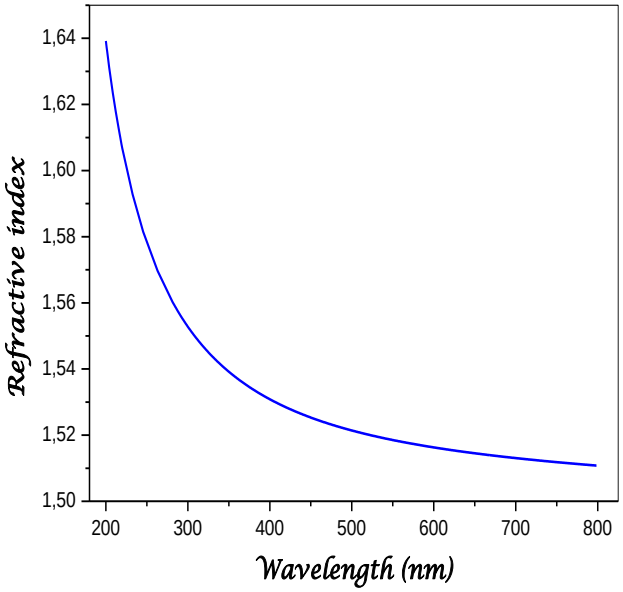

Figure II.18: *Variation of refractive index versus wavelength for ZnO thin films deposited at 350°C using Zinc acetate.*

II.6.5 Electrical proprieties

The electrical measurements were performed at room temperature and in dark with the electrical D.C transport. The dark conductivity is measured by this method.

The electrical D.C transport characterization was performed using coplanar structures in samples with two evaporated golden strips used as electrodes as showing in Figure II.19. The electrodes spacing is 5 mm. The applied voltage is varied from 0 to 20V, Keithley electrometer 610 is used for current measurements. We have checked the ohmicity of this contact by plotting the IV characteristics.

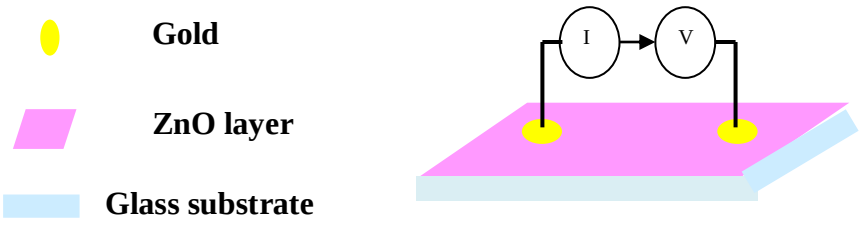

Figure II.19: *Schematic diagram of coplanar structures*

Chapter III

Results and Discussion : ZnO Thin Films and One dimensional Nanostructure

In this chapter, different ZnO thin films with various investigation parameters and the synthesis of ZnO one dimensional nanostructure (1D) are presented with their characterization; structural, morphological and optical.

III.1 ZnO THIN FILMS

III.1.1 Influence of Dye Concentration

The objective of this study aimed to know the influence of dye concentration on photocatalytic activity. The concentration of Red Reactive 184 used was varied (10^{-5} mol/l and 10^{-6} mol/l). The photocatalysts used in this investigation are ZnO thin films prepared via Pneumatic Spray Equipment (HOLMARC) with the same elaboration conditions; 0.1 M of zinc chloride, 100 µl/ min as flow rate, 350°C as substrate temperature and 5 min as a growth time.

III.1.1.1 Concentration of 2.10^{-5} mol/l

For the concentration 2.10^{-5} mol/l of RR-184 by the samples of zinc chloride with the same conditions of deposition, we observed that the photodegradation is significant when the solution is on contact with ZnO photocatalyst. Figure III.1 shows the variation of absorbance of this dye during 300 min of UV light irradiation. The absorbance peak intensity at 542 nm is decrease gradually with the increase of time from 0 min to 300 min.

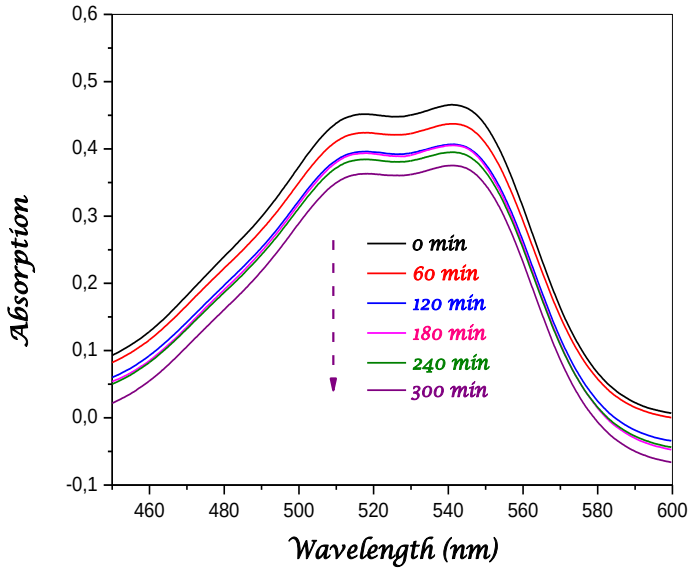

Figure III.1: *Variation of absorbance of Red dye during 300 min of UV light irradiation.*

The photodegradation kinetic of Red dye by ZnO thin films was drawn in Figure III.2. As can be seen, the ratio C/C_0 of this polluant is reduced gradually to reach the maximum 0.8 after 300 min of irradiation times.

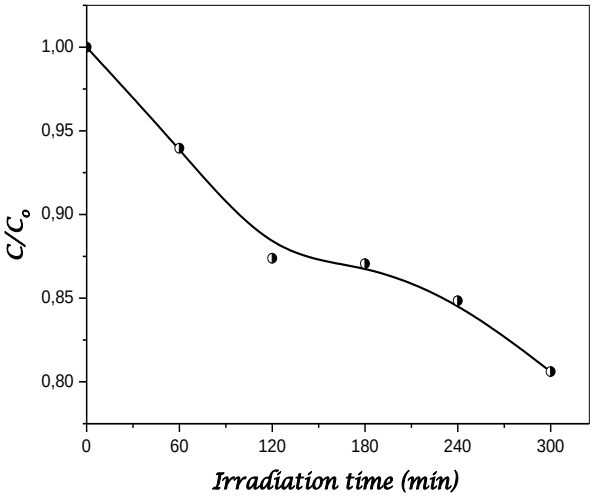

Figure III.2: *Photodegradation kinetic of Red dye by ZnO thin films with C= 2.10^{-5} mol/l.*

The constant of reaction rate k was given through the exploitation of Ln (C/C_0) vs time. Figure III.3 exhibits the plot Ln (C/C_0) as function as time exposure of UV light of Red dye by ZnO thin films. The estimated value of rate K was found 6.61x10^{-4} min^{-1} (R^2= 0.92).

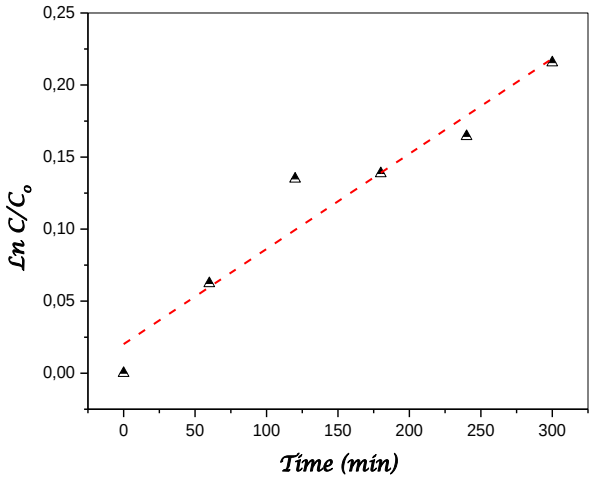

Figure III.3: *Representation of Ln (C/C_0) as function as time exposure of UV light of Red dye by ZnO films.*

The degradation efficiency of this dye was computed by the law which was expressed in the equation (III.3) in the next paragraph of this chapter. Figure III.4 presented the degradation efficiency of Red dye during irradiation times by ZnO photocatalyst. As shown the decolorization of this RR-184 dye is reached ~ 20 % after 300 min of exposure of UV light.

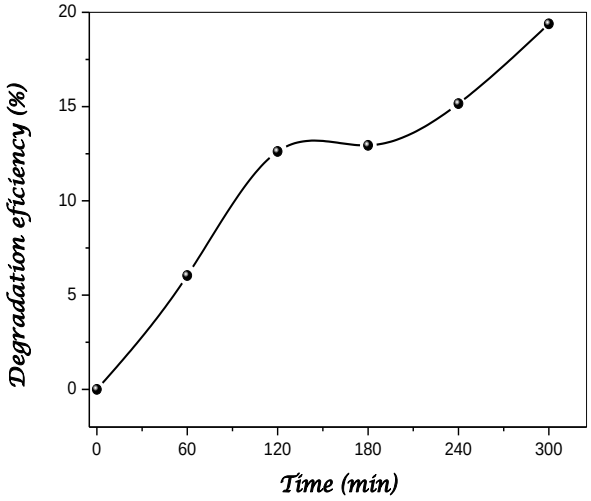

Figure III.4: *Degradation efficiency of Red dye during 300 min of irradiation.*

III.1.1.2 Concentration of 4.10^{-6} mol/l

The results of this concentration are well presented in details in the next section of influence of salt source of zinc oxide.

III.1.2 Influence of time deposition

In this section, we start by introducing the results of the influence of thickness or deposition time on the films properties. By Spray Pyrolysis Equipments (HOLMARC), we deposited ZnO thin films by using 0.1 M of Zinc Chloride ($ZnCl_2.2H_2O$) diluted in methanol. The prepared solution is then sprayed on the heated glass substrates by a Syringe pump with flow rate of 100 µl /mn. The substrates temperature was kept at 350°C. In order to vary the film thickness**,** the duration of deposition is changed between 5 and 10 min.

III.1.2.1 Growth rate

In Table III.1, we have reported the film thickness and the deposition rate with different deposition time. The deposition rate is estimated from the ratio of the thickness of the layer on the deposition time. As can be seen the deposition rate of ZnO thin films deposited with zinc chloride during 5 min is almost similar to the deposited rate of the films obtained with the same precursor after 10 min. The difference in thickness originates from the difference in the deposition time that may alter the films growth mechanism. The formation of the films is produced by the pyrolytic reaction on the surface of substrate.

Table III.1: *Films thickness and the deposition rate of ZnO with various deposition times.*

Zinc Chloride	*Thickness (nm)*	*Deposition rate (nm/min)*
T_d = 5 min	85	17
T_d = 10 min	188	19

III.1.2.2 Structural properties

In Figure III.5 we have reported the XRD spectrum of ZnO thin film prepared after 5 and 10 minutes of deposition time; Film A and Film B, respectively. The films obtained are polycrystalline with a hexagonal wurtzite structure and a preferential orientation of c axis perpendicular to the substrate. The several diffracted peaks observed in the diffractograms of

both films (100), (002), (101), (102), (110), (103) and (113) can be exactly indexed as the hexagonal wurtzite ZnO with lattice constants a = 0.3249 nm and c = 0.5206 nm, which are agreed well with the values in the standard card (JCPDS 36-1451). In addition, all peaks of the film B and have much higher intensity than Film A, which indicate that films formed have higher crystallinity ,a narrower shaped and lower surface defects.

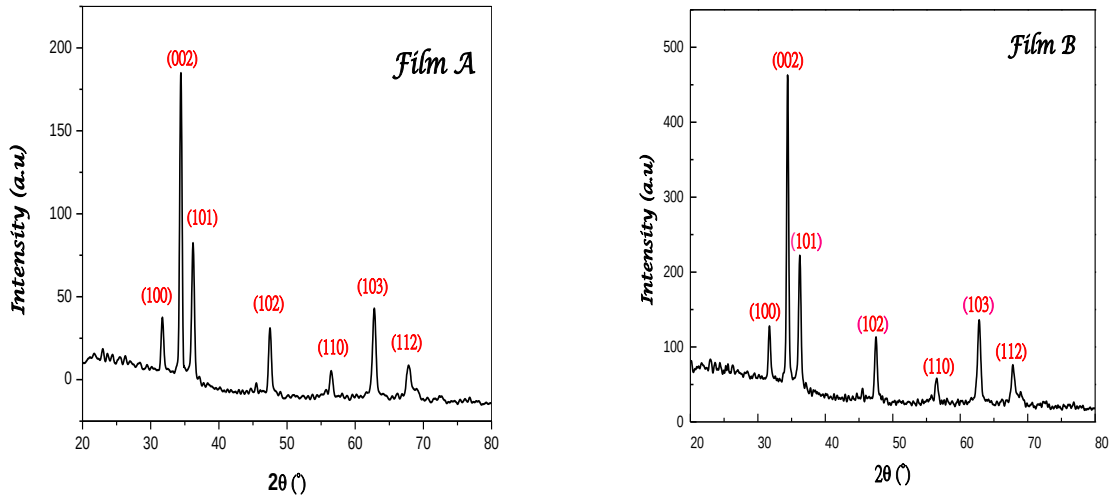

Figure III.5: *XRD pattern of ZnO film obtained after 5min (Film A) and 10 min (Film B) of deposition time*

The average crystallite size D and the internal lattice strain ε values were calculated from the least square fit to β cosθ/λ vs sinθ/λ plot as shown in Figure III.6.

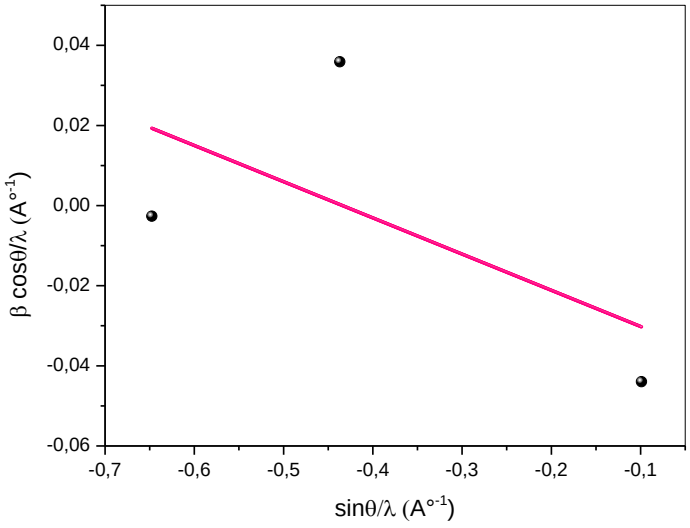

Figure III.6: *Plot of Hall equation for ZnO thin film deposited for 10 min*

The intercept of the plot to y-axis gives rise to the average grain size; the obtained values are recorded in Table III.2. The values of crystallite size and strain of ZnO thin films obtained after 5 and 10 min of deposition time are 27 nm, 0.35 and 25 nm, -0.09 respectively. It's seems that the crystallite size of films is approximately the same. While the strain is the opposite, a positive slope was observed for Film A which means confirms the presence of tensile strain in the crystal lattice. Moreover, a negative slope was noticed in the Hall equation plot for ZnO films deposited for 10 min indicating the presence of compressive strain in the crystal lattice.

Table III.2: *Crystallite size, Number of crystallites, Strain and Dislocation density of ZnO with various deposition times.*

ZnO Films	*Crystallite size D (nm)*	*Number of crystallites/unit area ($10^{-3}nm^{-2}$)*	*Strain ε*	*Dislocation density $\delta * 10^{-4}$ ($lines/m^2$)*
Film A (5 min)	27	9.54	0.35	14
Film B (10 min)	25	12.02	-0.09	16

III.1.2.3 Film morphology and surface

III.1.2.3.1 SEM analysis of films

As can be seen, the morphology of films was observed by SEM. As shown in Figure III.7 (a and b), Film A is porous and exhibits a non continuous network (Figure III.7.a) ended with a rod like structure. While, film B is dense and has a continuous structure with a smooth surface as shown in Figure III.7 b. Due to its structure film A have a larger specific surface then film B, consequently film A will offers larger reactive surface with the environment, this feature is required for gas sensing or for water treatment.

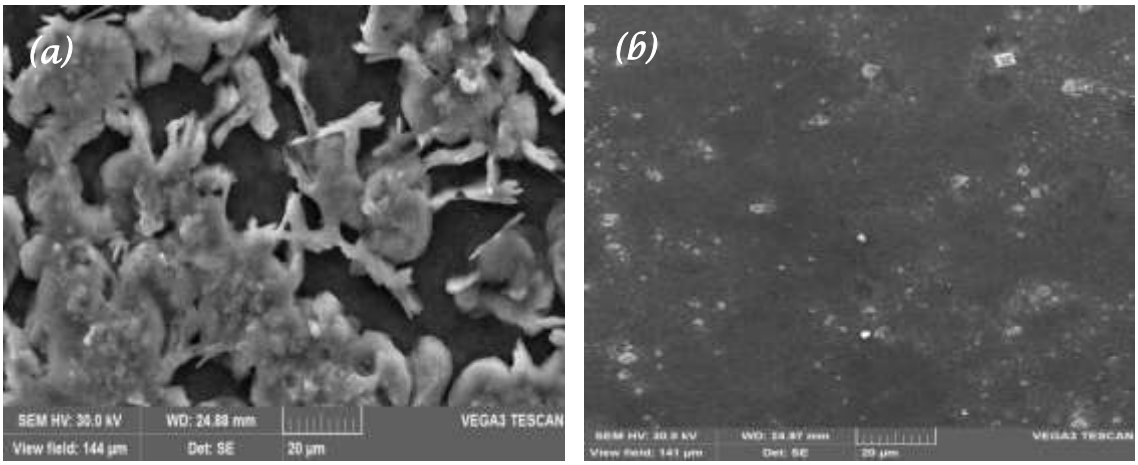

Figure III.7: *SEM image of ZnO thin films: (a) film A; prepared 5 min and (b) film B prepared with 10 min.*

III.1.2.3.2 AFM images of ZnO films

Atomic Force Microscopy (AFM) has been proved to be a unique method to analyze surface morphology of a film. The films AFM images are reported in Figure III.8, as shown film A exhibits a rough and nanostructured surface composed with nanorods normal to the substrate surface. However, the film B exhibits a more dense and continuous surface without noticeable nanostructure. Films surface roughness was estimated from these AFM images, film A is rougher than film B as reported in Table III.3 and they are respectively 36 and 8 nm.

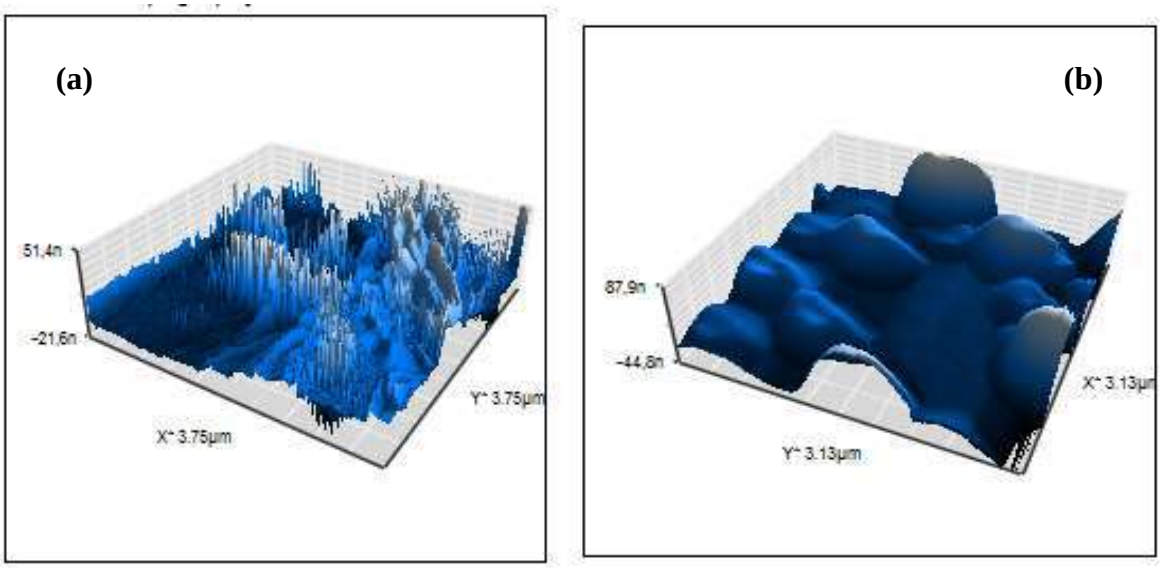

Figure III.8: *AFM images of ZnO: (a) film A (5 min) and (b) film B (10 min)*

III.1.2.4 Photocatalysis process

In the present work, we have studied the photocatalysis application of ZnO thin films for the degradation of the red reactive dye. The used solution was prepared from Red Reactive 184 powder (Cibacron Red FB) dissolved in distilled water to obtain a solution with concentration of 10^{-5} mole/l.

ZnO samples were placed inside a beaker containing 250 ml of solution. The beaker was exposed to an UV irradiation with a wavelength of 365 nm and 2W power. During light exposure the dye solution is slowly stirred. The distance between the samples and the light source was fixed at 20 cm. Each 15 minutes of light exposure a small quantity of dye solution is withdrawn to monitor the dye degradation through recording the UV visible absorption spectrum of the solution by using a Shimadzu UV 3101-PC spectrophotometer.

In Figure III.9 (a) and (b), we have reported the variation of absorbance spectra of polluted solution after different UV light exposure times. The wavelength region is ranged from 450 to 600 nm; this broad absorption band is a characteristic of the used red dye. From this Figure III.9, according to the progressively absorbance intensities, we conclude that the photo degradation is more significant when solution is in contact with film A then with film B.

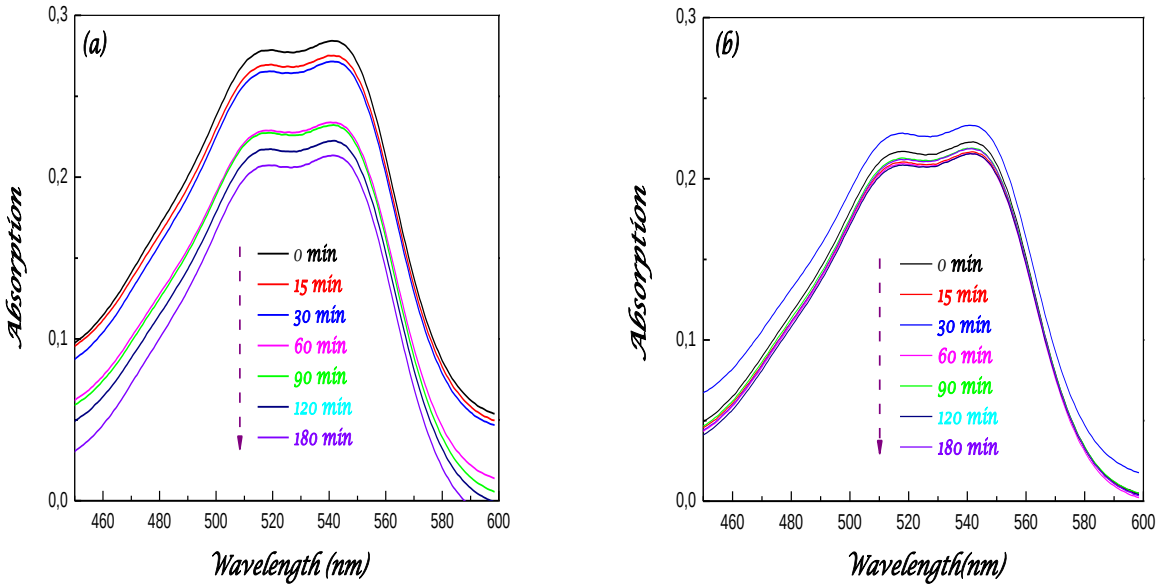

Figure III.9: *UV-Vis absorption spectra of the degradation of dye red solution in contact with ZnO thin films deposited in (a) 5 min and (b) 10 min.*

To have more insight on the photodegradation kinetics and the influence of ZnO film thickness we have monitored the variation of the intensity of the absorption located at 542 nm. The variation of the ratio C_0/C of ZnO thin films deposited in 5 and 10 min is illustrated in Figure III.10.

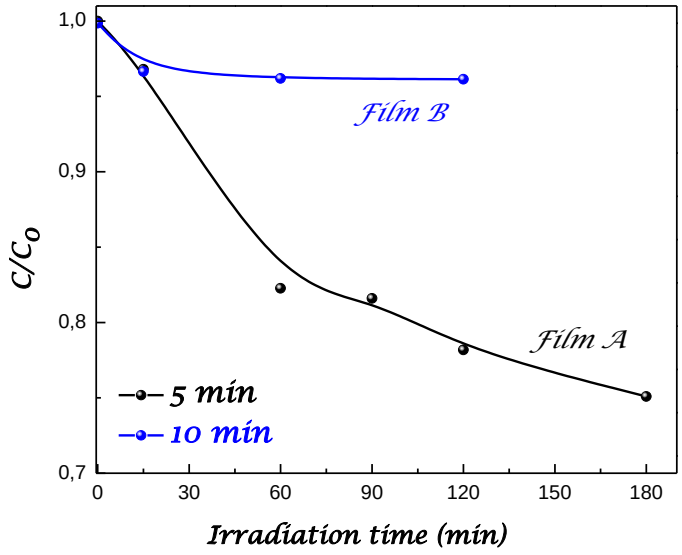

Figure III.10: *Photo degradation Kinetic of dye red pollutant by ZnO thin films.*

As can be seen from Figure III.10, the photo degradation is more important when using film A, the ratio is reduced with increasing exposure time, and it reaches 0.75 after 180 minutes of irradiation. However in the case of thicker film B; the ratio is slightly reduced up to 0.9 during the first 30 minutes to saturate with further increasing exposure time.

As shown in Figure III.11, the photocatalytic decomposition of red pollutant, in contact with the surface of ZnO thin films A and B, follow a pseudo first-order kinetic law, it can be expressed by the following relation [2]:

$$-Ln\left(\frac{C}{C_0}\right) = kt \qquad \text{(III.2)}$$

Where C and C_0 are the reactant concentration at time t and $t = 0$, respectively and k rate constant (reaction rate constant) [2]. In Table III.4, we have reported the calculated value of the rate k for both ZnO thin films. Film A is characterized by a larger rate k then the film B.

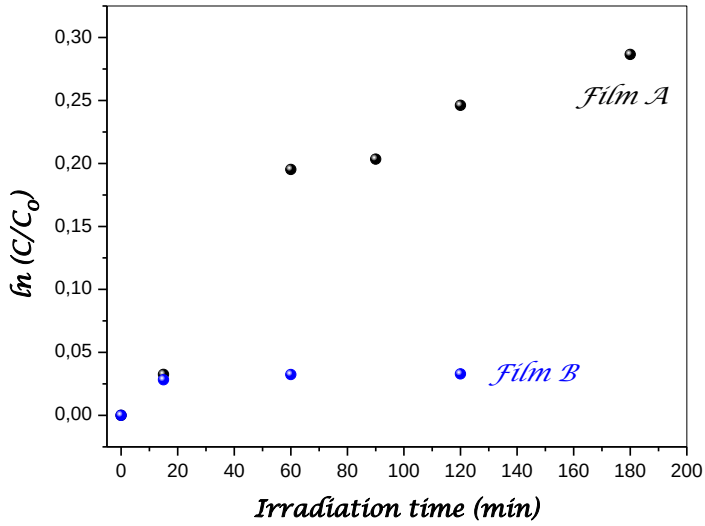

Figure III.11: *Representation of ln C/C_0 of red pollutant during 180 min irradiation*

The degradation efficiency of films defined as:

$$\tau = \frac{C_0 - C_t}{C_0} * 100 \qquad \text{(III.3)}$$

This rate τ is an interesting quantity that can yield information about the pollutant degradation; it represents the relative quantity of removed pollutant from the solution.

The variation of the degradation efficiency obtained with films A and B is shown in Figure III.12. In the case of film A, 25 % of polluant is removed after 180 minutes of exposure time, while only less than 2% is removed when using film B.

The discrepancy in the photocatalysis activity of both films A and B may found explication in the difference between their microstructure. Films morphology and specific surface play an important role in the photocatalysis kinetics. Morphology and structural properties of ZnO may be altered by film thickness thereafter their photocatalytic activity.

As deduced from AFM and SEM images, film A is rough and has a porous structure while film B is smoother and has a continuous structure. Therefore the reactive specific surface of film A is larger than in film B, thereafter, more reactive surfaces are available for the water than in film B. The same conclusion has been outlined by Li et al [3] in ZnO/CuO structure, they reported that a material with an open and porous surface exhibit higher degradation efficiency.

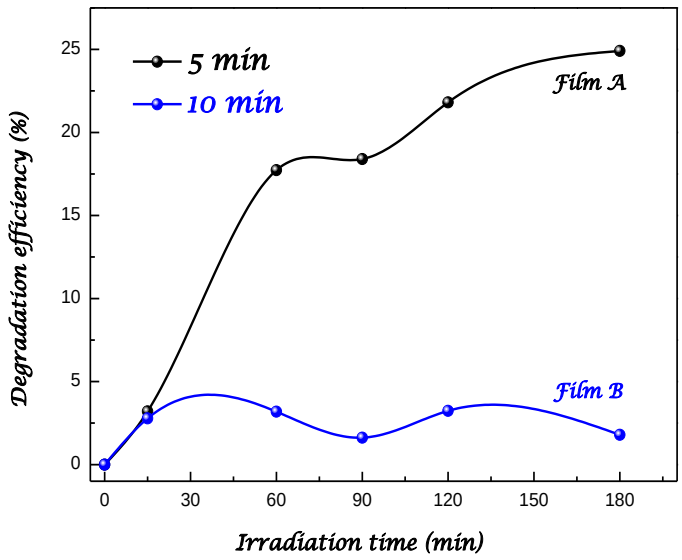

Figure III.12: *Degradation efficiency of dye red pollutant as function of Irradiation time by ZnO thin films deposited at : 5 min. and 10 min.*

Owing to their large specific surface nano-sized particles are well recommended for the photocatalysis [4-6]. Unfortunately they agglomerate and their recycling after photocatalysis is drawback for a massive water treatment thus the preparation of nanostructured ZnO in a substrate or the deposition of porous thin film may be a durable solution for water de-pollution. ZnO thin films have attracted much attention in recent years due to their various applications to the photocatalytic degradation of organic pollutants in water and air and dye sensitized photovoltaic solar cell.

Table III.3: *Surface roughness, rate constant k and degradation efficiency of ZnO films*

ZnO samples deposition time	*R_a (nm)*	*Rate k $*10^{-4}(min^{-1})$*	*Degradation efficiency (%)*
Film A (5 min)	36.00	16.30	25.00
Film B (10 min)	8.50	2.00	1.80

III.1.3 Influence of Zn salt source

In order to investigate the influence of the precursor's salt nature on ZnO photocatalytic activity, we have studied the photodegradation of a red dye polluant in contact with irradiated ZnO thin films. In spray deposition technique several Zn salts have been used. We have prepared ZnO thin films with three different precursors Zinc acetate ($Zn(CH_3COO)_2.2H_2O$), Zinc nitrate ($Zn(NO_3)_2.6H_2O$) and Zinc chloride ($ZnCl_2.2H_2O$). All the other parameters are fixed for all salts: the molarity was 0.1 M; the substrate temperature is equal to 350°C, the flow rate was 100 µl /min and the deposition time was set 5 min.

III.1.3.1 Growth rate

In Figure III.13, we have reported the growth rate for the three different used precursors. The growth rate of thin films prepared by Zinc nitrate is larger compared with both Zinc acetate and chloride precursors. However, zinc acetate yields to slower deposition rate. The influence of precursor nature on the deposition rate may be explained in terms of the difference in the involved pyrolytic reactions on the substrate surface during film growth. The values of thickness and growth rate of these ZnO films are listed in Table III.4.

Table III.4: *Thickness and deposition rate of ZnO films deposited with different precursors.*

ZnO precursors	Thickness d (nm)	Growth rate (nm/min)
Nitrate	210	42
Chloride	203	40
Acetate	135	27

The difference between the behaviors of the solutions used is due to that of the enthalpy of formation and the chemical nature of each precursor. It should be remembered that ΔH formation of Zinc acetate is equal to 0.1 Kcal / mol (0.043 eV) while that of Zinc nitrate is 10 Kcal / mol (0.43 eV) and zinc chloride is 30 Kcal / mol (1.30 eV).

These values show that in the deposition phase, the acetate dissociates more easily than the nitrate and chloride. This explains, at the substrate temperature of 350 °C, the high value of the

growth rate obtained in the case of the films deposited with the acetate but in our study it's for nitrate films. Ayouchi et al. [7] observed a decrease in the rate of growth of films deposited by zinc acetate as a precursor. So the deposition rate of films depends to nature of precursor used and substrate temperature.

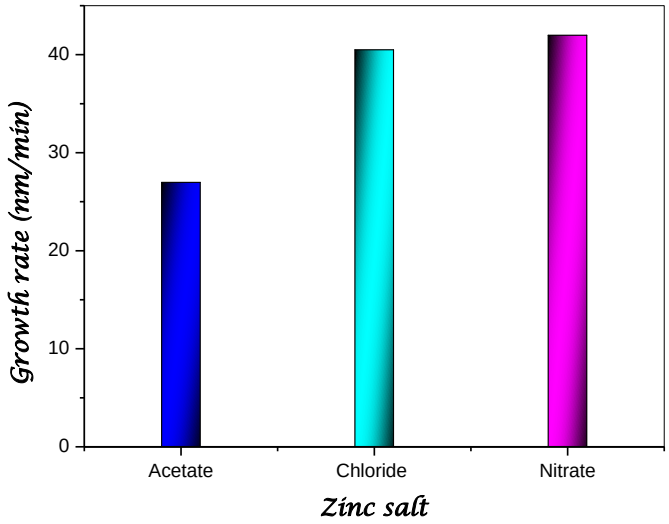

Figure III.13: *The growth rate of Zinc salt source*

III.1.3.2 Films structure

Figure III.14 shows XRD spectra of different films deposited with the three used salts. As can be seen, the ZnO films prepared from zinc nitrate and zinc chloride were polycrystalline with hexagonal wurtzite structure. While, films prepared with zinc acetate exhibits an amorphous phase due to the absence of any relevant peak. The XRD diffraction pattern of both films deposited using nitrate and zinc chloride are composed with several peaks assigned to (101), (002), (101), (110) planes as shown in Figure III.14.

We noticed that when we using a chloride as a precursor, diffraction peak, assigned to the plane (002) became the preferential orientation indicating that the film have the Wurtzite hexagonal and the growth is achieved along the axis c normal to the substrate surface. However in the case of zinc nitrate precursor, the deposited film shows that the plane (101) is the most intense peak. The XRD results are in good agreement with Lehraki et al. [8] ones, they reported that ZnO thin films obtained by zinc chloride and zinc nitrate are polycrystalline in contrary to films prepared using zinc acetate that exhibit an amorphous phase. A. Hafdallah et al. [9] studied the effect of precursor solution on the structural and optical properties of ZnO

thin films prepared by Spray pyrolysis. They found that zinc acetate and nitrate are polycristalline with hexagonal wurtzite structure. While films obtained through Zinc chloride have totally an amorphous phase.

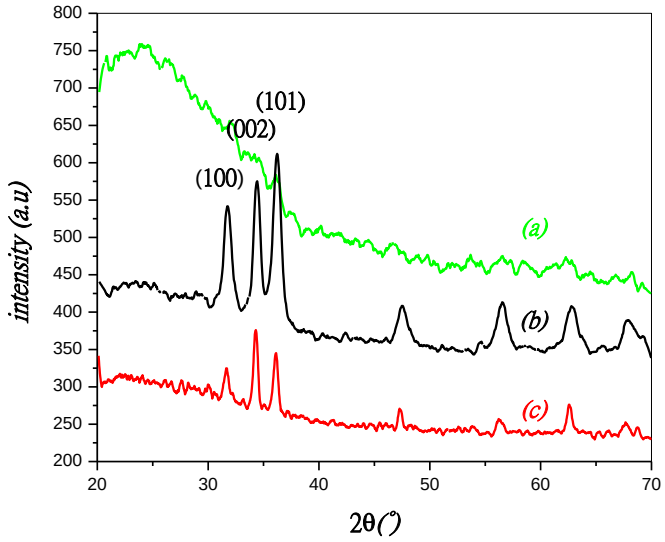

Figure III.14: *XRD diffraction pattern of ZnO thin films obtained by various precursors: (a) zinc acetate, (b) zinc nitrate and (c) zinc chloride*

The D and ε values were calculated from the least square fit to β cosθ/λ vs sinθ/λ plot as shown in Figure III.15. The intercept of the plot to y-axis gives rise to the average crystallite size; the obtained values are recorded in Table III.6.

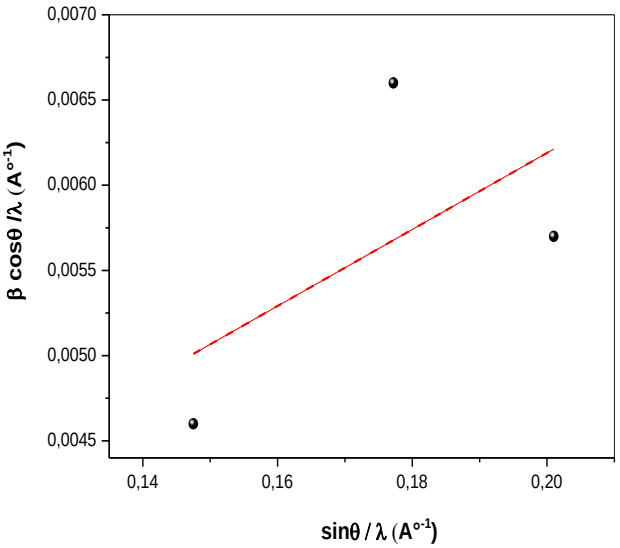

Figure III.15: *Plot of Hall equation for ZnO film using Zinc nitrate as precursor*

In Table III.5 we have regrouped the calculated structural parameters estimated from the all (hkl) atomic plan for the ZnO films elaborated with Zinc nitrate and Zinc chloride. The crystallite size values are 22 and 23 nm for the obtained films using Zinc nitrate and Zinc chloride salt respectively. A positive slope (0.22) has been observed in the Hall equation plot for ZnO thin films deposited with Zinc nitrate, which confirms the presence of tensile strain in the crystal lattice. However, a negative slope (-0.16) has been found for ZnO thin films prepared by Zinc chloride which means the presence of a compressive strain. The Dislocation density is defined as the length of dislocation lines per unit volume of the crystal, and it indicates the amount of defects as a result of the strain in films. This explained the difference between the values of δ for both films.

Table III.5: *The crystallite size and the strain of ZnO thin films prepared with various precursor*

ZnO Precursors	*Crystallite size D (nm)*	*Number of crystallites/unit area ($10^{-3}nm^{-2}$)*	*Strain ε*	*Dislocation density δ*10^{-4} ($lines/m^2$)*
Nitrate	22	19.72	0.22	21
Chloride	23	16.64	-0.16	19

III.1.3.3 SEM analysis

Figure III.16 shows typical SEM images of ZnO films prepared using the three different precursors. As shown, the films morphology depends strongly on the nature of the used precursor. Film prepared with zinc nitrate as starting solution is porous and exhibits a non continuous network (Figure III.16 a). However film prepared with zinc chloride exhibits a rough surface morphology and non continuous structure (Figure III.16 b). While as can be seen in Figure III. 16 c, zinc acetate precursor yields to a dense and continuous structure film with a smooth surface. Due to its structure, zinc nitrate films have a larger specific surface then the others films, so this film will offers larger reactive surface with the environment which is required for gas sensing or water treatment.

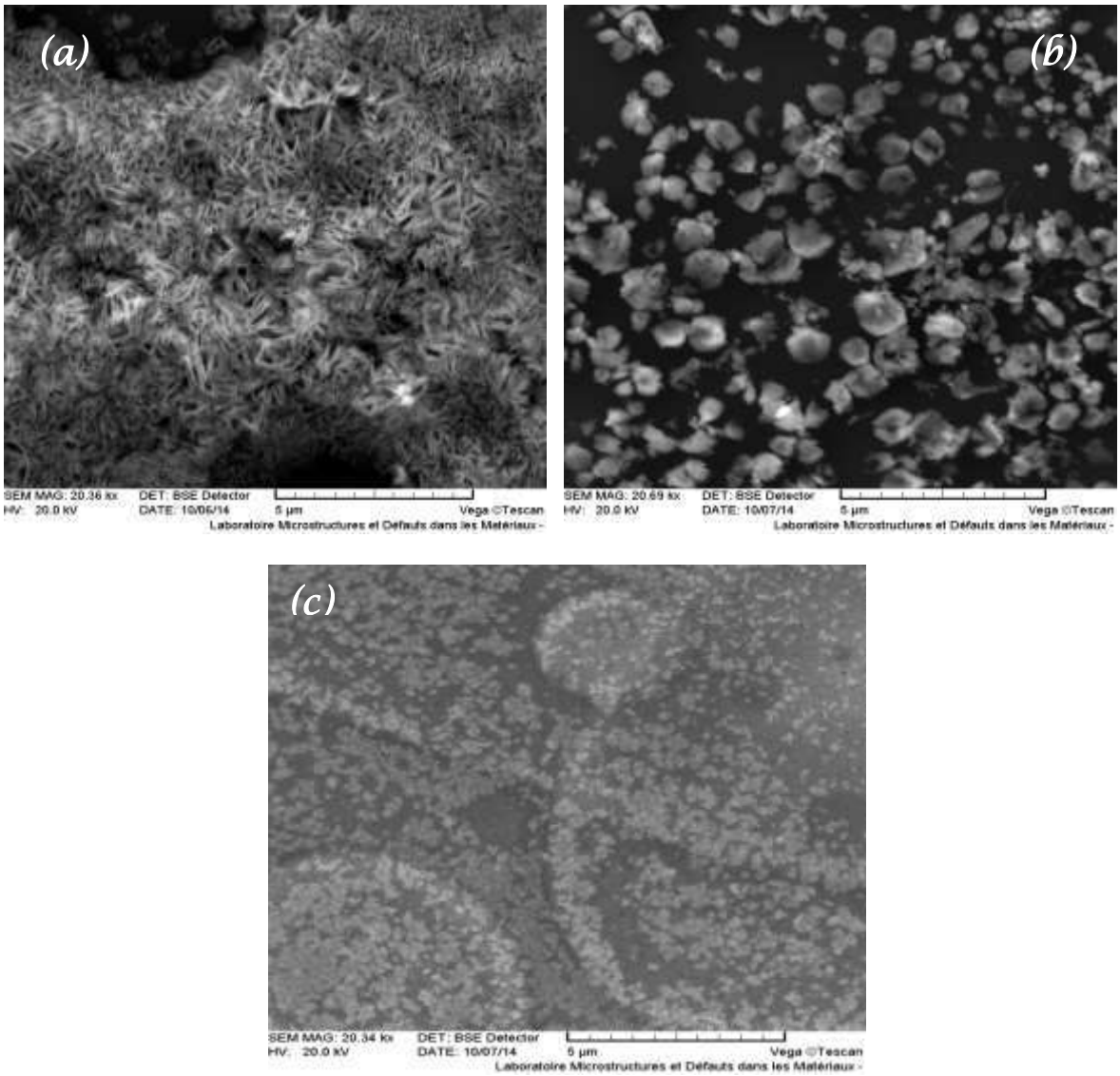

Figure III.16: *SEM images of ZnO thin films deposited at substrate temperature equal to 350°C with different solutions: (a) Zinc nitrate (b) Zinc chloride and (c) Zinc acetate*

III.1.3.4 Optical properties

In Figure III.17 we have reported the transmittance spectra in the UV-visible range of ZnO films prepared with different precursors. The film deposited with zinc acetate (Figure III 17 a) has the higher transparency of 87% than films deposited with zinc nitride and zinc chloride (curves 17 b and c). This is due to the smooth surface of the former. It is well known that rough surface causes the light scattering resulting in transmittance reduction. This explains the low transmittances measured in films deposited with zinc chloride and nitrate despite that their better crystallinity then the films deposited with zinc acetate. This is consistent with

films surface morphology observed in SEM images (Figure III.16). On the other hand, the variation in transmittance T can be explained by the variation in the thicknesses d of the films, knowing that the thickest films are the least transparent, in accordance with the Berr-Lambert formula:

$$T = \exp(-\alpha d) \qquad \text{(III.4)}$$

Where α is the absorption coefficient of the film. It is clearly seen that the increase in thickness is accompanied by a reduction in transmittance [9].

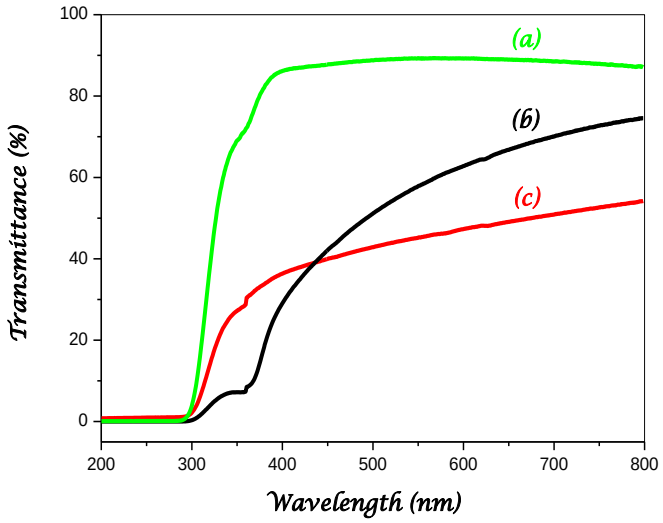

Figure III.17: *UV-visible transmittance spectrum of ZnO thin films deposited at 350 °C using different salts: (a) Zinc acetate-(b) Zinc nitrate-(c) Zinc chloride.*

For determination of Eg value of ZnO thin films with various precursors, we use the habitual method which relies to the plotting a curve of $(\alpha h\upsilon)^2$ against hυ. Figure III.18 illustrated typical variation of the quantity $(\alpha h\upsilon)^2$ as a function of photon energy hυ of different salt of Zinc oxide. The found optical band gaps are equal to 3.12 and 3.20 eV for films prepared with zinc nitrate and zinc acetate respectively .While the optical gap of film deposited with zinc chloride is 3.25 eV which less than that of the bulk ZnO.

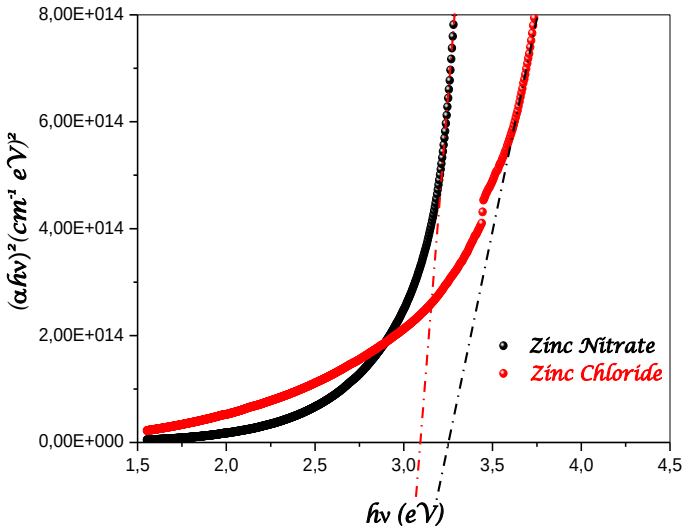

Figure III.18: *Typical variation of $(\alpha h\upsilon)^2$ as a function of hυ of different salt of Zinc oxide for the determination of the optical gap*

The films refractive index and optical band Eg deduced from optical transmittance spectra were drawn in Figure III.19.

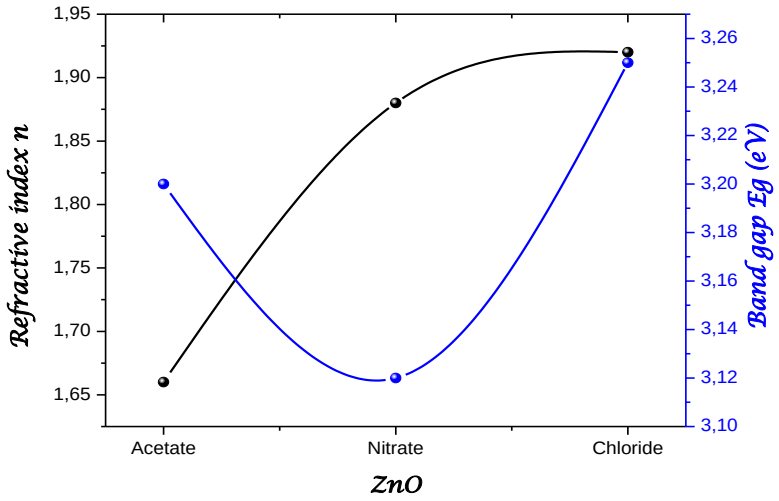

Figure III.19: *Band gap E_g and refractive index of ZnO with different precursors.*

In Figure III.20 we have represented the variation of absorption coefficient (α) as function of the wavelength. It is clear that the prepared ZnO films have a high absorption coefficient with a value of 10^7 (cm^{-1}) in the visible range of the wavelength. However, the film deposited with Zinc acetate as a precursor shows the highest absorption coefficient and it is the double value of α of film obtained by zinc chloride. This explains also the calculated optical band gap.

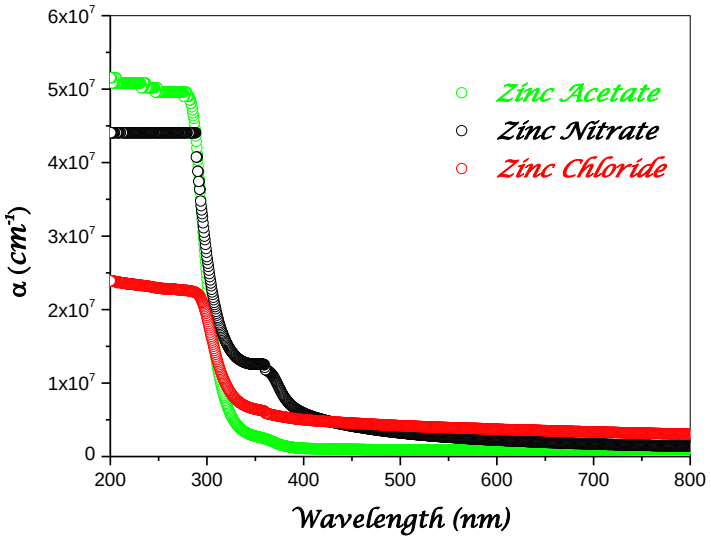

Figure III.20: *Variation of absorption coefficient of ZnO precursor versus wavelength*

III.1.3.5 Electrical properties

Figure III.21 shows the variation of the electrical conductivity of ZnO thin films with different source salt, measured in the dark at room temperature. As can be seen the conductivity variation have a bell U shape behavior with maximum values found for the deposited films through Zinc nitrate. It is well know that conductivity is altered by the substrate temperature.

The film growth rate can be considered to be able to induce the resistivity variation. With slower growth rate, the ad- atoms may have enough time to find energetically stable location and move on the surface, so that the resulting film would have higher density of dislocation and lower resistivity in turn which means higher conductivity [10].

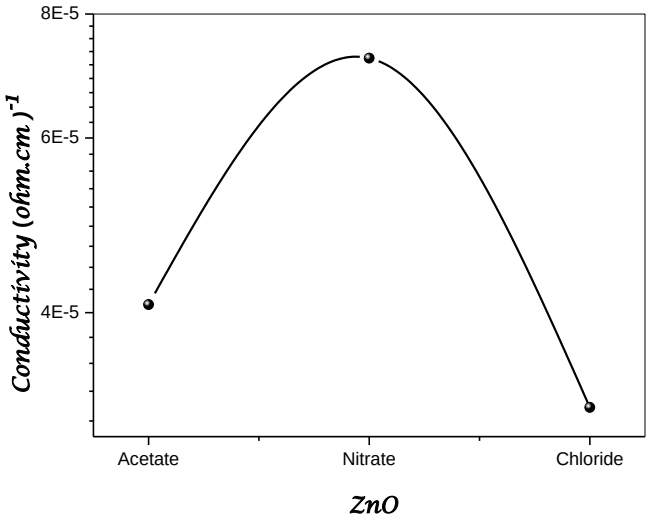

Figure III.21: *Variation of the conductivity for the three precursors.*

III.1.3.6 Photocatalytic activity

The photocatalytic activities of ZnO thin films with various salt sources were evaluated via the degradation of Red Reactive dye. An aqueous solution of Red dye (concentration was chosen 4 x10^{-6} mol/ L and the volume used was 75 mL) was taken into the glass reactor covered with aluminium layer which prevents the exterior light. The initial pH of aqueous solution was determined at 4.2.

Before irradiation, the aqueous solution was magnetically stirred in the dark for few minutes to obtain the Red dye adsorption equilibrium. Then the reaction solution was irradiated by an UV light lamp (20 W) placed about 13 cm above the photocatalyst surface.

During the illumination, 5 ml of dye solution was collected at regular time intervals and analyzed by a UV–visible spectroscopy in wavelength region between 450 nm and 600 nm.

Figure III.22 exhibit the variation of absorbance spectra of polluted solution after various irradiation times from 0 min to 240 min. As shown, the intensities of absorption of ZnO thin films with several salt sources decrease gradually with exposure time of UV light.

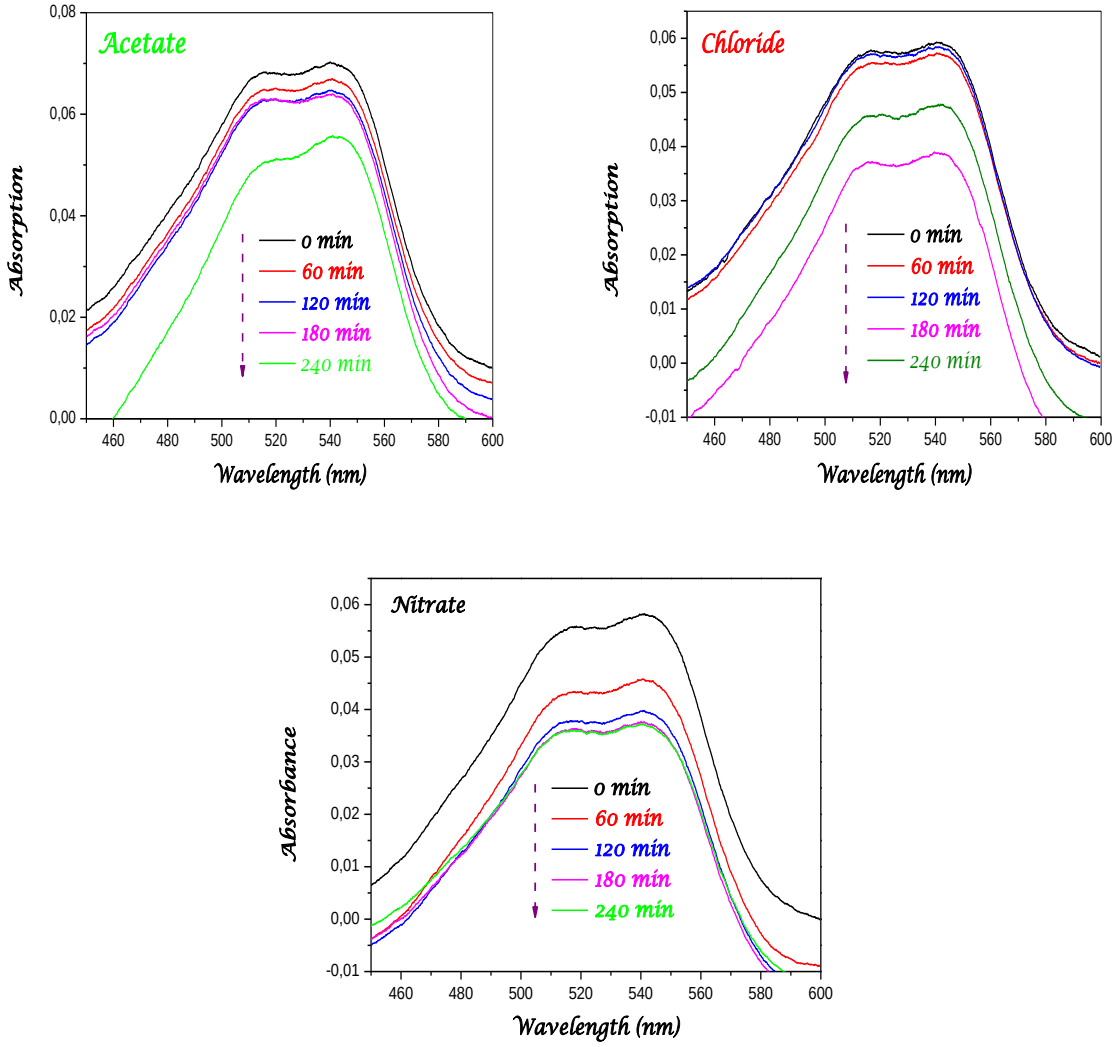

Figure III.22: *UV-Vis absorption spectra of the degradation of dye red by ZnO thin films*

As shown in Figure III.23, the ratio C/C_0 of Zinc nitrate film is reduced with increasing exposure time; it reaches 0.64 after 240 minutes of irradiation. However in the case of zinc acetate and zinc chloride films, the ratio is slightly reduced up to 0.78 and 0.83 after 240 minutes, respectively. We observed from this Figure III.23 that Zinc nitrate film represents a rapid photodegradation compared to the others films. The last sampling point of kinetics after 300 min of reaction showed us which precursors has better degradation. So the photo degradation is more important when using films obtained with zinc nitrate salt.

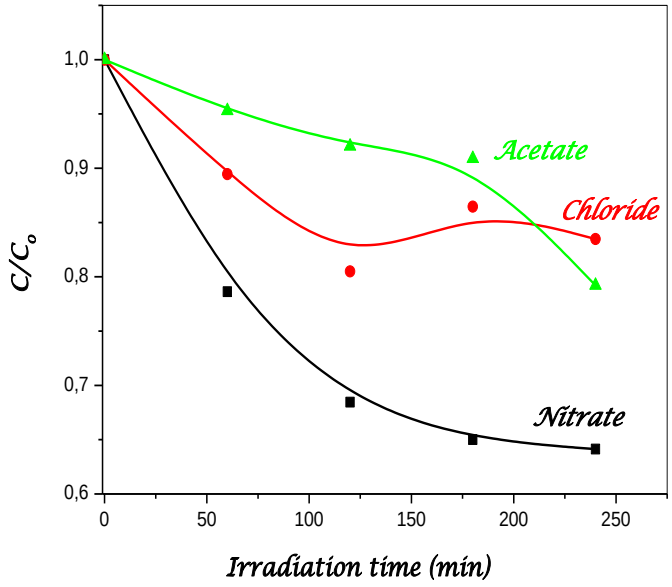

Figure III.23: *Photo degradation Kinetic of dye red pollutant by all the ZnO films.*

As deduced from SEM images, zinc nitrate and zinc chloride films are rough and have a porous structure however zinc acetate film is smoother and has a continuous structure. Moreover, the reactive specific surface of the first film is larger than in the other ones. Thereafter, more reactive surfaces are available for the water than in the other ones (acetate and chloride).

From this investigation we inferred that the starting salt source nature and morphology of the Zn salt play an important role on the ZnO photocatalytic activity. Thin and porous films offer more reactive sites due the large surface to volume ratio. According to films morphology, we concluded that zinc nitrate source is the best precursor for the preparation of ZnO thin film suitable for red dye photo degradation. Consequently, the reactive specific surface is one of the important parameters controlling the photocatalytic activity of ZnO thin films.

III.1.4 ZnO thin films and Gold Nanoparticles

Metal nanoparticles (NPs) have long been considered to exhibit unique physical and chemical properties different from those of the bulk state or atoms, due to the quantum size effect resulting in specific electronic structures [11–17]. Gold nanoparticles (Au NPs) are probably the most remarkable members of the metal NP groups [18–21] and have attracted considerable interest and driven a variety of potential applications in catalysis [22–31], biology [32–36], and optics [37–39]. Indeed, more than 70,000 publications have appeared on Au NPs to date.

During the last years there has been a renewed interest in nanoparticles specially the NPS of Nobel metal like Gold, Argent and Platinum. In this section, we are interesting about the inclusion of Gold nanoparticles in ZnO thin films deposited by spray pyrolysis and study their structural and optical properties in order to investigate the effect of these Nanoparticles especially in photocatalysis application. The concentration of Au NPs is varied from 0; 2.5; 10 to 30 %.

III.1.4.1 Synthesis of gold nanoparticles

Nanoparticles of gold have been prepared by simple chemical method, we using 0.29 m mol of $HAuCl_4 3H_2O$ dissolved in distilled water and the solution was heated to boiling in the bath of water at 60°C. Then 1.03 m mol of Tri-sodium citrate dehydrate ($C_6H_5Na_3O_7.2H_2O$) dissolved in distilled water and some of tri sodium citrate were added to the first solution after boiling. Finally, the solution was left for 30 min at 60°C for heating and then it was cooled to room temperature.

III.1.4.2 Preparation of ZnO solution

We prepared two solutions for deposition of ZnO thin films with and without nanoparticles of gold. The second solution is composed with 0.1 M of zinc acetate ($C_4H_6O_4.2H_2O$) as precursor diluted in methanol. Then we mixed the both solution to obtain thin films of pure ZnO and ZnO: Au with different inclosing of 2.5 %, 10 % and 30 % Au. The prepared solution is then sprayed on the heated glass substrates by an ultrasonic with flow rate of 7

ml/h. During the deposition, the substrates temperature was kept at 350°C and time of each sample was 5 min.

III.1.4.3 Absorption of Au NPs

Figure III.24 shows the absorption spectra of Au nanoparticles as function of wavelength. As displays in this Figure that the absorption of gold NPs was centered at 529.85 nm. In the literature they reported that the wavelength of Au NPs is ranged between 512-519 nm [40].

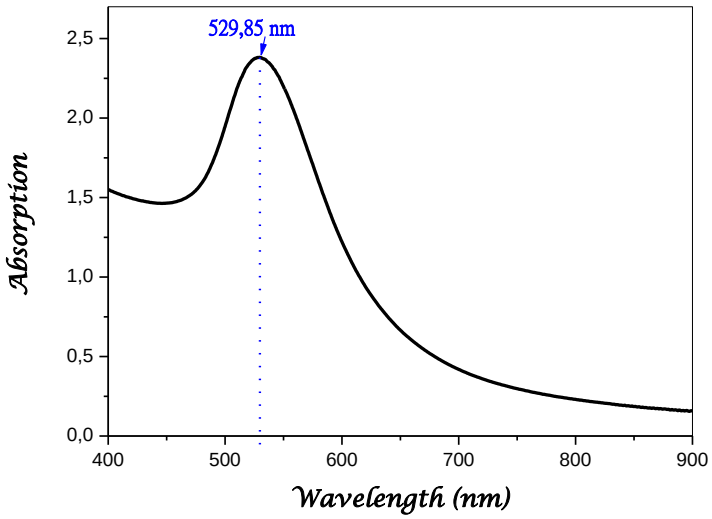

Figure III.24: *UV–vis absorption spectra of the gold nanoparticles*

III.1.4.4 Growth rate of films

As shown in the Table III.6, the thickness of films is increase with the increasing of concentration of Au nanoparticles and the growth rate of films is ranged from 40-44 nm/min.

Table III.6: *Thickness and deposition rate of ZnO: Au NPs*

ZnO : Au	Thickness (nm)	Growth rate (nm/min)
0 % Au	211	42,24
2.5 % Au	203	40,65
10 % Au	204	40,82
30 % Au	223	44,66

III.1.4.5 Films structure

Figure III.25 exhibits the XRD patterns of thin films of ZnO with and without inclusion of Gold nanoparticles. The deposited film shows that the plane (100) is the most intense peak. The presence of intense peaks in the XRD patterns of the films shows that the ZnO with Au NPs films are polycrystalline with Hexagonal wurtzite structure. The XRD diffraction pattern of ZnO films with 0, 2.5,10 % Au NPs are composed two peaks assigned to (100) and (110) planes. However when we using 30 % of Au NPs in ZnO films, we noticed several diffraction peak assigned to planes (100), (002), (101) and (110) as shown in Figure III.25. We observed that the intensity of peaks decrease with the increasing of concentration of Au NPs.

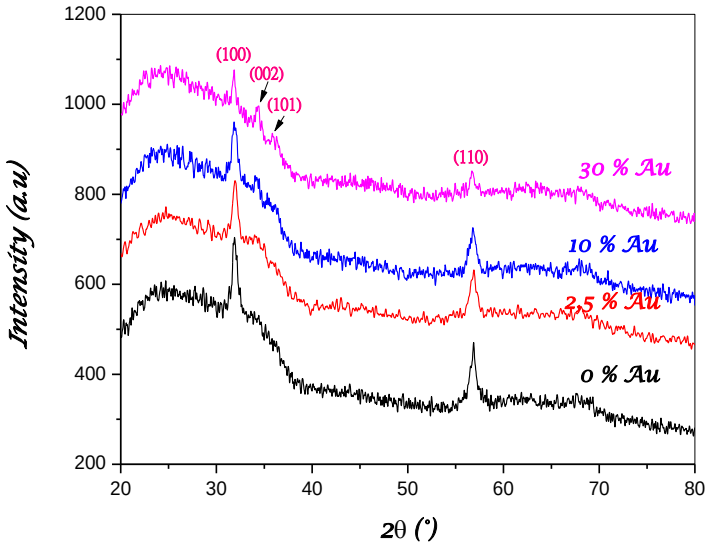

Figure III.25: *XRD diffraction pattern of ZnO thin films obtained with various concentrations of Au NPs*

The films crystallites size was estimated from the most intense peak namely (100) and (110) by using Debye Scherrer formula. In Figure III.26 we have represented the variation of the crystallites size as function of incorporation of Au NPs in ZnO thin films. It is clear from this figure that crystallites size decrease with increasing of concentration of Au NPs. The calculated crystallites size diminishes from 23 to 14 nm for incorporation of Au NPs.

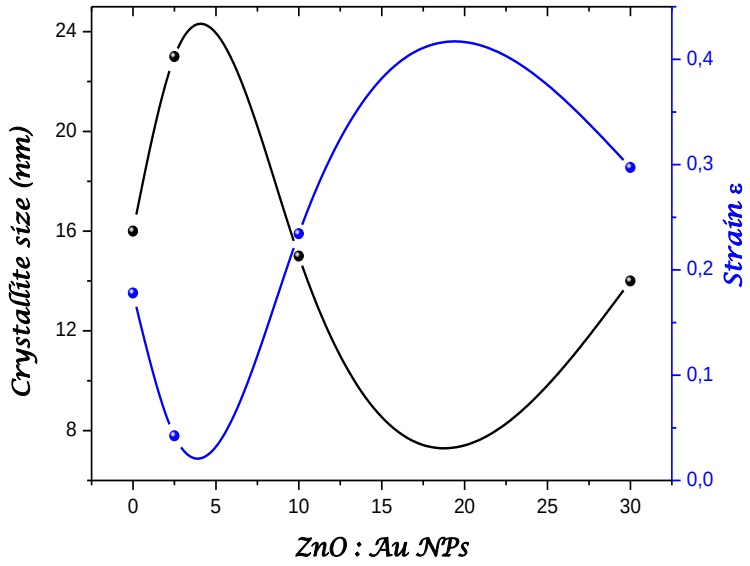

Figure III.26: *Variation of crystallites size and strain as function of ZnO: Au NPs*

The dislocation density and the number of crystallite of ZnO: Au NPs thin films were computed and the estimated values were registered in Table III.7.

Table III.7: *Values of dislocation density and number of crystallite of ZnO: Au NPs thin films*

ZnO : Au	Number of crystallites/unit area (10^{-3} nm^{-2})	Dislocation density δ (10^{-4}) ($line/m^2$)
0 %	51.56	39.06
2.5 %	16.70	18.90
10 %	60.48	44.44
30 %	81.38	51.02

Dislocations are the imperfections in a crystal associated with the mis-match of the lattice in one part of the crystal with respect to another part. The dislocation density (δ) is calculated from the equation (II.13). As observed form this Table III.8, the values of dislocation density for ZnO thin films with different nanoparticles of gold are ranged between 18.90 $x10^{-4}$ -51.02 $x10^{-4}$ lines/m^2. The dislocation density in our case is found to be increases with the increase of gold nanoparticles.

III.1.4.6 Morphology of films

Figure III.27 (a and b) shows typical two dimensional (2-D) and three dimensional (3-D) AFM image of pure ZnO and ZnO thin films with different incorporation of gold Nanoparticles; 2.5, 10 and 30% which deposited at 350°C.

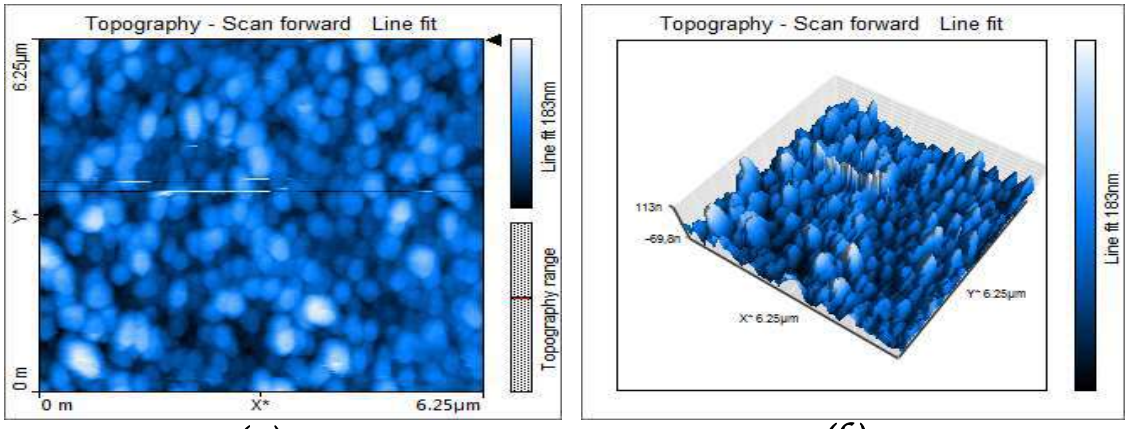

(a) (b)

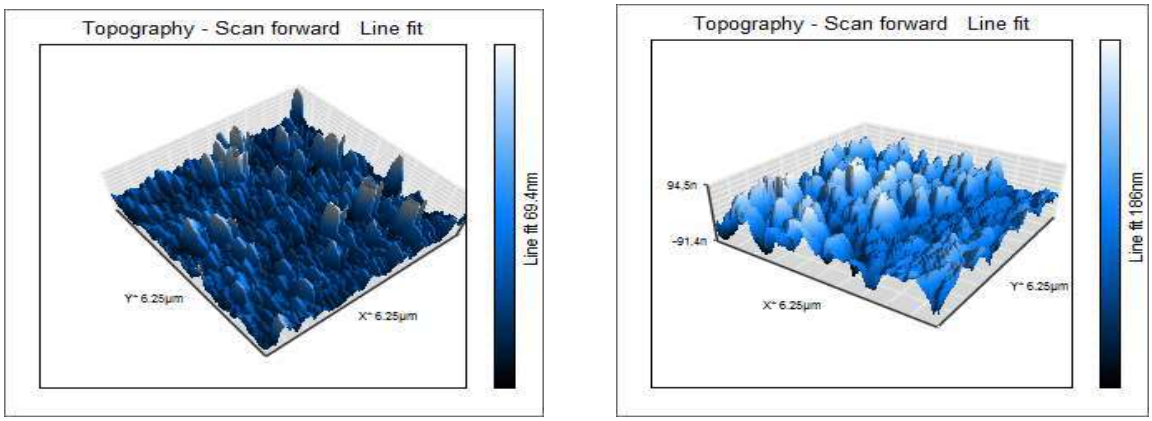

(c) (d)

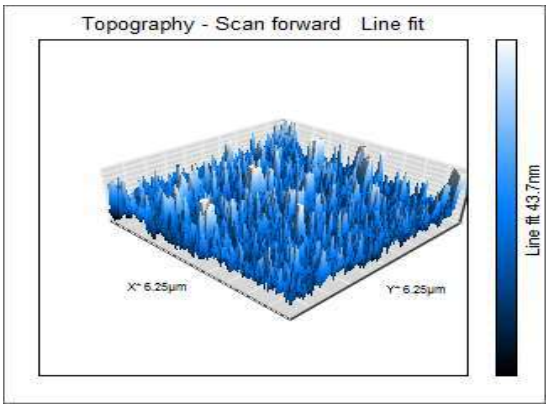

(e)

Figure III.27: *2-D and 3-D.AFM images of the deposited ZnO film (a-b) 0 % Au, (c) 2.5 % Au, (d) 10 % Au and (e) 30 % Au.*

The (3-D) image indicate that the surface evolution of the ZnO film shows hills and valley like structures, which are uniformly distributed over the entire substrate surface as displayed in Figure III.27-b. The 2-D images of the deposits show compact and granular morphology with presence of pores in the surface as shown in Figure III.27-a. However, Figure III.27 (c, d and e) represent the 3-D images of ZnO with 2.5%, 10% and 30% of Au NPs. As observed from AFM analysis, the surfaces of these films are porous with the presence of hills and valley in the full surface substrate especially for ZnO: 10 % Au NPs.

The values of roughness of these films are estimated from AFM analysis and listed in Table III.8. As seen the high values of roughness is for ZnO: 10 % Au NPs which found 35.12 nm.

Table III.8: *Roughness R_a of ZnO thin films with different inclusion of Au NPs*

ZnO: Au NPs	*0 %*	*2.5%*	*10%*	*30%*
R_a (nm)	29.01	15.50	35.12	5.15

III.1.4.7 Optical properties

Figure III.28 exhibits the transmittance spectrum in UV–visible region of ZnO films prepared with different including of gold nanoparticles. The measurements were performed in the UV-visible, corresponding to the wavelength range: 300-800 nm. As can be seen, all films have a high transparency more than 90% and with a sharp absorption edge at 390 nm. For the ZnO with Au NPS the value of transmission, in the visible region, is located in the average 91.45-

94.59 %. As shown in Figure III.28, an increase in the thickness is then followed by a slight decrease in the transmittance. So, the reduction in the film transparency can be attributed to the increase in thickness. As can be seen, we note the absence of interference fringes in the deposited films. The presence of interference fringe is due to multiple reflections at films/substrate and films/ air interface. These reflections appear only when the films are thick enough and mainly when the film surface is smooth. Furthermore, the rough surface film favors the light scattering at the surface which reduces the reflection and then the extinction of interference fringes this indicates that the surface of all the deposited films is rough.

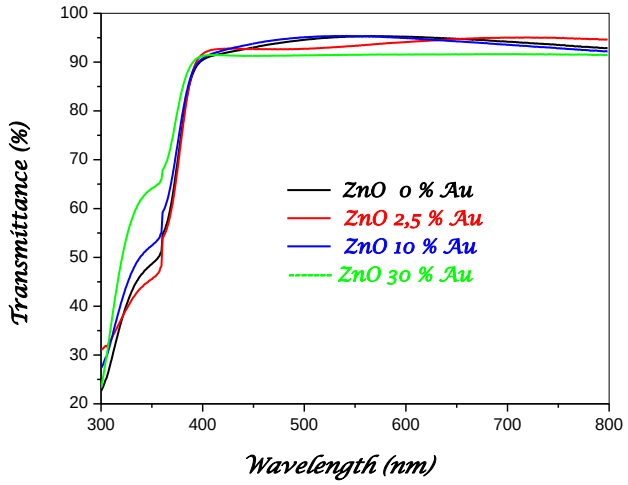

Figure III.28: *UV–visible transmittance spectrum of ZnO thin film deposited with different including of Au NPs*

Figure III.29 shows the absorption spectrum of ZnO thin films with and without Au nanoparticles. The absorption measurements were performed by UV-visible spectroscopy in the range of wavelength from 200 to 600 nm. As shown, ZnO film with 30% Au nanoparticles is more absorber than the others films. All films have a sharp absorption edge at 390 nm. The region of the absorption edge in all layers, due to the transition between the valence band and the conduction band, is located between 325–390 nm and in this region the transmission decreased because of the onset fundamental absorption.

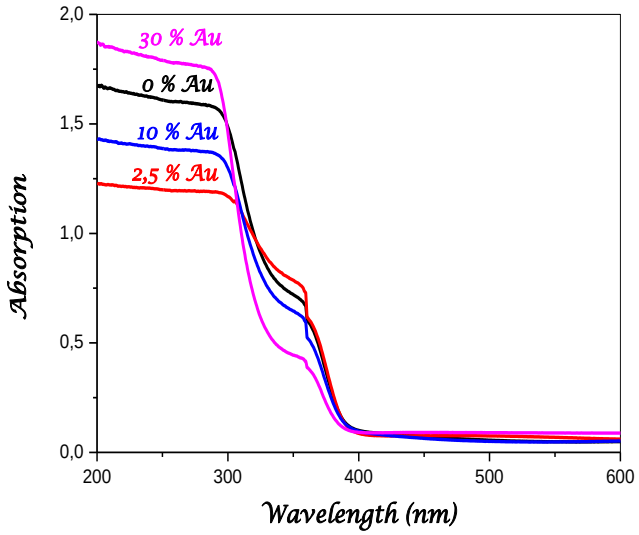

Figure III.29: *Absorption spectrum of ZnO: Au NPs*

Film optical band gap is estimated from Tauc formula for direct band gap semi- conductors. The obtained optical gaps are within the range from 3.30–3.39 eV. As offering the values of Eg increase with the increasing of Au nanoparticles. The variation of the refractive index n, deduced from the experimental transmittance data adjusted using the Swanepoel equations, is reported in Figure III.30. As shown in this Figure, the index n of the thin layers studied varies in the range 1.56 - 1.71.

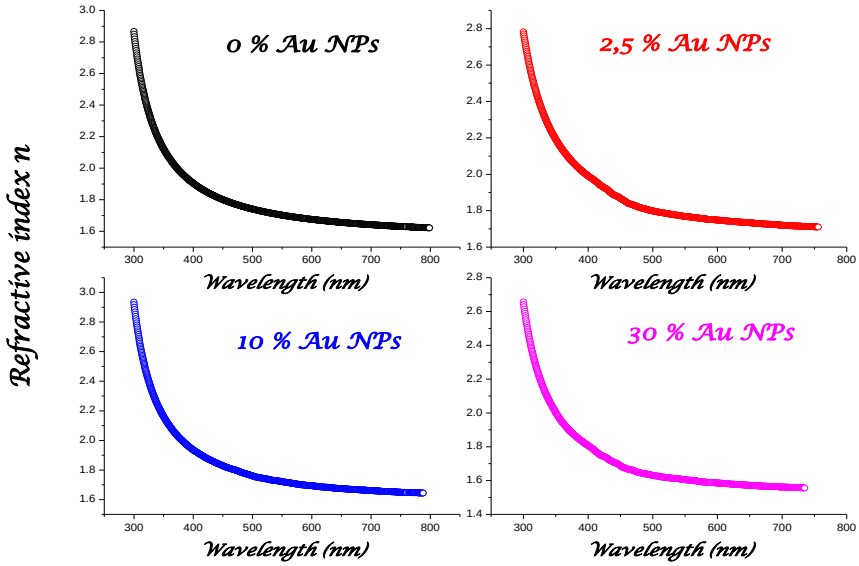

Figure III.30: *Refractive index of ZnO thin films with diverse nanoparticles of gold.*

Refractive index was estimated from fitting optical transmission data. The estimated refractive indices were plotted as a function of wavelength in Figure III.30. In the wavelength range between 750 and 800 nm the refractive index was found to be ~1.62 for 0 % Au NPs, 1.71 for 2.5 % Au NPs, 1.64 for 10 % Au NPs and 1.56 for 30 % Au NPs.

Figure III.31 presented the variation of thickness and refractive index as function of the incorporation of Au nanoparticles in ZnO thin films. In general, these two quantities have an opposite behavior. As remarked both variations have a U shape behavior also. The refractive index is varied from 1.56 to 1.71 with several nanoparticles of gold. It's obvious that the thickness of films obtained is decrease for both concentrations of 2.5% and 10 % Au NPs. Then an increase of thickness was observed for 30 % Au NPs, this explain the increase in band gap.

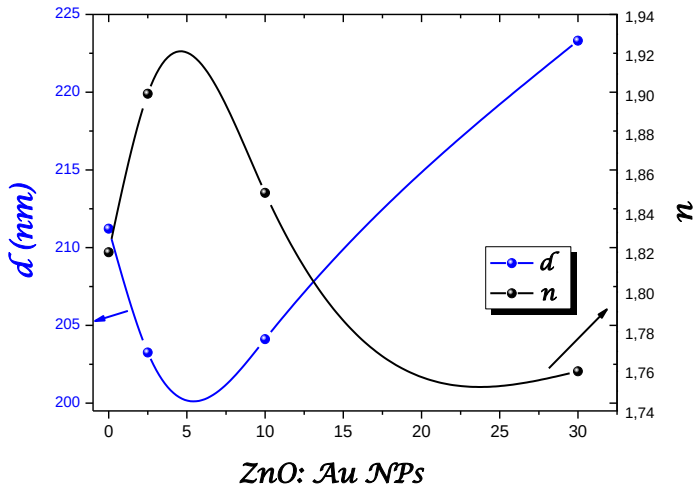

Figure III.31: *Variation of thickness and refractive index of ZnO versus Au NPs.*

III.1.4.8 Electrical properties

Conductivity measurements were made in the dark on coplanar structures, as mentioned previously. We used electrical gold contacts deposited on the surface of the films by DC sputtering. In Figure III.32 we have notified the variation of dark conductivities of ZnO thin films with several nanoparticles of Au measured at ambient temperature. As seen the conductivity of these films increases with increasing of the amount of gold nanoparticles and reach to the maximum values for 2.5% Au NPs. Then the conductivity decrease rapidly with the increase of Au nanoparticles (10 and 30% Au NPs).

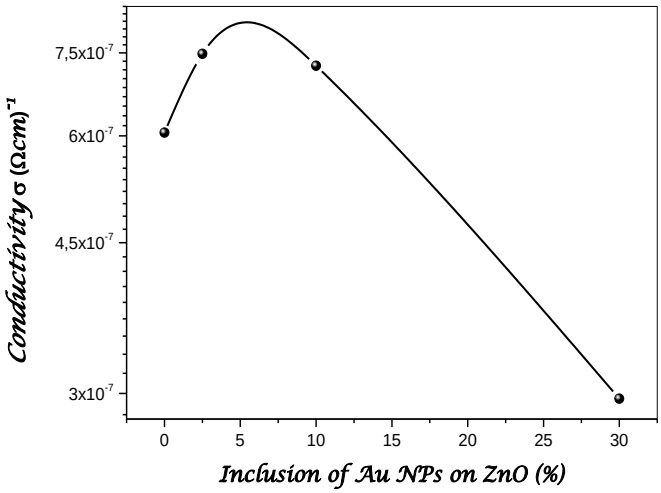

Figure III.32: *Dependence of the ZnO film conductivity to the inclusion of Au nanoparticles*

III.1.4.9 Photocatalytic activity

In this part, we have studied the degradation of Red reactive solution under different UV light radiation during 420 min via ZnO thin films with inclusion of Au nanoparticles in the wavelength region from 450 to 600 nm. The concentration of Red dye was 10^{-5} mol/l with pH of 4.6. In Figure III.33 we have manifested the distinction of absorbance of ZnO thin films with different Au nanoparticles. A decrease in the intensity of the pollutant peaks is observed between 0 and 360 min for the ZnO films with amount of 0 %, 2.5% and 30 % Au NPs.

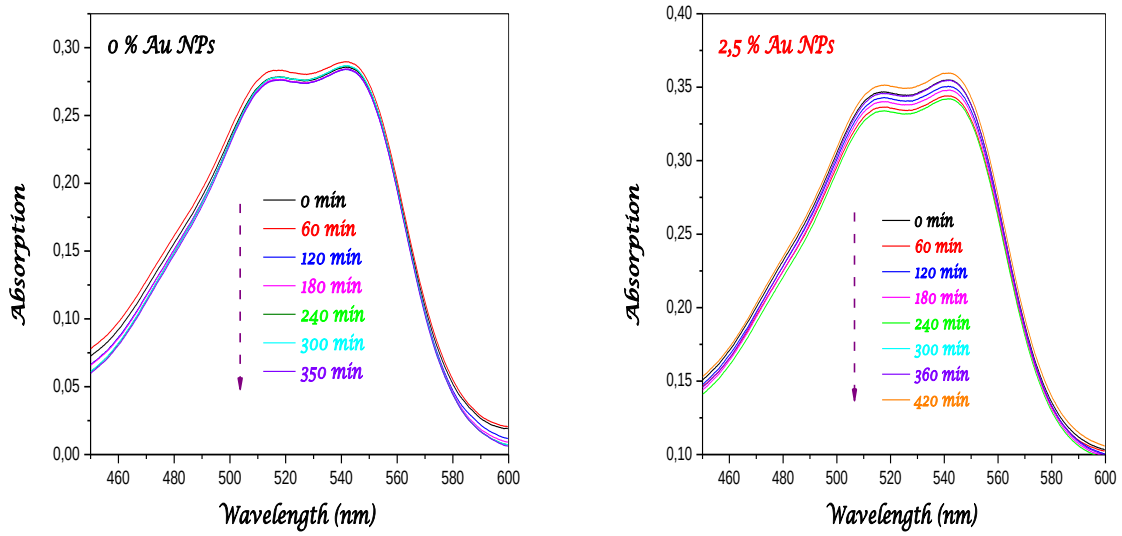

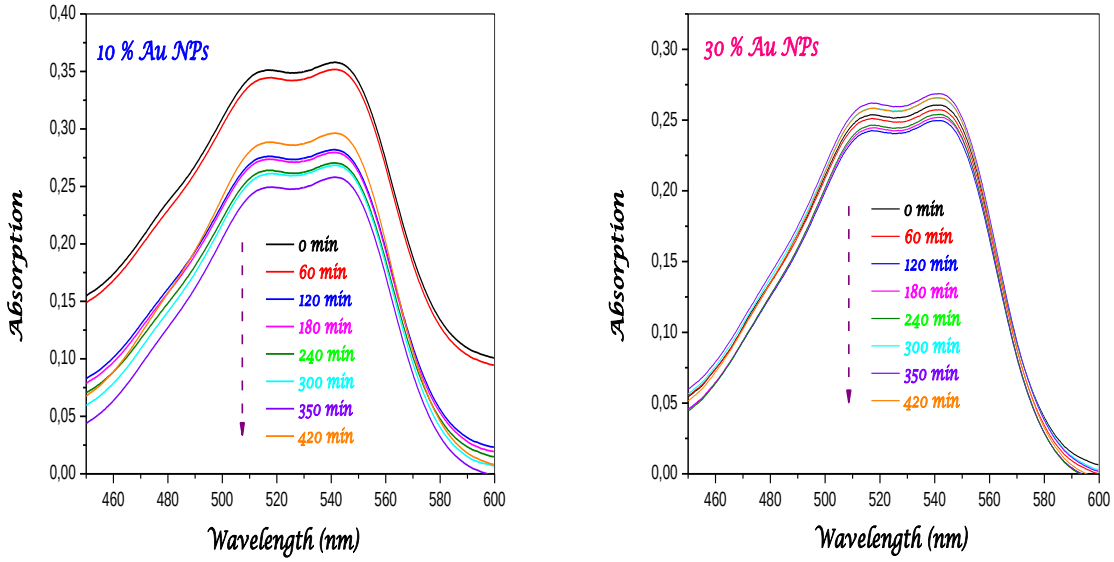

Figure III.33: *UV-Vis absorption spectra of the degradation of dye solution with ZnO: Au NPs*

However for ZnO incorporated 10 % Au NPs films, the absorbance is rapidly degraded after 60 min of irradiation time. Then the photodegradation of this Red dye is gradually slow after 120 min of reaction. This explains the degradation of the molecule as a function of the irradiation time by our films.

The kinetics of photodegradation of Red dye with a concentration C = 10^{-5} mol / l by ZnO films with various gold NPs is well displayed in Figure III.34. The ratio C/C_0 of ZnO: 10% Au NPs is reduced with increasing exposure time; it reaches 0.72 during 360 minutes of irradiation. Whereas in the case of the others films ZnO: 0% Au NPs and ZnO: 30% Au NPs, the ratio is slightly reduced up to 0.99 and 0.92 after 360 minutes, respectively. It's very clear that the photo degradation is more important when using of ZnO films included 10 % Au NPs.

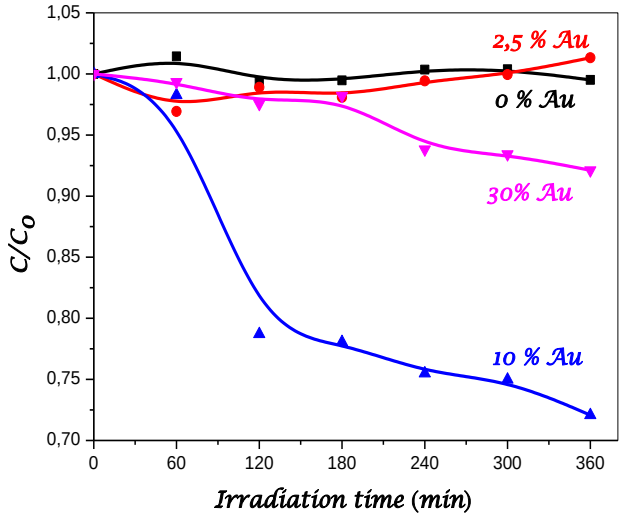

Figure III.34: *Photo degradation Kinetic of dye pollutant by ZnO thin films with Au NPs.*

III.2 ZnO NANOSTRUCTURED FILMS

Nanoscale materials have unique mechanical, electrical and thermal properties that make them very attractive in research and health related applications. Among these, one dimensional (1D) Zinc oxide (ZnO) nanorods (NRs) is a multilateral semiconductor which has been intensely studied as a promoting materiel for many industrial applications. For all their applications we focused our interest to the photocatalytic activity of organic dye. In this part of this chapter, the results of the different investigation parameters are presented with discussion.

III.2.1 Influence of salt source of ZnO

In this section, we present the results of ZnO nanostructures synthesis through the hydrothermal process with various seed layers of different precursors namely: zinc acetate, zinc nitrate and zinc chloride in order to investigate the photodegradation of Methylene Blue.

III.2.1.1 Deposition of seed layers

ZnO seed layers were deposited via Ultrasonic Spray pyrolysis with 0.1 Molarity of each precursor; zinc acetate, nitrate and chloride. The substrate temperature was fixed at 350°C; the solution was sprayed on glass substrate with flow rate of 6 ml/ h. The time deposition was specified as 10 min.

III.2.1.2 Synthesis of ZnO NRs

ZnO nanostructures were synthesized by a simple chemical route using hydrothermal process from aqueous solutions of Zinc nitrate hexahydrate ($Zn(NO_3)_2 \cdot 6H_2O$ and NaOH. In a typical synthesis, calculated amounts of $Zn(CH_3COO)_2 \cdot 2H_2O$ was added into 100 mL of doubly distilled water under stirring to prepare the Zinc solution. Then, NaOH solution was added directly into this solution under stirring to obtain the growth solution of ZnO nanostructures. The stirring was continued for 3 h at room temperature. Subsequently, the solution was allowed to cool down and left undisturbed overnight.

III.2.1.3 XRD analysis of ZnO NRs

Figure III. 35 (a, b and c) represent the XRD spectra of the various ZnO nanorods obtained by the hydrothermal method at 120 ° C during 3 h as a deposition time. In order to study the influence of the precursor (chemical source) of zinc on the growth of nanorods, we have separately used three precursors of Zinc acetate, Zinc nitrate and Zinc chloride. As shown in this Figure III.35 the X-ray diffraction spectra of ZnO Nanorods is depend strongly on salt source of Zinc which means on seed layer used for the growth of ZnO nanostructured.

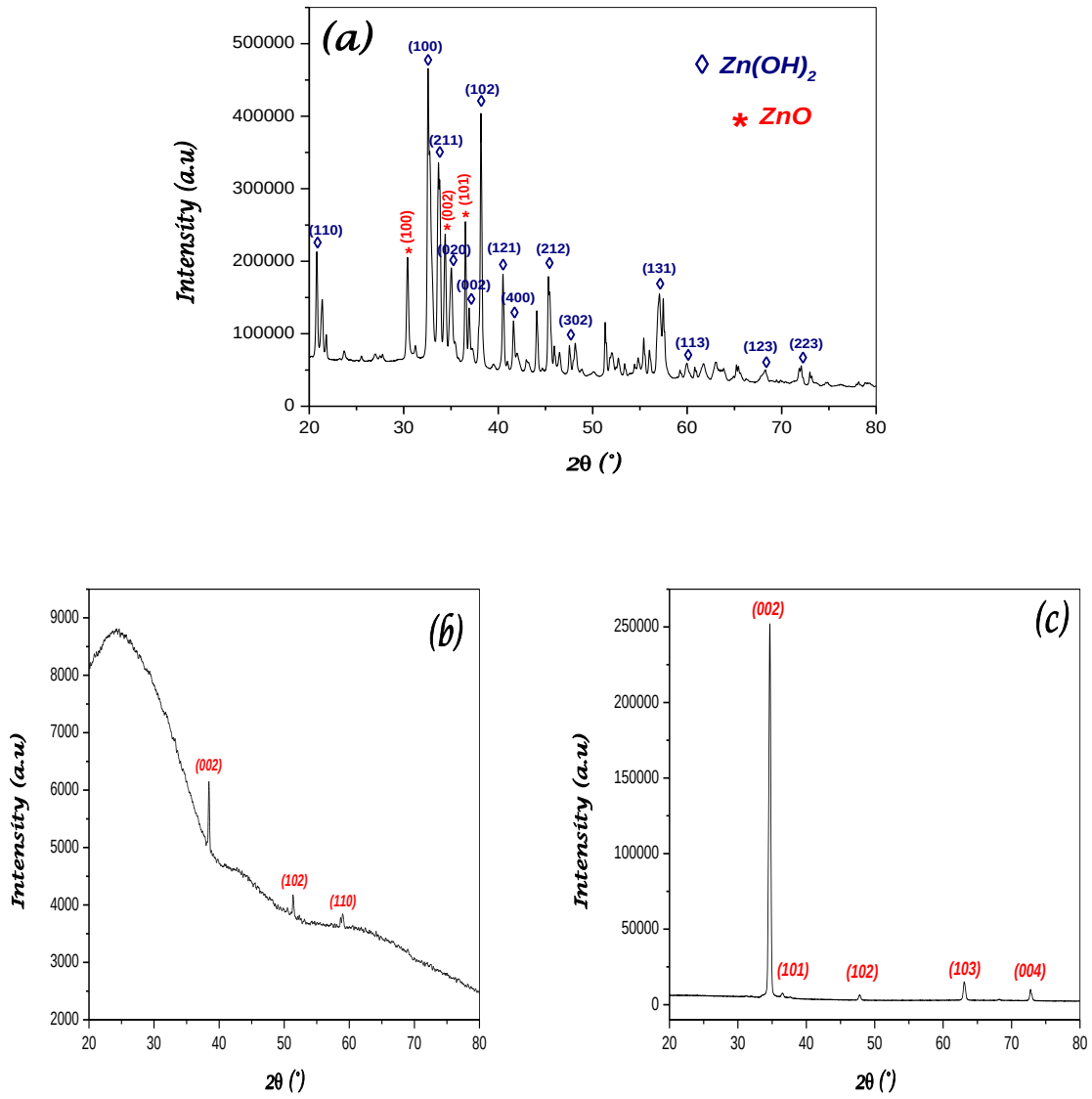

Figure III.35: *XRD spectrum of ZnO Nanorods prepared by hydrothermal at 120 °C for 3 h with various seed layers of Zinc salt: (a) acetate (b) nitrate and (C) chloride.*

Figure III.35 (a) illustrated ZnO nanorods growing on seed layers of ZnO films based on zinc acetate. As can be seen the spectrum contains several diffracted peaks; some of which are assigned to Zinc oxide planes while the others are relative to those of the Zinc hydroxide Zn (OH) $_2$. The ZnO diffraction planes are (100), (002) and (101) located at 31.4°, 34.4° and 36.5°, respectively, with (101) which is the most favorable plane, this indicates that the structure is Hexagonal würtzite. In addition, the other planes (110), (100), (211), (020), (002), (121), (400), (212), (302), (123) and (223) are corresponding to Zinc hydroxide Zn (OH) $_2$ phases with (100) is the most intense plane. It is probably that the presence of Zinc Hydroxide (OH) in nanorods plays an important role in the photodegradation of Methylene blue as a result of its reaction with free radicals created by light.

For ZnO Nanorods deposited through Zinc nitrate seeds, we note that the XRD spectrum (Figure III 35.b) is characterized by the planes (002), (102) and (110) corresponding to the peaks 38.43 °, 51.37 ° and 58.96 ° respectively (JCPDS No 00-024-1444). The shape of the diffractograms reveals a material composed of an amorphous matrix in which its crystallites are formed along c axis and (002) which is the most intense plane, while the other two planes have low intensities. The nature of the nanorods obtained is a zinc hydroxide and the structure is Hexagonal würtzite.

Figure III.35 (c) shows that the XRD spectrum of ZnO nanorods prepared from zinc chloride have a textured crystalline character with a preferential orientation of crystal growth along the plane (002) which having a hexagonal würtzite structure. The XRD analysis indicates that the crystallographic structure of ZnO nanorods contains planes (002), (101), (102), (103) and (004) coinciding to angles 34.67 °, 36.56 °, 47.79 °, 63.05 ° and 78.72 ° respectively and no intermediate $Zn(OH)_2$ peaks were detected which means the high purity and good crystallinity of ZnO nanostructure obtained. These results are confirmed by the work of Boqian Yang et al. [41].

III.2.1.4 Analysis by Raman spectroscopy

The Raman spectroscopy used to analyze our ZnO Nanostructures samples, it is BRUKER RAMAN SENTEERA R 200 L (Germany) spectroscopy with an Argon laser power of 25 mW with an excitation line at 532 nm at room temperature.

The ZnO belongs to the space group $P_3^6\,mc\ (C_{6v}^4)$ with two formula units in the primitive cell. All the atoms occupy the C_{3v} sites. The group theoretical calculation based on the

correlation method suggested by Fateley et al., [42] predicts nine optical modes which are distributed as follows:

$$\Gamma_{ZnO}^{optrical} = A_1\,(IR+R) + 2\,B_1 + E_1\,(IR+R) + 2\,E_2\,(R)$$

Where A_1 and E_1 modes are active in both Raman and IR spectra whereas E_2 modes are active only in Raman spectrum and B2 mode is inactive in both Raman and IR spectra.
So the main modes are: 1A1 (TO) + 1A1 (LO) + 1E1 (TO) + 1E1 (LO) + 2E2 and the two modes B1 are not active [43]. When A1 (Vibrational mode of the transverse and longitudinal optical phonon), E1 (Vibrational mode of the transverse and longitudinal optical phonon), E2 (low and high mode) and two B1 modes. Based on earlier Raman investigations the different Raman modes of the ZnO films can be expected as follows: A $_1$-TO modes ~ 382 cm^{-1}, E $_1$-TO modes ~ 407 cm^{-1}, A_1 - LO modes ~ 576 cm^{-1}, E_1-LO modes ~ 587 cm^{-1}, E_2 - low modes ~ 102 $cm^{-1}$and E_2- high modes ~ 438 cm^{-1} [44].

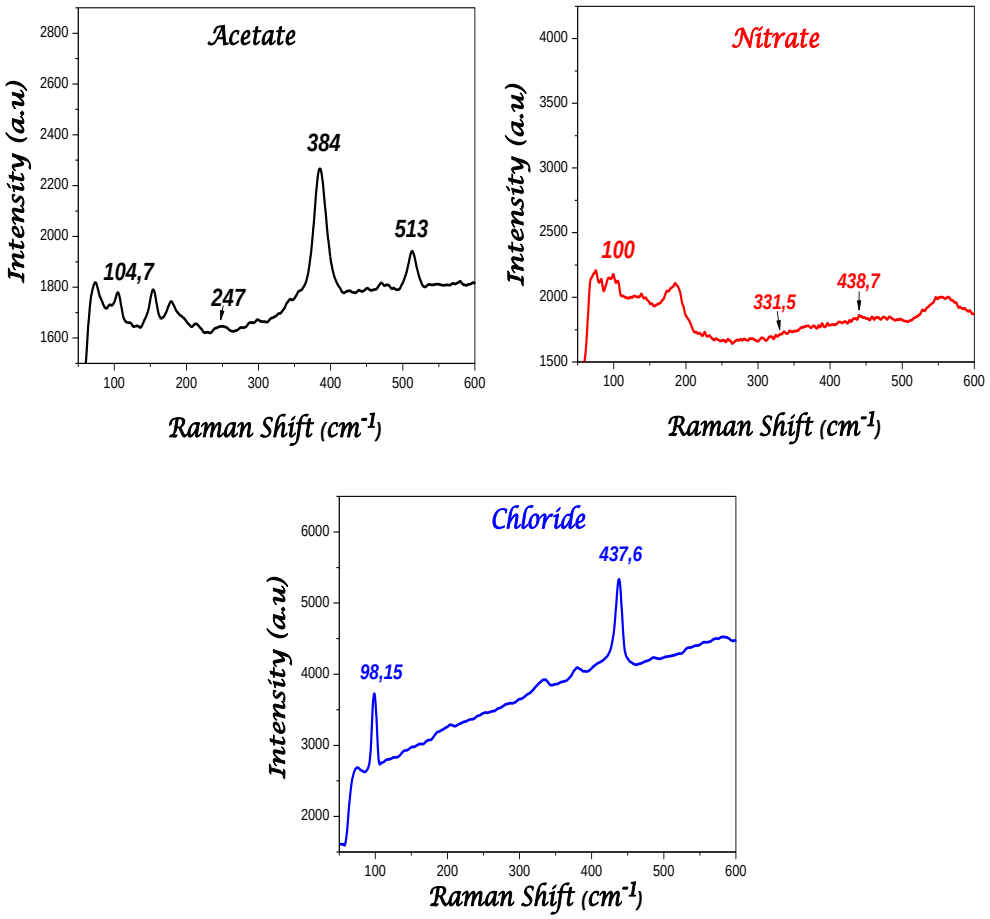

Figure III.36: *Raman spectra of ZnO nanorods prepared with various precursors*

In Figure III.36 we have presented the Raman analysis spectra of the as prepared ZnO Nanorods with various precursors (zinc acetate, nitrate and chloride). The Raman spectra of ZnO Nanorods based on zinc acetate are composed with four main photon modes E2 (low), A1, 2E2 (M) and E1 (LO) modes, respectively located at 104,7, 247, 384 and 513 cm $^{-1}$, as well as other weaker bands. These peaks are largely reported in the literature [44].

For ZnO Nanorods obtained by zinc nitrate, we observed the presence of the following bands: 100, 331, 5 and 438, 7 cm^{-1} which are corresponding to the vibration modes E2 (low), 2E2 (M) and E2 (high) respectively. The appearance of vibration mode E2 (high) at 438, 7 cm $^{-1}$ shows that the structure of this sample is a Hexagonal würtzite structure [42]. This result is in good agreement with those of the XRD which indicate that the plane (002) constitutes the preferential orientation, along the axis c of the crystallites.

Moreover, the Raman spectrum of samples deposited from Zinc chloride contains two vibration modes E2 (low) and E2 (high) which are located at 98.15 and 437, 6 cm $^{-1}$, respectively. The same result was found by Boqian Yang et al. [41].

As can be seen on this spectrum, the appearance of the vibration modes specific is only related to pure ZnO. The band located at 437, 6 cm $^{-1}$ is due to the E2 (high frequency) mode characteristic of the ZnO hexagonal würtzite phase, which is confirmed by the X-ray diffraction analysis of this sample. According to R.Vinodkumar et al. [45] the low frequency E2 mode is associated with the vibration of the heavy Zn sub- lattice, while the high frequency E2 mode involves only the oxygen atoms [44].

III.2.1.5 The morphology of ZnO nanorods

III.2.1.5.1 Analysis by Scanning Electron Microscope (SEM)

The Scanning Electron Microscopy (SEM) was carried out to study the evolution of the surface morphology of our ZnO Nanostructures deposited through hydrothermal process at 120°C during 3 h. Figure III.37 shows SEM images ZnO Nanorods which prepared hydrothermally at 120 °C over 3 h with zinc chloride as seed layer and solution growth of zinc acetate. It's very clear that the morphology acquired is really nanometric, made up of Nanorods which have a high density on the whole of surface substrate. Furthermore the direction of the NRs is oriented perpendicular to the substrate surface.

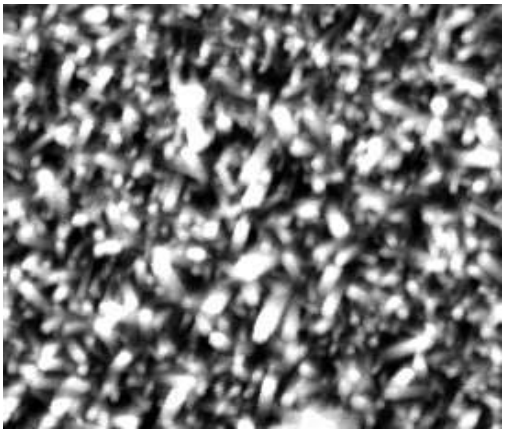

Figure III.37: *Typical Micrographs of ZnO Nanorods by hydrothermal at 120°C for 3 h.*

In Figures III.38 we notified the SEM images of ZnO Nanorods produced by three different photocatalysts: zinc acetate, nitrate and chloride.

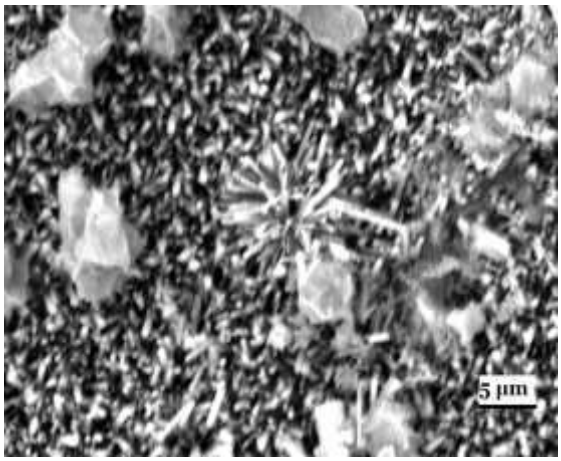

Acetate

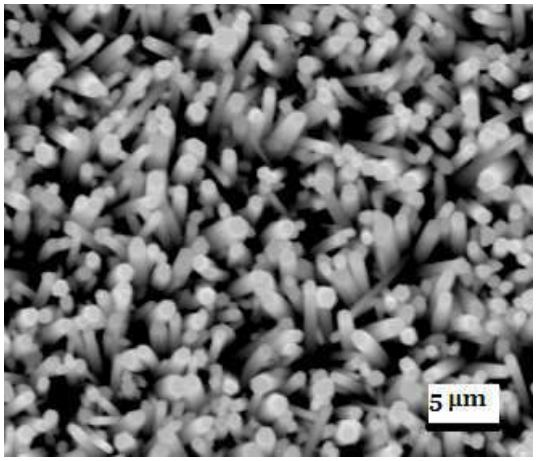

Nitrate

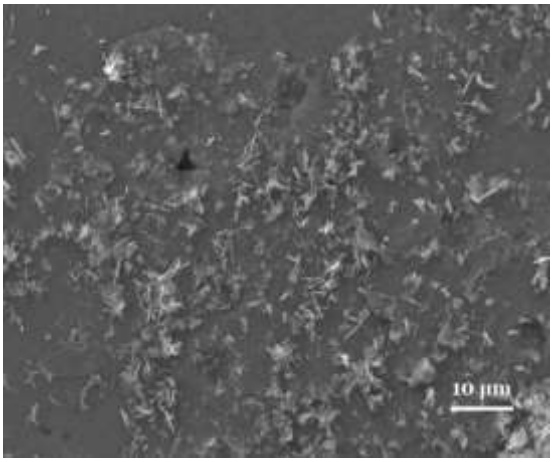

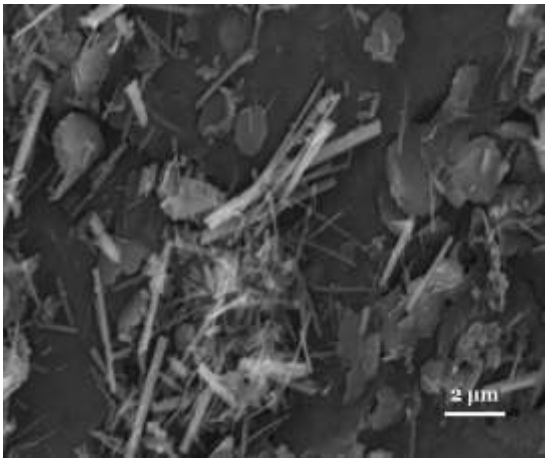

Chloride

Figure III.38: *SEM images of ZnO Nanostructured via different photocatalysts.*

The images clearly show that each precursor generates a different surface and morphology of ZnO Nanostructures. It is observed that the surfaces have a porous aspect and the network is discontinuous for both precursor's zinc acetate and nitrate. The preparation of ZnO Nanorods by zinc chloride give us a surface which contains nanorods of random orientations and of variable dimensions going up to a length of 2 µm and a variable nanometric diameter.
According to this study, we emphasize that the morphology of ZnO Nanorods strongly depends on the nature of the used precursor.

III.2.1.5.2 Analysis by Atomic Force Microscope (AFM)

Surface roughness is a fundamental feature in most solids which plays a very important role in the physics of nanoparticles, particularly in the optical field. It was found that the elaboration parameters influence the surface state of the samples. In our work, the surface morphology of ZnO nanorods is investigated by Atomic Force Microscopy (AFM).
The observation of the surface morphology and the measurement of its roughness contribute to the structural study carried out on the ZnO samples. The determination of the roughness enables us to judge the quality of the layers deposited from various precursors.
The AFM images (3-D) of Zinc oxide nanorods prepared separately from three different precursors (acetate, chloride and zinc nitrate) are shown in Figure III.39. As shown our ZnO films have a large roughness. For ZnO NRs with acetate precursor is characterized by a large amount of sharp tops on the whole of substrate surface. When ZnO NRs obtained by zinc nitrate have hills with uniform distribution. However ZnO NRs prepared via zinc chloride, hills and valley were observed with non-homogeneous distribution.

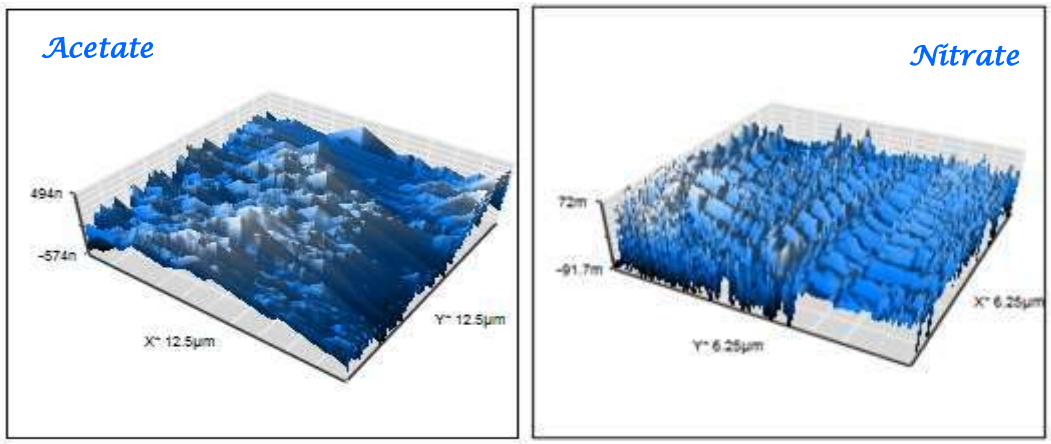

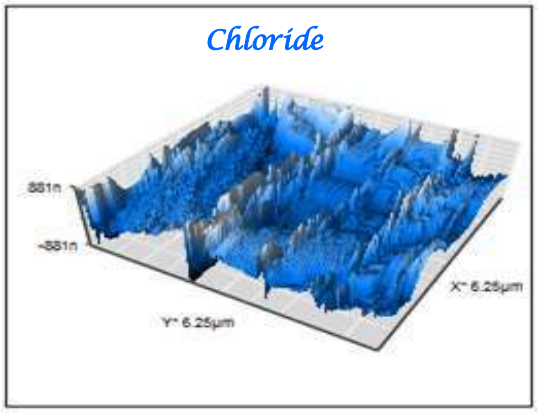

Figure III.39: *3-D AFM images of ZnO Nanorods; Acetate, Nitrate and Chloride.*

Atomic force microscopy (AFM) is proved to be a useful tool for surface roughness determination. There are several roughness parameters that are used to fully characterize the surface. The most common ones is the arithmetic roughness (R_a). The estimated values of this parameter R_a for all samples are presented in the form of a histogram in Figure III.40. From this Figure III.40, we seen that the roughness values R_a of the ZnO NRs made from zinc acetate is rougher than those of the ZnO NRs via nitrate and chloride precursors. It is nearly twice as large as that of chloride.

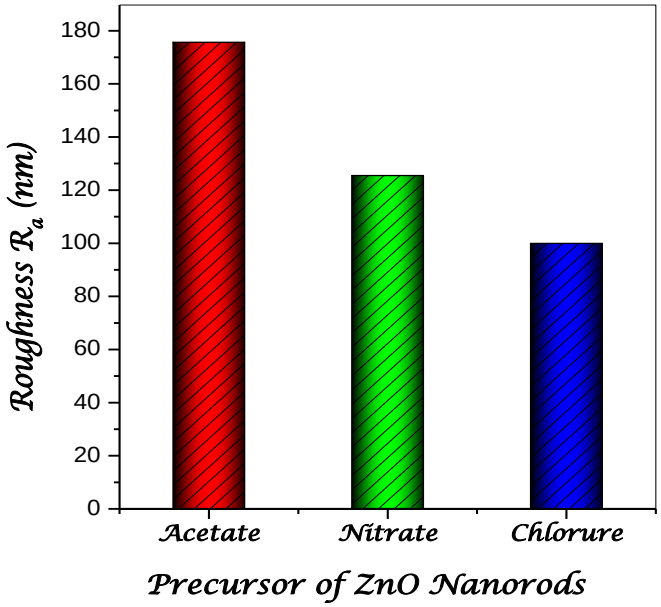

Figure III.40*: Roughness R_a concerning the surface of ZnO Nanorods produced by several precursors*

It is noted that these surface morphologies play an important role in improving the trapping of light, increasing the area of contact with the pollutant, particularly in the field of treatment water and specifically in our study of Photocatalytic application.

III.2. 1.6 Optical properties of samples

The optical properties of ZnO thin films deposited by Spray Pyrolysis at 350 ° C for 10 min with a flow rate of 6 ml / min for different precursors: zinc acetate, nitrate and chloride. The optical transmittance of ZnO thin films is analyzed in the visible range by UV-visible spectrophotometer SHIMADZU.

III.2.1.6.1 Transmittance of ZnO thin films

Figure III.41 shows the transmittance spectra of ZnO thin films prepared with three precursors in the wavelength range between 200-800 nm. For all samples, the optical transmittance is very high, which indicates the good quality of these films. It is obvious that the spectra are composed of two regions:

- A region characterized by a strong absorption located in the UV range (λ <400 nm). This absorption is due to the electronic inter-band transition.
- A region of high transmittance. It is around 85 to 90% for all films over a wide wavelength range from 400 to 800 nm. This high transparency is one of the optical properties which explain the interest in ZnO thin films.

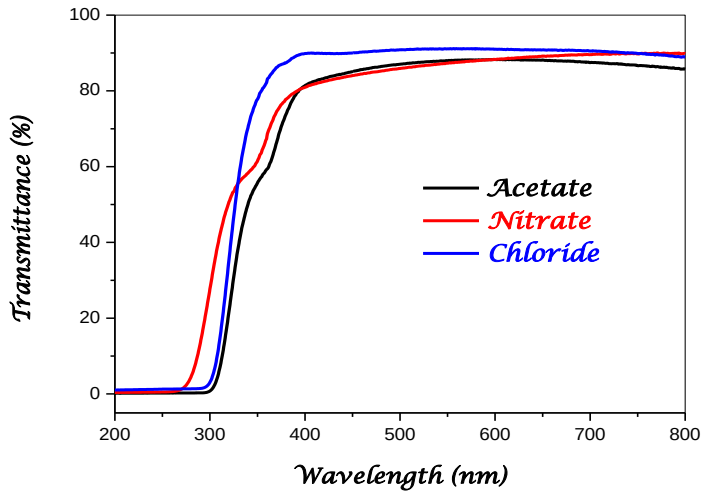

Figure III.41: *Transmittance spectrum of ZnO thin films deposited by different precursors at 350°C.*

The thickness values and the refractive index of our films prepared by three various precursors are deduced from the transmittance spectra of ZnO thin films using the equation of software (Hebal Optics). The results are regrouped in Table III.9.

***Table III.9**: Values of thickness and refractive index of ZnO thin films.*

ZnO Films	Acetate	Chloride	Nitrate
Thickness (nm)	130	196	240
Refractive Index	1.72	1.71	1.70

The value of the refractive index is almost constant for the three films (1.72-1.70) but the thicknesses are different. We observed that the thicknesses of these films are between 130-240 nm, which indicates that the thickness of seed layers has a considerable effect on the growth and the morphology of ZnO nanorods as we seen from SEM images.

L.W. Ji et al, [46] have been studied the effect of thickness (20-1000 nm) of seed layers on the growth of ZnO nanorods. They found that the vertical well-aligned ZnO NWs were grown on 500 and 1000 nm seed layers. However the NWs with 20- and 240-nm thin seed layers show somewhat poor vertical alignment. Also they reported that the thicker seed layers (500 and 1000 nm) with strong (0 0 2) XRD intensities were oriented preferentially in the c-axis direction, which may affect the growth direction of ZnO NWs. Hence the NWs can be grown well-aligned on such a seed layer oriented along the c-axis direction.

The growth mechanism of ZnO NRs with the effect of the thickness of seed layers is shown in Figure III.42. We know that the property of seed layer can affect the growth of ZnO NWs [47]. Thinner seed layers with poor crystal characteristics make Nanowires to be poor-aligned. However, vertical well-aligned Nanowires were grown on thicker seed layers with good crystalline structure.

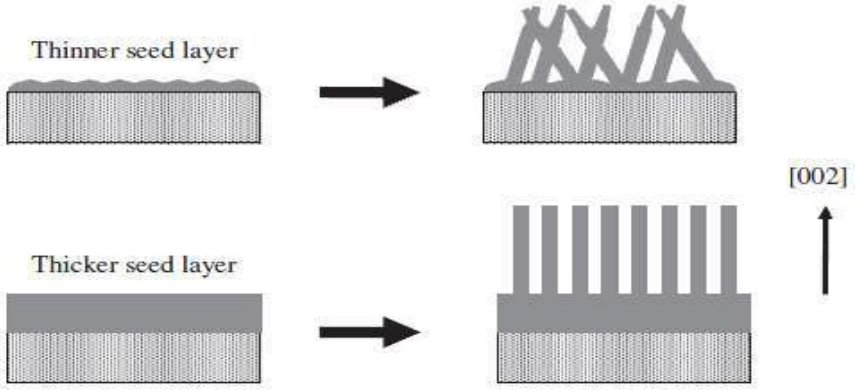

Figure III.42: *Schematic diagram illustrating the growth of Nanowires with different thicknesses of seed layers [46].*

III.2.1.6.2 Transmittance of ZnO Nanorods

The optical transmittance spectra of ZnO Nanorods, through several zinc salt source by hydrothermal method at 120°C for 3 h, in the wavelength varied from 200-800 nm is presented in Figure III.43. As seen the transmission of ZnO Nanorods obtained is ranged between 8-14 %. The insert in Figure III.43 shows the enlargement of the transmission spectrum of these ZnO nanostructures in the wavelength range from 200 to 375 nm. The results showed that all the ZnO Nanorods which were prepared from various precursors exhibited strong excitonic absorption peaks at 280 nm. These peaks indicate that the ZnO Nanorods obtained have good optical quality and a high exciton binding energy.

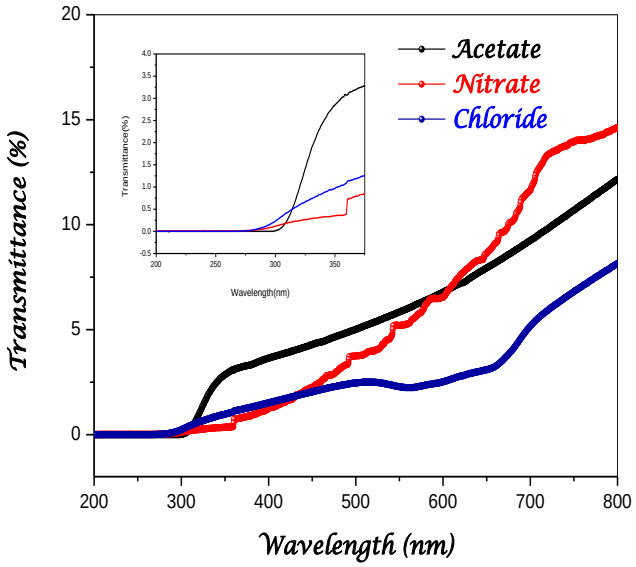

Figure III.43: *Optical transmittance spectra of ZnO Nanorods by hydrothermal method.*

The transmittance of nanorods in the studied range is very low compared to its value for seed layers of ZnO. These results are in good agreement with those reported by K. L. Foo et al. [48]. They found that the transmittance of ZnO nanorods varying between 7 and 17%, which coincides well with our measurements. This reduction in transmittance can be due to two phenomena, one is related to the geometric nature of the nanowires and their orientation which causes a large multiple reflections of light and the other can come from the high porosity (space between nanorods) in the material.

III.2.1.7 Photocatalytic activity

Photocatalytic activities of the ZnO products were evaluated by decomposition of Methylene Blue (MB) and an aqueous solution with an initial concentration of C = 10^{-5} mol / l. The ZnO samples were placed in a quartz beaker with 75 ml of MB. Then the solution was magnetically stirred in dark before irradiating with a 20 W mercury lamp (TUNGSRAM, λ = 430 nm), which was 13 cm above the surface of the quartz beaker containing ZnO nanostructures and MB. During the process of photodegradation, 5 ml of the solution was sampled every 60 min for UV–vis characterization to determine the absorbance of MB.

In Figure III.44 we have displayed the UV-visible absorbance spectra of the MB solution as a function of irradiation time for various photocatalyst of ZnO with three precursors (acetate, nitrate and chloride). The wavelength region is between 500-750 nm.

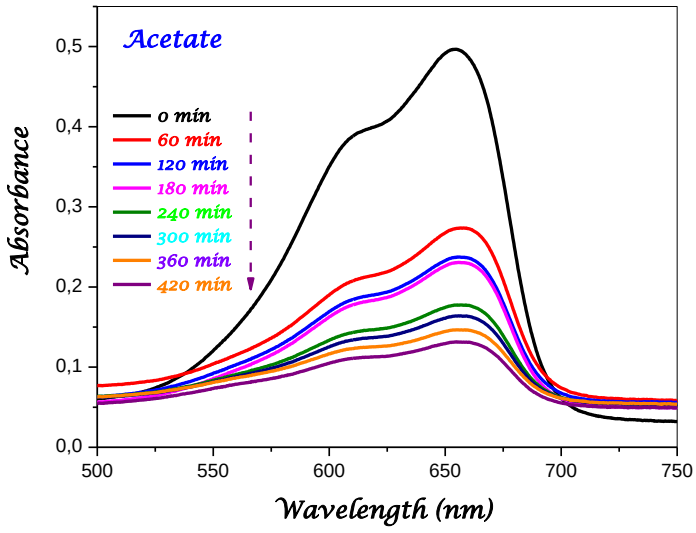

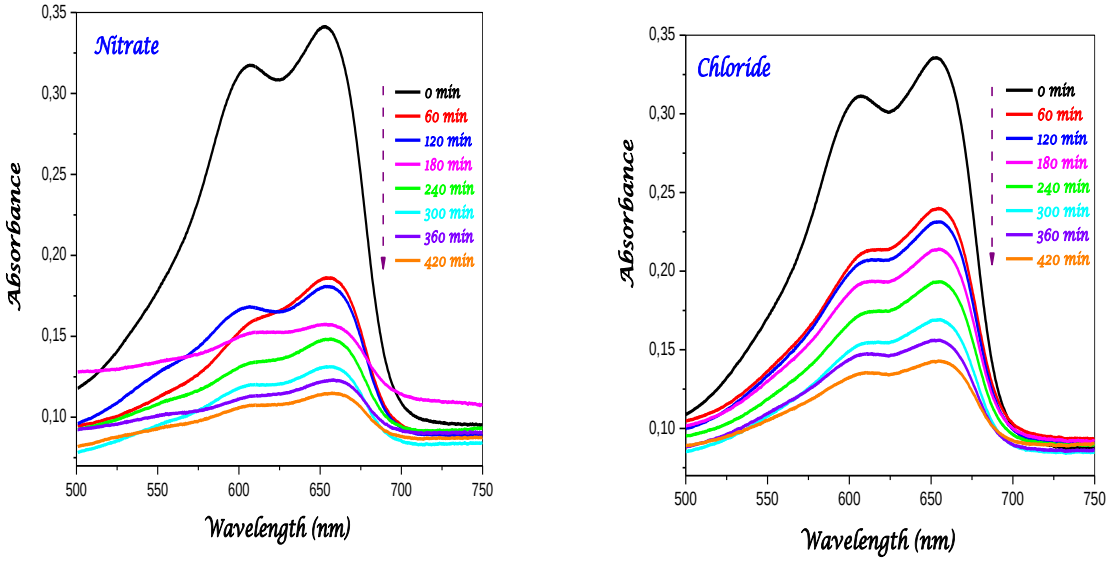

Figure III.44: *Variation of absorbance as a function of the wavelength of the MB solution with different exposure times.*

It's very clear that the absorbance value decreased swiftly for all ZnO nanostructures at the characteristic peak location (654 nm) of MB, and was very close to zero after 420 min irradiation for ZnO nanorods obtained by Zinc acetate films, consistent with the result of visual inspection in Figure III.44, suggesting that the ZnO nanorods behaved as effective catalysts for photodegrading MB.

Upon UV irradiation, the color of the MB solution with addition of ZnO nanorods was rapidly degraded with time, and the corresponding digital photographs were recorded and shown in Figure III.45. The photographs of MB solutions upon photodegradation catalyzed by ZnO nanorods (zinc acetate) showing the decolorization of the organic dye with time. It can be seen that the MB solution was relatively colorless after irradiation for 420 min, indicating the MB molecules had been approximately photo-decomposed by ZnO nanorods. The results were further confirmed by the temporal UV–vis adsorption spectra in Figure III.44.

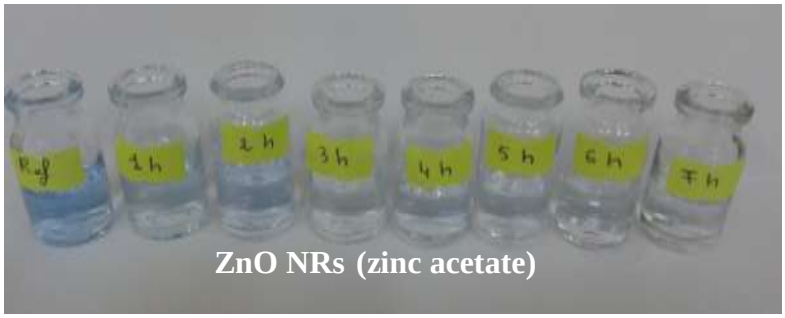

Figure III.45: *Photographs of MB solutions upon photodegradation catalyzed by ZnO nanorods showing decolorization of the dye with time.*

In order to investigate the kinetic of photodegradation and the influence of various photocatalyst of ZnO, we followed the variation of the absorption intensity located at 654 nm. Figure III.46 illustrated the variation of the ratio C / C_0 as function as the irradiation time for ZnO nanostructured deposited at 120°C during 3 h as deposition time by hydrothermal process. We observe in this Figure III.46 that ZnO NRs by zinc acetate films represents a quickly photodegradation compared to the other samples. The last sampling point, after 420 min of kinetics, showed us that the Zinc acetate Nanorods give the best degradation of the pollutant.

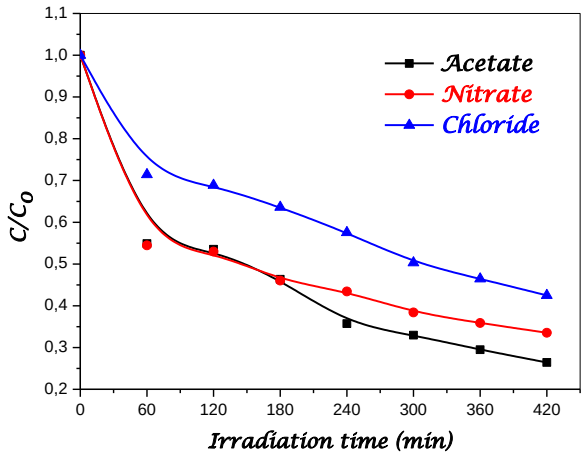

Figure III.46: *The photodegradation kinetics of MB with C = 10^{-5} mol / l by ZnO nanostructures.*

To quantitatively understand the reaction kinetics of MB degradation over different ZnO samples in our experiments, we re-plotted the data in Figure III.47 according to the

pseudo first-order kinetic model as expressed by equation (III. 2), which is generally used for photocatalytic degradation process took place at the interface between the catalysts and the organic pollutants with low concentration [49].

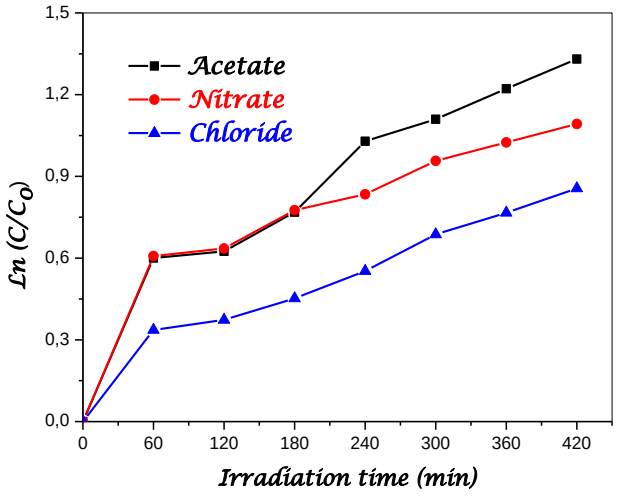

Figure III.47: *Representation of Ln (C_0 / C) as a function of photocatalytic degradation time for different ZnO NRs.*

As can be seen, the photodecomposition reaction of MB molecules on the ZnO nanostructures based on zinc chloride followed the pseudo first-order kinetics (R^2 = 0.94) with k = 18.2 x10^{-4} min^{-1}, whereas those on the ZnO nanorods, prepared by zinc acetate and nitrate films, deviated from the pseudo first-order model. Probably this abnormal photocatalytic behavior of the prepared ZnO nanorods was primarily caused by their morphologies and microstructures [50].

The estimation of the photocatalytic degradation constant k of Methylene Blue by ZnO nanorods almost follows a first-order model whose values are included in the range: 18.2-28.1x10^{-4} min^{-1}. These values are comparable with k values obtained by J. Mu et al. [51] and F. Kayaci et al. [52] who found k varied from 14x10^{-3} and 7x10^{-2} min^{-1}.

According to the equation (III.2), the concentration of MB is linearly proportional to the intensity of the absorption peak at 654 nm, and thus the decomposition efficiency of MB dye can be calculated through the equation (III.3).

Figure III.48 depicts the decomposition efficiency of MB over ZnO nanorods obtained with several films of zinc acetate, nitrate and chloride for comparison. Obviously, the ZnO nanorods with acetate exhibited the best photocatalytic activity, which was significantly

higher than that of ZnO NRs with nitrate precursor and comparable to that of zinc chloride salt source. The photocatalytic performance of ZnO nanorods (74%) was still much superior to that of the others photocatalysts (64 and 58%). This difference might be attributed to their larger specific surface area and one-dimensional characteristic of the nanorods acquired through several precursors of zinc oxide.

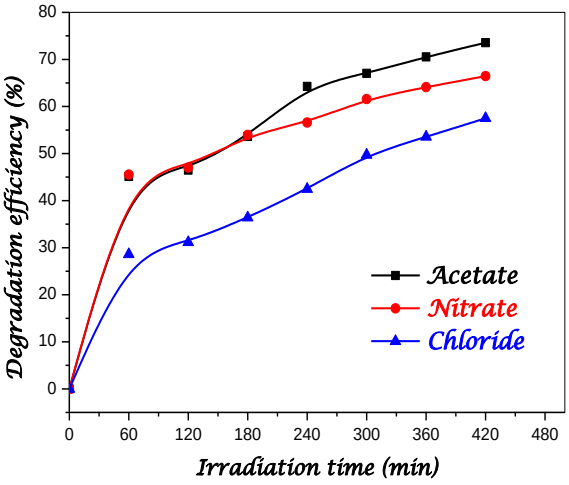

Figure III.48: *Degradation efficiency of MB by ZnO nanostructures with different photocatalyst*

Table III.10 represents the values of the degradation efficiency and the reaction constant of the solution degraded by the different ZnO nanorods. We observe that the BM is degradable for 420 min at more than 74% for ZnO nanorods based on zinc acetate, at 67% for Nitrate NRs and at 58% for Zinc Chloride NRs. The conversion rate varies significantly depending on the zinc precursor, the morphology and the composition of nanostructured ZnO.

Table III.10: *Degradation efficiency and reaction constant of the final BM solution photodegraded by different ZnO NRs*

ZnO NRs	Acetate	Nitrate	Chloride
Constant $k*10^{-4}$ (min^{-1})	28.1	21.3	18.2
Degradation efficiency τ (%)	74	67	58

III.2.2 Influence of deposition time of ZnO Nanomaterials

In this section, we are investigated the effect of time deposition of ZnO nanostructured obtained by hydrothermal process with several growth times on the photocatalysis activity of Methylene Blue.

III.2.2.1 Preparation of ZnO Seeded

Before ZnO nanostructured synthesis by hydrothermal, ZnO seed layers with 100 nm thickness were deposited onto soda lime glass substrates using radio frequency (RF) magnetron sputter-deposition technique. A glass substrate was placed on the top of an anode, which was placed 50 mm from the ZnO target of 3 in. diameter. During 60 min of the growth, the working pressure of the chamber was 10 m Torr while the RF power was 40 W and the Ar gas flow was maintained at 5, 5 sccm. No substrate heating and bias were applied during the deposition.

III.2.2.2 Growth of ZnO Nanostructures

For preparing ZnO nanostructures with diverse growth times by hydrothermal method we use zinc nitrate hexahydrate [Zn $(NO_3)_2$. $6H_2O$, 98%] as precursor and sodium hydroxide [NaOH] which were purchased from Aldrich and used as received. The growth solution was prepared by dissolving a calculated amount of zinc nitrate hexahydrate and sodium hydroxide in deionizer (DI) water (pH = 6.8). Successively, the addition of the hydroxide sodium is to adjust the pH of the growth solution. Then the glass substrates with ZnO seed layers were immersed in the growth solution in Teflon Lined Stainless Steel Autoclave and put them in oven at 120°C for 3 h, 5 h and 8 h. Finally, the ZnO nanostructures obtained were removed from the solution after cooling, rinsed with distilled water and dried in air at 60°C.

III.2.2.3 XRD analysis

Figure III. 49 shows XRD spectra of ZnO NRs prepared by hydrothermal at 120°C with different deposition time deposited with 5 H and 8 H. As can be seen, the both samples are polycrystalline in nature. As shown, the ZnO NRs obtained are primally well aligned and perpendicular to the substrate. Moreover, ZnO nanorods can be grown with a strong

orientation along (101) and exhibit a wurtzite crystal structure in an XRD spectrum and possessed a high crystal quality. İn addition the strong relative intensity of the (002) lines reveals a texture effect of the arrays consistent with c-axis oriented nanorods.

Moreover the ZnO NRs with 8 H have more intensities than the previous one. It could be seen that the diffraction peaks were more intensive and narrower implying a good crystalline nature of the as-synthesized ZnO NRs, and all of the peaks can be well indexed to hexagonal phase ZnO reported in JCPDS card (NO.36-1451, a = 0.3249 nm, c = 0.5206 nm). Diffraction peaks related to the impurities were not observed in the XRD pattern, confirming the high purity of the synthesized NRs. These results are in a good agreement with those found in the literature [53].

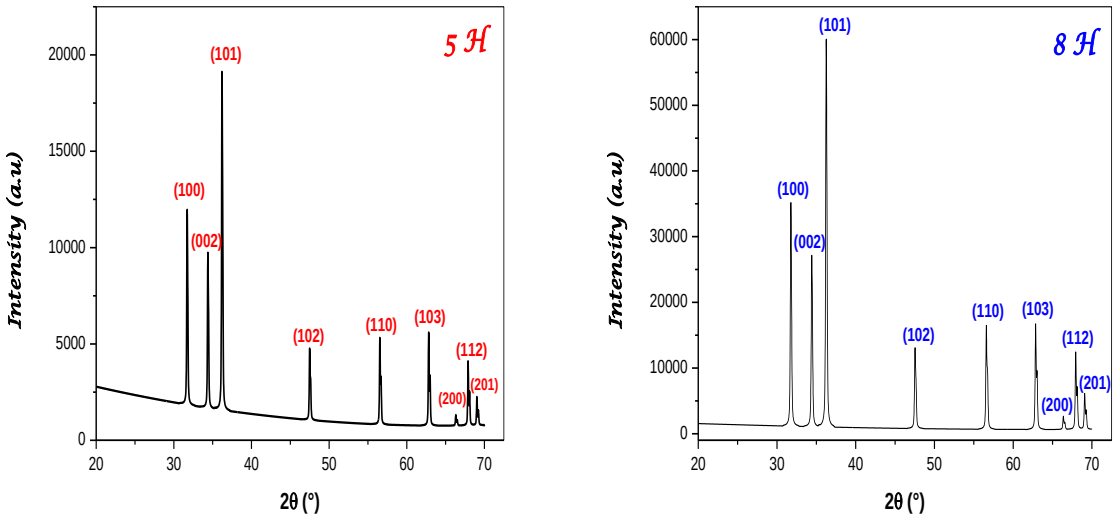

Figure III.49: *XRD patterns for ZnO Nanostructures with two deposition time; 5 h and 8h*

III.2.2.4 Photodegradation of MB

The samples prepared were used to research for treatment of water sush as the photocatalysis activity. The photocatalysis performance was investigated by the decolorization of Methylene Blue as a polluant with a concentration of 10^{-5} mol/l and the UV lamp with a wavelength of 254 nm.

We have studied the variation of absorbance spectra of polluted solution after UV light exposure times. The wavelength region is ranged from 500 to 700 nm. From the variation of this absorption peak with exposure time, we concluded that the photo degradation is more significant when solution is in contact with ZnO Nanorods which deposited for film tested with 3 H as time deposition.

For understood the kinetics of photodegradation of MB and the influence of deposition times of Zinc Oxide Nanorods, we have checked the intensity of the absorption located at 654 nm. Figure III.50 exhibit the variation of the ratio C/C_0 of several photocatalyst of ZnO. As shown, the photo degradation is more efficiency after 60 min when using 5 hours as a deposition time for ZnO Nanorods. The ratio is reduced with increasing exposure time; it reaches 0.35 after 240 minutes of irradiation for film with 3 h. However in the case of the other films the ratio is slightly increased up to 1.03 and 1.45 after 240 minutes for films deposited for 5 h and 8 h respectively.

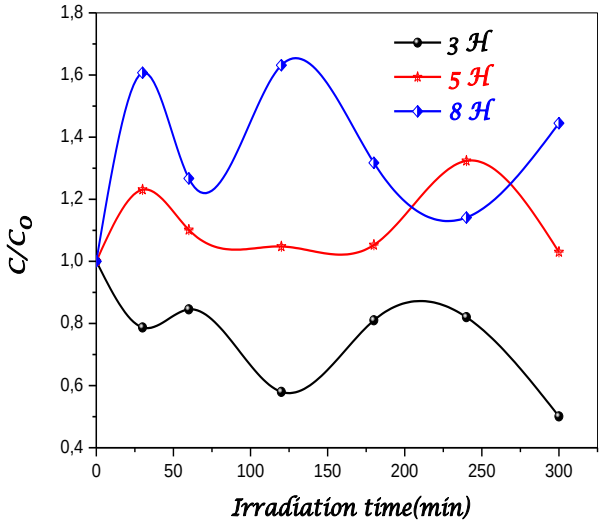

***Figure III.50**: Photo degradation Kinetic of Methylene Blue by ZnO NRs with different deposition time*

According to this survey, the photodegradation of MB is more significant when ZnO NRs deposited after 3 h are on contact with solution compared with the other samples.

III.2.3 Influence of surface position

In this part of our work, we are studied the influence of seed layer surface position (slanted, surface up and surface down) on the morphology of ZnO nanostructured (Nanorods and Nanoflowers) and on the photocatalysis activity of Methylene Blue. The results founding are well presented and discussed in the following way.

III.2.3.1 Synthesis of ZnO seeds

The seed layers were deposited on soda lime glasses substrate by Radio Frequency Sputtering (RFS) Nanovak NVTS 400 vacuum system. The ZnO thin films prepared, as seed layers via RF Sputtering, by means of a target of ZnO. The pressure, Argon gas flow and the power as conditions of deposition were mentioned as 8 mToor, 40 W and 5.5 sccm, respectively. At room temperature (27°C) and during 120 min, the soda lime glasses were coated with 200 nm thickness of ZnO thin films.

III.2.3.2 Growth of ZnO Nanostructures

In order to synthesis ZnO Nanorods and Nanoflowers, an aqueous solution was prepared with a 2.1 M of sodium hydroxide NaOH (99.99 % Sigma Aldrich) and 0.15 M of Zinc nitrate hexahydrate $Zn(NO_3)_2.6H_2O$ (99.99 % Sigma Aldrich) were dissolved in deionized water (pH = 6.8). The growth solution was transformed to three Teflon Lined Sealed Stainless Steel Autoclaves and the seeds deposited by RF sputtering were immersed in this solution with three different positions: slanted, surface up and surface down. The ZnO nanostructures were grown over seeds in oven at 120°C during 3 h as deposition time. After this process, the ZnO Nanorods and Nanoflowers obtained were removed from the solution after cooling, rinsed with deionized water and dried in air at 60°C. The schema of ZnO nanorods and nanoflowers formation is illustrated in Figure III.51.

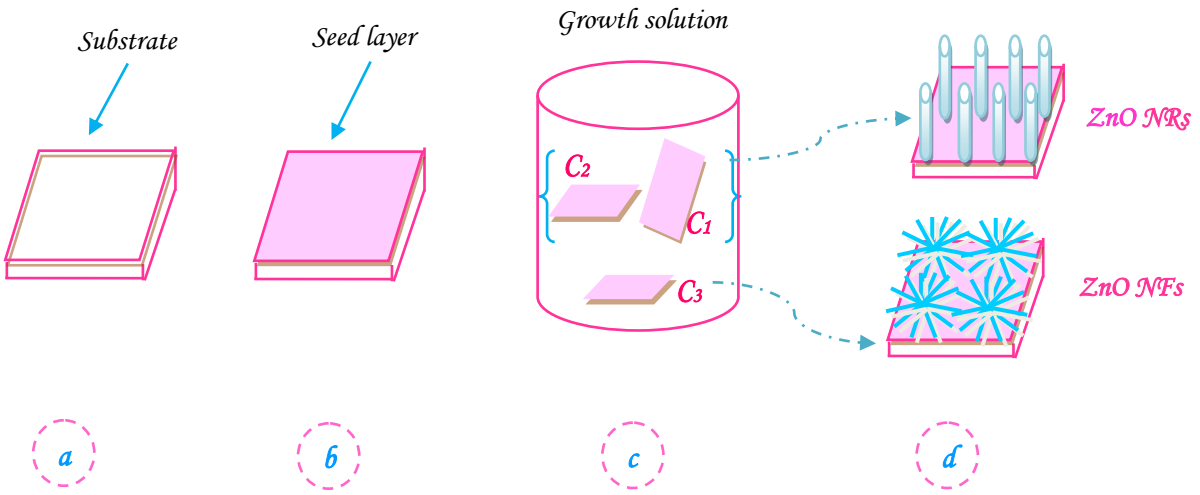

Figure III.51: *Schema of the ZnO nanorods and nanoflowers formation: (a) Soda lime glasses substrate; (b) Seed layer of ZnO by RF Sputtering; (c) Growth solution of NaOH and Zn (NO_3). $6H_2O$ in Teflon Lined Sealed Stainless Steel Autoclaves with: (C_1) Substrate slanted, (C_2) surface down and (C_3) surface up; (d) ZnO nanoflowers and nanorods growth at 120°C during 3 h.*

III.2.3.3 XRD analysis of ZnO NRs and NFs

Figure III.52 shows XRD pattern of ZnO Nanorods (Figure III.52 a, b) and Nanoflowers (Figure III.52 c) synthesis via different seed layer substrate position at 120 °C during 3 h (a- substrate slanted, b- substrate surface up and c- substrate surface down). As can be seen, all diffracted peaks are indexed the hexagonal wurtzite structure of ZnO with space group $P6_3mc$ and the lattice constants; a = 0.3249 nm, c = 0.5206 nm according to JCPDS: 36-1451. No additional peaks of Zn (OH) $_2$ detected in XRD pattern which means the formation of pure ZnO phase with high quality and impurity free. The ZnO Nanorods and Nanoflowers show higher intensity of (002) peak which indicated the preferential growth of rods and flowers is in the c-axis orientation [54].

As observed, in ZnO nanostructures synthesized with various substrate positions, that there is an appearance of peaks such as (004) and (202) for ZnO nanoflowers (Figure III.52 c) and disappearance of peaks (100), (102), (200), (201), (004), (202) for ZnO nanorods (Figure III. 52 a). Moreover, a sharp, strong and dominant peak at 34.59° confirms that the as-grown nanorods are single-crystalline with wurtzite hexagonal phase and grown along the [0 0 0 1] direction. However, the well-aligned ZnO Nanorods indicated that the rods are aligned vertically on substrate.

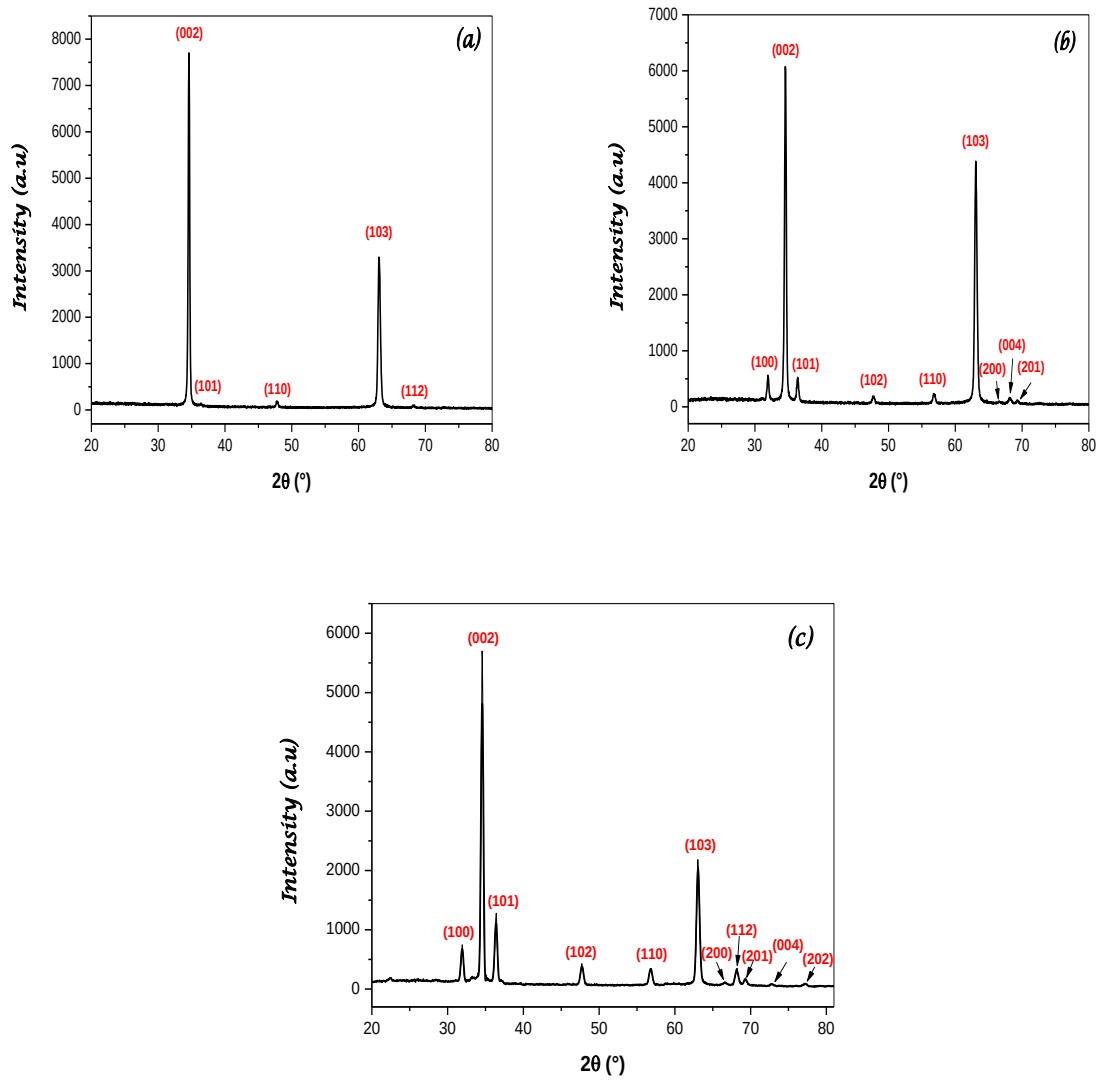

Figure III.52 : *XRD pattern of ZnO nanostructures : (a- surface down) Nanorods (b-surface up) Nanorods and (c- surface slanted) Nanoflowers*

Furthermore, an X-ray diffraction analysis showed that both ZnO nanostructures obtained by [53, 55] have a hexagonal wurtzite phase without any impurity observed. Several researches indicate the hexagonal wurtzite structure of ZnO nanomaterials. Sun et al. [56] deposited ZnO nanorods on Si substrate at 600°C, and the XRD analysis exhibits that well-aligned ZnO nanorods have a hexagonal wurtzite structure with high c-axis aligned. Lepot et al. [57] prepared ZnO nanorods at 80°C for 48 h. Also, they assigned a hexagonal wurtzite type as a crystal structure for the ZnO nanorods obtained, and no intermediate Zn $(OH)_2$ peaks were detected. That means the high purity and good crystallinity of the ZnO nanorods fabricated.

III.2.3.4 SEM images of ZnO NRS and NFs

The surface morphology of ZnO nanostructures synthesized by hydrothermal with different substrate position at 120 °C and a 3 h as a growth time was characterized by SEM and illustrated in Figure III.53. Figure III.53 (a-f) exhibits SEM images of ZnO Nanorods and Nanoflowers at low and high magnification. As offered below in Figure III.53, the surface substrate position has a great effect on the growth of ZnO nanostructures. Figure III.53 (a-b) exposed that the grown products are hexagonal nanorods and are vertically aligned to the substrate. It is very clear seen from these images that the aligned hexagonal-shaped ZnO nanorods are grown onto the whole substrate surface in a high density.

The well-defined and perfect hexagonal faceted morphologies of the as-grown ZnO nanorods indicated that the synthesized products are single-crystalline with the wurtzite hexagonal phase (Figure III.53 b). The nanorods obtained (Figure III.53 b), when the surface down, have a hexagonal shape with different size of diameters which confirmed the XRD results. The measured diameters of the as-synthesized nanorods are ranged between 133.8 nm and 146.9 nm.

Figure III.53 (c-d) indicated ZnO Nanorods which were grown consequently of the slanted position of seed layer substrate in low and high magnification. As display, a high density of ZnO nanorods was formed on the full surface substrate as illustrated in Figure III.53 c.

Figure III.53 (e-f) shows flower-like ZnO nanostructures were distributed on surface glass substrate for the both magnification low and high. From this Figure III.53 (e-f), the growth of ZnO nanoflowers have a large scale fabrication on the total surface of substrate. The process of growth of ZnO nanoflowers is concerning to the precipitation of $Zn(OH)_2$ which produced by the meeting of ions Zn^{2+} and OH^- in the solution. The formation of $Zn(OH)_4^{2-}$ ions was happened by a successively dissolving of $Zn(OH)_2$ in water. When the concentrations of $Zn(OH)_4^{2-}$ ions exceeded the critical value, ZnO nanoflowers were developed, and the relevant chemical reactions can be written as follows [58, 59]:

$$Zn^{2+} + 2\,OH \longrightarrow Zn(OH)_2 \quad (1)$$

$$Zn(OH)_2 + 2\,OH^- \longrightarrow Zn(OH)_4^{2-} \quad (2)$$

$$Zn(OH)_4^{2-} \longrightarrow ZnO + HO + 2OH^- \quad (3)$$

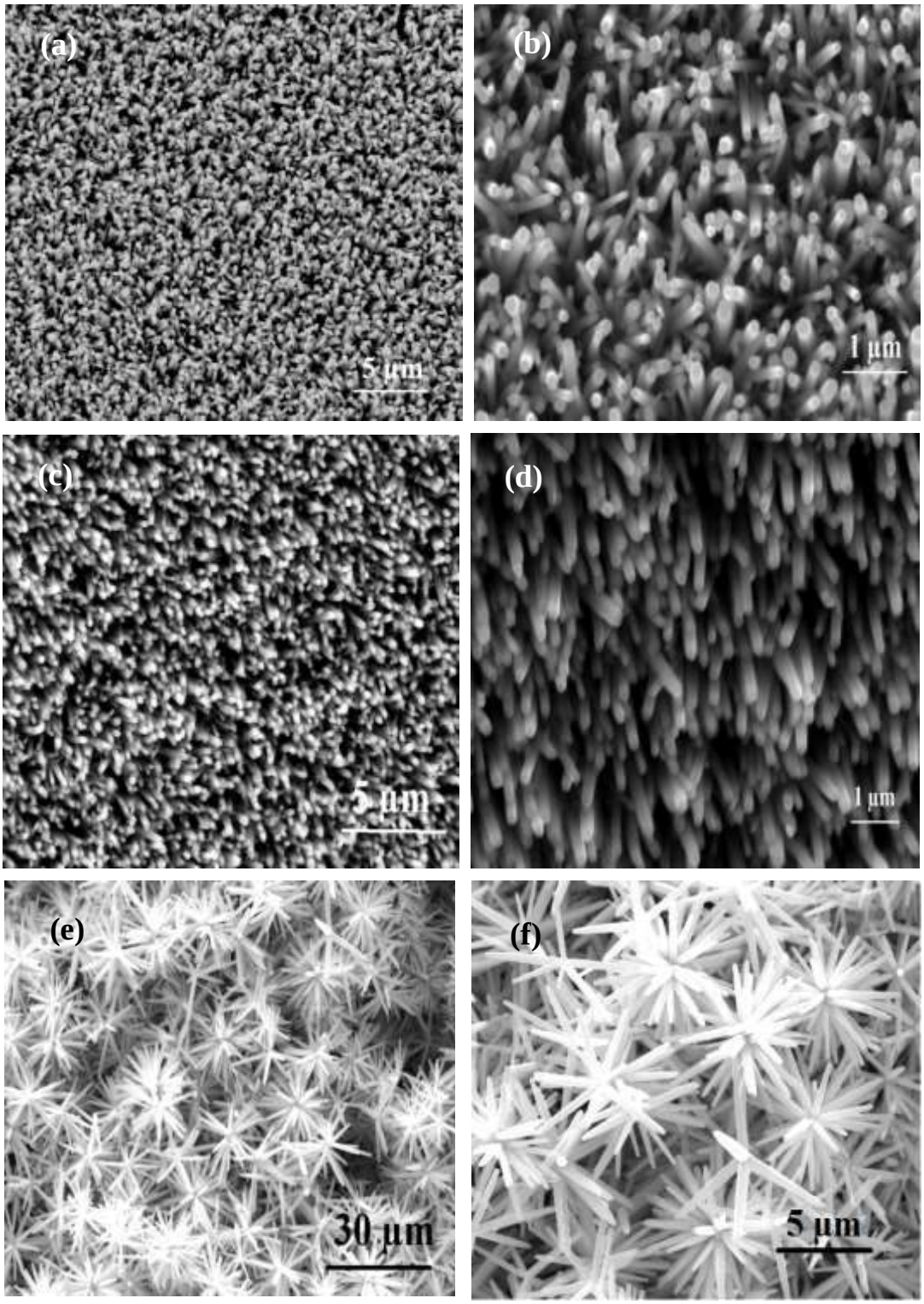

Figure III.53: *SEM images of ZnO Nanorods (a-b ; c-d) and Nanoflowers (e-f) at low and high magnification.*

III.2.3.5 EDS analysis

The EDS spectrostocpy was used to identify the chemical composition of ZnO nanoflowers. Figure III.54 illustrated the typical EDS spectrum of ZnO Nanoflowers which indicate that the synthesized products are composed of zinc and oxygen only. The EDS analysis affirms the formation of a pure ZnO phase which was in well agreement with the XRD results (Figure III. 52 c).

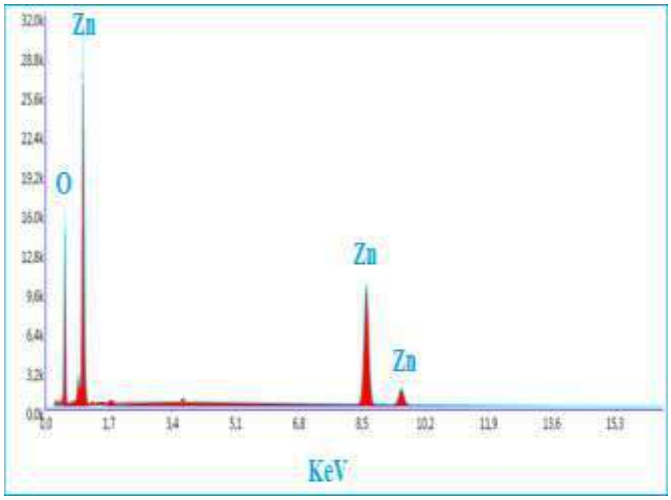

***Figure III.54**: A typical EDS spectrum of ZnO Nanoflowers*

III.2.3.6 Photocatalysis process

To investigate the photocatalytic activity, of Methylene Blue ($C_{16}H_{18}C_lN_3S$) with a concentration of 2 mg/l, ZnO nanostructures were formed at various substrates surface through the hydrothermal method. The ZnO nanorods and nanoflowers prepared were dipped in the solution of MB and irradiated with UV light source of $\lambda = 254$ nm.

To estimate the photocatalysis activities of ZnO nanostructures; ZnO Nanorods/glasses and ZnO Nanoflowers/glasses were immersed into 30 ml Methylene Blue (MB) aqueous solution. Then 3 ml reaction samples were retired periodically for UV-vis analysis. The removal of MB dye was analyzed by following the absorbance variation of the peak at 654 nm after every 60 min during 300 min.

The photocatalysis achievement was investigated by means of ZnO nanostructures for the applicability in photodegradation of organic dyes like Methylene Blue (MB). Figure III.55 (a, b and c) shows the photocatalytic performances of ZnO Nanorods and Nanoflowers. The variance of absorbance spectra of Methylene Blue solution under UV light irradiation with

different ZnO nanostructures was carried out in wavelength region between 500 nm and 700 nm. As mentioned, the absorption peak intensity is indicated as signature of the dye degradation. As can be seen the absorbance intensities decreases gradually with increase of irradiation time from 0 to 300 min. Consequently, the photodegradation is very considerable when the solution of MB is in contact with ZnO nanoflowers then with ZnO nanorods that's indicating the successful reduction of ZnO nanoflowers.

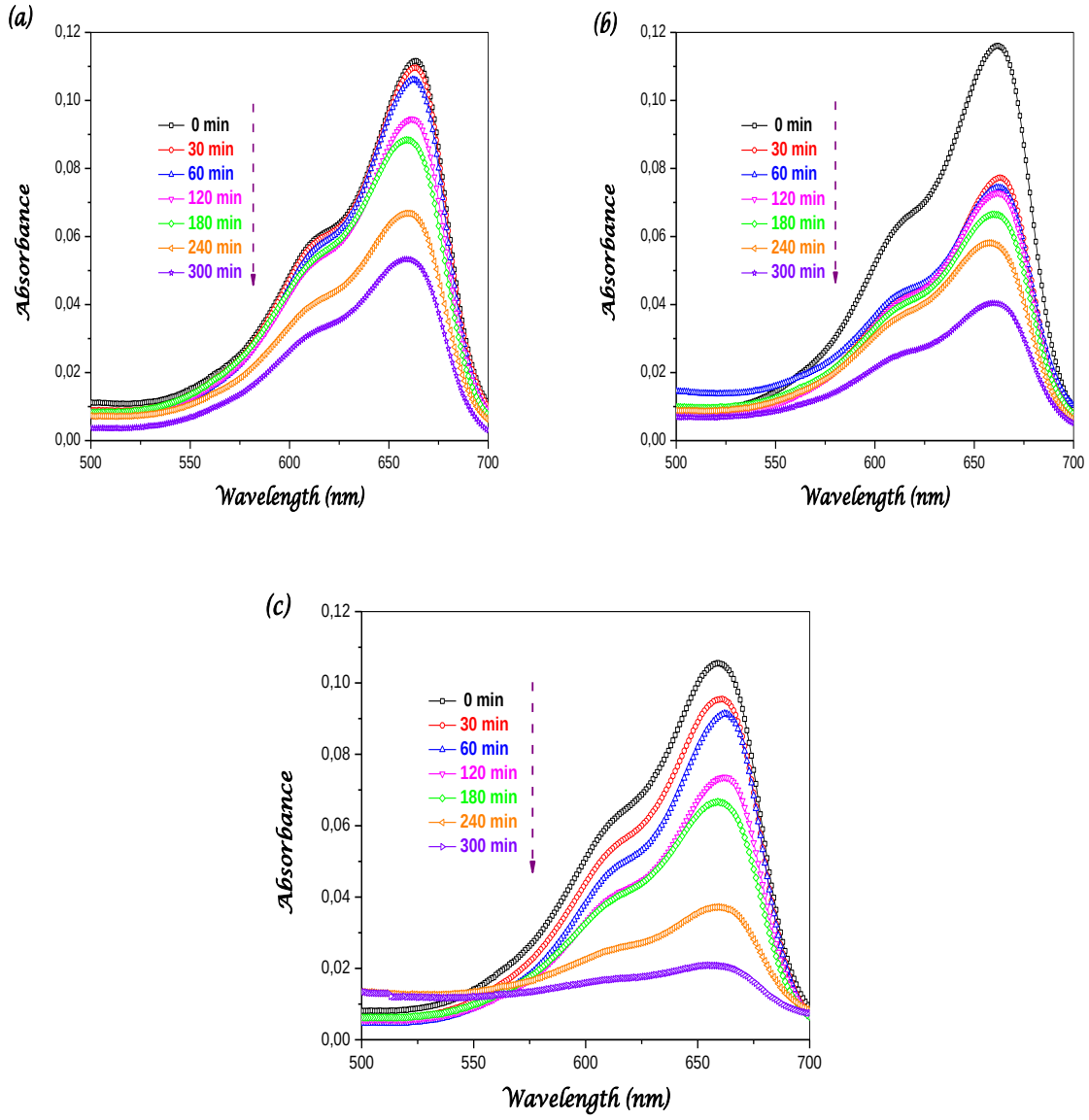

***Figure III.55**: UV-Vis absorption spectra of the degradation of dye MB solution in contact with ZnO: (a and b) Nanorods, (c) Nanoflowers*

For more understanding photodegradation kinetics and the influence of seed layers position of ZnO nanostructures, we have monitored the variation of the intensity of the absorption located

at 654 nm. Figure III.72 exhibits the variation of ratio C/C_0 of the as-growth of ZnO Nanorods and Nanoflowers, where C is the relative concentration at time t and C_0 is the initial relative concentration. As shown in Figure III.56 the photodegradation kinetic of MB dye is reduced rapidly with increasing irradiation times for ZnO Nanoflowers. However, the ratio is reduced slightly for the both nanostructures samples; ZnO NRs 1 and 2. Furthermore, this ratio C/C_0 is reaches 0.19, 0.34 and 0.44 after 300 minutes of irradiation for ZnO NFs, ZnO NRs 1 and 2, respectively. The enhanced photocatalytic activity of flower-like ZnO nanostructures as compared to ZnO nanorods can be attributed mainly to the large surface area, which arises from the three dimensional flower-like ZnO structures consisting of porous nanostructure. The large surface area results in an enhanced adsorption of MB. Earlier studies have shown that the surface morphology of the ZnO nanostructures plays a very important role in the photocatalytic activity [60-64]. Differences mainly originate from differences in surface area, polar planes or oxygen vacancies.

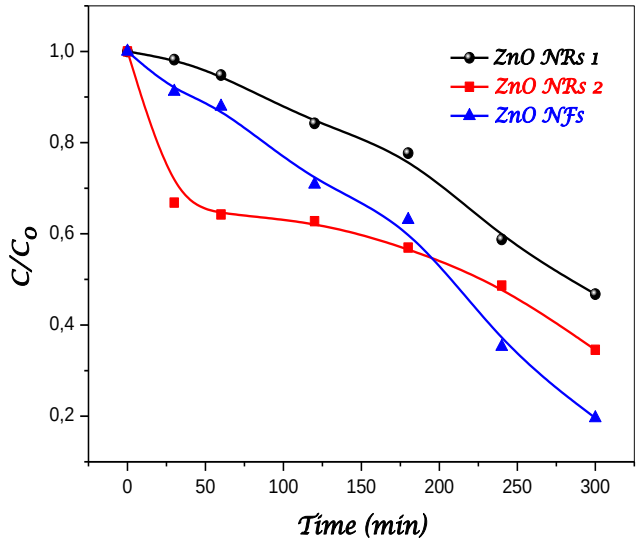

Figure III.56: *Photodegradation kinetic of MB dye by ZnO nanostructures.*

Figure III.57 displays the photodegradation efficiency of Methylene Blue for all photocatalysts. The highest photocatalytic degradation efficiency was achieved 81 % by ZnO Nanoflowers with the larger rate constant K = 50.8 x 10^{-4} min^{-1} for 300 min irradiation time. However, ZnO NRs 1 and ZnO NRs 2 as photocatalysts could degrade only 54 % and 66 % of MB during the same time of irradiation, respectively. The rate constant K for the both nanostructures like rods was found 24.9 x 10^{-4} min^{-1} and 28.6 x 10^{-4} min^{-1} for ZnO NRs 1, 2,

respectively. As a result, ZnO Nanoflowers is very suitable photocatalyst for organic dyes photodegradation (MB). The results obtained indicate that the surface position of seed layers can effectively modify the morphology of ZnO nanostructures, leading to the improvement of their photocatalytic performance. So these ZnO nanoflowers are extremely significant for treatment of water and gas sensing.

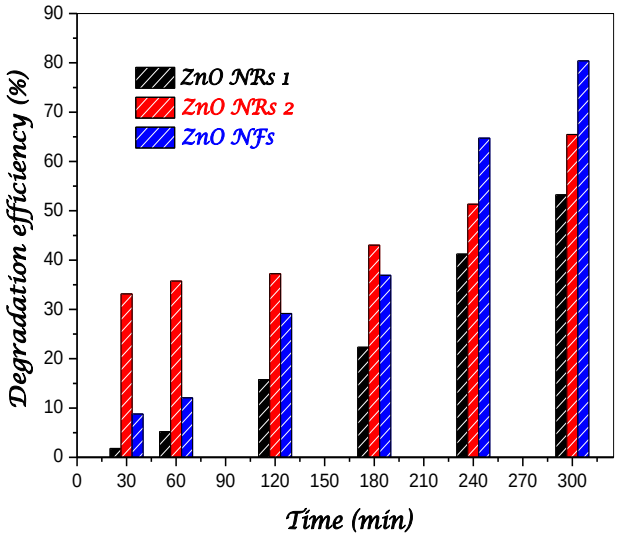

Figure III.57: *The photodegradation efficiency of MB dye by using ZnO Nanorods and Nanoflowers as photocatalysts*

ZnO nanostructures have also tested different pollutants other than the Methylene Blue by various researches. Fan et al. [55] fabricated ZnO nanoflowers on Si substrate by the hydrothermal method at 70 and 80°C for 70 min, and the photocatalysis activity of Rhodamine dye with a concentration of 5 mg/l by ZnO nanoflowers/Si was investigated. The photodegradation efficiency after 3 h of irradiation time was found 42% and 52% for ZnO nanoflowers at 70 and 80°C, respectively.

Kuriakose et al. [53] synthesized flower-like ZnO nanostructures at 60°C for 3 h with different concentrations of zinc acetate 0.02, 0.05, and 0.1M for preparing three samples S1, S2, and S3. The photodegradation of Methylene Blue by these photocatalysts was studied with a concentration of 22.4 μM while the efficiency of each sample was achieved 97.8%, 99.6%, and 66.8% for S1, S2, and S3, respectively, after 60 min of sunlight exposure.

Habba et al. [65] studied the photocatalytic activity of the ZnO NWs of Methylene Blue (MB), Methyl Orange (MO) and Azorubine (acid red 14—AR14) with concentration of 10 μM for each dye. The undoped ZnO NWs and Fe-doped NWs were synthesized at 95°C and

for 4 h by the hydrothermal process. The degradation rate of ZnO NWs and ZnO: 1% Fe NWs, respectively, was found 49%-69% for MO, 86%-95% for MB, and 93%-98% for AR14 after 3 h of illumination.

The rate constant k was calculated by using the pseudo first-order kinetic law which can be defined by the equation (1) and the photocatalytic degradation efficiency τ of MB was computed through the relation (III.3). The values of τ and k of each photocatalyst after 300 min of UV light exposure are given in Table III.11.

Table III.11: *Reaction rate constant and photodegradation efficiency of various photocatalysts of ZnO.*

ZnO nanostructures	*Irradiation time (min)*	*Rate constant k *10^{-4} (min^{-1})*	*Photodegradation efficiency, τ (%)*
ZnO NRs 1	300	24.9	54
ZnO NRs 2		28.6	66
ZnO NFs		50.8	81

The discrepancy in the photocatalytic activity of ZnO photocatalysts may found explication in the difference between their nanostructures. The porous structure, gap energy, lifetime of electron-hole pairs and •OH radicals concentration are fundamental parameters to ameliorate the efficiency of photocatalyst [66]. The migration of free charges to the surface of photocatalyst without recombining can participate in several oxidation and redaction reactions with adsorbed species such as oxygen, water and other organic species by generating the hydroxyl radicals •OH which possess a high oxidation power. All reactions of the photocatalytic mechanism can be summarized by the following equations and Figure III.58:

$$ZnO + h\nu \rightarrow e^-_{CB} + h^+_{VB} \quad (6)$$

$$e^- + O_2 \rightarrow {}^\bullet O_2^- \quad (7)$$

$$h^+ + OH^- \rightarrow {}^\bullet OH \quad (8)$$

$$h^+ + H_2O \rightarrow H^+ + {}^\bullet OH \quad (9)$$

$${}^\bullet OH + MB\ (dye) \rightarrow \text{degradation products} \quad (10)$$

$${}^\bullet O_2^- + MB\ (dye) \rightarrow \text{degradation products} \quad (11)$$

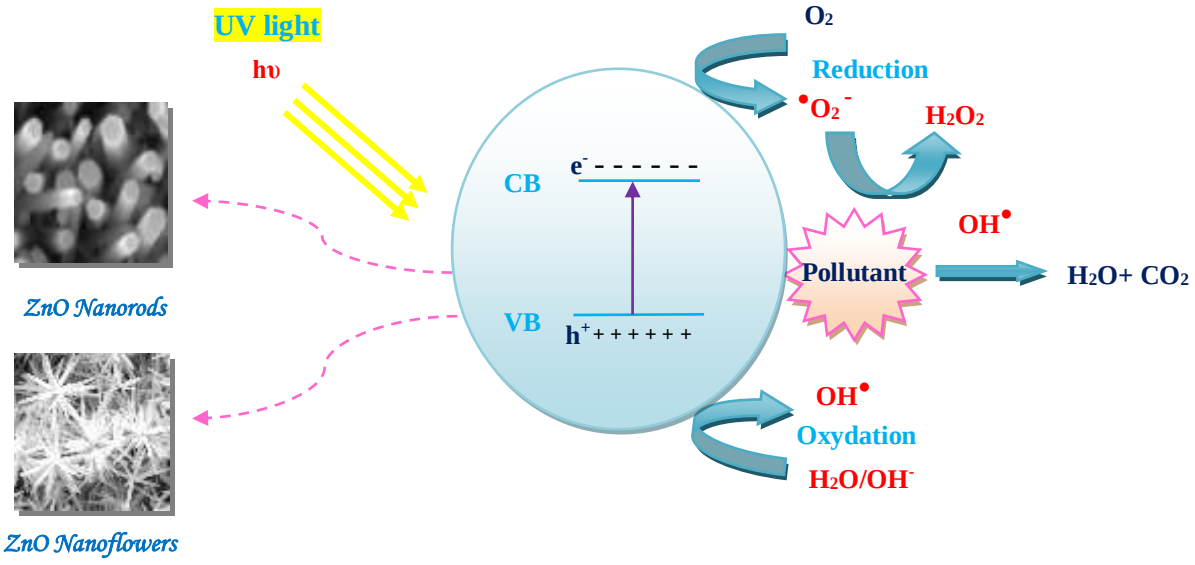

Figure III.58: *Schematic diagram describing of photocatalysis mechanisms of ZnO Nanostructures*

Generally nanostructured films such as nanowires, nanobelts and nanorods are recommended for humidity gas sensing, photocatalysis, antibacterial activity due to the large specific surface [67-73] and to their high surface to volume ratio [74]. It has been demonstrated that photo generated carrier's recombination in ZnO, which is faster than the redox reactions involved in photocatalysis process [75] hinders the photocatalytic activity [76]. Recently material with a large surface to volume ratio such as nanostructured ZnO have achieved higher photocatalytic activity due to the large charge transfer in an open or porous structure [77, 78]. Thereafter, the enhancement in the photo generated carriers from ZnO to the liquid in a porous structure may explain the observed large photocatalytic efficiency in ZnO Nanoflowers than in ZnO Nanorods.

Chapter IV

Applications of ZnO : Antibacterial activity and Solar Cells

Zinc oxide as an agent antibacterial was tested against E. coli with several doping and in the form of thin layers and nanostructures. Also ZnO thin films were used as a photodiode for Solar Cells and the results of both applications are presented in this chapter.

This chapter was devised on two sections: one concerned on the antibacterial activity of ZnO thin films against Gram negative of Klebsiellapneumoniae ATCC 700603 and Gram negative of Escherichia coli. The other part is based on the application of ZnO thin films in photovoltaic field and in solar cells.

Antibacterial Activity

IV.1 Introduction

Population explosion and environmental pollution encourage researchers to seek hygienic and secure production methods to facilitate human living conditions [1]. In recent decades, there have been a lot of developments using nanotechnology in the textile industry. For instance, different kinds of antimicrobial treatments have been utilized to protect garments against harmful microorganisms [2, 3].

Nanomaterials often show unique and considerably changed physical, chemical and biological properties compared to their macro scaled counterparts [4]. Synthesis of noble metal nanoparticles for applications such as catalysis, electronics, optics, environmental, and biotechnology is an area of constant interest [5–11]. Gold, silver, and copper have been used mostly for the synthesis of stable dispersions of nanoparticles, which are useful in areas such as photography, catalysis, biological labeling, photonics, optoelectronics and surface-enhanced Raman scattering (SERS) detection [12,13].

Silver is widely known as a catalyst for the oxidation of methanol to formaldehyde and ethylene to ethylene oxide [14]. In the United States, more than 4×10^6 tons of silver were consumed in 2000. Colloidal silver is of particular interest because of distinctive properties, such as good conductivity, chemical stability, catalytic and antibacterial activity [15]. For example, silver colloids are useful substrates for surface enhanced spectroscopy (SERS), since it partly requires an electrically conducting surface [16-18]. Also, the exposure of silver ions to light reduces them into 3–5 atoms clusters of silver, which catalyzes a gain of $\sim10^8$ atoms in latent image to be visible [19].

Silver is known for its antimicrobial properties and has been used for years in the medical field for antimicrobial applications and even has shown to prevent HIV binding to host cells [20-24]. Additionally, silver has been used in water and air filtration to eliminate microorganisms [25–27].

Chemical reduction is the most frequently applied method for the preparation of silver nanoparticles (Ag NPs) as stable, colloidal dispersions in water or organic solvents [28, 29]. Commonly used reductants are borohydride, citrate, ascorbate, and elemental hydrogen [30–38]. The reduction of silver ions (Ag^+) in aqueous solution generally yields colloidal silver with particle diameters of several nanometers [29]. Initially, the reduction of various complexes with Ag^+ ions leads to the formation of silver atoms (Ag^0), which is followed by agglomeration into oligomeric clusters [39]. These clusters eventually lead to the formation of colloidal Ag particles [39]. When the colloidal particles are much smaller than the wavelength of visible light, the solutions have a yellow color with an intense band in the 380–400 nm range and other less intense or smaller bands at longer wavelength in the absorption spectrum [16-18]. This band is attributed to collective excitation of the electron gas in the particles, with a periodic change in electron density at the surface (surface plasmon absorption) [40-42].

IV.1.1 The antibacterial tests

IV.1.1.1 Characteristics

In the beginning, it is important to introduce the terms and biological aspects that will be involved in the presentation of the results from the anti-bacterial tests carried out on our films. We introduce here a terminology linked to the structure of the bacteria as well as its genera and species.

The fine structure of bacteria is a cellular structure, one of the characteristics of which is that it has no nucleus. It is classic to distinguish mandatory structures (Figure IV.1), present in all bacteria, and structures whose presence is optional and characterizes bacterial groups. Water is the main component of a bacterium. It represents approximately 80% of the weight of this prokaryote. Analysis of the composition of a bacterium from its dry weight identifies and quantifies the following components: carbon (50%), oxygen (20%), nitrogen (15%), hydrogen (10%), and phosphorus (3 %).

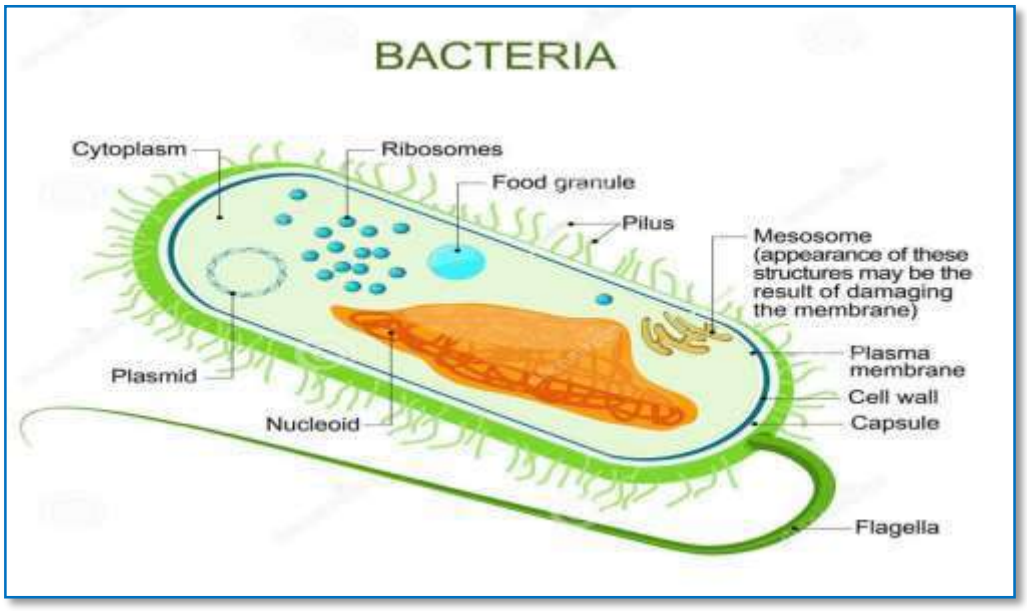

Figure IV.1: *Mandatory components of a bacterium*

Various elements are used to classify bacteria into different groups, such as their shape or morphology. Among the morphological criteria we will mention the Gram stain. It is a staining that allows to highlight the properties of the bacterial wall, and to use these properties to distinguish and classify them. In 1884, a Danish doctor, Christian GRAM, classified bacteria into two large groups: Gram-positive bacteria (Gram +) and Gram-negative (Gram -) bacteria. This method consists in coloring the cells in purple-black and observing whether the final coloration after a few minutes remains purple-black or whether it becomes pink. You should know that the bacterium has a cytoplasm which is surrounded, as for any cell, by a plasma membrane made up of phospholipids. Around it is always a more or less thick peptide wall. It is therefore the thickness of the wall which determines the reaction to Gram staining. In summary, the results of the Gram test indicate that if the coloration remains purple-black, the bacteria is classified as Gram + and the wall is a homogeneous layer of relatively thick peptidoglycan (20 to 80 nm thick). If the coloration turns pink, then the bacteria is Gram - and the wall is a thin layer of peptidoglycan (1 to 3 nm) provided with a thin outer membrane (7 to 8 nm) composed of lipopolysaccharides and proteins.

In our study we use two kinds of bacteria: a Gram negative of Klebsiella Pneumoniae and Gram negative of Escherichia coli.

Several systems have been used for the production of bacterial strains of E. coli, the liquid medium, the petri dishes, the incubation are grouped in Figure IV.2. The role of each system, is necessary for the antibacterial test, is cited one by one as following:

* The autoclave 'nuve steam art' of OT 40 L brand for the preparation of the suspension of the bacteria and the liquid medium (Figure IV.2-a),
* An apparatus of type nuve and LN 120 brand with UV irradiation room was exploited for elaboration the Petri dishes (Figure IV.2-b),

(a)

(b)

(c)

(d)

Figure IV.2: The systems used in antibacterial activity: (a) autoclave (b) preparation chamber with UV irradiation (c) the shaker (d) bacteriological oven.

- A bacteriological oven type MEMMERT for the incubation of the samples prepared (Figure IV.2-c),
- The 'shaker' ST 402 was used for treatment of samples by its vibrations at 37.5°C (Figure IV.2-d).

Klebsiella Pneumoniae Bacterium

IV.1.2 Synthesis of Ag Nanoparticles

Silver nanoparticles were synthesized injecting sodium citrate solution into the solution of silver nitrate at high temperature. The synthetic process was carried out in aqueous solution, making the method versatile and ecofriendly. The silver colloid was prepared by using a chemical method. All solutions of reacting materials were prepared by distilled water. In typical experiment silver nitrate $AgNO_3$ was dissolved in 200 ml distilled water and then the solution was heated to boiling. Then trisodium citrate was dissolved in 50 ml distilled water and 2 ml of trisodium citrate were added to solution of $AgNO_3$ after boiling (drop by drop). During the process, the solution was mixed vigorously. Later, the solution was left on hot plate for 2 hours at 90°C for heating only. Finally it was cooled to room temperature and the solution color was Yellow. The concentration of this solution was 6.77 x 10^{-4} mol/l.

The mechanism of reaction could be expressed as follows [43]:

$$4Ag^{+} + C_6H_5O_7Na_3 + 2H_2O \longrightarrow 4Ag^{0} + C_6H_5O_7H_3 + 3Na^{+} + H^{+} + O_2 \uparrow$$

IV.1.3 Deposition of ZnO thin films by sol-gel

The solution sol-gel is performed at room temperature in the following way: Zinc acetate was dissolved in methanol and the solution was left under stirring at 60°C. Then Methethanolamine (MEA) (C_2H_7NO) was added drop by drop. The solution was left on hot plate for 2 hours under stirring.

The Dip-Coating was used as a method for deposition of ZnO thin films with 5 dipping onto glass substrates and tissue. The concentration of Ag NPs were used for each sample was varied between 5 % and 10% added to 30 ml of ZnO solution. The samples were immersed in the sol-gel solution with speed of 6 mm/s during 15 s and dried at 100°C for 15 min while samples on tissue were dried at 80°C for 10 min. Then ZnO thin films deposited on glass annealing in oven at 500°C for 2 hours.

IV.1.4 Preparation of the bacteria

The antibacterial activity of the extract on tissue impregnated is investigated against a Gram negative test bacterium Klebsiella Pneumoniae ATCC 700603 obtained from the American Type Culture Collection (ATCC). The first set of ZnO (pure, 2 layers and 5 layers) on tissue cut as rectangle with 1.5 x 2.5 cm^2 as first bacterial test. Then, the samples on tissue cut out in circular form with 5 mm diameter for ZnO with 5 % 10 % Ag NPs while the others samples their diameter was 10 mm.

From an 18 hour culture on the trypticasesoy agar medium (TSA), a suspension of each bacteria-test in physiological water (0.9% NaCl) is prepared.

The cell density of each suspension was adjusted by dilution in sterile physiological water and in comparison with the 0.5 Mc Farland solutions (an optical density of 0.2 to 650 nm) so as to obtain a final concentration of 10^6 UFC / ml after incorporation in Mueller Hinton medium [44].

IV.1.5 Antibacterial activity

The pieces of tissues with diameter of 5 and 10 mm are sterilized in Petri dishes made of glass in the Pasteur oven (at 180 °C for 30 min). The tissues are then covered with a thin layer of the Mueller-Hinton medium previously inoculated with the test bacterium.

Before incubation at 37 °C, the optimum growth temperature of the test strain, the dishes were left for 2 hours at + 4 °C to allow pre-diffusion of the bioactive substances [45]. The results are read after 24 hours of incubation. Any zone of inhibition of bacterial growth around on pieces of tissue, even of small diameter, is considered as a positive result.

In the beginning, we will display the first testing of Zinc acetate against Gram negative of Klebsiella Pneumoniae. The samples were prepared by sol gel dip-coating technique on tissue and cut them in 1.5 x 2.5 cm^2. Figure IV.3 shows antibacterial test of Zinc oxide on tissue against Klebsiella Pneumoniae with different samples; pure ZnO, ZnO washed after deposition, ZnO 2 layers and ZnO 5 layers. As observed, this bacterium was grown on all surface of the ZnO pure. However for the other samples, there is an inhibition zone around each ZnO piece. This means that these samples can resist the growth of the bacterium Klebsiella Pneumoniae.

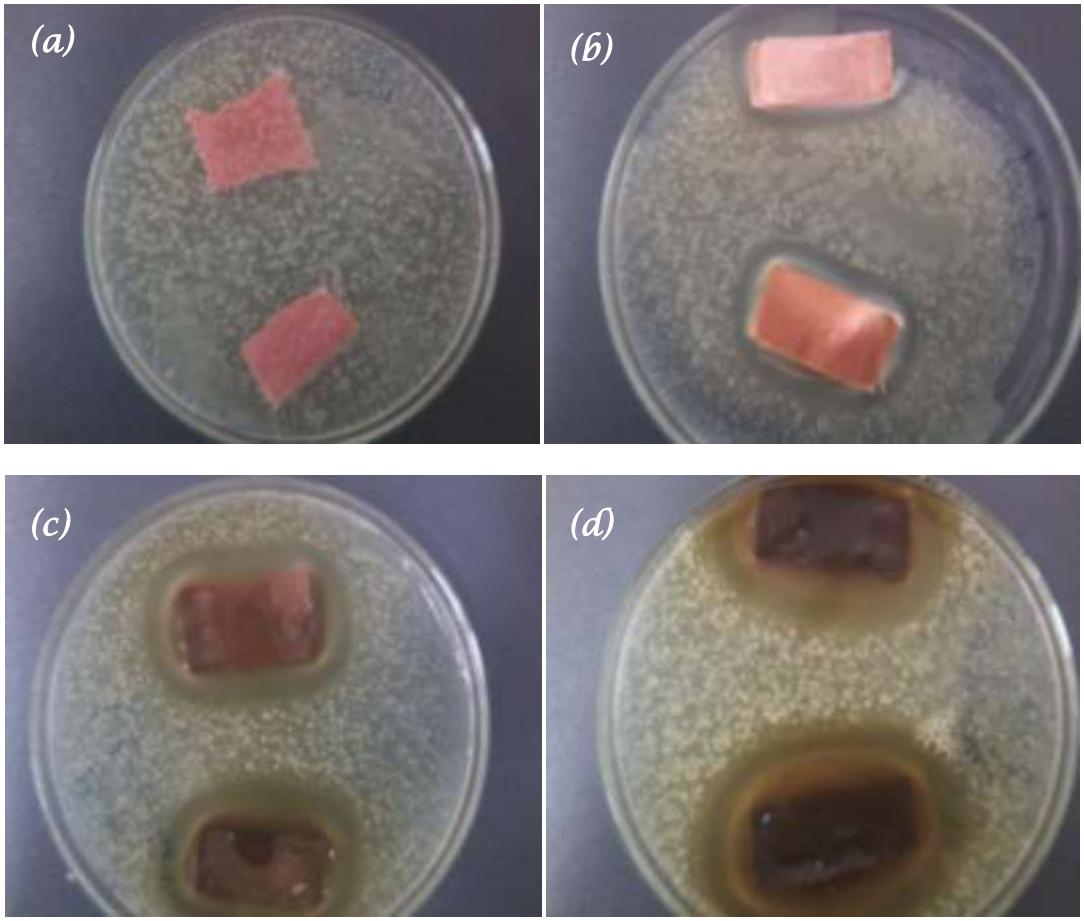

Figure IV.3: *Deposition of Zinc oxide on tissue and tested by* ***Klebsiella Pneumoniae*** *bacteria: (a) pure ZnO, (b) ZnO washed after deposition, (c) ZnO 2 layers and (d) ZnO 5 layers.*

IV.1.6 Ag Nanoparticles characterization

IV.1.6.1 Raman spectroscopy

Figure IV.4 illustrated the Raman spectrum of Ag Nanoparticles prepared at 90°C by simple method. As shown the peak of vibrational modes is situated at 860 cm^{-1}.

Y. Cai et al. [46] synthesis silver nanoparticles via a microwave method using silver nitrate as a silver source, MEA as a reducing reagent, PAA as capping agent, and DI water as a medium. The Ag NPs prepared with various mass ratio of silver nitrate to water is 1: 1, 1: 2, 1: 4, and 1: 6. The Raman results showed that the strongest SERS peaks are at 1391 cm^{-1}, 855 cm^{-1}, and 229 cm^{-1}, which are attributed to the ν_sO– C–O, ν_sC–C, and νAg–OCO^- bands, respectively [47]. These peaks clearly indicated that the main interaction of the capping agent

(PAA) with the Ag surface was through the carboxylic group, i.e. through the Ag–O interaction (the moderate 855 cm^{-1} peak indicated that there was also an interaction through the hydrophobic part of the polymer).

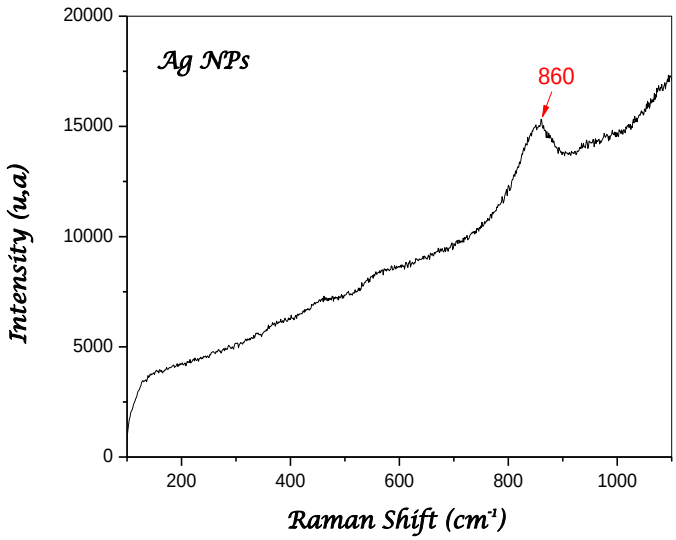

Figure IV.4: *Raman spectrum of Ag Nanoparticles prepared at 90°C.*

IV.1.6.2 UV-Visible measurement

The UV–Vis absorption spectroscopy is one of the most widely used simple and sensitive techniques for the observation of nanoparticles synthesis. In order to monitor the formation of silver nanoparticles, the absorption spectra of synthesized silver nanoparticles were recorded in the wavelength range 300-800 nm. Figure IV.5 exhibits the absorbance spectrum of Silver Nanoparticles synthesized by a simple chemical bath deposition at 90°C. In the UV-Vis spectra a single strong peak with a maximum around 351 nm was observed, which corresponds to the typical surface plasmon resonance (SPR) of conducting electrons from the surface of silver nanoparticles. The SPR absorption of metal nanoparticles like gold and silver is very sensitive to the changes of the size and shape of the nanoparticles formed [48].

Many studies found that the peak of absorbance centered at 360 nm [49, 50]. So the Ag nanoparticles are depends to the experimental conditions: the quantity of Ag in the solution, the temperature, the reducing agent and stabilizer or protecting agent according to Amany et al. [51].

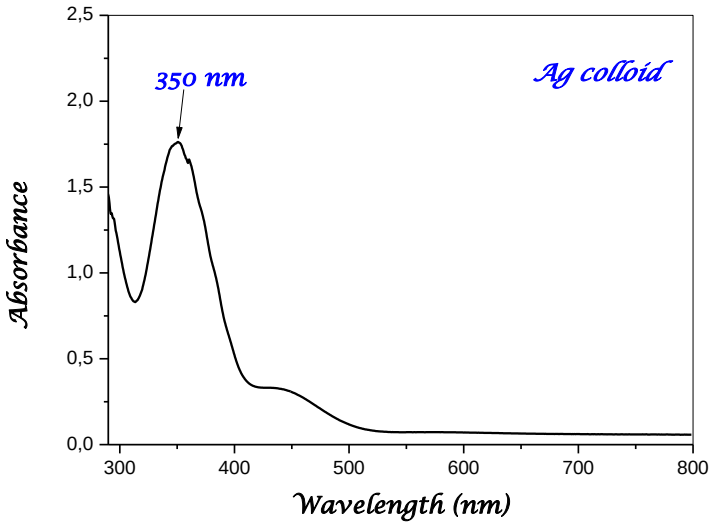

Figure IV.5: *Absorbance spectrum of Ag Nanoparticles*

Several researches found another peak of absorbance characterized the Ag Nanoparticles. Y. Cai et al. [46] reported that at high concentrations of $AgNO_3$ (the mass ratio of $AgNO_3$ to DI was 1: 1), except for an obvious peak at 425 nm, an additional band at 635 nm appeared, indicating that the nanoparticles were not uniform, which was in accordance with the SEM morphology. As the concentration decreased, there was only one unique peak at about 420 nm, and the peak became narrow, which meant that the uniformity in the size of the nanoparticles was very good. The peak located at 420 nm was the typical plasma resonance peak of silver nanoparticles. K. Virender et al. [52] which prepared Ag nanoparticles by green synthesis approaches. They found that the peak of Ag nanoparticles was centered at 420 nm. Kora et al. [53] synthesized silver nanoparticles by gum ghatti and they reported that the absorbance peak of these NPs was located at 412 nm. Y. Zhang et al. [54] assigned that a strong absorption peak at approximately 413 nm originates from the surface plasmon absorption of Nanosized silver NPs [55, 56]. The narrow and symmetric absorption peak implies that the size of NPs is uniform [57].

So the purity of water and reagents, cleanliness of the glass ware are critical parameters. Solution temperature, concentrations of the metal salt and reducing agent and reaction time also influences particle size. Controlling size and shape of metal nanoparticles remains a challenge [58].

IV.1.6.3 Zeta Sizer analyzer

The diameter and the size distribution by intensity and volume of Ag NPS were measured by Zeta Sizer. Figure IV.6 present the spectrum of the size distribution by volume of Ag Nanoparticles. As shown the colloids obtained have a small size of particles which ranged from 2 -110 nm. So the Ag nanoparticles depend to time of preparations, the temperature of boiling and the concentration of silver in the solution.

Y. Zhang et al. [54] also determined the size distribution of Ag NPs by Nanosight system. They reported that the most of particle sizes are around 43 nm, which supports the result from the UV–vis spectrum. The uniform Ag NPs provides a good condition for further synthesis of Ag/ZnO compositions.

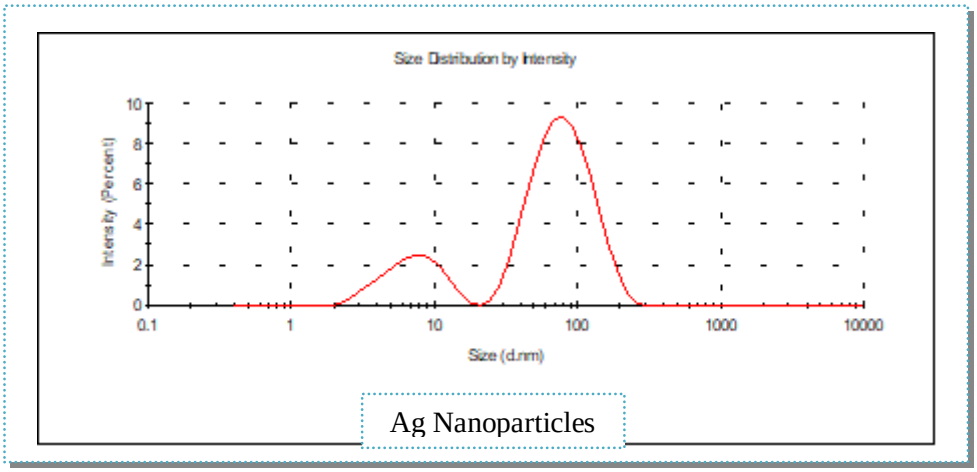

Figure IV.6: *Spectrum of size distribution by volume of Ag Nanoparticles*

Another preparation of ZnO thin films with and without silver nanoparticles by dip coating method was done in order to investigate the effect of gram negative of ***Klebsiella Pneumoniae*** on these films.

IV.1.7 Characterization of films

IV.1.7.1 Films Structure of ZnO: Ag

Figure IV.7 reported the XRD spectra of the pure ZnO and ZnO with 5 % and 10% Ag nanoparticles for 5 layers annealed at 500°C. As can be seen, film deposited without Ag NPs is polycrystalline in nature with crystal growth according the plane (002) having a hexagonal wurtzite structure. Whereas, three peaks diffracted of ZnO films with 5% Ag NPs are recorded at 2θ angles 31.65; 34.5 and 36.32° corresponding to (100), (002) and (101) of the

hexagonal wurtzite structure, respectively. Moreover, ZnO films with account of 10% Ag and 5 dipping exhibited a strong preference to (100) plane and a small peak at 2θ = 66.27°correspond to the plane (200). The sharp diffraction peaks (100) indicate the well crystallization of 10 % Ag NPs/ZnO. The presence of strong preferential orientation to (100) plane means that the crystalline structure is Hexagonal wurtzite. No diffraction peak of silver was observed in ZnO films with 5 % and 10 % Ag NPs may be the amount of Ag was too small. And no characteristic peaks from other impurities were detected in the patterns, demonstrating that all samples have high phase purity. It suggests that the obtained products are Ag/ZnO samples [54].

L. N. Wang [59] deposited (1% wt) Ag: ZnO thin films on c-plane sapphire substrates by pulsed laser deposition method at 500 and 600°C for 90 min. Some samples were annealed at 700°C in oxygen ambient for 30 min and the others kept an annealed. The XRD analysis shows that all the samples have a strong ZnO (002) peak, which indicates that the films have the preferred orientation with the c-axis normal to the substrate.

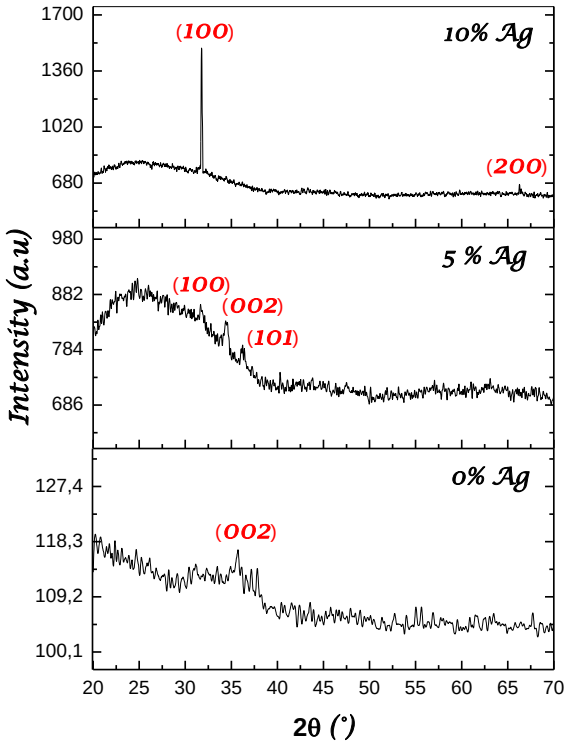

Figure IV.7: *XRD spectra of ZnO films: 0%, 5% and 10 % Ag NPs with 5 layers obtained by sol-gel*

IV.1.7.2 Surface morphology

The SEM micrographs of ZnO films for 5% and 10 % Ag Nanoparticles with 5 layers are shown in Figure IV.8 (a and b). The surface morphology of films obtained was dense and compact with the appearance of the small white spot which possible related to silver Nanoparticles. As a result these characteristic of surface make the films more suitable against the growth of bacteria. So the antibacterial activity is more important when the films have a large specific surface which is dense and compact.

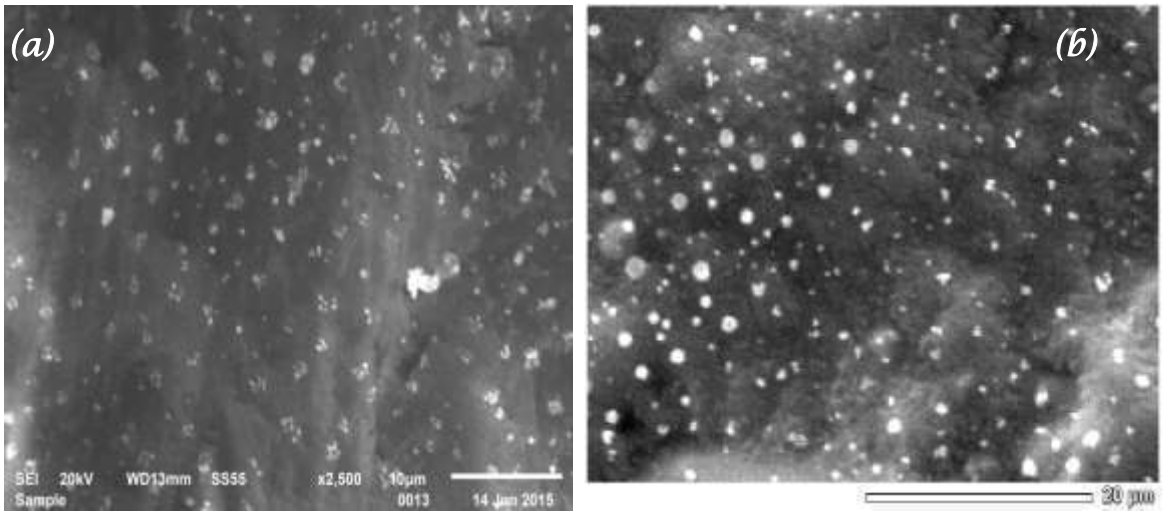

Figure IV.8: *SEM images of ZnO thin films: (a) 5% Ag 5 layers and (b) 10% Ag 5 layers.*

IV.1.7.3 Optical properties

The optical properties of ZnO thin films, deposited by dip-coating with different content of Ag colloidal for 5 dipping, determined from the transmission measurement in the wavelength range of 200 - 800 nm. Figure IV.9 shows the transmittance spectra of Zinc acetate deposited by dip-coating onto the glass substrates with 0 -5 and 10 %Ag NPs for 5 dipping. The spectra showed that ZnO films deposited with different incorporation of Silver nanoparticles present high transparency. A decreasing in transmittance was observed while concentration of Ag NPs increased until it reached 10 % Ag, above this value the transmittance decreased from 88% to 81%. The decrease of transmittance can be explained by the increase in thickness and the variation of concentration of Ag nanoparticles. All the films have a steeper absorption around 300 nm.

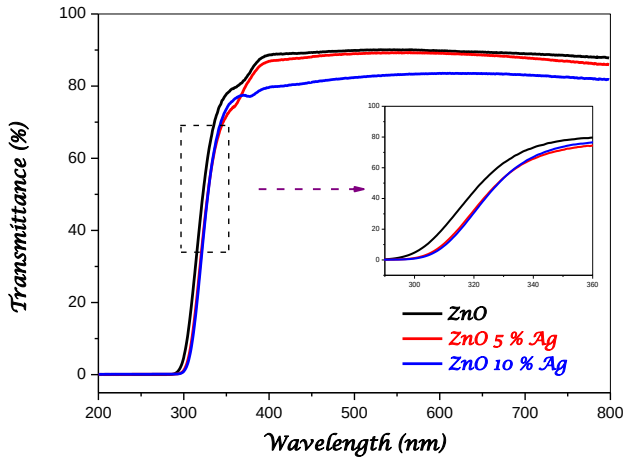

Figure IV.9: *Transmittance spectra of the ZnO thin films deposited with various content of Ag NPs with 5 dipping.*

The thickness and refractive index of ZnO thin films for 5 dipping with 5 % and 10 % Ag NPs are listed in Table IV.1. As shown the values of refractive index the films obtained are decrease with the increase of the incorporation of silver nanoparticles. While, the thickness values of these films increase with the raise of Ag NPs from 0 %, 5 % to 10 %.

Table IV.1: *Thickness and refractive index of ZnO films with various Ag NPs*

ZnO: Ag NPs with 5 dipping	*Thickness (nm)*	*Refractive index n*
0 % Ag NPs	142.656	1.702
5 % Ag NPs	147.053	1.687
10 % Ag NPs	173.153	1.672

Figure IV.10 exhibits the plot of $(\alpha h\upsilon)^2$ versus photon energy hυ for the obtained ZnO films. The plots linearity indicates that the materials of direct band gap nature. The extrapolation of the straight line to $(\alpha h\upsilon)^2 = 0$ axis gives the energy band gap of the film material.

The obtained optical bang gaps (Eg) are reported in Figure IV.10. The band gap energy is equal to 3.20 eV, 3.12 eV and 3.06 eV for the deposited films; ZnO pure, ZnO 5% Ag NPs

and ZnO 10 % Ag NPs, respectively. The decrease of the band gap energy of these films with the increase of Ag nanoparticles content is mainly due to the inclusion of silver nanoparticles. From the enlarge area of the absorption band edges in the inset of Figure IV.9, it can be seen that with Ag doping concentration increases, the absorption band edge is shifted to the long wavelength. The red shift demonstrates that the band gap of ZnO films decreases with Ag doping density increases [60].

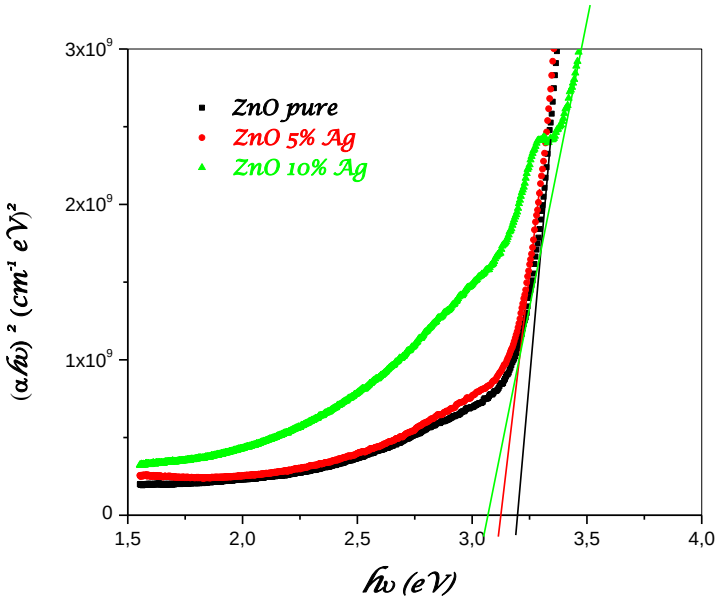

Figure IV.10: *Typical variation of the quantity* $(\alpha h\upsilon)^2$ *as a function of* $h\upsilon$ *for ZnO with various content of Ag NPs*

IV.1.7.4 Antibacterial activity

In this study, the antibacterial effect of Gram negative of the bacteria Klebsiellapneumoniae ATCC 700603 was studied on the prepared samples of ZnO with Ag NPs on tissue.

Figure IV.11 and Figure IV.12 exhibit the inhibition zone of different pieces of tissue with and without ZnO and Ag NPs for 5 dipping for two diameters 5 and 10 mm. The results indicated that the zone of inhibition is about 0, 12,14 and 18 mm in diameter for reference, ZnO pure with 5 dipping , ZnO 5 % Ag with 5 dipping and ZnO 10% Ag with 5 dipping respectively. As can be seen the ZnO samples on tissue with 10 mm of diameter can resist the growth of the bacteria while the specie without ZnO as a reference, the bacteria is growing on its surface.

However the samples of ZnO with 5 % Ag nanoparticles have a big zone of inhibition than ZnO pure. This means that the addition of Ag nanoparticles in the solution of ZnO has a great effect on the bacteria. The Silver nanoparticles are harmful to bacteria [61]. Consequently, zinc oxide and silver nanoparticles could resist the growth of this bacterium ATCC 700603 but together have more efficiency on Klebsiellapneumoniae. Finally, smaller particles of Ag NPs having larger surface area for interaction and have efficient bactericidal effect. These antibacterial properties can been used to prevent and reduce the bacteria used in this work.

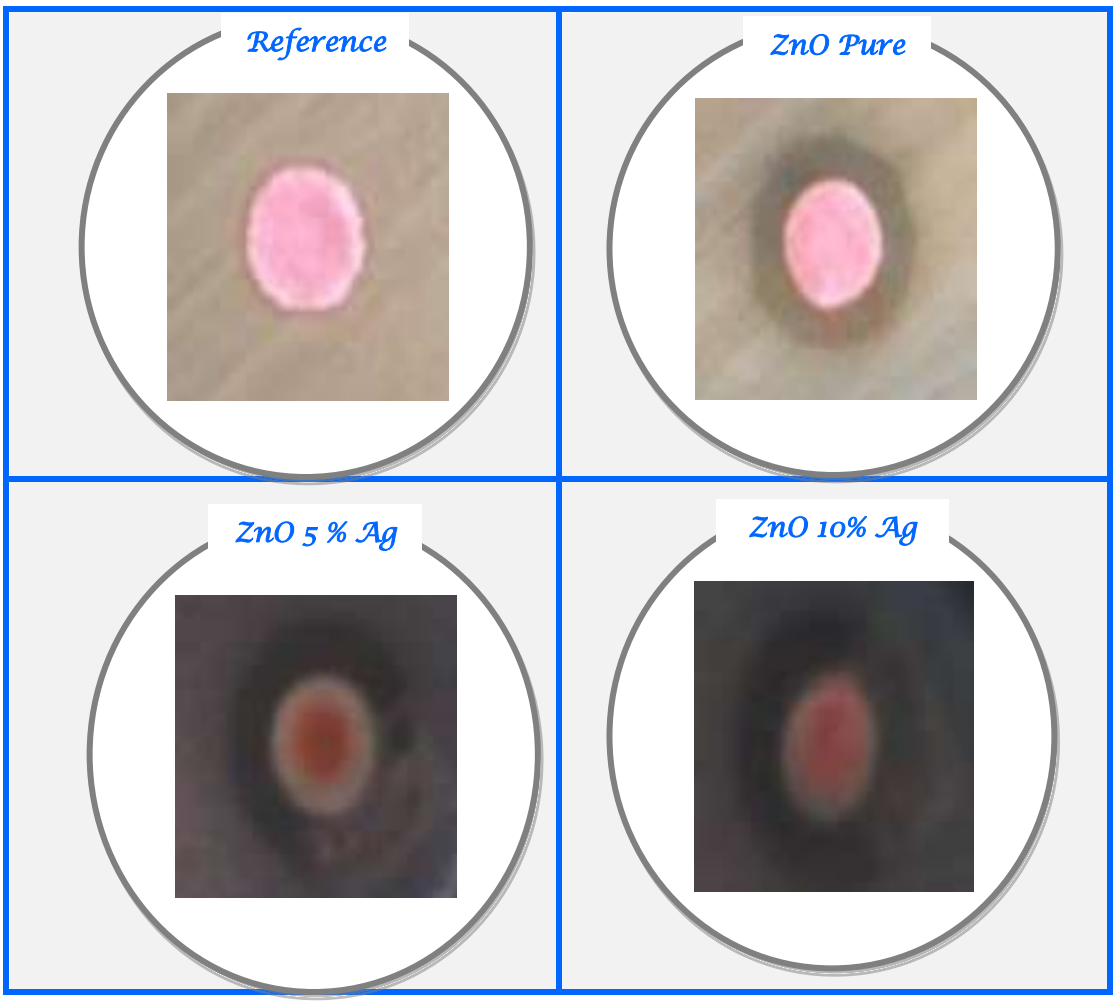

Figure IV.11: *ZnO with inclusion of Ag NPs deposited on tissue for 5dipping and tested by* ***Klebsiella pneumoniae*** *bacteria*

Figure IV.12 shows histogram of Zone of inhibition of ZnO with Ag NPs against the bacteria tested. As shown the high value of zone of inhibition was presented by ZnO incorporated 10 % Ag NPs. So the results obtained are encouraged for the antibacterial activity.

The mechanism of the bactericidal effect of silver and Ag NPs remains to be understood. Several studies propose that Ag NPs may attach to the surface of the cell membrane disturbing permeability and respiration functions of the cell [62]. Smaller Ag NPs having the large surface area available for interaction would give more bactericidal effect than the larger Ag NPs [62]. It is also possible that Ag NPs not only interact with the surface of membrane, but can also penetrate inside the bacteria [63].

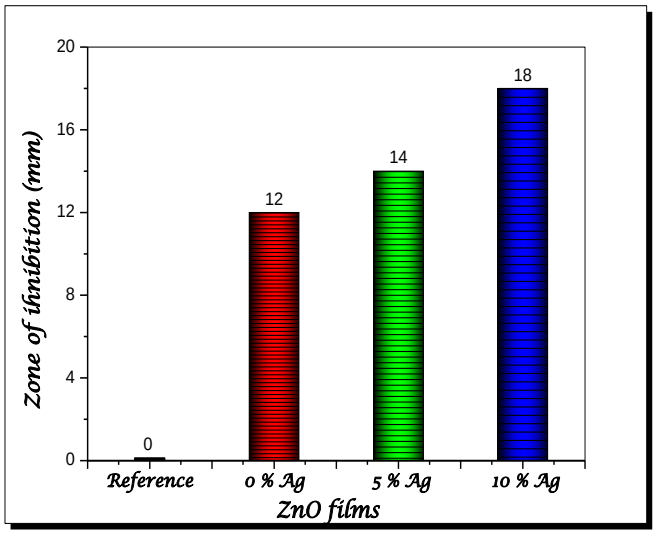

Figure IV.12: *Histogram of Inhibition zone of ZnO with Ag NPs against bacteria tested*

Escherichia coli Bacterium

IV.1.8 Protocols of antibacterial testing

The Absorption method is an evaluation method in which the bacterial suspension under test is inoculated directly on samples.

Before carrying out the antibacterial test, a bacterial culture is necessary for each strain used. Pure ZnO thin films are prepared by ultrasonic spray on glass substrate with a flow rate of 1 ml / min, deposition time of 12 cycles and 400 ° C as substrate temperature, respectively. The deposition time was varied from 5 min to 30 min for ZnO thin films.

To prepare the liquid medium and an agar medium for bacteria, we have:

- For the liquid medium: Nutrient Broth in 1 L of water ----► 8 g.
- For Nutrient agar for plates (colony) in 1 L of water ----► 20 g.

The two products are of the MERK brand and the solutions are treated with distilled water in an autoclave at 121 bar for 20 minutes, which it presents in Figure IV.2 (a). The procedure used by the adsorption method is as follows.

IV.1.8.1 Adsorption Method

- We use E. coli and N.B (Nutrient medium)
- We take 1 ml of bacteria and add 9 ml of N.B medium ------▶ this is suspension 1
- After the first step, we take 100 µl of solution 1 and add 900 µl of medium ----▶ so this is suspension 2.
- Then we take 1 ml from suspension 2 and we put this quantity on our films.
- Finally, we put all samples of this method in the shaker for 2 hours at 37.5 ° C temperature.
- After two hours, we take 250 µl of sample suspension and then sprayed on the petri dishes with agar medium.
- Finally, all the petri dishes waited 1 or 2 days in the incubation at 37.5 ° C. After checking the samples and the reference, we counted the colonies.

The antibacterial activity of zinc oxide, which deposited by ultrasonic spray pyrolysis with different deposition times; 5, 15 and 30 min at 400°C to coated soda lime glasses, against gram negative of E. coli is illustrated in Figure IV.13. Zinc acetate with 0.1 M showed that this precursor on tissue can resist the growth of two kinds of bacteria tested K. pneumonia and E. coli. But in this case we observed that ZnO thin films with different thicknesses cannot eliminate the E. coli strain. As seen in FigureIV.13, there is no inhibition zone around all ZnO samples.

Consequently, the antibacterial test of ZnO with different deposition times; 5, 15 and 30 min show that these set films have inability for removed the E. coli bacterium which indicated the positive sign (+) in the antibacterial test by the Adsorption method. While, ZnO: Ag NPs (5 and 10 min) have a high ability to eliminate the strains of K. Pneumoniae with inhibition zone of 18 mm.

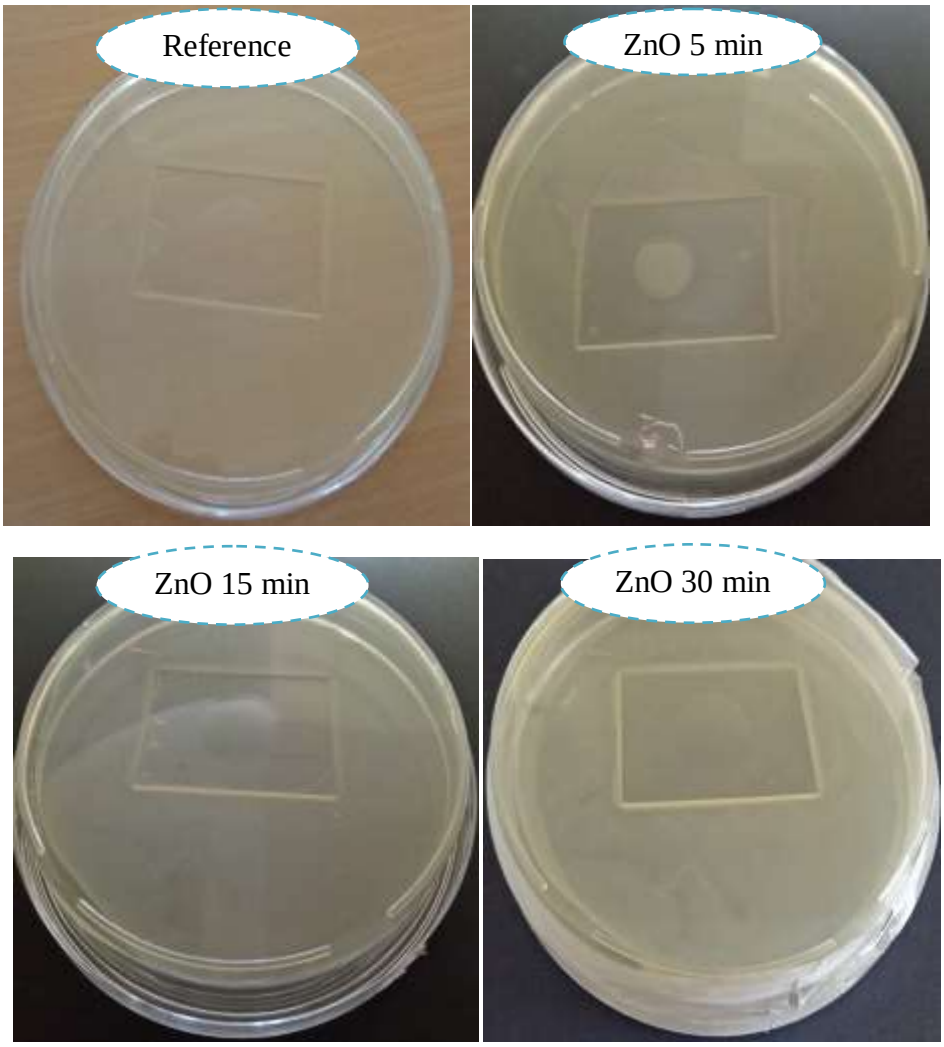

Figure IV.13: *Test antibacterial of ZnO films with various deposition times against E. coli*

In this section we present different results of ZnO thin film as dye synthesis solar cells, photovoltaic behavior, photodiode and photosensing properties under various light intensities.

Dye Synthesis Solar Cells

IV.2 Introduction

Solar cells or photovoltaic cell are made of a special material which named as semiconductors such as silicon or metal oxide. Basically, when light hit the cell, a certain portion of its energy is absorbed within the semiconductor material. The energy knocks electrons loose, allowing them to flow freely. Fundamentally, the device needs to fulfill only two functions: photogeneration of charge carriers which are electrons and holes in the material, and the separation of the charge carriers to a conductive contact that will transmit the electricity.

Heterojunction solar cells consisting of a wide band gap transparent conductive oxide on a single crystal silicon wafer have a number of potential advantages such as an excellent blue response, simple processing steps, and low processing temperatures. Zinc oxide (ZnO) thin films are of considerable interest for their efficient use in the fabrication of solar cells [64, 65] and it finds many applications in solid state and electronic devices [66, 67]. Furthermore, both undoped and doped ZnO films with Al, In, [68] and other dopants are used in optoelectronic display devices and in ultrahigh frequency electro-acoustic transducer [69].
In our study we will offer different properties of ZnO thin film deposited by ultrasonic spray pyrolysis on p type silicon and its applications in solar cells.

IV.2.1 Procedure of preparation

IV.2.1.1 Process of substrate cleaning

The p-type Si wafers were boiled in trichloroethylene for 5 min, and ultrasonically cleaned in acetone and methanol to remove any organic contamination. The wafers were etched in a solution of HF: H_2O (1:10) for 30 s to remove the native oxide, as illustrated in Figure IV.14, washed using deionized water (resistivity 18.2 MΩ) to remove any chemical residues and then

dried in N_2 gas before inserting them into the vacuum chamber. The back contacts were formed by evaporating a 200-nm-thick aluminium (Al) contact layer on the unpolished side of the wafer, followed by rapid thermal annealing at 570°C for 3 min under a N_2 atmosphere.

Figure II.14: *Schematic showing the silicon cleaning step*

IV. 2.1.2 Films deposition

The chemical deposition technique by ultrasonic spray is characterized by a very sophisticated and suitable system for depositing thin films and controlled the various processing parameters: the flow rate, the temperature of the substrate (which is homogeneous at all points of the heating plate), the program used (the number of cycles and at each cycle the spray sprayed the solution prepared for a few seconds or minutes and pauses for a few moments), the deposition time, etc.

The spray is well equipped with two types of gas, nitrogen and oxygen with a specified percentage. The sweep of the nozzle is connected with xyz positions and the diameter of this nozzle is 8 µl. the distance between the substrate holder and the nozzle is 9.5 cm. The device is operated with a computer which performs all the operations ordered.

In this work, the deposition of Zinc oxide thin films was carried out by the ultrasonic spray deposition pyrolysis (USPD) SONO-TEK at a substrate temperature of 400 °C with a flow rate of 1 ml / min and 12 cycles as deposition time while in one cycle the solution is sprayed for 30 seconds and 20 seconds on pause. Zinc nitrate hexahydrate (Sigma-Aldrich) was used as precursor with 0.1 M diluted in methanol for preparing ZnO solution which atomized by the spray system using compressed oxygen as the carrier gas with a value of 6.

ZnO thin films are deposited on soda lime glasses and on monocrystalline silicon P type with an orientation (100), resistivity of 1–10 Ω.cm and thickness of 380 µm.

Figure IV.15 illustrate the SONO-TEK system of deposition of ZnO thin films for preparing dye synthesis solar cells.

Figure II.15: *The deposition system SONO-TEK ultrasonic spray pyrolysis*

IV.2.1.3 The front and back contact of Al

The front and back contact of the Al / ZnO /p-Si/ Al heterojunctions was achieved using thermal evaporation for the deposition of a layer of aluminum with the following conditions as mentioned in Table IV.2. The source of used Al is fine wires.

Table IV.2: *Deposition conditions of front and back contact of Al / ZnO /p-Si/ Al structure*

Thickness (nm)	Pressure(Toor)	Voltage (V)	Current (A)	Time (min)
250	$8.81x10^{-6}$	3.8	44.5	30

The Al front contacts were evaporated onto the ZnO thin film using a shadow Mask. The diameter of circular contacts is 1.5 mm. Metallization with aluminum was performed by a thermal evaporation system NANOVEK NVTS-400 as illustrated in Figure IV.16.

(a) **(b)**

Figure IV.16: *Deposition system (a): thermal evaporation, (b) mask for making contact of Al*

IV.2.2 The measurement system

IV.2.2.1 In dark

Figure IV.17 shows the I-V measurement system in the dark using a Keithley 2400 source meter. The samples were placed in the gray box as shown in the Figure IV.17. The current measured by two electrodes with a voltage applied between -2 V and 2 V. The I-V measurements were carried out at room temperature and the results obtained are saved in the computer.

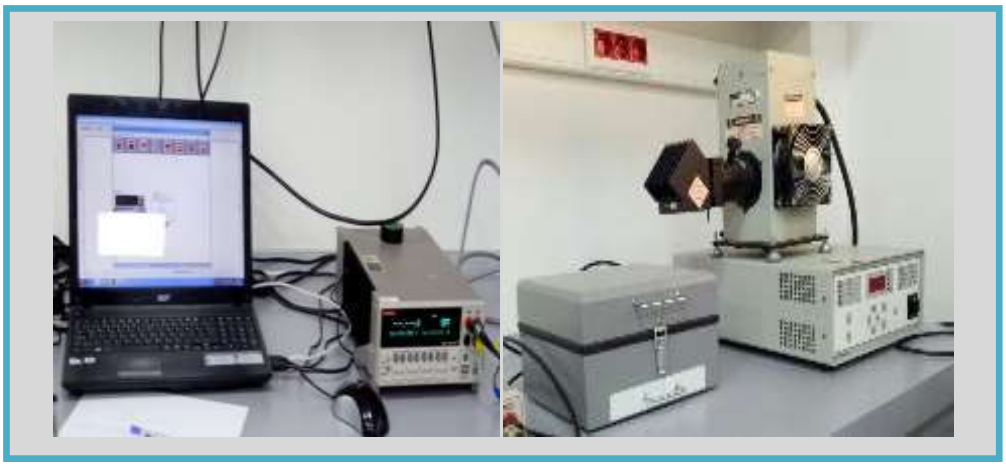

Figure IV.17: *I-V measurement system in the dark*

IV.2.2.2 Under illumination

Figure IV.18 shows the I-V measurement system with various illuminations of 40, 60, 80 and 100 mW / cm^2. The I-V measurements were carried out at room temperature under a Newport 96000 solar simulator with AM 1.5 global filter for various illuminations.

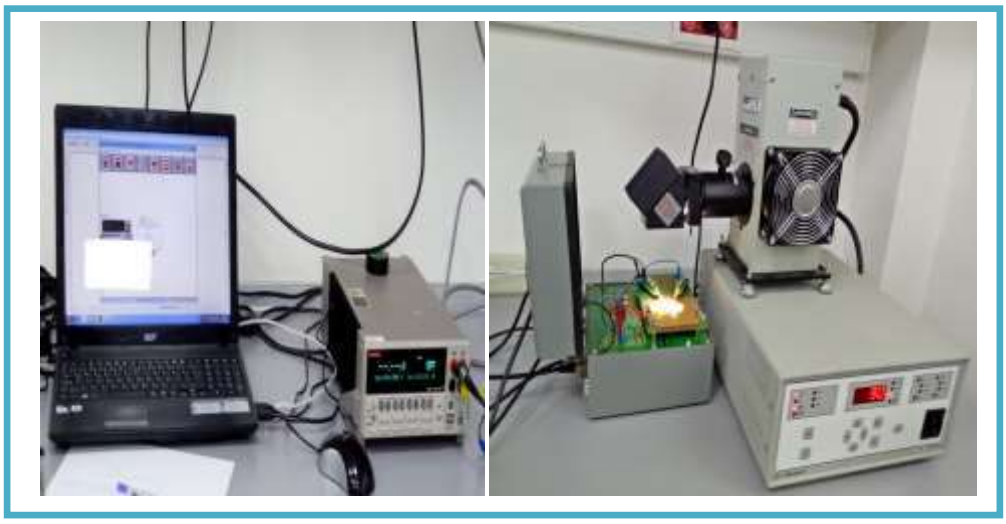

Figure IV.18: *I-V measurement system under illumination*

Figure IV.19 (a), (b) present respectively, the cross section of a diode based on pure ZnO with a front and back contact of Al and the schematic diagram of a typical solar cell based on ZnO thin films.

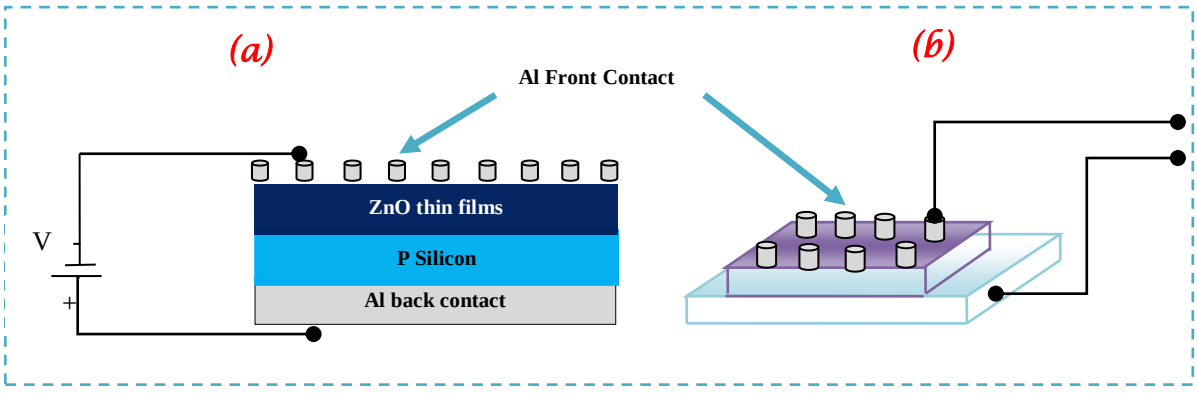

Figure IV.19: *(a) Cross section and (b) Schematic diagram of a typical ZnO based solar cell.*

IV. 2.3 Films structure

Figure IV.20 illustrated the X-Rays Diffraction pattern of ZnO thin film deposited by ultrasonic spray pyrolysis technique at p-Si for 5 min with 1 ml/min as flow rate and 400°C as substrate temperature. As shown in this Figure, the film shows a dominant diffraction peak for (002) plane indicates a high degree of orientation with the c-axis which means that the structure is hexagonal wurtzite. The diffracted peaks with 2θ equal to 30.79, 34.25, and 57.39° assigned to (100), (002), and (110) according to JCPDS: 36-1451. So the ZnO film prepared is polycristalline with preferential growth of crystallites along the c-axis orientation.

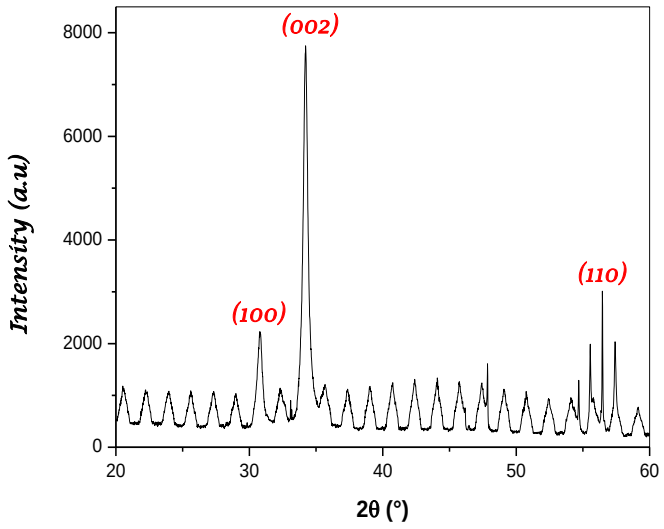

Figure IV.20: *XRD pattern of ZnO thin films deposited at p-Si*

IV.2.4 SEM images

The surface morphology of ZnO film at p-Si is analyzed by SEM and presented in Figure IV.21. As can be seen the film is porous and discontinuous structure with inhomogeneous distribution of rock on the full substrate surface.

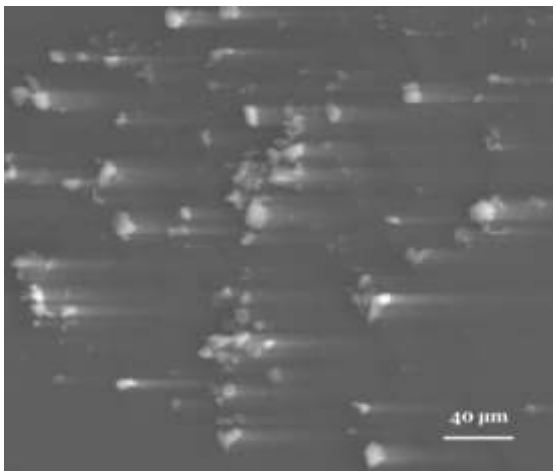

Figure IV.21: *SEM images of ZnO films deposited at p-Si*

IV.2.5 EDS analysis

The chemical composition of ZnO thin films was investigated by EDX analysis. Figure IV.22 depicts the typical EDX spectrum taken from ZnO film grown on a silicon substrate at 400°C. The chemical analysis of the prepared film measured by EDX analysis shows that only Zn, O and Si signals have been detected, which indicated that ZnO film are indeed made up of Zn and O and also the presence of Si element in the spectrum originated from the silicon substrate. The EDS analysis confirms the chemical composition of pure ZnO phase. This result was in well agreement with those found by XRD analysis.

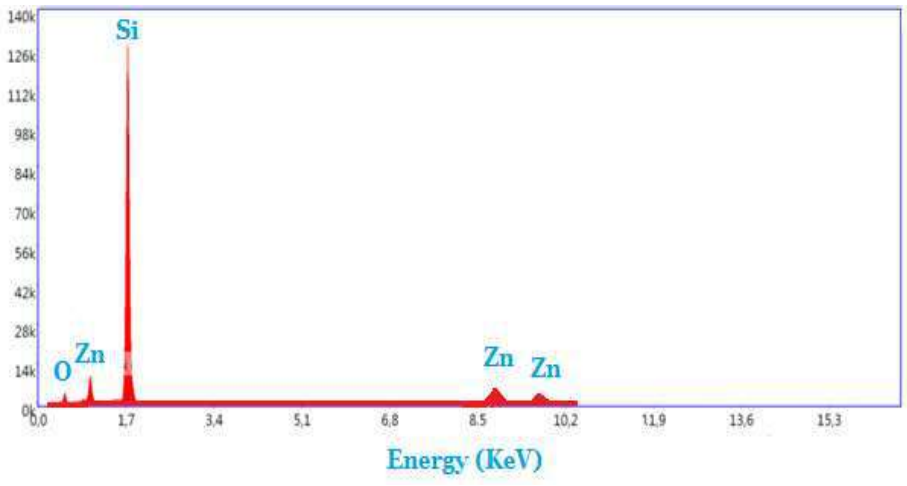

Figure III.22: *Typical EDS spectra for ZnO thin film deposited at p-Si*

IV.2.6 Optical properties

In Figure IV.23, it is reported that the variation of the optical transmittance spectra as a function of the wavelength in the UV, visible range of the undoped ZnO film deposited at soda lime glass for 5 min and 400°C. The film exhibit very high transparency (~ 91%) in the visible region 400-800 nm with a very sharp absorption edge located at about 380 nm wavelength which corresponds to the intrinsic band-gap of ZnO (3.2 eV). Our film is more transparency than ZnO films deposited at 400°C which found their transmission is only 81% [84].

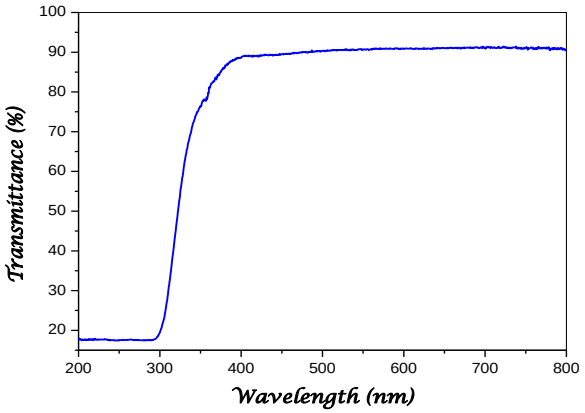

Figure IV.23: *Transmittance spectra of ZnO thin films deposited at 400°C.*

IV.2.7 Analysis of the Al / ZnO/ p-Si heterojunctions

IV.2.7.1 Current-Voltage characteristic (I-V)

The current–voltage (I–V) measurements have been used to extract electrical parameters of Schottky diode. The experimental I–V curves could be analyzed on the basis of conventional thermionic emission model. Figure IV.24 shows the semi-logarithmic I–V characteristics of the Al/ZnO/p-Si/Al diode under dark and various illumination intensities. It is clear from this figure that the diode exhibited an illumination sensitive behavior. It was found that the reverse current increases with illumination intensity for a given reverse voltage and is higher than the dark current. This indicates that the diode exhibits a photodiode behavior. When a photon of sufficient energy strikes the diode, it creates an electron–hole pair. The free carriers generated by photons can lead to an increase in reverse current depending on the number of generated electron– hole pairs [70–74]. Also, the forward current of the diode deviates from the linear I–V behavior which could be due to presence of series resistance and interface states [75–79].

Besides, the voltage values deviated from zero volts with increasing light intensity confirms that the produced diode shows photovoltaic behavior. The device exhibited rectification property, and the rectification ratio were calculated from the ratio of the forward-biased current (at +2 V) to the reverse-biased current (at - 2 V). The ratio RR was found 8.75×10^2.

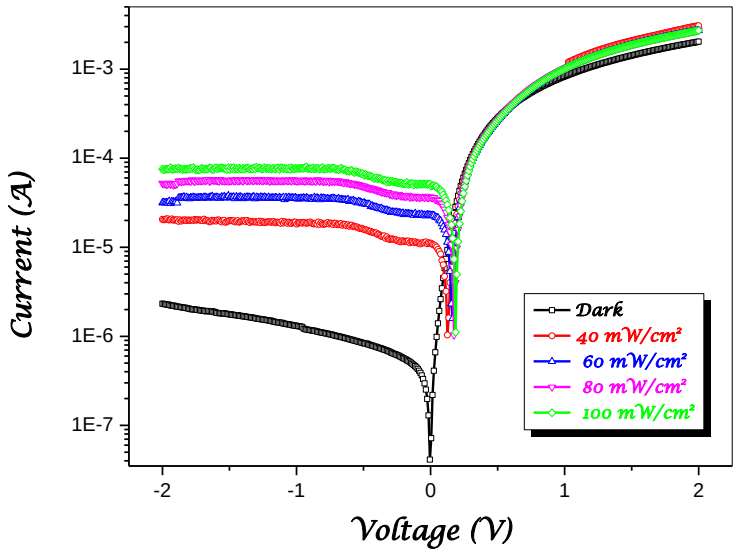

Figure IV.24: *The semi-logarithmic I–V characteristics of Al/ZnO/p-Si/Al diode under dark and various illumination intensities*

According to the simple theory of thermionic emission TE model, the I–V characteristics are given by the relation [80]:

$$I = I_0 \left[e^{\left(\frac{q(V - IR_S)}{n\,KT} \right)} \right] \qquad \text{(IV.1)}$$

Where R_s is the series resistance and n is the dimensionless ideality factor and I_0 is the saturation current and defined as:

$$I_0 = A\,A^{*} \left[e^{\left(\frac{-q\Phi_b}{KT} \right)} \right] \qquad \text{(IV.2)}$$

Herein q is the electronic charge, V is the applied voltage, k is the Boltzmann constant, T is the ambient temperature in Kelvin. A is the effective contact area ($5.024 \times 10^{-3} cm^{-2}$), ϕ_b is the energy barrier of diode (at V = 0), A * is the Richardson constant and is equal to 32 and 110 A cm^{-2} K^2 for p-Si and n-Si, respectively [81] and n is a dimensionless ideality factor, which

were determined from the slope of the linear region of Ln I–V plots using the following expression:

$$n = \frac{q}{kT}\frac{dV}{d\ln(I)} \quad \text{(IV.3)}$$

If the ideality factor n is greater than unity, this implies the deviation of the ideal diode. If n = 2, the recombination current dominates; if n = 1, the diffusion current dominates.

The current conduction mechanism and the capacitance behavior at the interface have been controlled by the barrier height. Furthermore, inorganic interface layer allows us to modify and, control the magnitude of barrier height, and it has been expressed as:

$$\Phi_b = \frac{kT}{n}\ln\left(\frac{AA^*T^2}{I_0}\right) \quad \text{(IV.4)}$$

The calculated value of ideality factor n of our Schottky diode Al/ ZnO /p-Si was found 1.39. S. Baturay et al. [82] fabricated heterojunctions based on ZnO pure and doped 1%, 3% and 5% Gd thin films deposited on p-Si by spin coating method. They indicate that ideality factor of the ZnO/p-Si heterojunction was 2.01. F. Yakuphanoglu et al. [83] formed heterojunctions with undoped and B-doped nanostructure ZnO films on p-Si prepared by sol-gel method using spin coating technique. The ideality factor n values of the undoped, 0.1% B-doped and 0.3% B-doped ZnO diodes are given as 2.53, 2.36 and 2.17 respectively. Also they assigned that the reasons for the n values exceeding unity can be: the presence of insulation layer, image force, charges trapped in surface states and series resistance. The higher series resistance causes a downward curvature in the I-V characteristics of the diodes at higher forward bias values.

The barrier height ϕ_b for our heterojunction ZnO/p-Si is ~ 0.67 eV from Ln I-V measurement. Similarly, N. Zebbar et al. [84] reported heterojunctions formed with undoped ZnO and In-doped ZnO thin films on p-Si substrates by ultrasonic spray method on p-Si substrates (100) at varied substrate temperatures from 200 to 400°C. They found from the I-V measurements, the ϕ_b value is about 0.65 eV for different substrate temperatures.

Alyamani et al. [85] prepared (3% at.) Al doped ZnO thin films deposited by PLD in order to fabricate Au/AZnO/p-Si/Al. The barrier height and ideality factor values of the diode were found to vary in the range of 0.71–0.64 and 1.78–2.86 eV, respectively. This behavior of n is

attributed to the presence of thin film layer, inhomogeneities of the barrier height, interface states and series resistance [75-79, 86–88].

Table IV.3: *Electrical parameters obtained from I-V measurements for the diode Al/ZnO/p-Si*

Diode	Ln I-V		Norde			
	n	ϕ_b (eV)	V_0	$F(V_0)$ (V)	ϕ_b (eV)	R_s (kΩ)
Al/ZnO/p-Si	1.35	0.67	0.1454	0.6421	0.69	1.194

In addition, the electrical parameter of the rectification structure can be determined from the Norde function [89]:

$$F(V) = \frac{V}{\gamma} - \frac{kT}{q} \ln\left(\frac{I(V)}{AA^* T^2}\right) \quad \text{(IV.5)}$$

Where I (V) is the current obtained from the I–V curve and γ is the first integer greater than n. In our study γ was taken as 2. Figure IV.25 presents the curve F (V) versus V of Schottky diode Al/ ZnO /p-Si at room temperature and in dark. The computed value of F (V_0) and V_0 are 0.6421 and 0.1454 V respectively.

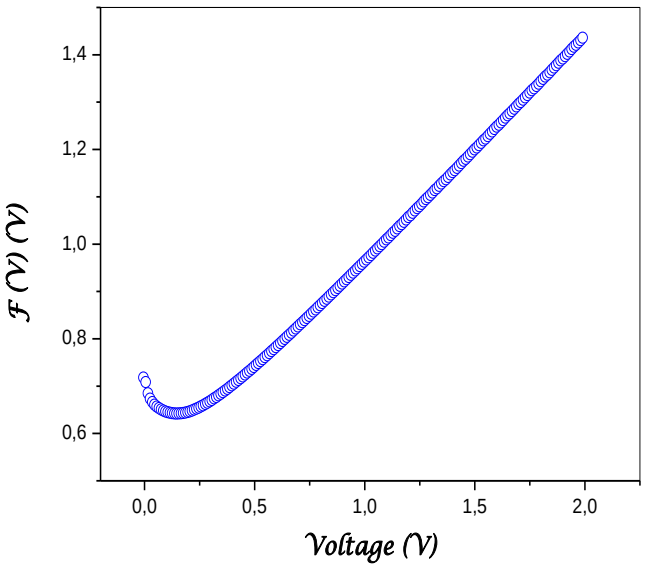

Figure IV.25: *F (V) as a function of V of Al/ZnO/p-Si heterojunction*

The barrier height of this diode Al/ ZnO /p-Si was expressed by:

$$\Phi_b = F(V_0) + \frac{V_0}{\gamma} - \frac{kT}{q} \quad \text{(IV.6)}$$

Here F (V_0) is the minimum value of F (V) and V_0 is the corresponding voltage value. The series resistance R_s also can be computed by Norde's function as the following:

$$R_s = \frac{kT(\gamma - n)}{q\, I_{min}} \quad \text{(IV.7)}$$

Where I_{min} is the corresponding current at V_0. The estimated values of the barrier height and the series resistance of the studied heterojunction by Norde's function are found 0.69 eV and 1194 Ω, respectively. The values of barrier height ϕ_b obtained from Ln (I-V) measurement and Norde function are in good agreement.

The fundamental solar cell parameters such as short circuit current I_{SC}, open circuit voltage V_{OC} were determined for the heterojunction based on ZnO with various incident light power, and given in the Table IV.4. The light sensitivity of the device at -2 V was extracted. As seen in Table IV.4, the values of estimated parameters of heterojunction are not suitable for the solar cell application, but it is good enough for photodiode, optical sensor application [92].

Table IV.4: *The values of V_{OC}, I_{SC} and light sensitivity under various illumination intensities for Al/ZnO/p-Si structure*

Illuminations **mW/cm^2**	***Light Sensitivity (times)***	***I_{sc} (μA)***	***V_{oc} (mV)***
40	13.78	11.12	125.33
60	08.78	22.82	155.82
80	22.44	36.27	175.16
100	32.05	50.73	185.55

IV.2.7.2 Photoresponsivity of diode

For further assessment about the photoresponsivity of fabricated heterojunction with various light powers, the relation can be expressed [93];

$$R = I_{PH} / L.S \qquad (IV.9)$$

Where, S is the illuminated area. The estimated values of R were given in Table IV.5. As seen in the table, these values are exponentially dependent on the illumination power. This confirms that the enhancement in the responsivity of the heterojunction with the illumination power is resulted in the generated free carriers by the absorption of the incident photons' energy. As observed from the Table IV.5, the values of responsivity for the studied heterojunction based on ZnO are higher than that of device reported in the reference [94]. According to the results of the heterojunction, it can be possible to use the innovative fabrication process for the improvement of the photovoltaic parameters in solar cells, and dye sensitized solar cell devices.

Table IV.5: *The values of R under various illumination intensities for Al/ZnO/p-Si structure.*

Illuminations (mW/cm^2)	*Photoresponsivity R (A/W) (x10^{-5})*
40	2.92
60	2.98
80	3.71
100	4.28

IV.2.7.3 Photosensing of light

The transient photocurrent-time measurements are a well known technique for the analysis of photoconducting mechanism. Figure IV.26 exhibits the linear and semilogarithmic plots of photocurrent of Al/ZnO/p-Si/Al diode with various illumination intensities at -2 V. As seen in Figure IV.26, the photocurrent of the diode increases rapidly up to certain level with switching on of the illumination and then, it comes back to initial level with switching off. The increase in photocurrent is due to the number of photogenerated charge carries in the

depletion region of the diode. The decrease in photocurrent is due to the trapping of the charge carriers in the deep levels; thus coming back to its initial state [95–100].

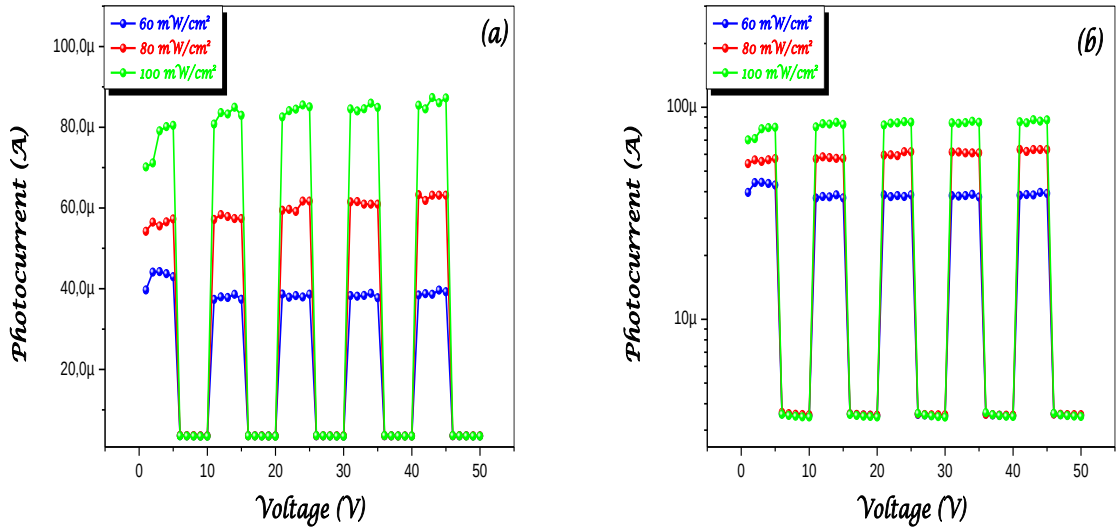

Figure IV.26: *Transient photocurrent-time of Al/ZnO/p-Si at various illumination intensities and -2 V: (a) linear and (b) semilogarithmic*

According to Figure IV.26 and Table IV.6 of this diode Al /ZnO/p-Si, the transient photocurrent of the device enhances after exposing to the light, which indicates an increment in the number of generated free carriers with the illuminating. Also, the magnitudes of the photocurrent at every I_{on}/I_{off} cycle are steady and reproducible. The ratio of I_{on}/I_{off} of the different devices has been given in Table IV.6 for the different illumination intensities from 60 mW / cm^2 to 100 mW / cm^2. The ratio I_{on}/I_{off} increases with increasing illumination. This means that this diode has significant photodetection by light. The diode exhibits photovoltaic behavior which is expressed by the photoresponse. This study further suggests that the fabricated device has photoconducting behavior and could be used as photosensor.

Many works indicate the photosensing of light by several diodes. The ratio I_{on}/I_{off} of the n-Si/SiO_2/ MEH-PPV/Al has been determined as ~ 35 by Yakuphanoglu [101]. NiO/p-Si and 0.2%Cu-NiO/p-Si photodiodes were fabricated by Gupta et al. [102] and evaluated the ratio of I_{on}/I_{off} under the illumination of 100 mW/cm^2 as 50.2 and 518, respectively. They reported the optimum Cu doping for NiO is 0.2% to improve the photoresponse property. Gencer et al. [103] have studied the photosensing properties of Al/ DMY /p-Si and the variation of the ratio I_{on}/I_{off} with illumination intensities. They indicated that the ratio is 6.89,

42.7 and 102.1 and 56.81, 640, 0 and 976.4 under intensity of 100 mW/cm^2 for D3, D2 and D1, respectively.

Table IV.6: *The ratio of I_{on}/I_{off} under different light intensity for Al/ZnO/p-Si structure*

Illuminations (mW/cm^2)	*Ratio I_{on} /I_{off}*
60	10.89
80	17.41
100	24.61

IV.2.7.4 Capacitance and Conductance measurement

Another important analysis is capacitance (*C-V*) and conductance (*G-V*) measurements at high and low frequencies to characterize of device. The capacitance and conductance of heterojunction concern about the diffusion capacitance and depletion capacitance. The capacitance-frequency measurement was carried out using an HP 4294A IMPEDANCE ANALYZER apparatus from Agilent Technologies, Santa Clara, California, United States (40 Hz-110 MHz) as shown in Figure IV.27.

Figure IV.27: *The C-V characterization device*

The frequency dependent *C-V* and *G-V* plots of heterojunction are presented in Figure IV.28 (a -b) in the range from 100 kHz to 3 MHz. As seen in the Figure IV.28 (a), the capacitance of studied structure changed with both; applied voltage and frequency. The value of capacitance is very close to each other at reverse bias regime under various frequencies. For the forward bias region, there is a peak related to the interface states. The maximum value of that peak decreases with the increasing in frequency. Because, at sufficiently high frequency, these charges have not enough sensitive to the AC signal, resulted in the decrease at the capacitance value [104].

Figure IV.28 (b) shows the effect of voltage on the conductance of the Zinc oxide/silicon junction at different applied frequencies. It is observed that the conductance of the Zinc oxide /silicon junction depends on voltage and frequency. As seen in Figure IV.28 (b), the conductance of the diode is almost constant in the reverse bias regime, while it increases at the forward bias with the increasing the frequency. Similar results have been presented for Al/Alq3/p-Si Schottky diode by Farag et al. [105].

As stated above the fabricated diode shows a non-ideal behavior which may be due to the series resistance, density of the interface states and the formation of insulator layer between the metal and semiconductor [106].

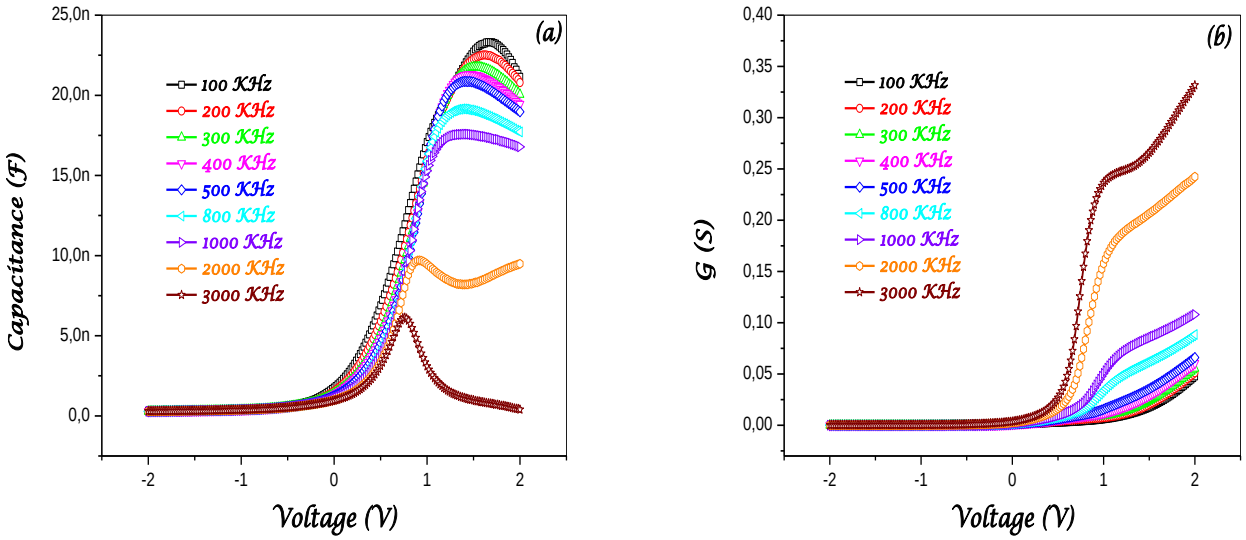

Figure IV.28: *C–V and G–V characteristics of the Al/ZnO /p-Si/Al diode at various frequencies.*

The depletion region of capacitance of device is given by [107]:

$$\frac{1}{C^2} = \frac{2\,(V_{bi}+V)}{q\,\varepsilon_s\,\varepsilon_0\,A^2\,N_a} \qquad \text{(IV.14)}$$

Here ε_S is dielectric constant of semiconductor (= 11.7 for Si), ε_0 is dielectric constant of free space, A is the effective area of diode, N_a is concentration of ionized acceptors and V_{bi} is the built in potential.

Figure IV.29 shows the variation of C^{-2} as a function of the voltage V for the diode Al/ZnO/p-Si with different frequency from 100 kHz to 3 MHz. As can be seen, all plots of C^{-2}-V for this device are similar. From these curves, we can calculate the different electrical parameters such as N_a, ϕ_b, V_{bi} and Fermi energy E_f. The concentration of ionized acceptors N_a and the built in potential V_{bi} were determined by the slope and extrapolation of linear reverse bias C^{-2}-V plot to the V axis, respectively, as shown in Figure IV.29. The results of all these parameters are given in Table IV.7.

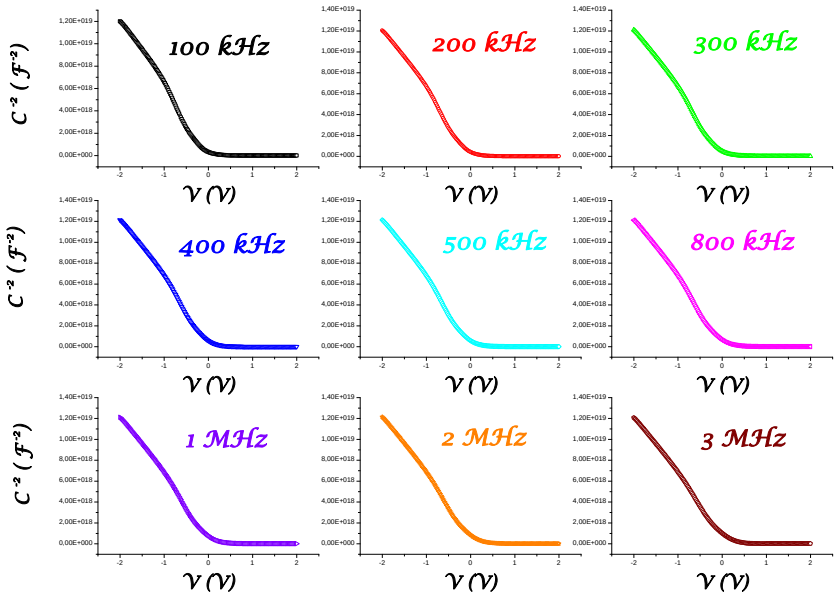

Figure IV.29: *C^{-2}-V for various frequencies of Al/ZnO /p-Si structure*

The barrier height value from C-V measurement is calculated by mean of the following relation:

$$\Phi_{b/(C-V)} = V_{bi} + kT \ln(\frac{N_a}{N_v}) \quad \text{(IV.10)}$$

Herein, N_v is the density of states in the valence band. The computed values of $\phi_{b\ /(C\text{-}V)}$ of the device is listed in Table IV.7.

E_f is the energy difference between the bulk Fermi level and conduction band edge, and is given by [108, 109]:

$$E_f = \frac{kT}{q} \ln(\frac{N_v}{N_a}) \quad \text{(IV.11)}$$

As observed from Table IV.7, the concentration of ionized acceptors, the barrier height and the built in potential of Al/ ZnO /p-Si heterojunction increase with the increasing frequencies and the high values of N_a, ϕ_b and V_{bi} were indicated for the high frequency 3 MHz.
However the value of Fermi energy is approximately the same.
It is noteworthy that the value ϕ_b (0.53 eV) obtained from C – V measurement is less than ϕ_b value (0.67 eV) obtained from I – V measurement. This is ascribed to the inhomogeneities such as non-uniformity of the interfacial layer thickness and distributions of the interfacial charges [110]. The higher effective barrier heights are related with small and then close to unity ideality factors.
Divya et al. [111] reported that the computed parameters such as concentration of ionized acceptors, the built in potential and the barrier height from $1/C^2$ for ZnO nanowires (NWs)/p-Si heterojunction are 1.54 x10^{15} cm^{-3}, V_{bi} ~ 0.55 V and ϕ_b ~ 0.75 eV, respectively, for 1 MHz at room temperature.

Table IV.7: *Electrical parameters calculated from C - V measurements of the Al / ZnO /p-Si diode at different frequencies.*

Frequency	Donor concentration N_a x10^{15} (cm^{-3})	Barrier height ϕ_b (eV)	Built-in-potential V_{bi} (V)	Fermi Energy E_f (eV)
100 *kHz*	7.371	0.471	0.272	0.199
200 *kHz*	7.338	0.488	0.290	0.199
300 *kHz*	7.099	0.487	0.287	0.200
400 *kHz*	7.113	0.495	0.295	0.200
500 *kHz*	7.129	0.499	0.299	0.200
800 *kHz*	7.172	0.510	0.311	0.199
1 MHz	7.186	0.518	0.319	0.199
2 MHz	7.257	0.528	0.329	0.199
3 MHz	7.325	0.529	0.330	0.199

IV.2.7.5 Series Resistance of diode

The series resistance (R_s) is a considerable parameter causing deviation from ideal diode behavior. Furthermore, the series resistance profile is important to understand the charge transport mechanism. The R_s can be determined using conductance method developed by Nicollian and Goetzberger [112].

According to this method, the R_s of Schottky diode Al/ ZnO /p-Si/Al by the C-V measurement is expressed by the following equation:

$$R_s = \frac{G_{ma}}{G_{ma}^2 + (\omega C_{ma})^2} \qquad \text{(IV.15)}$$

Where C_{ma} is the measured capacitance and G_{ma} is the measured conductance of the diode from C-V measurement.

Figure IV.30 shows the variation of the series resistance of the Al/ZnO/p-Si/Al Schottky diode with applied bias and different frequencies 100-3000 kHz. It is observed that the R_s–V plots have a peak and there is a small shift in the peak position of the Al/ZnO/p-Si/Al diode towards lower positive bias voltage with increase in the frequency. The peaks intensity of the series resistance for 100 kHz is so higher than that of the 1 MHz. Thereby, the peaks intensity of the series resistance decreases with increasing frequency. This behavior indicates that the interface states change with frequency. The high value of series resistance at low frequencies is evoked to the interface states can follow the AC signal and yield an excess capacitance at low frequency. Whereas at higher frequencies, the low series resistance is explained, as the interface states cannot follow the AC signal and do not make a contribution to capacitance [113]. The presence of the peak in every plot of R_s is due to the interface states [114].

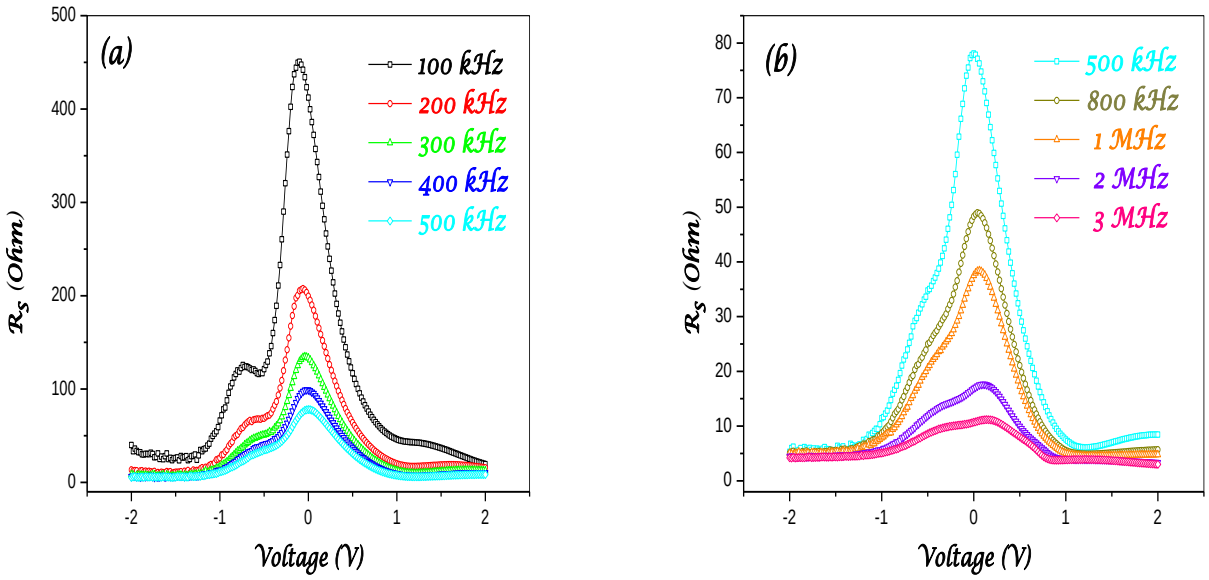

Figure IV.30: *Characteristics R_S - V of the diode Al / ZnO /p-Si: (a); 100 - 500 kHz and (b) 500 kHz – 3 MHz*

The similar behavior of R_s was reported by Gunduz et al. [114]. They fabricated Al/$NiAl_2O_4$/p-Si/Al as new Schottky diode spinel using the sol–gel spin coating approach. They indicated that R_s was high at low frequency and decreases with high frequency and the peaks intensity of the series resistance for 1 kHz is higher than that of the 1 MHz.

Mekki et al. [115] were prepared the Au/GO: coumarin /p- Si/Al diodes by sol–gel spin coating method. They found that the R_s plots exhibit peaks which shift towards the lower

positive bias voltage with decreasing frequency, suggesting that the interface states depend strongly on frequency. The high value of series resistance at low frequencies can be explained on the basis that the interface states can follow the AC signal thereby exhibiting excess capacitance at low frequencies [116, 117].


Conclusion

Conclusion

The main goal of this thesis is the preparation, characterization of zinc oxide with different shapes and morphologies and their applications in various field such as photodegradation of organic dyes, antibacterial activity and solar cells.

The ZnO thin films were deposited by spray pyrolysis (Syringe pump, Pneumatic and Ultrasonic) with various precursors in order to investigate the photocatalysis activity of Red dye polluant. Several parameters could influenced the photodegradation efficiency of organic dye as well as dye concentration, deposition time of films, the precursor's salt nature and the inclusion of gold nanoparticles on ZnO films.

According to the variation of dye concentration of Red Reactive 184, the concentration 2.10^{-5} mol/l of RR-184 by zinc chloride thin films with 0.1 M which prepared via pneumatic spray at 350°C, a flow rate of 100 µl/ min and 5 min as deposition time, the ratio C/C_0 of this polluant is reduced to reach the maximum 0.8 after 300 min of irradiation times. So the photodegradation (~ 20 %) is significant when the solution is on contact with ZnO photocatalyst.

The influence of deposition time on the films properties and photodegradation of organic dye was also checked. The same elaboration conditions (0.1 M of Zinc Chloride, 100 µl /mn and 350°C) were used to prepare ZnO thin films by Syringe pump with 5 min (Film A) and 10 min (Film B). The photodegradation efficiency of Red dye with a concentration of 10^{-5} mol/l by films A and B, respectively, was found 25 % and 2% after 180 minutes of irradiation time. The discrepancy in the photocatalysis activity of both films A and B may found explication in the difference between their microstructure.

Another investigation was done about the effect of ZnO precursor's salt nature on photocatalytic activity. By spray technique several Zn salts have been deposited with the same previous parameters conditions. The photocatalysis activity of ZnO thin films with several precursors were studied by the degradation of Red dye with a concentration of 4 $x10^{-6}$ mol/ l and volume of 75 ml. The degradation efficiency was considerable for zinc nitrate films during 240 minutes of UV light exposure. Consequently, the starting salt source nature and the morphology of the Zn salt play an important role on the photocatalytic activity of this organic dye.

We have also investigated the effect of gold nanoparticles on photocatalysis activity through the incorporation of 2.5 %, 10 % and 30 % in zinc acetate thin films deposited by spray ultrasonic with 7 ml/h at 350°C and 5 min. The ratio C/C_0 of ZnO: 0% Au NPs, ZnO: 10% Au and ZnO: 30% Au NPs is reduced with increasing exposure time; it reaches 0.99, 0.72 and 0.92 during 360 minutes of irradiation. We conclude that the photodegradation is more important when using of ZnO films included 10% Au NPs.

The influence of ZnO Nanostructured has also tested for the photodegradation of Methylene Blue. ZnO nanorods were growing on seed layers of ZnO with various precursors by hydrothermal process at 120°C for 3 h as a growth time. We noted that the absorbance value decreased swiftly for all ZnO nanostructures at the characteristic peak location (654 nm) of Methylene Blue, and was very close to zero after 420 min irradiation for ZnO nanorods obtained by Zinc acetate films. The ratio C / C_0 represents a quickly photodegradation of samples. The last sampling point, after 420 min of kinetics, showed us that the photocatalytic performance of ZnO nanorods (74% for acetate) give the best photocatalyst. However, the photodegradation efficiency of zinc nitrate and zinc chloride NRs were 64% and 58%, respectively, and the rate k was varied from 18.2×10^{-4} to 28.1×10^{-4} min^{-1}.

Another effect of time deposition of ZnO nanostructured synthesis by hydrothermal process on the photocatalysis activity of Methylene Blue was investigated. ZnO nanorods were prepared with several growth times (3h, 5h and 8h) on seed layers with 100 nm thickness which deposited using RF magnetron sputtering. According to this survey, the photodegradation of MB is more significant when ZnO NRs deposited after 3 h are on contact with solution.

The influence of seed layer surface, with several positions (slanted, surface up and surface down), on the morphology of ZnO nanostructures (from Nanorods to Nanoflowers) and on the photocatalysis activity of Methylene Blue was reported. The photodegradation is very considerable when the solution of MB is in contact with ZnO nanoflowers then with ZnO nanorods that's indicating the successful reduction of ZnO nanoflowers. The highest photodegradation efficiency was reached 81 % for ZnO Nanoflowers with the larger rate constant K = 50.8 x 10-4 min-1 for 300 min irradiation time. However, 54 % and 66 % of MB was degraded by ZnO NRs 1 and ZnO NRs 2 during the same time of irradiation, respectively.

In the second part of our work, the antibacterial activity of ZnO thin films was tested against Gram negative of Klebsiellapneumoniae ATCC 700603 and Gram negative of Escherichia coli. The inhibition zone is found 0, 12,14 and 18 mm in diameter for reference, ZnO pure with 5 dipping, ZnO 5 % Ag NPs with 5 dipping and ZnO 10% Ag NPs with 5 dipping, respectively. The antibacterial activity of zinc oxide, which deposited by ultrasonic spray pyrolysis with different deposition times; 5, 15 and 30 min at 400°C to coater soda lime glasses, against gram negative of E. coli indicates that ZnO thin films with different thicknesses cannot eliminate the E. coli strain and there is no inhibition zone around all ZnO samples. Our findings are very encouraged and the use of zinc oxide as an agent is so exciting for killing bacteria, fungals and microbes.

The heterojunction ZnO/p-Si was prepared based on zinc nitrate thin film deposited by ultrasonic spray at p-type silicon (100). The front and back contact of this structure Al/ZnO/p-Si/Al was deposited trough the thermal evaporation system. The I-V measurement in dark shows that the diode has a rectification property with a ratio $8.75x10^2$. The ideality factor n and the barrier height ϕ_b for our heterojunction ZnO/p-Si is 1.39 and 0.67 eV from Ln I-V measurement. The calculated value of F (V_0) and V_0 are 0.6421 and 0.1454 V respectively. While, the barrier height and the series resistance calculated of the studied diode through Norde's function are found 0.69 eV 1194 Ω. The values of barrier height ϕ_b obtained from Ln (I-V) measurement and Norde function are in well agreement. The fundamental solar cell parameters I_{SC} and V_{OC} were determined to be 11.12- 50.73 µA and 125.33- 185.22 mV, respectively, for various illuminations from 40-100 mW/cm^2.

The enhancement in the responsivity of the diode Al/ZnO/p-Si/Al with the illumination power is resulted in the generated free carriers by the absorption of the incident photons' energy. The structure Al/ZnO/p-Si/Al has a photosensing property which is explained by the enhancement in photocurrent after exposing to light with various illuminations. This study further suggests that the fabricated device has photoconducting behavior and could be used as photodiode, photosensor applications and optoelectronics applications.

The capacitance and the conductance of the Zinc oxide /silicon junction depend on voltage and frequency. The effect of interfaces states on the total capacitance was reported. Several electrical parameters such as the concentration of ionized acceptors N_a, the barrier height ϕ_b and the built in potential V_{bi} of the Al/ ZnO /p-Si heterojunction are increased with

the increasing frequencies and the high values of N_a, ϕ_b and V_{bi} were registered for the high frequency 3 MHz. The series resistance of the Schottky diode Al/ZnO/p-Si/Al varied with applied bias and frequency from 100 kHz to 3MHz. The high value of series resistance at low frequencies and the low series resistance at higher frequencies are due to the interface states.

References

References Introduction

[1**]** Lu B., Ms Thesis: "Methylene Blue degradation in water using sol-gel made TiO_2 supported oxide photocatalysts", The Graduate School of Engineering and Sciences of Izmir Institute of Technology (2011).

[2] Nihalani S., Vijay A. and Bhardwaj S.," Use of a new nanosized photocatalyst $BaO_3TiO.SrO_3TiO_2$ for degradation of Azure B: An eco friendly process". Archives of Applied Science Research, 5 (6) (2013)103-108.

[3] Akpan U., Hameed B.," Parameters affecting the photocatalytic degradation of dyes using TiO_2 based photocatalysts" A review-. Journal of Hazardous Materials, 170 (2009) 520–529.

[4] Punjabi P., Ameta R., Kumar A. and Jain M., "Visible light induced photocatalytic degradation of some Xanthene dyes using immobilized Anthracene". Bull. Chem. Soc. Ethiop., 22(3) (2008) 361-368.

[5] Ramíreza R., Sánchezb V. Martínezc S.," Solar assisted degradation of acid orange 7 textile dye in aqueous solutions by Ce-doped TiO_2". Mexican Journal of Scientific Research, 1(1) (2012) 42-55.

[6] Puzyn T., "Organic Pollutants Ten Years After the Stockholm Convention", Environmental and Analytical Update (2012).

[7] Konstantinou I., Albanis T.,"TiO_2-assisted photocatalytic degradation of azo dyes in aqueous solution: kinetic and mechanistic investigations": A review. Applied Catalysis B: Environmental, 49 (2004) 1–14.

[8] Rajamohan N., "Equilibrium studies on sorption of an anionic dye onto acid activated water hyacinth roots". African Journal of Environmental Science and Technology, 3 (11) (2009) 399-404.

[9] Sharma V., Kakodia A., Sharma B., Pamecha S. and Khandelwal R., "Photocatalytic Degradation of Brilliant Blue-R by ZnO in Aqueous Media. IJGHC". 2 (3) (2013) 730-736.

[10] Hathway T., Ph. D thesis: "Titanium dioxide photocatalysis: studies of the degradation of organic molecules and characterization of photocatalysts using mechanistic organic chemistry" (2009).

[11] Rio J., PhD thesis: "Photocatalytic degradation of Phenolic compounds in water and kinetic modeling" (2011).

[12] Sathishkumar P., Pugazhenthirana N., Mangalarajab R., Asiri A., Anandana S., "ZnO supported $CoFe_2O_4$ nanophotocatalysts for the mineralization of Direct Blue 71 in aqueous environments". Journal of Hazardous Materials, 252– 253 (2013) 171– 179.

[13] http://www.loc.gov/pictures/item/2006679062/Reproduction Number: LC-USZ62-51233).

[14] K. Kotloff, J. Winickoff, B. Ivanoff, J.D. Clemens, D. Swerdlow, P. Sansonetti, G. Adak, M. Levine, Global burden of Shigella infections: implications for vaccine development and implementation of control strategies. Bull. World Health Organ 77(8), 651–666 (1999)

[15] Dubas, S.T., Kumlangdudsana, P. and Potiyaraj, P. Colloids and Surfaces A: Physicochemical and Engineering Aspects, 289, p. 105 (2006).

[16] Kulpinski, P. e-Polymers art.no.068, (2007).

[17] Lee, H.Y., Park, H.K., Lee, Y.M., Kim, K., et al. Chem. Commun., 15, p. 2959 (2007).

[18] Snouqiang, J., Newton, E., Chun-Wah Marcus, Y. and Chi-Wai, K. Textile Research Journal, 77, p. 85 (2007).

[19] Yang, C., Liang, G., Xu, K., Gao, P., et al. Journal of Materials Science, 44, p. 1894 (2009).

[20] Morones, J.R., Elechiguerra, J.L., Camacho, A., Holt, K., et al. Nanotechnology, 16, p. 2346 (2005).

[21] Singh, M., Singh, S., Prasada, S. and Gambhir, I.S. Digest Journal of Nanomaterials and Biostructures 3, p. 115 (2008).

[22] Bosman, A.W., Janssen, H.M. and Meijer, E.W. Chemical Reviews, 99, p. 1665 (1999).

[23] Kobayashi, H., Kogetsu, Y., Ishida, T., and Nakato, Y., 1993, Increases in photovoltage of ‘‘indium tin oxide/silicon oxide/mat-textured n-silicon’’ junction solar cells by silicon preoxidation and annealing processes. J. Appl. Phys, 74, 4756.

References Chapter I

[1] G. Crini, Non-conventional low-cost adsorbents for dye removal: a review, Bioresource Technology, 97 (2006) 1061-1085.

[2] V. Gupta, Application of low-cost adsorbents for dye removal–A review, Journal of environmental management, 90 (2009) 2313-2342.

[3] L. El Mostapha, Analyse de la corrélation entre structure et propriétés ferroélectriques de phases non stoechiométriques isolés au voisinage de $LiTaO_3$ au sein des diagrammes ternaires Li_2O-Ta_2O_5-$(CuO)_2$ et Li_2O-Ta_2O_5-$(WO_3)_2$, Mohammed V University in Rabat Morocco (2007).

[4] N. Shaham-Waldmann, Y. Paz, Away from TiO_2: A critical minireview on the developing of new photocatalysts for degradation of contaminants in water, Materials Science in Semiconductor Processing, 42 (2016) 72-80.

[5] E. Kaldis, Current Topics in Materials Science. Vol. 1, North-Holland Publishing Co, (1978) 770.

[6] J. Ravez, A. Simon, Lead-free ferroelectric relaxor ceramics derived from $BaTiO_3$, The European Physical Journal Applied Physics, 11 (2000) 9-13.

[7] Fujishima, A.; Honda, K. Nature, 238 (1972) 37–38.

[8] D. S. Bhatkhande, V. G. Pangarkar and A. A. Beenackers, “Photocatalytic degradation for environmental applications–a review,” J. Chem. Technol. Biotechnol., 77 (2001) 102-116.

[9] Rasul A., Brown R. and Hashib M.," Influence of parameters on the heterogeneous photocatalytic degradation of pesticides and phenolic contaminants in wastewater: a short review". Journal of Environmental Management, 92 (3) (2011) 311-330.

[10] Baruah S., Pal S., Dutta J.," Nanostructured Zinc Oxide for Water Treatment. Nanoscience & Nanotechnology" 2 (2012) 90.

[11] Chen Ch., Liu J., Liu P. and Yu B.," Investigation of Photocatalytic Degradation of Methyl Orange by Using Nano-Sized ZnO Catalysts". Advances in Chemical Engineering and Science, 1 (2011) 9-14.

[12] Elamin N. and Elsanousi A., "Synthesis of ZnO Nanostructures and their Photocatalytic Activity". Journal of Applied and Industrial Sciences, 1 (1) (2013) 32-35.

[13] Umar M. and Abdul Aziz H.," Photocatalytic Degradation of Organic Pollutants in Water" (2013) 165-208

[14] Siuleiman S., Raichev D., Bojinova A., Dimitrov D. and Papazova K., "Nanosized composite ZnO/TiO_2 thin films for photocatalytic applications" Bulgarian Chemical Communications (orange II), 45 (4) (2013) 649–654.

[15] Mehra M. and Sharma R., "Photo catalytic degradation of two commercial dyes in aqueous phase using photo catalyst TiO_2". Advances in Applied Science Research, 3 (2) (2012) 849-853.

[16] Ameta A., Ameta R. and Ahuja M., "Photocataytic degradation of mythelene blue over ferric tungstate". Sci. Revs. Chem. Commun., 3 (3) (2013) 172-180.

[17] Lu B., Ms Thesis:" Methylene Blue degradation in water using sol-gel made TiO_2 supported oxide photocatalysts" The Graduate School of Engineering and Sciences of Izmir Institute of Technology (2011).

[18**]** S. Banerjee, J. Gopal, P. Muraleedharan, A. K. Tyagi and B. Raj, "Physics and chemistry of photocatalytic titanium dioxide: Visualization of bactericidal activity using atomic force microscopy," Current Science, vol. 90, 2006, pp. 1378-1383.

[19] T. Sato, K. Masaki, K. Sato, Y. Fujishiro and A. Okuwaki, "Photocatalytic properties of layered hydrous titanium oxide/ CdS-ZnS nanocomposites incorporating CdS-ZnS into the interlayer," J. Chem. Tech. Biotechnol., 67 (1996) 339-344.

[20] Ibhadon A. and Fitzpatrick P.," Heterogeneous Photocatalysis: Recent Advances and Applications". Catalysts (2013) 2073-4344.

[21] Meng Zh. and Juan Zh.," Wastewater treatment by photocatalytic oxidation of Nano-ZnO", Global Environmental Policy, 12 (2008) 1-9.

[22] Curria M., Comparellib R., Cozzolib P., Mascoloc G. and Agostianoa A., "Colloidal oxide nanoparticles for the photocatalytic degradation of organic dye". Materials Science and Engineering C 23, (2003) 285–289.

[23] Wahi R., Yu W., Liu Y., Mejia M., Falkner J., Nolte W. and Colvin V., "Photodegradation of Congo Red catalyzed by nanosized TiO_2". Journal of Molecular Catalysis A: Chemical, 242 (2005) 48–56.

[24] Meng Z. and Juan Z., "Wastewater treatment by photocatalytic oxidation of Nano-ZnO". Global Environmental Policy in Japan (12) (2008) 1-9.

[25] W. Shangguan,"Hydrogen evolution from water splitting on nanocomposite photocatalysts," Science and Technology of Advanced Materials, 8 (2007) 76–81.

[26] J. S. Dalton, P. A. Janes, N. G. Jones, J. A. Nicholson, K. R. Hallam and G. C. Allen, "Photocatalytic oxidation of NOx gases using TiO_2: a surface spectroscopic approach," Environmental Pollution, 120 (2002) 415–422.

[27] F. Zhang, R. Jin, J. Chen, C. Shao, W. Gao, L. Li, and N. Guan, "High photocatalytic activity and selectivity for nitrogen in nitrate reduction on Ag/TiO_2 catalyst with fine silver clusters," Journal of Catalysis, 232 (2005) 424–431.

[28] Linsebigler, A. L.; Lu, G.; Yates, J. T. Chem. Rev. 95 (3) (1995) 735–758.

[29] Hoffmann, M. R.; Martin, S. T.; Choi, W.; Bahnemannt, D. W. Chem. Rev. 95 (1) (1995**)** 69–96.

[30] Yu, P.; Cardona, M. Fundamentals of Semiconductors: Physics and Materials Properties; (1996).

[31] Rajeshwar, K. In Encyclopedia of electrochemistry (2001).

[32] Mills, A.; Le Hunte, S. J. Photochem. Photobiol. A Chem, 108 (1997) 1–35.

[33] Bard, A. Science (80-.) 207 (4427), 139–144.

[34] Bott, A. Curr. Sep., 3 (1998) 87–91.

[35] V. Subramanian, V. G. Pangarkar, A. A. C. M. Beenackers, "Photocatalytic degradation of para-hydroxybenzoic acid: Relationship between substrate adsorption and photocatalytic degradation," Clean Products and Processes, 2 (2000) 149-156.

[36**]** T. Noguchi, A. Fujishima, P. Sawunyama, and K. Hashimoto, "Photocatalytic degradation of gaseous formaldehyde using TiO_2 film," Environ. Sci. & Tech., 32 (23) (1998) 3831-3833.

[37**]** A. A. Yawalkar, D. S. Bhatkhande, V. G. Pangarkar and A. A ACM Beenackers, "Solar-assisted photochemical and photocatalytic degradation of phenol," J. of Chem. Technol. and Biotechnol., 76 (2001) 363-370.

[38**]** L. Yang, and Z. Liu, "Study on light intensity in the process of photocatalytic degradation of indoor gaseous formaldehyde for saving energy," Energy Conversion and Management, 48 (2007) 882-889.

[39**]** J. Theurich, M. Lindner, and D. W. Bahnemann, "Photocatalytic Degradation of 4-Chlorophenolin Aerated Aqueous Titanium Dioxide Suspensions: A Kinetic and Mechanistic Study," Langmuir, 12 (26) (1996) 6368-6376.

[40**]** S. Tanaka and U. K. Saha, "Effects of pH on photocatalysis of 2, 4, 6-trichlorophenol in aqueous TiO_2 suspensions," Water Science and Technology, 30 (9) (1994) 47–57.

[41**]** Y. Ku, R. Leu, and K. Lee, "Decomposition of 2-chlorophenol in aqueous solution by UV irradiation with the presence of titanium dioxide," Water Research, 30 (11) (1996) 2569-2578.

[42] I. M. Soganci, E. Mutlugun, S. Tek, I. O. Huyal, D. Yucel, G. Celiker, and H. V. Demir, "The critical role of nanoparticle size and spectral activation in the photocatalysis of titanium dioxide nanocomposites," submitted.

[43] S. Tek, E. Mutlugun, I. M. Soganci, N. K. Perkgoz, D. Yucel, G. Celiker, and H. V. Demir, "Comparative study of optically activated nanocomposites with photocatalytic TiO_2 and ZnO nanoparticles for massive environmental decontamination," J. Nanophoton.1 (2007).

[44] J. Yu, X. Zhao, and Q. Zhao, "Effect of surface structure on photocatalytic activity of TiO_2 thin films prepared by sol-gel method," Thin Solid Films, 379 (2000) 7-14.

[45**]** M. M. Caldwell, "Plant Life and Ultraviolet Radiation: Some Perspective in the History of the Earth's UV Climate," BioScience, 29 (9) (1979) 520-552.

[46**]** M. Sasaki, S. Takeshita, M. Sugiura, N. Sudo, Y. Miyake, Y. Furusawa and T. Sakata, "Ground-based observation of biologically active solar ultraviolet-B irradiance at 35 degrees N latitude in Japan," J. Geomagn. Geoelectr. (Japan), 45 (1993) 473-85.

[47**]** A. L. Stroyuk, A. I. Kryukov, S. Ya. Kuchmii, and V. D. Pokhodenko, "Quantum size effects in semiconductor photocatalysis," Theoretical and Experimental Chemistry, 41 (4) (2005) 207-228.

[48] S. Yanagida, T. Ogata, A. Shindo, H. Hosokawa, H. Mori, T. Sakata, and Y. Wada, "Semiconductor Photocatalysis: Size Control of Surface-Capped CdS Nanocrystallites and the Quantum Size Effect in Their Photocatalysis," Bull. Chem. Soc. Jpn., 68 (3) (1995) 752-758.

[49] A. L. Stroyuk, A. I. Kryukov, S. Ya. Kuchmii, and V. D. Pokhodenko, "Quantum size effects in the photonics of semiconductor nanoparticles," Theoretical and Experimental Chemistry, 41 (2) (2005) 67-91.

[50] Liu, G.; Wang, L.; Yang, H. G.; Cheng, H.-M.; (Max) Lu, G. Q. J. Mater. Chem. 20 (5) (2010) 831.

[51] Lam S., Sin J., Abdullah A., Mohamed A., "Degradation of wastewaters containing organic dyes photocatalysed by zinc oxide: a review". Desalination and Water Treatment, 41 (1-3) (2012) 131-169.

[52] A. Laplanche, La photocatalyse, une technique prometteuse en émergence, La revue trimestrielle du réseau Ecrin, N°60 (2005) 20-26.

References Chapter II

[1] Neeraj Mittal, Synthesis and photocatalytic studies of ZnO Nanoparticles, Master thesis (1997).

[2] Zhong Lin Wang, Zinc oxide nanostructures: growth, properties and applications, Journal of Physics: Condensed Matter, 16 (2004) R829- R858.

[3] Zhiyong Fan and Jia G. Lu, Zinc Oxide Nanostructures: Synthesis and Properties, Journal of Nanoscience and Nanotechnology. 5 (2005) (10) 1561-1573.

[4] S. Baruah and J Dutta, Hydrothermal growth of ZnO nanostructures, Sci. Technol. Adv. Mater, 10 (2009) (1).

[5] Hernandezbattez, A; Gonzalez, R; Viesca, J; Fernandez, J; Diazfernandez, J; MacHado, A; Chou, R; Riba, J; CuO, ZrO_2 and ZnO nanoparticles as antiwear additive in oil lubricants. (2008) 265.

[6] Porter, F, Zinc Handbook: Properties, Processing, and Use in Design, CRC Press. (1991).

[7] Dapeng Wu, Zhengyu Bai, Kai Jiang,Temperature induced hierarchical growth of ZnO microcrystal, Materials Letters. 63 (2009) 1057-1060.

[8] Chen, Z., Z. Shan, S. Li, C.B. Liang, and S.X. Mao. A novel and simple growth route towards ultra-fine ZnO nanowires. J. Cryst. Growth, 265 (2004) 482–486.

[9] Sekar, A., S. H. Kim, A. Umar, and Y. B. Hahn. Catalyst-free synthesis of ZnO nanowires on Si by oxidation of Zn powders. J. Cryst. Growth, 277 (2005) 471–478.

[10] Zhang, J., Y. Yang, B. Xu, F. Jiang, and J. Li. Shape-controlled synthesis of ZnO nano and micro-structures. J. Cryst. Growth, 280 (2005) 509–515.

[11] T. K. Subramanyam, B. Srinivasulu Naidu, S. Uthanna, Physical Properties of Zinc Oxide Films Prepared by DC Reactive Magnetron Sputtering at Different Sputtering Pressures, Cryst. Res. Technol, 35 (2000) (10) 1194-1202.

[12] Yang Liu, Jian-er Zhou, Andre Larbot , Michel Persin, Preparation and characterization of nano Zinc oxide, Journal of Materials Processing Technology. 189 (2007) 379–383.

[13] T. K. Subramanyam, B. Srinivasulu Naidu, S. Uthanna, Physical Properties of Zinc Oxide Films Prepared by dc Reactive Magnetron Sputtering at Different Sputtering Pressures, Cryst. Res. Technol. Vol. 35 (2000), pp. 1193–1202.

[14] Zhiyong Fan and Jia G. Lu, Zinc Oxide Nanostructures: Synthesis and Properties, Journal of Nanoscience and Nanotechnology. 5 (2005) (10) 1561-1573.

[15] Wang, Zhong Lin, Zinc oxide nanostructures: Growth, properties and applications, J. Phys.: Condens. Matter. 16 (2004) R829–R858.

[16] Zhong Lin Wang, Nanostructures of ZnO, Materials Today. 7 (2004) (6) 26-33.

[17] S. Music´, S. Popovic´, M. Maljkovic´, D. Dragc˘evic, Influence of synthesis procedure on the formation and properties of Zinc oxide. Journal of Alloys and Compounds. 347 (2002), 324–332.

[18] T. K. Subramanyam, B. Srinivasulu Naidu, S. Uthanna, Structure and Optical Properties of DC Reactive Magnetron Sputtered Zinc Oxide Films. Cryst. Res. Technol. 34 (1999), 981–988.

[19] Zhiyong Fan and Jia G. Lu, Zinc Oxide Nanostructures: Synthesis and Properties, Journal of Nanoscience and Nanotechnology. 5 (2005) (10) 1561-1573.

[20] T. K. Subramanyam, B. Srinivasulu Naidu, S. Uthanna, Physical Properties of Zinc Oxide Films Prepared by dc Reactive Magnetron Sputtering at Different Sputtering Pressures, Cryst. Res. Technol. 35 (2000) 1193–1202.

[21] Y. Q. Fu, J.K. Luo, X.Y. Du, A.J. Flewitt, Y. Li, G.H. Mark, A.J. Walton, W.I. Milne, Sensors and Actuators B, 143 (2010) 606–619.

[22] O. Hayden, R. Agarwal, W. Lu, 2008 Semiconductor Nanowire Devices, Nanotoday, 3, 12, 17480-1321

[23] P. J. Pauzauskie, P. Yang, 2006 Nanowire Photonics, Materials Today, 9, 36, 1369-7021

[24] P. Yang, R. Yan, M. Fardy, 2010 Semiconductor Nanowire: What's Next?, Nano letter, 10 152936

[25] W. Lu, C. M. Lieber, 2007 Nanoelectronics from the Bottom Up, Nat. Mater., 6 841850 1476-1122

[26] L. Cao, J. S. White, J. S. Park, J. A. Schuller, B. M. Clemens, M. L. Brongersma, 2009 Engineering Light Absorption in Semiconductor Nanowire Devices, Nat. Mat., 8 643647, 1476-1122

[27] R. E. Algra, M. A. Verheijen, M. T. Borgstrom, L. F. Feiner, G. Immink, W. J. P. van Enckevort, E. Vlieg, E. P. A. M. Bakkers, 2008, Nature, 456 369372, 0028-0836.

[28] Kehan Yu, Junhong Chen. Enhancing Solar Cell Efficiencies through 1-D Nanostructures. Nanoscale Res Lett (2009) 4:1–10.

[29] Basma EL ZEIN, PhD thesis “Growth and characterization of ZnO nanostructures for photovoltaic applications” (2012).
[30] Ü. Özgür, Y. I. Alivov, C. Liu, A. Teke, M. A. Reshchikov, S. Dogan, V. Avrutin, S. J. Cho, and H. Morkoc, “A comprehensive review of ZnO materials and devices,” J. Appl. Phys., vol. 98, 2005.
[31] A. F. Kohan, G. Ceder, D. Morgan, and C. G. Van de Walle, “First-principles study of native point defects in ZnO,” Phys. Rev. B, vol. 61, pp. 15019–15027, Jun 2000.
[32] A. Janotti and C. G. Van de Walle, “Native point defect in ZnO,” Phys. Rev. B, vol. 76, October 2007.
[33] C. G. Van de Walle, “Defect analysis and engineering in ZnO,” Physica B: Condensed Matter, vol. 308-310, pp. 899 – 903, 2001. International Conference on Defects in Semiconductors.
[34] J. I. Owen, Growth, Etching, and Stability of Sputtered ZnO: Al for Thin-Film Silicon Solar Cells, vol. 125. Forschungszentrum Jülich GmbH, 2011.
[35] C. G. Van de Walle, “Hydrogen as a Cause of Doping in Zinc Oxide,” Phys Rev Lett, vol. 85, pp. 1012–1015, Jul 2000.
[36] W. I. Park, D. H. Kim, S.-W. Jung, G.-C. Yi, Applied Physics Letters 80 (2002) 4232.
[37] M. H. Huang, S. Mao, H. Feick, H. Yan, Y. Wu, H. Kind, E. Weber, R. Russo, P. Yang,
Science 292 (2001) 1897.
[38] M. Zhao, Z. L. Wang, S. X. Mao, Nano Letters 4 (2004) 587.
[39] C. J. Lee, T. J. Lee, S. C. Lyu, Y. Zhang, H. Ruth, H. J. Lee, Applied Physics Letters, 81 (2002) 3648.
[40] E. Comini, G. Faglia, G. Sberveglieri, Z. W. Pan, Z. L. Wang, Applied Physics Letters 81 (2002) 1869.
[41] W. Hughes, Z. L. Wang, Applied Physics Letters 82 (2003) 2886.
[42] J. Grabowska, K. K. Nanda, E. McGlynn, J.-P. Mosnier, M. O. Henry, A. Beaucamp, A. Meaney, Journal of Material Science: Materials in Electleonics 16 (2005) 397.
[43] J. Grabowska, K. K. Nanda, E. McGlynn, J.-P. Mosnier, M. O. Henry, Surface & Coatings Technology 200 (2005) 1093.
[44] C. Ronning, P. X. Gao, Y. Ding, Z. L. Wang, Applied Physics Letters, 84 (2004) 783.
[45] J. Grabowska, A. Meaney, K. K. Nanda, J.-P. Mosnier, M. 0. Henry, J.-R. Duclere, E. McGlynn, Physical Review B, 71 (2005) 115439.

[46] Y. J. Xing, Z. H. Xi, Z. Q. Xue, X. D. Zhang, J. H. Song, Applied Physics Letters, 83 (2003) 1689.

[47] Z. L. Wang, J. Song, Science 312 (2006) 242.

[48] X. Wang, J. Song, J. Liu, Z. L. Wang, Science 316 (2007) 102.

[49] For a review, see S. Nakamura and G. Fasol, The Blue Laser Diode (Spring-Verlag, Berlin, 1997).

[50] S. B. Zhang, S.-H. Wei, A. Zunger, Journal of Applied Physics, 83 (1998) 3192.

[51] Sato, H., Minami, T., Takata, S., Mouri, T., Ogawa, N. Thin Solid Films, 220 (1992) 327 and 246 (1994) 86.

[52] B. G. Streetman and S. K. Banerjee, Solid State Electronic Devices. Pearson Prentice Hall, 6 ed., (2006).

[53] J. C. Fan, K. M. Sreekanth, Z. Xie, S. L. Chang, and K. V. Rao, "p-type ZnO materials: Theory, growth, properties and devices," Progress in Materials Science, vol. 58, no. 6, pp. 874 – 985, 2013.

[54] E. C. Lee, Y. S. Kim, Y. G. Jin, and K. J. Chang, "Compensation mechanism for N acceptors in ZnO," Phys. Rev. B, vol. 64, p. 085120, Aug 2001.

[55] A. Tsukazaki, A. Ohtomo, T. Onuma, M. Ohtani, T. Makino, M. Sumiya, K. Ohtani, S. F. Chichibu, S. Fuke, Y. Segawa, H. Ohno, H. Koinuma, and M. Kawasaki, "Repeated temperature modulation epitaxy for p-type doping and light-emitting diode based on ZnO," Nat. Mater., vol. 4, no. 1, pp. 42–46, 2005.

[56] H. Liu, V. Avrutin, N. Izyumskaya, Ü. Özgür, and H. Morkoc, "Transparent conducting oxides for electrode applications in light emitting and absorbing devices," Superlattices Microstruct, vol. 48, no. 5, pp. 458 – 484, 2010.

[57] S.-M. Park, T. Ikegami, and K. Ebihara, "Effect of substrate temperature on the properties of Ga-doped ZnO by pulsed laser deposition," Thin Solid Films, vol. 513, pp. 90–94, 2006.

[58] X.-L. Chen, J.-M. Liu, J. Ni, Y. Zhao, and X.-D. Zhang, "Wide-spectrum Mg and Ga co-doped ZnO TCO thin films for solar cells grown via magnetron sputtering with H2 introduction," Applied Surface Science, vol. 328, pp. 193 – 197, 2015.

[59] C.-S. Tian, X.-L. Chen, J.-M. Liu, D.-K. Zhang, C.-C. Wei, Y. Zhao, and X.-D. Zhang, "Wide-spectrum Mg and Ga co-doped ZnO - TCO thin films with introduced hydrogen grown by magnetron sputtering at room temperature," Applied Surface Science, vol. 314, pp. 786 – 793, 2014.

[60] Kanokwan Thongsuriwong, thesis “Effect of aminoalcohols on morphology of nanocrystalline ZnO powders and its optical properties”, Prince of Songkla University (2009). [61] Manish Kumar, Zinc oxide nanostructures synthesized by oxidation of zinc, (2010) thesis of bachelor of technology, National Institute of Technology Rourkela, India.
[62] S Roy and S Basu, Improved zinc oxide film for gas sensor applications. Bull. Mater. Sci. Vol. 25 (2002) (6), pp. 513–515.
[63] S. Tewari and A. Bhattacharjee, Pramana - J. Phys. 76, (2011)153.
[64] Y. Natsume, Thin Solid Films 372 (2000) 30.
[65] T. Negami, Y. Hashimoto and S. Nishiwaki, Sol. Energy Mater. Sol. Cells 67 (2001) 331.
[66] I. A. Ezenwa, Res. J. Chem. Sc. 2 (2012) 26.
[67] F. Paraguay, D. M. Miki-Yoshida, J. Morales, J. Solis and W. Estrada, Thin Solid Films 373 (2000) 137.
[68] L Yan, C K Ong and X S Rao, J. Appl. Phys. 96 (2004) 508.
[69] S. J. Pearton, D. P. Norton, Y. W. Heo, L. C. Tien, M. P. Ivill, Y. Li, B. S. Kang, F. Ren, J. Kelly and A. F. Hebard, J. Electron. Mat. 35 (2004) 862.
[70] 28. B. Baruwati, D. K. Kumar and S. V. Manorama, Sens. Actuators B119 (2006) 676.
[71] 11. K. Arshak and I. Gaiden, Mater. Sci. Engg. B118 (2005) 44.
[72] R. Ghosh, S. Fujihara and D. Basak, J. Electron. Mater. 35 (2006)1728.
[73] N. Shakti, Appl. Phys. Res. 2 (1010) 19.
[74] D. Kohle, J. Phys. D: Appl. Phys. 34 (2001) 124.
[75] K. L. Chopra and S. R. Das in “Thin Film Solar Cells” (Plenum Press, New York, 1983).
[76] H. L. Hartnagel, A. L. Dawar, A. K. Jain and C. Jagadish in “Semiconducting Transparent Films”, Institute of Physics Publishing, Techno House, Redcliffe Way, Bristol (UK, 1995), p. 134.
[77] F. R. Blom, F. C. M. Van De Pol, G. Bauhuis and Th. J. A. Popma, Thin Solid Films 4 (1991) 365.
[78] A. E. Jimenez-Gonzalez, Journal of Solid-State Chemistry 128 (1997) 176.
[79] D. J. Qiu, H. Z. Wu, A. M. Feng, Y.F. Lao, N. B. Chen and T. N. Xu, Appl. Surf. Sci. 222 (2004) 263.

[80] You, H.-C. (2013) Indium Doping Concentration Effects in the Fabrication of Zinc-Oxide Thin-Film Transistors. International Journal of Electrochemical Science, 8, 9773-9784.

[81] Kim, D., Yun, I. and Kim, H. (2010) Fabrication of Rough Al Doped ZnO Films Deposited by Low Pressure Chemical Vapor Deposition for High Efficiency Thin Film Solar Cells. Current Applied Physics, 10, S459-S462. http://dx.doi.org/10.1016/j.cap.2010.02.030.

[82] Fay, S., Steinhauser, J., Nicolay, S. and Ballif, C, Polycrystalline ZnO: B Grown by LPCVD as TCO for Thin Film Silicon Solar Cells. Thin Solid Films, 518 (2010) 2961-2966.

[83] Zhang, Y.A., et al. Synthesis and Efficient Field Emission Characteristics of Patterned ZnO Nanowires, Journal of Semiconductors, 33 (2012) 023001.

[84] Taabouche, A. et al. Effect of Substrates on the Properties of ZnO Thin Films Grown by Pulsed Laser Deposition. Advances in Materials Physics and Chemistry, 3 (2013) 209-213.

[85] Lee, C.-H. and Kim, D.-W., Thickness Dependence of Microstructure and Properties of ZnO Thin Films Deposited by Metal-Organic Chemical Vapor Deposition Using Ultrasonic Nebulization, Thin Solid Films, 546, (2013) 38-41..

[86] Saha, B., et al. Combined Effect of Oxygen Deficient Point Defects and Ni Doping in Radio Frequency Magnetron Sputtering Deposited ZnO Thin Films, Thin Solid Films, 562 (2014) 37-42.

[87] Wang, H., Liao, C., Chueh, Y., Lai, C., Chen, L. and Tsiang, R.C. Synthesis and Characterization of ZnO/ZnMgO Multiple Quantum Wells by Molecular Beam Epitaxy. Optical Materials Express, 3 (2013) 237-247.

[88] Dhawale, D.S., Dubal, D.P., More, A.M., Gujar, T.P. and Lokhande, C.D. Room Temperature Liquefied Petroleum Gas (LPG) Sensor. Sensors and Actuators B, 147 (2010) 488-494.

[89] Shinde, S.S., Bhosale, C.H. and Rajpure, K.Y., Photocatalytic Degradation of Toluene Using Sprayed N-Doped ZnO Thin Films in Aqueous Suspension. Journal of Photochemistry and Photobiology B: Biology, 113, (2012) 70-77.

[90] Kaneva, N., Stambolova, I., Blaskov, V., Dimitriev, Y., Bojinova, A. and Dushkin, C. A Comparative Study on the Photocatalytic Efficiency of ZnO Thin Films Prepared by Spray Pyrolysis and Sol-Gel Method., Surface & Coatings Technology, 207, (2012) 5-10.

[91] W. Tang, D.C. Cameron, Thin Solid Films 238 (1994) 83.

[92] Sahoo, T., Jang, L., Jeon, J., Kim, M., Kim, J., Lee, I., Kwak, J. and Lee, J. Photoluminescence Properties of ZnO Thin Films Grown by Using the Hydrothermal Technique. Journal of the Korean Physical Society, 56 (2010) 809-812.

[93] Fortunato E.M.C., et al., Wide-bandgap high-mobility ZnO thin-film transistors produced at room temperature. Applied Physics Letters, 2004. 85 (13): p. 2541-3.

[94] Navamathavan R., Choi, C.K., Yang, E.-J., Lim, J.-H., Hwang, D.-K., Park, S.-J., Fabrication and characterizations of ZnO thin film transistors prepared by using radio frequency magnetron sputtering, Solid-State Electronics, 52 (5): 2008 813-816.

[95] Weifeng Y., et al., Room-temperature deposition of transparent conducting Al-doped ZnO films by RF magnetron sputtering method. Applied Surface Science, 255 (11) (2009) 5669-73.

[96] Fortunato E., et al., Polycrystalline intrinsic zinc oxide to be used in transparent electronic devices, Thin Solid Films, 487 (1-2) (2005) 212-15.

[97] Zhiyong F., et al., ZnO nanowire field-effect transistor and oxygen sensing property. Applied Physics Letters, 85 (24) (2004) 5923-5.

[98] Dang W.L., et al., Deposition and characterization of sputtered ZnO films. Superlattices and Microstructures, 42 (1-6) (2007) 89-93.

[99] Zhenbo D., et al., An anode with aluminum doped on zinc oxide thin films for organic light emitting devices, Physics Letters A, 346 (1-3) (2005) 148-52.

[100] Kim H., et al., Effect of aluminum doping on zinc oxide thin films grown by pulsed laser deposition for organic light-emitting devices. 2000. Switzerland: Elsevier.

[101] Gerblinger, J. and H. Meixner, Electrical conductivity of sputtered films of strontium titanate. Journal of Applied Physics, 67 (12) (1990) 7453-9.

[102] Stadler, S. and P.K. Ajmera, Stress control in thin sputtered films towards potential application in micromachined structures. Materials Letters, 35 (1-2) (1998) 18-21.

[103] Harris, N., Modern Vacuum Practice. Third ed. 2007: McGraw-Hill. 44 - 46.

[104] Vayssieres L, Keis K, Lindquist SE, Hagfeldt A. Purpose-built anisotropic metal oxide material: 3D highly oriented microrod array of ZnO. J Phys Chem B. 2001; 105:3350-2.

[105] Willander M, Nur O, Zhao QX, Yang LL, Lorenz M, Cao BQ, et al. Zinc oxide nanorod based photonic devices: recent progress in growth, light emitting diodes and lasers. Nanotechnology. 2009; 20:332001.

[106] Wang ZL. Zinc oxide nanostructures: growth, properties and applications. Journal of Physics-Condensed Matter. 2004; 16: R829-R58.

[107] Wang ZL, Xu S, Lao C, Weintraub B. Density-controlled growth of aligned ZnO nanowire arrays by seedless chemical approach on smooth surfaces. Journal of Materials Research. 2008; 23:2072-7.

[108] Willander M, Ul Hasan K, Nur O, Zainelabdin A, Zaman S, Amin G. Recent progress on growth and device development of ZnO and CuO nanostructures and graphene nanosheets. Journal of Materials Chemistry. 2012; 22:2337-50.

[109] Ko SH, Lee D, Kang HW, Nam KH, Yeo JY, Hong SJ, et al. Nanoforest of hydrothermally grown hierarchical ZnO nanowires for a high efficiency dye-sensitized solar cell. Nano Lett. 2011;11:666-71.

[110] Z. L. Wang, Nanostructures of zinc oxide Materials Today, 7 (2004) 26-33.

[111] H. T. Ng, J. Li, M. K. Smith, P. Nguyen, A. Cassel, J. Han, M. Meyyappan, Science 300 (2003) 1249.

[112] Z. R. Tian, J. A. Voigt, J. Liu, B. McKenzie, M. J. McDermott, M. A. Rodriguez, H. Konishi, H. Xu, Nature Materials 2 (2003) 821.

[113] A. Tsukazaki, A. Ohtomo, T. Onuma, M. Ohtani, T. Makino, M. Surniya, K. Ohtani, S. F. Chichbu, S. Fuke, Y. Segawa, H. Ohno, H. Koinuma, M. Kawasalu, Nature Materials 4 (2005) 42.

[114] W. Yang, R. D. Vispute, S. Chooun, R. P. Shanna, T. Venkatesan, H. Shen, Applied Physics Letters 78 (2001) 27870

[115] M. S. Arnold, Ph. Avouris, Z. W. Pan, Z. L. Wang Journal of Physical Chemistry B 107 (2003) 659.

[116] C. J. Lee, T. J. Lee, S. C. Lyu, Y. Zhang, H. Ruth, H. J. Lee, Applied Physics Letters 81 (2002) 3648.

[117] W. Hughes, Z. L. Wang, Applied Physics Letters 82 (2003) 2886.

[118] E. Comini, G. Faglia, G. Sberveglieri, Z. W. Pan, Z. L. Wang Applied Physics Letters 81 (2002) 1869.

[119] H. T. Wang, B. S. Kang, F. Ren, L. C. Tien, P. W. Sadik, D. P. Nortan, S. P. Pearton, J. Lin, Applied Physics Letters 86 (2005) 243503.

[120] M. Law, H. Kind, F. Kim, B. Messer, P. Yang, Angewandte Chemie International Edition 41 (2002) 2405.

[121] Jincheng Fan, Tengfei Li and Hang Heng, Hydrothermal growth of ZnO nanoflowers and their photocatalyst application, Bull. Mater. Sci., 39 (1) (2016) 19–26.

[122] J. Grabowska, K. K. Nanda, E. McGlynn, J.-P. Mosnier, M. 0. Henry, A. Beaucamp, A. Meaney, Journal of Material Science: Materials in Electleonics 16 (2005) 397.

[123] J. Grabowska, K. K. Nanda, E. McGlynn, J.-P. Mosnier, M. 0. Henry, Surface & Coatings Technology 200 (2005) 1093.

[124] C. Ronning, P. X. Gao, Y. Ding, Z. L. Wang, Applied Physics Letters 84 (2004) 783.

[125] J. Grabowska, A. Meaney, K. K. Nanda, J.-P. Mosnier, M. 0. Henry, J.-R. Duclere, E. McGlynn, Physical Review B 71 (2005) 115439.

[126] Y. J. Xing, Z. H. Xi, Z. Q. Xue, X. D. Zhang, J. H. Song, Applied Physics Letters 83 (2003) 1689.

[127] J. Jortner, C. N. R. Rao, Pure and Applied Chemistly 74 (2002) 1489.

[128] G. Schmidt, Nanoparticles: From Theory to Applications, New York: Wiley, 2004.

[129] X. D. Bai, P. X. Gao, Z. L. Wang, Applied Physics Letters 82 (2003) 4806.

[130] G.K. Williamson, W.H. Hall, Acta Mater. 1 (1953) 22.

[131] Goldstein J. Scanning electron microscopy and x-ray microanalysis. New York: Kluwer Academic/Plenum Publishers; (2003).

[132] Zhou W. Advanced scanning microscopy for nanotechnology techniques and applications. New York, NY: Springer; (2007).

[133] J. Atteberry, http://science.howstuffworks.com/scanning-electron-microscope.htm Access date 03/28/2012.

[134 Zhong Q, Inniss D, Kjoller K, Elings VB. Fractured polymer/silica fiber surface studied by tapping mode atomic force microscopy, Surface Science Letters, 290 (1993) L688-L92.

[135] Geisse N. AFM and combined optical techniques, Materials Today, 12 (2009) 40-5.

[136] AFM. http://www.microbiologybytes.com/blog/2010/07/20/microbialnanoscopy/ Access Access date 04/09/2012.

[137] M. Pinczlits, G. Spingholz and G. Bauer, Appl. Phys. Lett, 73 (1998) 250.

[138] F. Urbach, Phys. 92 (1953) 1324.

References Chapter III

[1] J.J. Tauc, Amorphous and Liquid Semiconductors, Plenum, London, 1974.

[2] A. Fujishima, T. N. Rao and D. A. Tryk, J. of Photochem and Photobio. C: Photochem. Rev. 1 (2000) 1.

[3] B. X. Li and Y. F. Wang, Super lattice Microstruct., 47 (2010) 615.

[4] Q. Xiang, G. Meng, Y. Zhang, J. Xu, P. Xu, Q. Pan and W.Yu, Sens. Actuator B-Chem.143 (2010) 635.

[5] J. Xia, A. Wang, X. Liu and Z. Su, Appl. Surf. Sci., 257 (2011) 9724.

[6] M. M. Ba-Abbad, A. A. H. Kadhum, A. B. Mohamad, M. S.Takriff and K. Sopian, J. Alloy. Compd., 550 (2013) 63.

[7] Ayouchi et al. [14] R. Ayouchi, D. Leinen, F. Mart´ın, M. Gabas, E. Dalchiele, J.R. Ramos-Barrado, Preparation and characterization of transparent ZnO thin films obtained by spray pyrolysis, Thin Solid Films 426 (2003) 68–77.

[8] N. Lehraki, M.S. Aida,, S. Abed, N. Attaf, A. Attaf and M. Poulain, Jornal of Current Applied Physics 12 (2012) 1283-1287.

[9] Abdelkader hafdallah, Khaoula derrar, Mohamed Salah aida et Nadhir attaf. «Effet de la solution précurseur sur les propriétés structurales et otiques des couches minces de ZnO préparées par spray pyrolyse». Afrique Science, Vol.12, N°3 (2016), 1 mai 2016, http://www.afriquescience.info/document.php?id=6225. ISSN 1813-548X.

[10] Sang-Hwan Lee, Jae Hak Jung, Soo-Hyun Kim, Do-Kyung Lee, Chan-Wook Jeon, Effect of incident angle of target molecules on electrical property of Al-doped ZnO thin films prepared by RF magnetron sputtering, Current Applied Physics 10 (2010) S286–S289.

[11] V. Rotello (Ed.), Nanoparticles. Building Block for Nanotechnology, Kluwer Academic Publishers, New York, (2004).

[12] G. Schmid (Ed.), Nanoparticles: From Theory to Application, Wiley-VCH, Weinheim, (2006).

[13] F. Caruso, Colloids and Colloid Assemblies, Wiley-VCH, Weinheim, (2004).

[14] L.M. Liz-Marzan, P.V. Kamat, Nanoscale Materials, Kluwer Academic Publishers, New York, (2003).

[15] C. Burda, X. Chen, R. Narayanan, M.A. El-Sayed, Chem. Rev. 105 (2005) 1025.

[16] X. Chen, S.S. Mao, Chem. Rev. 107 (2007) 2891.

[17] Y. Xia, Y. Xiong, B. Lim, S.E. Skrabalak, Angew. Chem. Int. Ed. 48 (2009) 60.

[18] M. Faraday, Philos. Trans. 147 (1857) 145.

[19] M.-C. Daniel, D. Astruc, Chem. Rev. 104 (2004) 293.

[20] H. Hakkinen, Nat. Chem. 4 (2012) 443.

[21] C. Louis, O. Pluchery (Eds.), Gold Nanoparticles for Physics, Chemistry, Biology, Imperial College Press, (2012).

[22] M. Haruta, M. Date, Appl. Catal. A 222 (2001) 427.

[23] A. Corma, P. Serna, Science 313 (2006) 332.

[24] A.S.K. Hashmi, G.J. Hutchings, Angew. Chem. Int. Ed. 45 (2006) 7896.

[25] F. Porta, L. Prati, M. Rossi, G. Scari, J. Catal. 210 (2002) 464.

[26] C.G. Bond, D.T. Thompson, Gold Bull. 33 (2000) 41.

[27] C.K. Costello, J.H. Yang, H.Y. Law, Y. Wang, J.N. Lin, L.D. Marks, M.D. Kung, H.H. Kung, Appl. Catal. A 243 (2003) 15.

[28] M.S. Chen, D.W. Goodman, Acc. Chem. Res. 39 (2006) 739.

[29] G.C. Bond, C. Louis, D. Thompson, Catalysis by Gold, Imperial College Press, London, 2006.

[30] B.K. Min, C.M. Friend, Chem. Rev. 107 (2007) 2709.

[31] N. Dimitratos, J.A. Lopez-Sanchez, G.J. Hutchings, Chem. Sci. 3 (2012) 20.

[32] P.K. Jain, I.H. El-Sayed, M.A. El-Sayed, Nano Today 2 (2007) 18.

[33] R.A. Sperling, P. Rivera-Gil, F. Zhang, M. Zanella, W.J. Parak, Chem. Soc. Rev. 37 (2008) 1896.

[34] M.A. El-Sayed, Acc. Chem. Res. 37 (2004) 326.

[35] A. Schroeder, D.A. Heller, M.M. Winslow, J.E. Dahlman, G.W. Pratt, R. Langer, T. Jacks, D.G. Anderson, Nat. Rev. Cancer 12 (2012) 39.

[36] K. Saha, S.S. Agasti, C. Kim, X. Li, V.M. Rotello, Chem. Rev. 112 (2012) 2739.

[37] R. Bardhan, S. Lal, A. Joshi, N.J. Halas, Acc. Chem. Res. 44 (2011) 936.

[38] G.C. Schatz, Proc. Natl. Acad. Sci. U.S.A. 104 (2007) 6885.

[39] R. Elghanian, J.J. Storhoff, R.C. Mucic, R.L. Letsinger, C.A. Mirkin, Science 277 (1997) 1078.

[40] ISM, Univ. Bordeaux, 351 Cours de la Libération, 33405 Talence Cedex, France.

[41] Boqian Yang, Peterxian Feng, Ashok Kumar, R S Katiyar and Marc Achermann, Structural and optical properties of N-doped ZnO nanorod arrays, J. Phys. D: Appl. Phys. 42 (2009) 195402 (5pp), doi:10.1088/0022-3727/42/19/195402.

[42] William G. Fateley, Francis R. Dollish, Neil T. Mc Devitt, Freeman F. Bentley, Infrared and Raman Selection Rules for Molecular and Lattice Vibrations– The Correlation Method., Wiley-Interscience, New York (1972).

[43] X. Ke, F. Shan, Y. Shin Park, Y. Wang, Wenzhe, T. Won Kang and D. Fu, Surface and coatings technology, Volume 201, Issue 15, 6797-6799 (2007).

[44] U. Ozgür, Ya. I. Alivov, C. Liu, A. Teke, M. A. Reshchikov, S. Dogan, V. Avrutin, S. J. Cho, H. Morkoc, J. Appl. Phys. 98, 041301 (2005).

[45] R.Vinodkumar I. Navas , N. V. Unnikrishnan, V. P. Mahadevan Pillaib, Synthesis and characterization of pulsed laser deposited ZnO nanorods, Optoelectronics and Advanced Materials 6, No. 3-4 (2012) 411 – 415.

[46] Liang-Wen Ji , Shi-Ming Peng , Jun-Sheng Wu , Wei-Shun Shih , Cheng-Zhi Wu ITseng Tang, Effect of seed layer on the growth of well-aligned ZnO nanowires, Journal of Physics and Chemistry of Solids.70 (2009) 1359–1362.

[47] D.C. Kim, B.H. Kong, H.K. Cho, D.J. Park, J.Y. Lee, Nanotechnology 18 (2007) 015603.

[48] Kai Loong Foo, Uda Hashim, Kashif Muhammad and Chun Hong Voon, Sol–gel synthesized zinc oxide nanorods and their structural and optical investigation for optoelectronic application, Nanoscale Res Lett., 9(1) (2014) 429.

[49] C.H. An, S. Peng, Y.G. Sun, Facile synthesis of sunlight-driven AgCl: Ag plasmonic nanophotocatalyst, Adv. Mater. 22 (2010) 2570–2574.

[50] Shuaishuai Ma, Rong Li, Changpeng Lv, Wei Xu, Xinglong Gou, Facile synthesis of ZnO nanorod arrays and hierarchical nanostructures for photocatalysis and gas sensor applications, Journal of Hazardous Materials 192 (2011) 730– 740.

[51] J. Mu, C. Shao, Z. Guo, Z. Zhang, M. Zhang, P. Zhang, B. Chen, and Y. Liu, "High photocatalytic activity of ZnO carbon nanofiber heteroarchitectures," ACS Appl. Mater. Interfaces, vol. 3, no. 2 (2011) pp. 590-596.

[52] F. Kayaci, C. Ozgit-Akgun, I. Donmez, N. Biyikli, and T. Uyar, "Polymer-inorganic core-shell nanofibers by electrospinning and atomic layer deposition: flexible nylon-ZnO core-shell nanofiber mats and their photocatalytic activity," ACS Appl. Mater. Interfaces, 4 (11) (2012) 6185–6194.

[53] S. Kuriakose et al., Effects of swift heavy ion irradiation on structural, optical and photocatalytic properties of ZnO–CuO nanocomposites prepared by carbothermal evaporation method, Beilstein J. Nanotechnol., 6 (2015) 928–937.

[54] A. M. Peiró, P. Ravirajan, K. Govender et al., Hybrid polymer/ metal oxide solar cells based on ZnO columnar structures, Materials Chemistry, 16 (21) (2006) 2088–2096.

[55] Jincheng Fan, Tengfei Li and Hang Heng, Hydrothermal growth of ZnO nanoflowers and their photocatalyst application, Bull. Mater. Sci., 39 (1) (2016) 19–26.

[56] Ye Sun, Gareth M. Fuge, Michael N.R. Ashfold, Growth of aligned ZnO nanorod arrays by catalyst-free pulsed laser deposition methods, Chemical Physics Letters, 396 (2004) 21–26.

[57] N. Lepot, M.K. Van Bael, H. Van den Rul, J. D'Haen, R. Peeters, D. Franco, J. Mullens, Synthesis of ZnO nanorods from aqueous solution, Materials Letters, 61 (2007) 2624–2627.

[58] Sun Y J, Wang L, Yu X G and Chen K Z, Cryst. Eng. Comm., 14 (2012) 3199.

[59] Li P, Liu H, Lu B and Wei Y, J. Phys. Chem. C, 114 (2010) 21132.

[60] Xu, L.; Hu, Y.; Pelligra, C.; Chen, C.; Jin, L.; Huang, L.; Sithambaram, S.; Aindow, M.; Joesten, R.; Suib, S. L. Chem. Mater.**,** 21 (2009) 2875–2885. Doi: 10.1021/cm900608d.

[61] Liu, Z.; Zhang, Q.; Li, Y.; Wang, H. J. Phys. Chem. Solids**,** 73 (2012) 651–655. doi:10.1016/j.jpcs.2012.01.003.

[62] Umar, A.; Chauhan, M. S.; Chauhan, S.; Kumar, R.; Kumar, G.; Al-Sayari, S. A.; Hwang, S. W.; Al-Hajry, A. J. Colloid Interface Sci. 363 (2011) 521–528. doi:10.1016/j.jcis.2011.07.058.

[63] Wang, X.; Zhang, Q.; Wan, Q.; Dai, G.; Zhou, C.; Zou, B. J. Phys. Chem. C, 115 (2011) 2769–2775. Doi : 10.1021/jp1096822.

[64] Lu, F., Cai, W., Zhang, Y., Adv. Funct. Mater., 18 (2008) 1047. doi:10.1002/adfm.200700973.

[65] Y. G. Habba, Martine Capochichi-Gnambodoe and Yamin Leprince-Wang, Enhanced Photocatalytic Activity of Iron-Doped ZnO Nanowires for Water Purification, Appl. Sci., 7 (2017) 1185; doi:10.3390/app7111185.

[66] Reddy CV, Babu B and Shim J, Phys. Chem. Solids, 112 (2017) 20–28.

[67] Q. Wan, Q.H. Li, Y.J. Chen, T.H. Wang, X.L. He, X.G. Gao and J.P. Li, Appl. Phys. Lett., 84 (2004) 3085.

[68] S.P. Chang, S.J. Chang, C.Y. Lu, M.J. Li, C.L. Hsu, Y.Z. Chiou, T.J. Hsueh and I.C. Chen, Super lattices Microstruct., 47 (2010) 772.

[69] N. Zhang, K. Yu, Z.Q. Zhu and D.S. Jiang, Sens Actuators A, 143 (2008) 245.

[70] X.L. Hu, J.M. Gong, L.Z. Zhang and J.C. Yu, Adv. Mater., 20 (2008) 4845.

[71] Y.F. Qiu, S.H. Yang, Adv. Funct. Mater., 17 (2007) 1345.

[72] A. Erol, S. Okur, B. Comba, O. Mermer and M.C. Arikan, Sens. Actuators B, 145 (2010) 174.

[73] W. Wang, Z.Y. Li, L. Liu, H.N. Zhang, Y. Wang, H.M. Huang, Z.J. Wang and C. Wang, Sens. Actuators B, 141 (2009) 404.

[74] L. Zhang, J.H. Zhao, H.Q. Lu, L. Li, J.F. Zheng, H. Li and Z.P. Zhu, Sens Actuators, B 161 (2012) 209.

[75] T. Xu, L. Zhang, H. Cheng and Y. F. Zhu, Appl. Catal. B: Environmental, 101 (2011) 382.

[76] B. J. Li and H. Q. Cao, Mater. Chem., 21 (2011) 3346.

[77] C. Zhang, L. W. Yin, L. Y. Zhang, Y. X. Qi and N. Lun, Mater. Lett., 67 (2012) 303.

[78] A. Wei, L. Xiong, L. Sun, Y. J. Liu and W. W. Li, Chin. Phys. Lett., 30 (2013) 046202–5.

References Chapter IV

[1] Y. Gao, R. Cranston, Recent advances in antimicrobial treatments of textiles, Text. Res. J. 78 (1) (2008) 60–72.

[2] A.P. Sawhney, K.V. Singh, S.S. Pang, Modern applications of nanotechnology in textiles, Text. Res. J. 78 (2008) 731–739.

[3] H.Y. Ki, J.H. Kim, S.C. Kwon, S.H. Jeong, A study on multifunctional wool textiles treated with nano-sized silver, J. Mater. Sci. 42 (2007) 8020–8024.

[4] Li L, Hu J, Alivistos AP. Nano Lett.1 (2001) 349.

[5] Hussain I, Brust M, Papworth AJ, Cooper AI. Langmuir; 19 (2003) 4831.

[6] Burleson DJ, Driessen MD, Penn RL. J Environ Sci Health A. 39 (2005) 2707.

[7] Cheng M-D. J Environ Sci Health A. 39 (2005) 2691–705.

[8] Obare SO, Meyer GJ. J Environ Sci Health A. 39 (2005) 2549.

[9] Yuan G. J, Environ Sci Health A., 39 (2005) 2545.

[10] Masciangioli T, Zhang W-X. Environ Sci Technol, 37 (2003) 102A–8A.

[11] Albrecht MA, Evans CW, Raston CL. Green Chem, 8 (2006) 417.

[12] Smith AM, Duan H, Rhyner MN, Ruan G, Nie SA. Phys Chem Chem Phys. 8 (2006) 3895.

[13] Kearns GJ, Foster EW, Hutchison JE. Anal Chem.78 (2006) 298.

[14] Nagy A, Mestl G. Appl Catal A. 188 (1999) 337.

[15] Frattini A, Pellegri N, Nicastro D, de Sanctis O. Mater Chem Phys.94 (2005) 148.

[16] Tessier PM, Velev OD, Kalambur AT, Rabolt JF, Lenhoff AM, Kaler EW. J Am Chem Soc. 122 (2000) 9554.

[17] Cao YW, Jin RC, Mirkin CA. Science 297 (2002) 1536.

[18] Rosi NL, Mirkin CA. Chem Rev. 105 (2005) 1547.

[19] Belloni J. Radiat Phys Chem. 67 (2003) 291.

[20] Nino-Martinez N, Martinez-Castanon GA, Aragon-Pina A, Martinez-Gutierrez F, Martinez-Mendoza JR, Ruiz F. Nanotechnology; 19(6) (2008) 065711/1-065711/8.

[21] Alt V, Bechert T, Steinrücke P, Wagener M, Seidel P, Dingeldein E, et al. Biomaterials, 25 (2004) 4383.

[22] Russell AD, Hugo WB. Prog. Med. Chem. 31 (1994) 351.

[23] Lee HY, Park HK, Lee YM, Kim K, Park SB. Chem Commun. (2007) 2959.

[24] Jeong S, Yeo S, Yi S. J Mater Sci. 40 (2005) 5407.

[25] Chou W-L, Yu D-G, Yang M-C. Polym Adv Technol. 16 (8) (2005) 600.

[26] Jin M, Zhang X, Nishimoto S, Liu Z, Tryk DA, Emeline AV, et al. J Phys Chem C. 111 (2007) 658.

[27] Chen Q, Yue L, Xie F, Zhou M, Fu Y, Zhang Y, et al. J Phys Chem C. 112 (2008) 10004.

[28] Tao A, Sinsermsuksaku P, Yang P. Angew Chem Int Ed.45 (2006) 4597.

[29] Wiley B, Sun Y, Mayers B, Xi Y. Chem-Eur J. 11 (2005) 454.

[30] Lee PC, Meisel D. J Phys Chem.86 (1982) 3391.

[31] Shirtcliffe N, Nickel U, Schneider S. J Colloid Interface Sci. 211 (1999) 122.

[32] Nickel U, Castell AZ, Poppl K, Schneider S. Langmuir,16 (2000) 9087.

[33] Chou K-S, Ren C-Y. Mater Chem Phys. 64 (2000) 241.

[34] Evanoff Jr D, Chumanov GJ. J Phys Chem B, 108 (2004) 13948.

[35] Sondi I, Goia DV, Matijević E. J Colloid Interface Sci. 260 (2003) 75.

[36] Merga G, Wilson R, Lynn G, Milosavljevic BH, Meisel D. J Phys Chem C, 111, (2007) 12220.

[37] Creighton JA, Blatchford CG, Albrecht MJ. J Chem Soc Faraday Trans, 75 (1979) 7902.

[38] Ahmadi TS, Wang ZL, Green TC, Henglein A, El-Sayed, M. Science 272 (1996) 1924.

[39] Kapoor S, Lawless D, Kennepohl P, Meisel D, Serpone N. Langmuir 10 (1994) 3018.

[40] Henglein A. Chem Rev; 89 (1989) 1861.

[41] Gutiérrez M, Henglein A. J Phys Chem; 97 (1993) 11368.

[42] Ershov BG, Janata E, Henglein A. J Phys Chem 97 (1993) 339.

[43] S. Harmami, D. Sondari, A. Haryono, Indonesian Journal of Materials Science (2008) 233.

[44] Cavalla M. et Eberlinberlin T., Isolement des streptomycetes du sol. L'opéron. XIX. (1994) 13-17.

[45] Totorano A. M., cabrini E. et Vivuani M.A. Sensibilité in vitro des levures a cinq antifongiques. Comparaison de deux methodes C.M.I. en gélose et méthode des disques. Bull. Soc. Fr. Myc. Med., 8. (1979) 69-74.

[46] Yaguo Cai, Xianqing Piao, Wei Gao, Zhejuan Zhang, Er Nie and Zhuo Sun, Large-scale and facile synthesis of silver nanoparticles via a microwave method for a conductive pen†, , RSC Adv.,7 (2017) 34041.

[47] A. K. Michael Grouchko, C. F. Mihailescu, D. Florin Anghel and S. Magdassi, ACS Nano,5 (2011) 3354–3359.

[48] Huanga NM, Lim HN, Radiman S, Khiew PS, Chiu WS, Hashim R, Chia CH, Sucrose ester micellar-mediated synthesis of Ag nanoparticles and the antibacterial properties. Colloids Surf A 353 (2010) 69–76.

[49] H. Karami and E. Fakoori, Synthesis and Characterization of ZnO Nanorods Based on a New Gel Pyrolysis Method, J. of Nanomater, 628203 (2011) 11.

[50] Y. Ni, X. Cao, G. Wu, G. Hu, Z. Yang and X. Wei. Preparation, Characterization and property study of zinc oxide nanoparticles via a simple solution-combusting method, Nanotech. 18 (6) (2007) 155603.

[51] Amany A. El-Kheshen, Sanaa F. Gad El-Rab , Der Pharma Chemica, 4 (1) (2012) 53-65.

[52] Virender K. Sharma, Ria A. Yngard, Yekaterina Lin, Silver nanoparticles: Green synthesis and their antimicrobial activities, Advances in Colloid and Interface Science, 145 (2009) 83–96.

[53] Aruna Jyothi Kora, Sashidhar Rao Beedu, Arunachalam Jayaraman, Size-controlled green synthesis of silver nanoparticles mediated by gum ghatti (Anogeissus latifolia) and its biological activity. Organic and Medicinal Chemistry Letters 2 (2012) 17.

[54] Y. Zhang, , Jian Xu, Qiuling Wang, Zhenzhu Pan, Shiyu Ma, Qiming Chen, Preparation and properties of ZnO loaded with uniform Ag nanoparticles, Materials Research Bulletin, 73 (2016) 119–124.

[55] A. L. Stepanov, V.N. Popok, I.B. Khaibullin, U. Kreibig, Optical properties of polymethylmethacrilate with implanted silver nanoparticles, Nucl. Instrum. Methods Phys. Res. B, 191 (2002) 473–477.

[56] M. Ji, X. Chen, C.M. Wai, J.L. Fulton, Synthesizing and dispersing silver nanoparticles in a water-in-supercritical carbon dioxide microemulsion, J. Am. Chem. Soc. 121 (1999) 2631–2632.

[57] S. He, J. Yao, P. Jiang, D. Shi, H. Zhang, S. Xie, S. Pang, H. Gao, Formation of silver nanoparticles and self-assembled two-dimensional ordered superlattice, Langmuir 17 (2001) 1571–1575.

[58] Budi Harmami S., D.Sondari, A. Haryono, Indonesian Journal of Materials (2008) 233.

[59] L.N. Wang, L .Z. Hu, H. Q. Zhang, Y. Qiu, Y. Lang ,G. Q. Liu ,J. Y. Ji ,J. X. Ma, Z. W. Zhao, Studying the Raman spectra of Ag doped ZnO films grown by PLD, Materials Science in Semiconductor Processing, 14 (2011) 274–277.

[60] Fenglin Xian, Kaibo Miao, Xuecheng Bai, Yun Ji, Feier Chen, Xiangyin Li. Journal Optik, 124 (2013) pp 4876– 4879.

[61] A. Chwalibog, E. Sawosz, A. Hotowy, International Journal of Nanomedicine, 5 (2010) 1085.

[62] Kvitek L, Panacek A, Soukupova J, Kolar M, Vecerova R, Prucek R, et al. J Phys Chem C, 112 (2008) 5825.

[63] Morones JR, Elechiguerra JL, Camacho A, Holt K, Kouri J, Ramirez JT, et al. Nanotechnology 16 (2005) 2346.

[64] L.D.E. Brodie, R. Singh, J.H. Morgan, J.D. Leslie, C.J. Moore, A.E. Dixon, in Proc. 14th Photovoltaic Specialists Conference, San Diego, CA, (1998) p.468.

[65] D. Goyal, P. Solanaki, B. Marathe, M. Takwale, V. Bhide, Jpn. J. Appl. Phys. 31 (1992) 361.

[66] M.J. Vellekoop, A. Venema, C.C.G. Visser, P.M. Sarro, Cream. Bull., 69 (1990) 1503.

[67] F.C.M. Van, D. Pol, Cream. Bull. 69 (1990) 1959.

[68] K.L. Chopra, S. Major, D.K. Pandya, Thin Solid Films, 102, (1983) 1.

[69] F.S. Hickermell, Proc. IEEE. 64 (1976) 631.

[70] I. Yun, Photodiodes-from Fundamentals to Applications (In Tech, Croatia, 2012).

[71] A. Tataroglu, H. Tuncer, A.A. Al-Ghamdi, A. Dere, B. Arif, S. Yol, N. Ozdemir, F. El-Tantawy, F. Yakuphanoglu, Synth. Metals 206 (2015) 15–23.

[72] I.A. Elsayed, M. Cavas, R. Gupta, T. Fahmy, A.A. Al-Ghamdi, F. Yakuphanoglu, J. Alloys Compd. 638 (2015) 166–171.

[73] I. Beinik, M. Kratzer, A. Wachauer, L. Wang, Y.P. Piryatinski, G. Brauer, X.Y. Chen, Y.F. Hsu, A.B. Djurisˇi, C. Teichert, Beilstein J. Nanotechnol. 4 (2013) 208–217.

[74] H. Aydın, A. Tataroglu, A.A. Al-Ghamdi, F. Yakuphanoglu, F. El-Tantawy, W.A. Farooq, J. Alloys Compd. 625 (2015) 18–25.

[75] E.H. Nicollian, A. Goetzberger, Bell Syst. Tech. J. 46 (1967) 1055–1133.

[76] R.T. Tung, Phys. Rev. B, 64 (2001) 205310.

[77] S.H. Kim, C.Y. Jung, H. Kim, Trans. Electr. Electron. Mater. 15 (2014) 324–327.

[78] R. Padma, V. Rajagopal Reddy, Adv. Mater. Lett. 5 (2014) 31–38.

[79] A. Tataroglu, A.A. Al-Ghamdi, S. Bin Omran, W.A. Farooq, F. El-Tantawy, F. Yakuphanoglu, J. Sol Gel Sci. Technol. 71 (2014) 421.

[80] E.H. Rhoderick, Metal–Semiconductor Contacts (Oxford: Oxford University Press, (1978) 121.

[81] S.M. Sze, Physics of Semiconductor Devices, 2nd ed. (New York: Wiley, 1978), p. 256.

[82] Silan Baturay, Yusuf Selim Ocak, Derya Kaya The effect of Gd doping on the electrical and photoelectrical properties of Gd: ZnO/p-Si heterojunctions, Journal of Alloys and Compounds 645 (2015) 29–33.

[83] F. Yakuphanoglu, Y. Caglar, M. Caglar, S. Ilıcan, Eur. Phys. J. – Appl. Phys. 58 (2012) 30101.

[84] N. Zebbara, M S. Aida, A E. K. Hafdallah, O. Daranfad, H. Lekiket and M. Kechouane, Properties of ZnO thin films grown on Si substrates by ultrasonic spray and ZnO/Si heterojunctions, Materials Science Forum, 609 (2009) 133-137.

[85] A. Alyamani, A. Tataroglu, L. El Mir, Ahmed A. Al-Ghamdi, H. Dahman and W. A. F. Yakuphanoglu, Photoresponse and photocapacitor properties of Au/AZO/p-Si/Al diode with AZO film prepared by pulsed laser deposition (PLD) method, Appl. Phys. A, 122, (2016) 297.

[86] R. Kumar, S. Chand, J. Mater. Sci.: Mater. Electron. 25 (2014) 4531–4537.

[87] E. Marıl, A. Kaya, H.G. C¸ etinkaya, S. Koçyigit, S¸ Altındal, Mater. Sci. Sem. Process. 39 (2015) 332–338.

[88] L. Changshi, L. Feng, Comput. Mater. Sci. 107 (2015) 170–174.

[89] H. Norde, J. Appl. Phys. 50 (1979) 5052.

[90] Tombak, A., Ocak, Y. S., Asubay, S., Kilicoglu, T. Ozkahraman, F. Fabrication and electrical properties of an organic–inorganic device based on Coumarin 30 dye. Mater. Sci. Semi. Proc. 24 (2014) 187-192.

[91] Kılıçoglu, T., Tombak, A., Ocak, Y.S., Aydemir, M. Electrical and photoelectrical characterization of a TTF/p-InP organic–inorganic heterojunction. Microelectron. Eng., 129 (2014) 91-95.

[92] Phan, D. T., Gupta, R. K., Chung, G. S., Al-Ghamdi, A. A., Al-Hartomy, O. A., El-Tantawy, F., Yakuphanoglu. Photodiodes based on graphene oxide–silicon junctions, Solar Energy, 86 (2012) 2961-2966.

[93] Tecimer, H., Türüt, A., Uslu, A., Uslu, I, Temperature dependent current-transport mechanism in Au/ (Zn-doped) PVA/n-GaAs Schottky barrier diodes. Sens. Actuators A 199 (2013) 194-201.

[94] Soylu, M., Cavas, M., Al-Ghamdi, A. A., Gafer, Z. H., El-Tantawy, F., Yakuphanoglu, F. Photoelectrical characterization of a new generation diode having GaFeO3 interlayer. Sol. Ener. Mater. Sol. Cells 124 (2014) 180-185.

[95] S. Wageh, A.A. Al-Ghamdi, Y. Al-Turki, A. Dere, S.C. Tjong, F. El-Tantawy, F. Yakuphanoglu, Opt. Quant. Electron. 47 (2015) 1779–1789.

[96] A.S. Dahlan, A. Tatarog˘lu, A.A. Al-Ghamdi, A.A. Al-Ghamdi, S. Bin-Omran, Y. Al-Turki, F. El-Tantawy, F. Yakuphanoglu, J. Alloys Compd. 646, (2015) 1151–1156.

[97] B. Varghese, B. Mukherjee, K.R.G. Karthik, K.B. Jinesh, S.G. Mhaisalkar, E.S. Tok, C.H. Sow, J. Appl. Phys. 111, (2012) 104306 (1–6).

[98] G. Cheng, X. Wu, B. Liu, B. Li, X. Zhang, Z. Dua, Appl. Phys. Lett. 99 (2011) (1–3) 203105.

[99] R. H. Al Orainy, A.A. Hendi, Microelectron. Eng. 127 (2014) 14–20.

[100] Y.-H. Chang, C.-M. Liu, Y.-C. Tseng, C. Chen, C.-C. Chen, H.-E. Cheng, Nanotech. 21 (2010) 225602.

[101] F. Yakuphanoglu, Synth. Metals 160 (2010) 1551–1555.

[102] R.K. Gupta, A.A. Hendi, M. Cavas, A.A.A. Hamdi, O.A.A. Hartomy, R.H. Aloraini, F. E. Tantawy, F. Yakuphanoglu, Physica E 56 (2014) 288–295.

[103] A. I. Gencer, O. Karadumana and F. Yakuphanoglu, Synthetic Metals, 221 (2016) 114–119

[104] Tascıoglu, I., Farooq, W. A., Turan, R., Altındal, S.,Yakuphanoglu, F. Charge transport mechanisms and density of interface traps in MnZnO/p-Si diodes. J. Alloy Compd., 590 (2014) 157–161.

[105] A. A. M. Farag, B. Gunduz, F. Yakuphanoglu, W.A. Farooq, Synth. Metals 160 (2010) 2559–2563.

[106] D.-T. Phan , R.K. Gupta ,G.-S. Chung , A.A. Al-Ghamdi, Omar A. Al-Hartomy, F. El-Tantawy, F. Yakuphanoglu, Photodiodes based on graphene oxide–silicon junctions Solar Energy, 86 (2012) 2961–2966.

[107] S.M. Sze, Physics of Semiconductor Devices, 2nd ed. John Wiley & Sons, 256 (1978).

[108] L. Taçolu, U. Aydemir, E. Altndal, B. Knac, and S. O¨zçelik, J. Appl. Phys.109 (2011) 054502.

[109] S. M. Sze, Physics of Semiconductor Devices, 2nd ed. (Wiley, New York, 1981).

[110] B. Gunduz, I.S. Yahia, F. Yakuphanoglu, Microelectron. Eng. 98 (2012) 41–57.

[111] Divya Somvanshi and S. Jit, Analysis of Temperature-Dependent Electrical Characteristics of n-ZnO Nanowires (NWs)/p-Si Heterojunction Diodes, IEEE Transactions on Nanotechnology 13 (1) (2014) 62-69.

[112] E.H. Nicollian, A. Goetzberger, Bell Syst. Tech. J. 46, (1967) 1055–1133.

[113] E. Ranjith Kumar, R. Jayaprakash, Rajesh Patel, Superlattices Microstruct. 62 (2013) 277–284.

[114] B. Gunduz, Ahmed A. Al-Ghamdi, A.A. Hendi, Zarah H. Gafer, S. El-Gazzar, Farid El-Tantawy, F. Yakuphanoglu, New Schottky diode based entirely on nickel aluminate spinel/p-silicon using the sol–gel spin coating approach, Superlattices and Microstructures 64 (2013) 167–177.

[115] A. Mekki, R.O. Ocaya, A. Dere, Ahmed A. Al-Ghamdi, K. Harrabia, F. Yakuphanoglu, New photodiodes based graphene-organic semiconductor hybrid materials, Synthetic Metals 213 (2016) 47–56.

[116] S. Karatas, A. Turut, Vacuum 74 (2004) 45.

[117] A. Tombak, Y.S. Ocak, S. Asubay, T. Kilicoglu, F. Ozkahraman, Mater. Sci. Semicond. Process. 24 (2014) 187–192.

Publications

International Publications

1. **Fouzia Bourfaa** , Abderhamane Boutelala, Mohamed Salah Aida, Nadir Attaf and Yusuf Selim Ocak, "Influence of Seed Layer Surface Position on Morphology and Photocatalysis Efficiency of ZnO Nanorods and Nanoflowers", Journal of Nanomaterials, Volume 2020, Article ID 4072351, 9 pages, https://doi.org/10.1155/2020/4072351.

2. Abderhamane Boutelala, **Fouzia Bourfaa**, Mohamed Mahtali, "Effect of light on electrical and photoelectrical characteristics of Al/TiO_2/p-Si Schottky diode", Journal of Materials Science: Materials in Electronics, 31 (2020) 11379–11389, https://doi.org/10.1007/s10854-020-03687-y.

3. **Fouzia Bourfaa**, Abderhamane Boutelala, Aida Mohammed Salah, Nadir Attaf and Yusuf Selim Ocak, "EFFECT OF DEPOSITION TIME OF ZNO NANORODS BY HYDROTHERMAL METHOD ON PHOTOCATALYSIS ACTIVITY", International journal of Health Services, 3 (1) (2018) 33-39.

4. **Bourfaa, F.**, Boutelala, A., Aida, M. S., Attaf, N. & Merouane, F., "Antibacterial activity of zinc oxide with silver nanoparticles". World Journal of Environmental Research, 7(2) (2017) 98-107.

5. **F Bourfaa**, M Lamri Zeggar, A Adjimi, M S Aida and N Attaf, "Investigation of photocatalytic activity of ZnO prepared by spray pyrolis with various precursors", IOP Conf. Series: Materials Science and Engineering, 108 (2016) 012049 doi:10.1088/1757-899X/108/1/012049.

Abstracts

تحضير شرائح رقيقة من ZnO لمعالجة المياه

ملخص

إن تقنية التحفيز الضوئي لأشباه الموصلات غير المتجانسة هي نوع من التكنولوجيا الخضراء التي تم استخدامها لحل مشاكل التلوث البيئي. تركز هذه الدراسة الحالية على فحص الأغشية الرقيقة والهيكلية النانوية التحفيزية ZnO باستخدامها لتحلل الأصباغ العضوية .بشكل أساسي ، تم اختبار أملاح كلوريد الزنك والنترات والأسيتات لنشاطها التحفيزي الضوئي من خلال تدهور اللون الأحمر التفاعلي والأزرق الميثيلين (MB) في محلول مائي. المركبات المختارة التي تم ترسيبها عن طريق الرش الحراري لديها كفاءة تحلل ضوئي معتبرة. مختلف الوسائط التي تمت دراستها مثل تركيز الصبغة, وقت الترسيب ومصدر الملح ووضعية سطح البذور لها تأثير كبير على التحلل الضوئي لهذه الصبغة. كما تم اختبار البنية النانوية الحرارية المائية ZnO لإزالة تلون MB ، والنتائج مشجعة للغاية لمعالجة المياه خاصة بالنسبة إلى ZnO Nanorods (ملح الأسيتات) وZnO nanoflowers .الأغشية الرقيقة ل ZnO و ZnO: Ag NPs على الزجاج والأنسجة والتي تم تحضيرها بواسطة محلول هلامي، أظهرت قدرة أكسيد الزنك والجسيمات النانوية الفضية و MgO على مقاومة نمو غرام سالب من بكتيريا الالتهاب الرئوي و Escherichia coli من خلال منطقة تثبيط والتي وصلت إلى 23 ملم. تم استخدام نترات الزنك لتحضير البنية الإلكترونية الهجينة Al / ZnO / p-Siعن طريق الرش الحراري بالموجات فوق الصوتية من أجل التحقق في الوسائط الكهروضوئية لصمام الخلايا الشمسية. تشير قياسات I-V إلى أن عامل المثالية n هو 1.35 و ارتفاع الحاجز ϕ_b هو0.67 eV . إن قيم الحاجز ϕ_b من قياس I-V و دالة (0.69 eV) Norde على توافق جيد. بينما المقاومة التسلسلية R_s التي تم الحصول عليها من دالة Norde وجدت 1194 Ω .الصمام الثنائي لديه خاصية تصحيح جيدة ، وسلوك كهروضوئي ، وخاصيتي التحسس الضوئي والاستجابة الضوئية. يؤكد التوصيف الكهربائي والكهروضوئي أن هذا الجهاز مناسب جدًا كصمام ضوئي ولتطبيقات جهاز الاستشعار الضوئي ولتطبيقات الإلكترونيات الضوئية. I_{SC} وV_{OC} يتغيران من 11.12 µA إلى 50.73 µA و 125, 33 mV إلى mV 185.22 من اجل عدة إضاءات. يوضح تحليل تردد السعة أن سعة و ناقلية الصمام الثنائي Al / ZnO / p-Si تتعلق بالجهد والتردد. إن قيم N_a و ϕ_b و V_{bi} تتزايد بازدياد التواتر.

الكلمات المفتاحية :أكسيد الزنك ،الأغشية الرقيقة، البنيةالنانوية،التحفيز الضوئي، النشاط المضاد للبكتيريا،الخلايا الشمسية

Dépôt des Couches Minces de ZnO pour le Traitement de L'eau

RESUME

La photocatalytique hétérogène à semi-conducteurs est une sorte de technologie verte qui a été utilisée pour résoudre les problèmes de pollution de l'environnement. La présente étude se concentre sur le criblage de ZnO couches minces et nanostructuré potentiellement photocatalytiques en les utilisant pour dégrader les colorants organiques. Principalement, les sels de chlorure, nitrate et acétate de zinc ont été testés pour leur activité photocatalytique par la dégradation du Rouge Réactif et du Bleu de Méthylène (MB) en solution aqueuse. Les composés choisis qui sont déposé par spray pyrolyse présentent une efficacité de photodégradation considérable. Les différents paramètres étudiés tels que la concentration du colorant, le temps de dépôt, la source de sel et la position de la couche de germination ont un grand effet sur la photodégradation de ce colorant. Des nanostructures hydrothermales de ZnO ont également été testées pour la décoloration du MB et les résultats sont très encourageants, en particulier pour ZnO nanorods (sel d'acétate) et ZnO nanofleurs pour le traitement de l'eau. Les films purs et ZnO: Ag NPs sur verre et tissu, préparés par sol-gel, montrent la capacité de l'oxyde de zinc et les nanoparticules d'argent à résister la croissance de Gram - de K. pneumonie et E. coli par leur zone d'inhibition qui atteint 23 mm. Le nitrate de zinc comme précurseur a été utilisé pour préparer l'hétérojonction Al / ZnO / p-Si par spray ultrasonique afin d'étudier les paramètres photovoltaïques de la cellule solaire de cette diode. Les mesures I-V indiquent que le facteur d'idéalité n est de 1,39 et la hauteur de barrière ϕ_b est 0,67 eV. Le ϕ_b de la mesure I-V et la fonction de Norde (0,69 eV) sont en bon accord. Alors que la résistance série R_s obtenue à partir de la fonction Norde est de 1194 Ω. La diode a une bonne propriété de rectification, un comportement photovoltaïque, des propriétés de photodétection et de photoréactivité. La caractérisation électrique et photoélectrique confirme que ce dispositif est un candidat très approprié comme photodiode, applications de photocapteurs et applications optoélectroniques. L'I_{SC} et V_{OC} variaient de 11,12 à 50,73 µA et de 125,33 à 185,22 mV pour diverses illuminations. L'analyse capacitance-fréquence montre que la capacité et la conductance de la diode Al / ZnO / p-Si dépendent de la tension et de la fréquence. Le N_a, ϕ_b et V_{bi} de cette structure sont augmentés avec l'augmentation des fréquences.

Mots clés: Oxyde de Zinc, Couches minces, Nanostructuré, Photocatalyse, Activité antibactérienne, Cellules solaires.

ABSTRACT

The semiconductor heterogeneous photocatalytic technique is a kind of green technology that has been used to solve environmental pollution problems. The present study focuses on the screening of potentially photocatalytic ZnO thin films and nanostructures by using them to degrade organic dyes. Primarily Zinc chloride, nitrate and acetate salts were tested for their photocatalytic activity through the degradation of Red reactive and Methylene Blue (MB) in aqueous solution. The select compounds which are deposited by spray pyrolysis show considerable photodegradation efficiency. The studied different parameters such as concentration of dye, time deposition, salt source and seed layer position have a great effect on the photodegradation of this dye. Hydrothermal ZnO nanostructured were also tested for decolorization of MB and the results are very encourage especially for ZnO Nanorods (acetate salt) and ZnO nanoflowers for water treatment and gas sensing. Undoped and ZnO: Ag NPs films on glass and tissue, which prepared by sol-gel, show the capability of zinc oxide and silver nanoparticles to resist the growth of Gram – of K. pneumonia and E. coli by their inhibition zone which reaches 23 mm. Zinc nitrate as a precursor was used to prepare the Al/ ZnO/p-Si heterojunction by ultrasonic spray in order to investigate the photovoltaic parameters of the solar cell of this device. The I-V measurements indicate that the ideality factor n is 1.39 and the barrier height ϕ_b is 0.67 eV. The ϕ_b from I-V measurement and Norde's function (0.69 eV) are in well agreement. While the series resistance R_s obtained from Norde's function is found 1194 Ω. The diode has a good rectification property, photovoltaic behavior, photosensing and photoresponsivity properties. The electrical and photoelectric characterization confirms that this device is a very suitable candidate as a photodiode, photosensor applications and optoelectronic applications. The I_{SC} and V_{OC} were varied 11.12- 50.73 µA and 125.33- 185.22 mV for various illuminations. The C-V analysis shows that capacitance and conductance of the Al/ZnO/ p-Si diode depends on voltage and frequency. The N_a, ϕ_b and V_{bi} of this structure are increased with the increasing frequencies.

Key words: *Zinc Oxide, Thin films, Nanostructured, Photocatalysis, Antibacterial activity, Solar cells.*